



HAL
open science

Propagation of atoms in a magnetic waveguide on a chip

Satyanarayana Bade

► **To cite this version:**

Satyanarayana Bade. Propagation of atoms in a magnetic waveguide on a chip. Physics [physics]. Université Pierre et Marie Curie - Paris VI, 2016. English. NNT : 2016PA066718 . tel-01927599v1

HAL Id: tel-01927599

<https://theses.hal.science/tel-01927599v1>

Submitted on 20 Nov 2018 (v1), last revised 24 Sep 2019 (v2)

HAL is a multi-disciplinary open access archive for the deposit and dissemination of scientific research documents, whether they are published or not. The documents may come from teaching and research institutions in France or abroad, or from public or private research centers.

L'archive ouverte pluridisciplinaire **HAL**, est destinée au dépôt et à la diffusion de documents scientifiques de niveau recherche, publiés ou non, émanant des établissements d'enseignement et de recherche français ou étrangers, des laboratoires publics ou privés.

**THÈSE DE DOCTORAT
DE L'UNIVERSITÉ PIERRE ET MARIE CURIE**

Spécialité : Physique

École doctorale : "Physique en Île-de-France"

réalisée

à SYRTE, Observatoire de Paris

présentée par

Satyanarayana BADE

pour obtenir le grade de :

DOCTEUR DE L'UNIVERSITÉ PIERRE ET MARIE CURIE

Sujet de la thèse :

**Propagation of atoms in a magnetic waveguide on a
chip**

soutenue le 18/11/2016

devant le jury composé de :

M.	T. Schumm	Rapporteur
M.	N. J. van Druten	Rapporteur
M ^{me}	S. Guellati-Khélifa	Examinatrice
M.	F. Bretenaker	Examineur
M.	C. Westbrook	Examineur
M.	A. Landragin	Membre invité
M.	C. Garrido Alzar	Directeur de thèse

Contents

1	Introduction	1
2	Existing and new configurations of magnetic waveguides	11
2.1	Magneto-static guides	11
2.1.1	Basic waveguide	12
2.1.2	Waveguide with three wires	15
2.1.3	Waveguides with multiple wires	16
2.1.4	Waveguides with curvature	17
2.2	Waveguides with time dependent magnetic fields	18
2.2.1	TOP guides	18
2.2.2	Rf dressed waveguides	24
2.2.3	Waveguide based on TAAPs	28
2.3	Modulated waveguides	30
2.3.1	Roughness due to wire corrugation and the concept of current modulation	30
2.3.2	Waveguide based on induction	32
2.3.3	Modulated TOP: New guide concept for an atom chip	34
2.3.4	Palaiseau solution to remove the waveguide roughness	38
2.4	Conclusion	40
3	Modulated waveguides and simulation of the atom dynamics	41
3.1	Generation of bias field through modulation	41
3.2	Adiabatic guide with tunable radius	42
3.3	Semiclassical simulations of the atom dynamics	45
3.3.1	Determination of a set of guide parameters for stable dynamics	46
3.4	Conclusion	52
4	Matterwave interferometry with propagating atoms	53
4.1	Atom propagation in a toroidal guide	53
4.1.1	Excitation of transverse modes: Classical analysis	54
4.1.2	Excitation of transverse modes: Quantum mechanical analysis	57

4.2	Matterwave interferometry	63
4.2.1	1D interferometer model	65
4.2.2	2D interferometer model	67
4.2.3	Interferometer with thermal atoms	79
4.3	Conclusion	82
5	Description of the experiment and characterisation of cold atom source	83
5.1	Mirror MOT	83
5.2	Experimental setup	85
5.2.1	Optical bench	85
5.2.2	Vacuum chamber	89
5.2.3	Optics for the MOT	91
5.2.4	Bias coils	94
5.2.5	Low noise power supplies	95
5.2.6	Computer control	97
5.2.7	Fluorescence imaging system	97
5.2.8	Absorption imaging system	102
5.3	Characterisation of the cold atom source	107
5.3.1	Phenomenological models	107
5.3.2	Loading rate	109
5.3.3	Lifetime of the MOT	111
5.3.4	Steady state atom number in the MOT	113
5.3.5	Estimation of the temperature	115
5.3.6	Pressure dynamics	118
5.4	Conclusion	121
6	Perspectives & Conclusion	123
6.1	Atom chip	123
6.1.1	Fabrication of the atom chip	124
6.2	Bragg system	127
6.3	Projected experimental sequence	128
6.3.1	U-MOT	128
6.3.2	Optical molasses and optical pumping	129
6.3.3	Z-trap	129
6.3.4	Forced rf evaporation	131
6.3.5	Guided Sagnac interferometer	131

Appendices

Bibliography	141
---------------------	------------

Chapter 1

Introduction

In 1851, Jean Bernard Léon Foucault suspended a pendulum¹ in the *Salle Cassini* (also known as Meridian room), located in the historical building of *Observatoire de Paris*, to demonstrate Earth's rotation. Foucault later coined the term gyroscope to describe an apparatus consisting of a rotor mounted in a gimbal frame (see Fig. 1.1), which he used to provide a simpler demonstration of the Earth's rotation. In the modern usage, a gyroscope is a device that measures a rotation or



Figure 1.1 *A model of the gyroscope built by Foucault in 1852 (Credits: Musée des Arts et Métiers, Paris).*

rotation rate with respect to an inertial frame. Over the past century, gyroscopes have evolved considerably, ever since they were first used as navigational aids. Although, inertial navigation [1] is the main impetus behind the development of gyroscopes, rotation rate sensors also have a place in geophysical studies and fundamental tests of physics. In geophysical measurements, linear displacements of Earth's surface are measured through seismometers. However, the motion of the Earth due to seismic activity can be fully described only by measuring the

¹The so called Foucault's pendulum.

local rotation using a gyroscope [2]. As far as fundamental tests of physics are concerned, Einstein's General Relativity (GR) predicts that a gyroscope orbiting a massive rotating body (for e.g. Earth) undergoes precession with respect to an inertial frame (for e.g. a distant star) due to: Geodetic and frame-dragging effects [3]. These effects were recently verified by the Gravity Probe B (GP-B) satellite launched by NASA. The results of the gyroscopes present in the satellite, confirm the predictions of GR up to few percent [4].

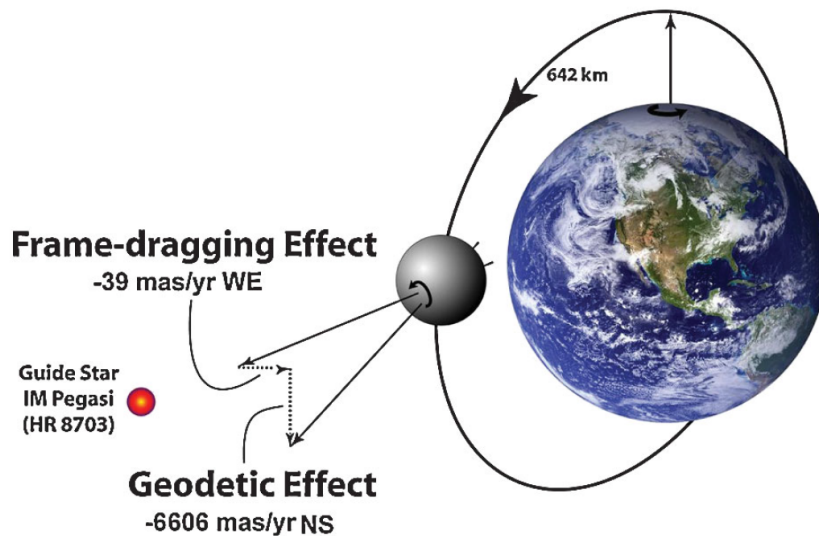


Figure 1.2 *An illustration of the precession of the gyroscope used in GP-B experiment. The precession due to geodetic and frame-dragging effects are orthogonal to each other. Drift rates expressed in units of milliarcseconds/year are measured with respect to the star IM Pegasi [4].*

Today, a wide range of gyroscopes are available at various levels of sophistication and technical specifications. Gyroscopes can be broadly put into one of the following categories:

Mechanical gyroscopes

Mechanical gyroscopes work on the same principle as Foucault's gyroscope and measure rotations. The frictionless gimbal frame holds the rotor and guards it from any external torque, hence the orientation of the rotor remains fixed with respect to an inertial frame due to the law of conservation of angular momentum. If the platform on which the device is mounted rotates, by measuring the angle between the gimbal frame and the axis of the rotor, we can measure the rotation. Since, these gyroscopes use rotating objects, friction between the gimbal frame and the rotor is unavoidable and causes wear and tear. Moreover, friction and

temperature changes lead to a drift in the measured angle.

MEMS gyroscopes

Micro-electro-mechanical-system (MEMS) based gyroscopes make use of the Coriolis force to measure rotations. In these devices, an object of mass m , moving in a rotating frame with a velocity \mathbf{v} experiences a force

$$\mathbf{F} = -2m\boldsymbol{\Omega} \times \mathbf{v} , \quad (1.0.1)$$

where $\boldsymbol{\Omega}$ is the rotation rate of the frame with respect to an inertial frame. If the mass oscillates in a plane, the Coriolis force excites the motion in the orthogonal plane. By measuring the amplitude of the excited motion, we can infer the rotation rate Ω . MEMS based gyroscopes consist of a micro-machined vibrating structure. Thanks to the advances in silicon fabrication technology, MEMS gyroscopes are inexpensive and compact. They are widely used in applications where precision is not needed (e.g. smart phones). The state-of-the-art commercially available MEMS gyroscopes have a sensitivity of about $3 \times 10^{-5} \text{ rad/s}/\sqrt{Hz}$ [5].

Interferometric gyroscopes

Gyroscopes based on the interference phenomena work on the Sagnac effect

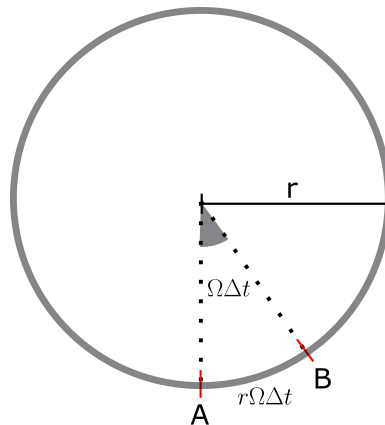


Figure 1.3 *Sagnac effect: light is launched into an optical fibre with a beam splitter located at point A. Due to rotation, the counter propagating photons reach the beam splitter at point B.*

[6]. To understand this effect, let us consider a loop of fibre with radius r as illustrated in Fig.1.3. Suppose that a light beam is launched into the fibre in both, clockwise and counter-clockwise directions using a beam splitter located at point A. If the loop rotates with an angular velocity Ω in the counter-clockwise direction, the light travelling in both directions reach the beam splitter at B (which

is nothing but point A after rotation) with a relative phase shift. This phase shift arises from the different times taken by the clockwise and counter-clockwise light beams to arrive at point B

$$\begin{aligned}\phi_{light} &= 2\pi\omega\Delta t = 2\pi\omega\left[\frac{2\pi r}{c - r\Omega} - \frac{2\pi r}{c + r\Omega}\right] \\ &\approx \frac{8\pi A\Omega}{\lambda c},\end{aligned}\tag{1.0.2}$$

where $A = \pi r^2$ is the enclosed interferometer area. As we can see from Eq.1.0.2, the acquired phase shift ϕ_{light} carries a signature of the rotation rate. A proper explanation of the Sagnac phase shift using electrodynamics can be found in the works of Arditty and Lefèvre [7, 8]. Although the above phase shift is only valid in vacuum, it can be shown that the Sagnac phase shift is independent of the medium in which the light propagates [7]. Note that the Sagnac phase shift increases linearly with the number of loops and it can be increased by winding a large number of loops. Fibre optic gyroscopes benefit from this large scale factor, which enormously increases the sensitivity of the device. For instance, the fibre optic gyroscope developed by iXBlue achieved a sensitivity of $7 \times 10^{-11} \text{ rad/s}/\sqrt{\text{Hz}}$ using a three kilometre long optical fibre [9].

Another closely related gyroscope using light is the ring laser gyroscope, where the counterpropagating modes of a laser in a ring cavity are frequency shifted due to rotation. Here, the angular velocity is related to the frequency difference $\delta\nu$ of the counter propagating modes through the relation [10]

$$\delta\nu = \frac{4A\Omega}{n\lambda_0 L},\tag{1.0.3}$$

where L is the perimeter of the ring laser cavity, λ_0 is the average of the wavelengths of the counter propagating modes and n is the refractive index of the optical medium that fills the cavity². The well-known realisation of this kind of gyroscopes is the giant ring laser gyroscope in Germany, aimed at geophysical studies. It reported a sensitivity of $6 \times 10^{-13} \text{ rad/s}/\sqrt{\text{Hz}}$ with an enclosed area of 16 m^2 [11].

Instead of photons, if we consider the above situation with massive particles like atoms, the resulting phase shift is given by [12]

$$\phi_{atom} = \frac{8\pi m A \Omega}{h},\tag{1.0.4}$$

where m is the mass of the atom. Note that we can obtain ϕ_{atom} from ϕ_{light} by replacing λ with the De Broglie's wavelength of the atom and c with the velocity

²Contrary to the fibre optic gyroscope where the phase shift is independent of the refractive index of the medium.

of atom. If we compare the phase shifts of the interferometers with light and atoms, for the same enclosed area, we get³

$$\frac{\phi_{atom}}{\phi_{light}} = \frac{m\lambda}{hc} = \frac{mc^2}{\hbar\omega} \sim 10^{11} . \quad (1.0.5)$$

This huge ratio highlights the advantage of atom based gyroscopes over optical gyroscopes and it is the driving force behind the development of high precision atom gyroscopes⁴.

Atom gyroscopes

In the 1980's, after the demonstration of the Sagnac effect with neutrons [13] and electrons [14], the experiment of Reihl *et al.* [15] using calcium atomic beams marked the beginning of atom gyroscopes. In 1997, two experiments using independent techniques, reported the measurement of rotation rates, of the order of $\Omega_{Earth} \sim 73 \mu rad/s$. Using nano fabricated gratings to diffract atoms, Lenef *et al.* [16] achieved a short term sensitivity of $3 \times 10^{-6} rad/s/\sqrt{Hz}$, whereas Gustavson *et al.* [17] used two photon Raman transitions to coherently split and recombine atoms (the equivalent of beam splitter) and achieved a short term sensitivity of $2 \times 10^{-8} rad/s/\sqrt{Hz}$. These experiments suggest that Raman transitions offer better control of atoms (hence a better sensitivity) compared to diffraction gratings which require a careful handling. For instance, it is difficult to isolate the gratings from the vibrations of the vacuum chamber. The performance of atomic beam gyroscopes was greatly improved with time, owing to the availability of large atom flux, reaching a short term sensitivity of $6 \times 10^{-10} rad/s/\sqrt{Hz}$ [18].

After achieving results comparable to the state-of-the-art fibre optic gyroscopes, the emphasis shifted towards building atom gyroscopes for practical applications. It became clear that the long term stability of atomic beam gyroscopes, which is important for metrological needs, was limited due to the lack of precise control of the velocity of the atomic beams. Using colder atoms (few micro kelvin) is a way to overcome this limitation. In 2000, a new generation atomic gyroscope experiment, using cold atoms, started at SYRTE. This experiment demonstrated the first cold atom gyroscope capable of measuring rotations and accelerations along the three axes (see Fig.1.4) [19]. The experiment used two counter propagating clouds of Cs atoms with the Raman beams along the three orthogonal directions. The phase shift of the interferometer depends on the acceleration \mathbf{a} and rotation rate $\mathbf{\Omega}$ through the relation

$$\Phi = \mathbf{k}_{eff} \cdot [\mathbf{a} - 2\mathbf{\Omega} \times \mathbf{v}]T^2 , \quad (1.0.6)$$

³Considering an alkali atom and a visible photon.

⁴However, as stated earlier, the scale factor of the fibre optic gyroscopes can be increased by winding more loops and comparable precision can be achieved.

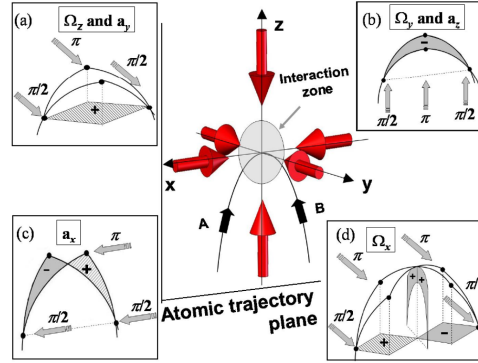


Figure 1.4 Six axis cold atom interferometer developed at SYRTE in 2006. The central image shows the parabolic trajectory of atoms. The images (a)-(d) show the configuration of Raman lasers that make the interferometer sensitive to accelerations and rotations along different directions [19].

where \mathbf{k}_{eff} is the difference between the wavevectors of the Raman beams that split, reflect and recombine the atom clouds. Combining the results of the two interferometers allows to distinguish the effect of accelerations from rotations. In fact, as demonstrated by Dickerson *et al.* [20] two interferometers are not strictly needed to separate the contribution of accelerations from rotation. The presence of the velocity dependent term in the phase shift (see Eq.1.0.6) can be exploited and the velocity dependence can be converted into a position dependence by imaging the atom cloud after some free expansion. The phase shift due to rotation can then be seen as a spatial modulation in the atom density [21].

A problem in cold atom based gyroscopes is the preparation time or dead time (i.e. the time needed for atom trapping and cooling) between two successive measurements, which limits the stability of the device. However, this limitation can be overcome. For instance, a four pulse configuration was recently used to demonstrate a joint operation of the interferometer, by sharing the Raman pulses between two successive measurements (see Fig.1.5). Such a configuration reduces the dead time [23] and this experiment eventually achieved a long term stability of 1 *nrad/s* [22], with an enclosed area of 11 *cm*², to date this is the largest realised area for a cold atom gyroscope. The main limitations of the present day cold atom gyroscopes are: limited interrogation time (which limits the sensitivity) and the distortion of wavefronts of the Raman beams (which affects the stability of the sensor) [24].

Instead of freely falling atoms, which is the case with the above mentioned cold atom gyroscopes, we can guide the atoms by holding them against gravity. Here, the interrogation time will no longer be a limit. Moreover, by controlling the position of the atoms precisely, the effect of wavefront distortion can be minimized.

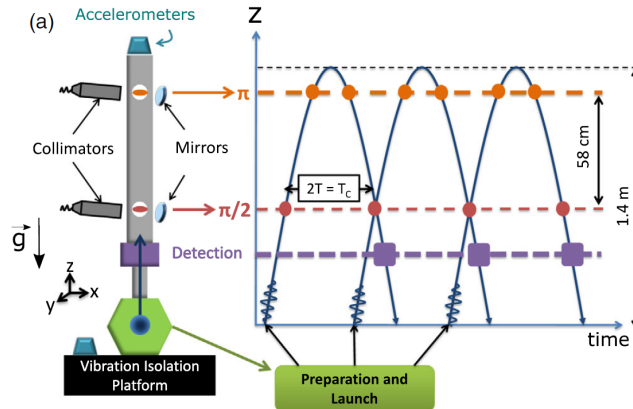


Figure 1.5 A schematic of the joint interrogation sequence using four pulses that removes the dead time of the interferometer [22]. The last $\pi/2$ pulse of a sequence is shared with the first $\pi/2$ pulse of the successive sequence, enabling a continuous operation of the interferometer.

The key elements needed for a guided atom interferometer are: coherent waveguide and beam splitters. Waveguides for atoms can be created by magnetic [25, 26, 27, 28, 29, 30] or optical fields [31, 32, 33]. Interferometers based on guided atoms have already been demonstrated [34, 35, 36], as well as coherent splitting [37]. In table 1.1, a compilation of the related investigations on guided atom interferometers is presented.

	Radius	Method	Support	Temperature	Status	Reference
Strathclyde	4.8 cm	magnetic	coils	BEC	demonstrated	[25]
Strathclyde	~ 5 mm	induction	coils	40 μ K	demonstrated	[38]
Berkeley	1.25 mm	magnetic	coils	22 nK	demonstrated	[26]
Crete	0.4-2.6 mm	rf dressing	coils	2 μ K	demonstrated	[27]
Oxford	0-85 μ m	rf dressing	coils	~ 80 nK	demonstrated	[28]
Georgia Tech	1 cm	magnetic	coils	3.4 μ K	demonstrated	[29]
US Airforce	-	magnetic	chip	-	proposed	[30]
Los Alamos	10&25 μ m	optical	AOD	BEC	demonstrated	[32]
Singapore	~ 550 μ m	magnetic	SC chip	-	proposed	[39]
St. Andrews	10 μ m	optical	LG beam	BEC	proposed	[31]
Queensland	150 μ m	optical	AOD	BEC	demonstrated	[33]

Table 1.1 A list of proposed or demonstrated ring guides around the world. Abbreviations of the terms used in the table: SC= Superconducting, AOD=Acousto optic deflector, LG= Laguerre-Gauss.

GyrAChip project

With a goal to develop a guided Sagnac interferometer using ultra cold atoms, the SYRTE started the gyroscope on an atom chip (GyrAChip) project in 2011.

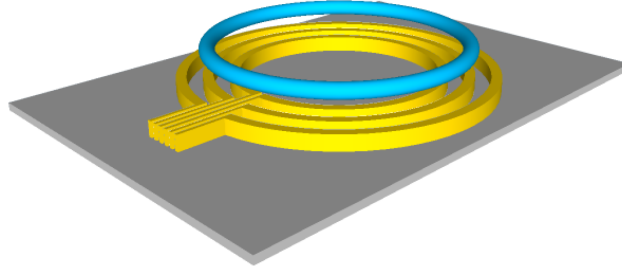


Figure 1.6 *A configuration of wires to generate a circular waveguide using microfabricated wires on an atom chip (credits: Wenhua Yan).*

The long term goal of the project is to establish a roadmap for the realisation of compact and mobile inertial sensors with guided cold atoms on a chip. The project envisages to use a magnetic waveguide (see Fig.1.6) to guide ^{87}Rb atoms in a circular path (analogous to the fibre optic gyroscope), which enables the measurement of angular velocities exploiting the Sagnac effect. Circular waveguides for atoms were demonstrated or proposed using different techniques (Tab.1.6).

In order to address the portability and low power consumption requirements which are essential for practical applications, the experiment is based on an atom chip [40, 41]. The guide is generated from the magnetic fields of micrometer sized wires which help to create a potential with strong confinement. As stated earlier, the interest behind guiding atoms lies in the fact that it permits relatively long interrogation times ($> 1\text{ s}$). The quantum projection noise limited expected sensitivity of the device in terms of interrogation time is given by [42]

$$\delta\Omega = \frac{h\pi^2}{C\sqrt{2N}mv_r^2(2T)^2 \sin(\theta_{lat})}, \quad (1.0.7)$$

where C is the contrast of the interferometer, N the atom number, v_r the launch velocity, $2T$ the interrogation time and θ_{lat} the latitude of the place where the device is located⁵. To have an order of magnitude of the expected sensitivity, let us consider a guide of radius $500\ \mu\text{m}$, with 10^4 atoms, launched at a velocity of $2v_r = 11\ \text{mm/s}$. Under these conditions, we get a short term sensitivity of $3.4 \times 10^{-8}\ \text{rad/s}/\sqrt{\text{Hz}}$ for an interrogation time of 3 seconds (or 12 turns around the guide). Alternatively, by using large momentum transfer techniques [43], the atoms can be launched at higher velocities and similar sensitivity can be obtained by reducing the duration of the interferometer (interrogation time).

The goal of this thesis is to study the propagation of atoms in a magnetic waveguide. The principle of the GyrAChip waveguide, based on the current modulation technique [44] is discussed in Chapter 3. An important emphasis is given to the understanding of the effects of the guiding potential on the Sagnac

⁵Assuming that the experiment is measuring Earth's rotation rate.

phase and the contrast of the interferometer. A model for a completely trapped Sagnac interferometer, considering the trapping potential was recently discussed by Stevenson *et al.* [45]. To our knowledge, for a guided Sagnac interferometer (where the azimuthal direction is free) a similar study does not exist in the literature. We quantify the systematic effects arising from the guiding potential with a simple model both for an ultra cold gas and a thermal gas. On the experimental side, the thesis describes the realisation and characterisation of a cold atom source and the atom detection systems. This thesis is organised as follows:

Chapter 2: Existing and new configurations of magnetic waveguides

Microfabricated atomic waveguide is a very key aspect of this experiment. Physical principles of the magnetic waveguides are discussed in this chapter. A review of the existing waveguide technology is presented with a special emphasis on circularly symmetric waveguides. Two configurations of already demonstrated guides using macroscopic coils are presented with a discussion on how to implement them with three wires on an atom chip.

Chapter 3: Novel modulated waveguide and simulation of atom dynamics

A novel configuration to generate circular guide with a combination of the magnetic fields from three wires on an atom chip and an external bias field perpendicular to the chip is presented. An important aspect of the guide is the use of alternating currents for the atom chip wires. This technique allows to simultaneously solve the problem of Majorana losses and coherence loss due to wire corrugation, thus overcoming a major technical challenge for waveguides based on atom chips. Results of a numerical simulation of classical atom dynamics in the modulated potential taking into account the spin dynamics are discussed.

Chapter 4: Matterwave interferometry with propagating atoms

Atom propagation in a toroidal guide is addressed both classically and quantum mechanically assuming that the radial potential of the waveguide is harmonic. Atom motion is shown to be multimode. A model for guided atom interferometer neglecting the inter-atomic interactions is discussed to quantify the effects of multimode propagation both, for an ultra cold gas and a thermal gas.

Chapter 5: Description of the experiment and the characterisation of cold atom source

This chapter presents an overview of the experimental apparatus as of now. Schematics of the optics to realize the mirror Magneto Optical Trap (MOT),

florescence imaging system, and absorption imaging system and their characterisation are discussed here. A detailed characterization of the cold atom source and a study of the pressure dynamics during the MOT phase of the experiment are also presented here.

Chapter 6: Perspectives & Conclusion

This chapter discusses the physical design of the first atom chip of the experiment and its fabrication. We present the detailed process used in its realisation, taking into account critical problems such as the power dissipation by ohmic heat and the quality of the microfabricated wires. We also present a schematic of the Bragg system that will be employed to realise the beam splitter for the guided wavepackets. A simulation of the cooling trap potential is presented, together with the projected experimental sequence to produce the ultra cold atom sample. Finally, we present an illustration of the wire configuration that will be used to generate the ring guiding potential.

Chapter 2

Existing and new configurations of magnetic waveguides

The use of magnetic fields to control the motion of atoms dates back to early 1920s. In the seminal Stern-Gerlach experiment [46], neutral silver atoms were deflected by a non-uniform magnetic field. A paramagnetic atom with magnetic moment $\boldsymbol{\mu}$, placed in an inhomogeneous field $\mathbf{B}(\mathbf{r})$, experiences a force

$$\mathbf{F} = \nabla(\boldsymbol{\mu} \cdot \mathbf{B}(\mathbf{r})) . \quad (2.0.1)$$

The interaction energy between the field and the atom is given by $V(\mathbf{r}) = -\boldsymbol{\mu} \cdot \mathbf{B}(\mathbf{r})$, where the magnetic moment for an atom with total spin \mathbf{F} is, $\boldsymbol{\mu} = -\mu_B g_F \mathbf{F}$ ¹. If the magnetic moment is aligned (or anti aligned) with the magnetic field, the atom is said to be a high (or low) field seeker as the atom is attracted towards a region of high (or low) magnetic field in order to minimize the interaction energy. Therefore, atoms gather either at the maxima or minima of magnetic field depending on the relative orientation of the atomic moment with the local field.

2.1 Magneto-static guides

Maxwell's equations do not allow local maxima in a static magnetic field. Hence it is only possible to trap low field seekers using static fields [47]. However, a high field seeking atom orbiting around a current carrying wire can be trapped due to the balance between the centripetal and the magnetic forces [48, 49]. For example, ⁸⁷Rb atoms in $|F = 2, m_F = 1, 2\rangle$ or $|F = 1, m_F = -1\rangle$ states are low field seekers (since $g_F m_F > 0$) and hence are trappable in a static field. If the atomic spin follows the magnetic field adiabatically, the interaction potential is proportional to the field magnitude. Therefore, under this adiabatic assumption,

¹ g_F is the Landé factor.

designing a potential amounts to designing a magnetic field of the corresponding shape. Magnetic fields for atom trapping (or guiding) can be produced by macroscopic coils or with microfabricated wires on a chip. Magnetic traps with miniaturized wires were first proposed by Weinstein *et al.* [50] and they offer interesting possibilities to explore low dimensional physical effects (collisions, phase transitions etc.), given the achievable strong confinements due to the close proximity of atoms to the chip surface. In the following sections, waveguides based on static fields generated from microfabricated wires are discussed.

2.1.1 Basic waveguide

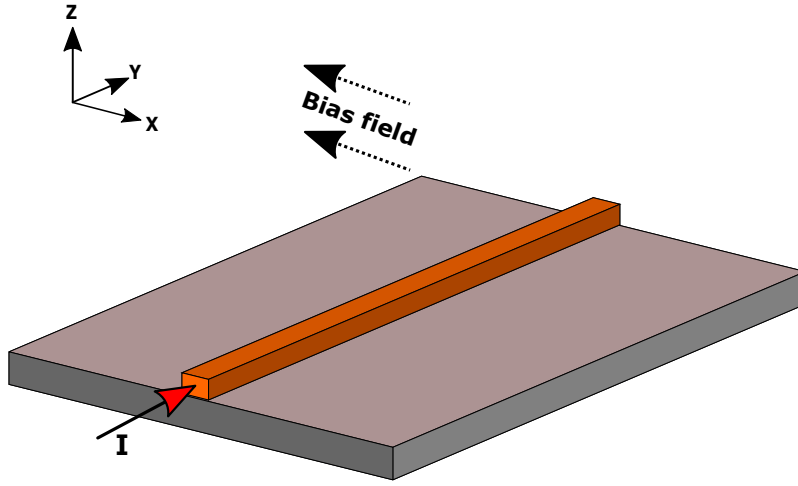


Figure 2.1 A simple configuration to generate a linear waveguide.

A linear quadrupole waveguide can be obtained by superimposing a homogeneous bias field perpendicular to a current carrying conductor [51]. This configuration is often referred as a side guide. The position of the guide depends on the current intensity in the conductor and the strength of the external bias field B_0 . If we assume that the conductor is infinitesimally thin and infinitely long, the magnetic field due to the conductor is exactly cancelled by the bias field along a line located at a distance

$$d = \frac{\mu_0 I}{2\pi B_0}, \quad (2.1.1)$$

above the conductor. For a given current in the conductor, the position of the guide can be controlled by changing the magnitude and the direction of the bias field. The field gradient b , at the guide centre, is given by

$$b = \frac{\mu_0 I}{2\pi d^2}, \quad (2.1.2)$$

hence strong field gradients can be obtained by applying a strong bias field. In the vicinity of the guide centre, the field can be approximated up to first order in

coordinates as $\mathbf{B}(\mathbf{r}') = bx'\mathbf{i}' - bz'\mathbf{k}'$ (note that $\nabla \cdot \mathbf{B}(\mathbf{r}') = 0$) in a reference system where the axes coincide with the symmetry axes of the quadrupole field. The strength of the field depends only on the distance from the guide centre and it possesses a cylindrical symmetry about the guide centre. As the atoms move in

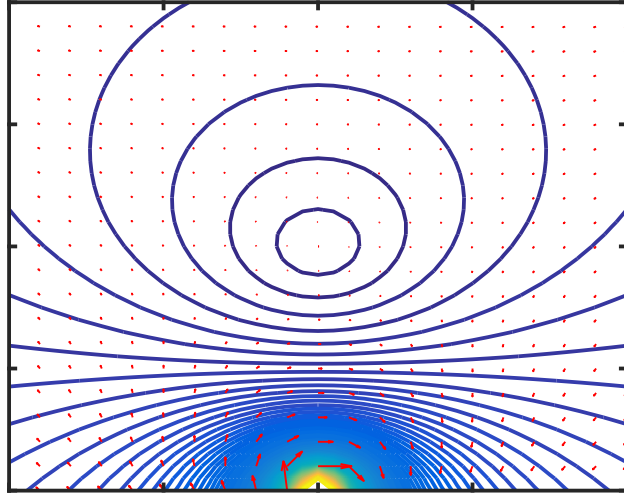


Figure 2.2 *Iso-B contours and field lines of a side guide.*

a direction transverse to the guide, their spin precesses about the local magnetic field at Larmor frequency $\omega_L = \mu_B g_F m_F |\mathbf{B}(\mathbf{r}')|$. Classically speaking, if the rate of change of the local magnetic field direction θ is less than the Larmor frequency ($\mathbf{v} \cdot \nabla \theta = |\dot{\theta}| \ll \omega_L$), atoms adiabatically follow the direction of the field while preserving the spin component along the local magnetic field. Adiabatic following is often violated in the regions where the magnetic field is weak, especially near the guide centre, resulting in the loss of atoms due to spin flips (also called Majorana losses) to an untrapped state. If we consider an atom orbiting with a speed v at a distance r from the guide centre, the direction of the field changes by 2π for every rotation. The rate of change of direction evaluates to v/r and the Larmor frequency is $\mu_B g_F m_F b r / \hbar$. Using the adiabaticity criteria we obtain the following condition for a stable orbit

$$r > \left(\frac{\hbar v}{\mu_B g_F m_F b} \right)^{\frac{1}{2}}. \quad (2.1.3)$$

Therefore, in a linear quadrupole guide the adiabaticity criteria fails within a circle of radius $r_0 = (\hbar v / \mu_B g_F m_F b)^{1/2}$. Early experiments with cold atoms loaded in quadrupole traps reported a lifetime of few milliseconds, making them impossible to trap very cold atoms. The energy spectra and the resonance widths that characterise the lifetime of the eigen states of a quadrupole trap were computed

by Bergeman *et al.* [52, 53] it was shown that the atoms in a low angular momentum number state have lower lifetime compared to the atoms with a higher angular momentum number state as the probability of finding the atom near the guide centre increases while the angular momentum quantum number decreases. The quantized motion of atoms in a quadrupole waveguide was analysed by Hinds *et al.* [54, 55, 56], where it was shown that the quadrupole guide does not contain any stable bound state for spin 1/2 and spin 1 atoms and all the low lying quasi bound states have a finite lifetime. In order to overcome atom losses, a constant bias field B_{bias} is usually added along the guide. A strong bias field provides a constant orientation to atomic spin, hence reduces the spin flip losses. The spin flip rate was shown to drop exponentially with the magnitude of the bias field [57]. The potential experienced by the atoms in a quadrupole field in the presence of the additional bias field is given by $V(\mathbf{r}') = -\boldsymbol{\mu} \cdot \mathbf{B}(\mathbf{r}')$, where $\mathbf{B}(\mathbf{r}') = bx'\mathbf{i}' - bz'\mathbf{k}' + B_{bias}\mathbf{j}$. Under the adiabatic approximation, the potential simplifies to $V(\mathbf{r}) = |\boldsymbol{\mu}||\mathbf{B}(\mathbf{r})|$ (here \mathbf{r} denotes the position in the coordinate system shown in Fig.2.2, which is rotated by 45° with respect to the primed coordinates) i.e.

$$V(\mathbf{r}) = \mu_B g_F m_F \sqrt{b^2(x^2 + z^2) + B_{bias}^2} , \quad (2.1.4)$$

Near the guide centre where $b(\sqrt{x^2 + z^2}) \ll B_{bias}$, the potential can be Taylor expanded resulting in a harmonic potential

$$V(\mathbf{r}) \approx \mu_B g_F m_F B_{bias} \left[1 + \frac{1}{2} \frac{b^2(x^2 + z^2)}{B_{bias}^2} \right] , \quad (2.1.5)$$

with a trap frequency $\omega_{trap} = b\sqrt{\mu_B g_F m_F / m B_{bias}}$. The bias field modifies the form of the transverse potential from linear to quadratic. For an atom in the transverse ground state (i.e. for a BEC ²), the Majorana loss rate is given by [57]

$$\gamma = \frac{\omega_{trap}}{2\pi} e^{-\frac{2\mu_B B_{bias}}{\hbar\omega_{trap}}} . \quad (2.1.6)$$

Note that the trap frequency is tunable with the bias field, lifetime of the guide increases with the bias field at the cost of a reduction in the trap frequency. If the effect of earth's gravity is included, the total potential is given by

$$V(\mathbf{r}) = \mu_B g_F m_F B_{bias} + \frac{1}{2} m \omega_{trap}^2 (x^2 + z^2) - mgz , \quad (2.1.7)$$

which can be rewritten as

$$V(\mathbf{r}) = \mu_B g_F m_F B_{bias} + \frac{1}{2} m \omega_{trap}^2 \left[x^2 + \left(z - \frac{g}{\omega_{trap}^2} \right)^2 \right] - \frac{1}{2} m \frac{g^2}{\omega_{trap}^2} . \quad (2.1.8)$$

²For a thermal atom cloud at temperature T , Majorana loss rate is $\gamma = \frac{\hbar\omega_{trap}^2}{4\pi k_B T} e^{-\frac{\mu_B B_{bias}}{k_B T}}$.

Therefore, gravity does not change the form of the potential it merely shifts the position of the minimum potential by an amount g/ω_{trap}^2 . For example, in a guide with a radial trap frequency of 1 kHz , the potential minimum gets displaced by $0.27\ \mu\text{m}$ due to gravitational force. Hence the influence of the gravity needs to be taken into account depending on the strength of the field gradient and the bias field.

2.1.2 Waveguide with three wires

Using an atom-chip the bias field necessary to create the guide can be easily generated by two additional wires located on the chip [58], meaning that the guide can be created entirely from the wires on a chip. Consider three wires that are parallel to y -axis located at $x = 0$, $x = l$ and $x = -l$, as indicated in Fig.2.3.

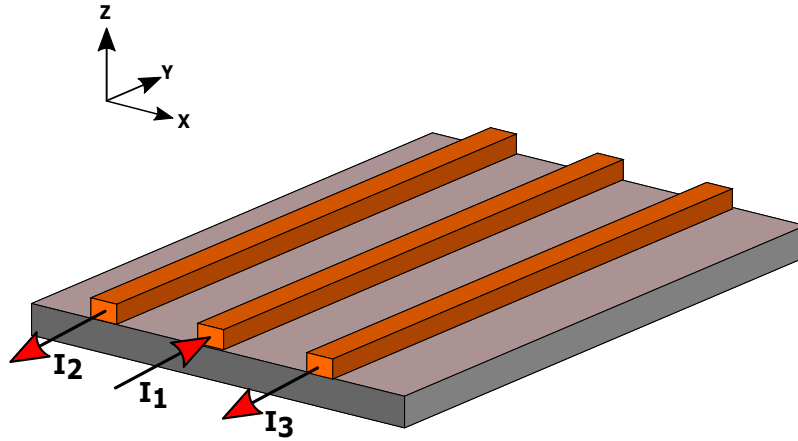


Figure 2.3 Configuration of currents to generate a waveguide with 3 wires.

If the direction of the currents in the external wires is opposite to that of the central wire, a bias field is generated by the external wires. If the wires carry currents I_1, I_2, I_3 respectively, a linear guide is formed at a location given by the coordinates

$$x = \frac{l}{2} \frac{I_2 - I_3}{I_2 - I_1 + I_3}, \quad z = \frac{l}{2} \frac{\sqrt{4I_2I_3 - (I_2 - 2I_1 + I_3)^2}}{I_2 - I_1 + I_3}. \quad (2.1.9)$$

The guide coordinates scale linearly with the separation between the wires l , which is usually few tens of microns. The position of the guide can be varied considerably by changing the current intensities in the three wires under the constraint $4I_2I_3 > (I_2 - 2I_1 + I_3)^2$. If the two external wires carry the same current i.e. when $I_2 = I_3$ a guide is formed at a distance $d = l\sqrt{I_1/2I_2 - I_1}$

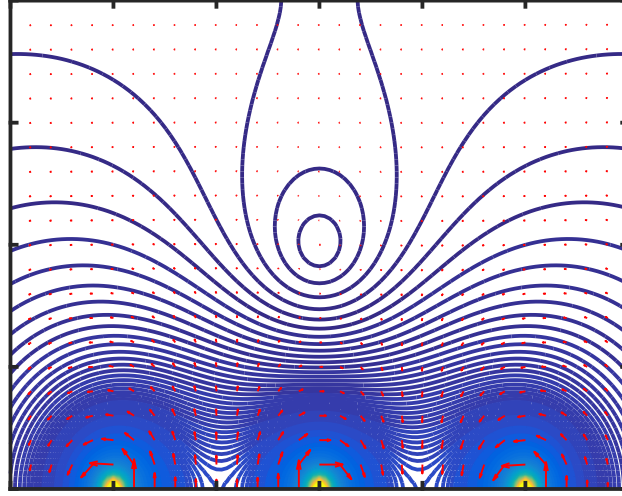


Figure 2.4 *Iso-B contours and field lines of a three wire guide with equal but opposite currents between adjacent wires.*

above the central wire. The field gradient close to the guide centre is given by

$$b = \frac{2\mu_0 I_2 l^2}{\pi(l^2 + d^2)^2} . \quad (2.1.10)$$

A bias field may be added along the guide to stabilize the guide against Majorana losses.

2.1.3 Waveguides with multiple wires

The bias field for the guide can in fact be created by multiple wires. Linear guides using four or five wires offer relatively tighter confinement as steeper field gradients can be generated. They have already been proposed [59] and demonstrated [60, 61]. Let us consider four wires parallel to the y -axis, with the inner wires located at $x = -l$ and $x = l$ and the external wires at $x = -\alpha l$ and $x = \alpha l$. Let the currents in the inner wires be $I_2 = I$ and $I_3 = -I$ and the currents in the external wires be $I_1 = -\beta I$ and $I_4 = \beta I$. A linear guide is formed along the y -axis at a location given by the coordinates

$$x = 0 , \quad z = \frac{l}{2} \sqrt{\frac{\alpha - \beta}{\beta - 1/\alpha}} . \quad (2.1.11)$$

The field gradient close to the centre of the guide is

$$b = \frac{\mu_0 I}{2\pi l^2} \frac{16}{(\alpha^2 - 1)^2 \beta} \sqrt{(\alpha\beta - 1)^5 (1 - \beta/\alpha)} . \quad (2.1.12)$$

The gradient of the quadrupole field attains an optimum value for $\beta_{opt} = u(u + \sqrt{1 + u^2/2})$ with $u = (3\alpha^2 - 1)/8\alpha$. Therefore, for a given separation between the external wires and a given current in the internal wires, optimum gradient can be obtained by running $\beta_{opt}I$ in the external wires.

A hexapole waveguide can be generated using five wires, the possibility of having more zeros allows to split the atom cloud into two by varying the currents responsible for the guide. In Esteve *et al.* [61], all the five wires were connected in series and in this particular configuration we have common noise rejection in the magnetic field generated by the five wires. Consider five wires that are located at $x = -3l$, $x = -l$, $x = 0$, $x = l$ and $x = 3l$.

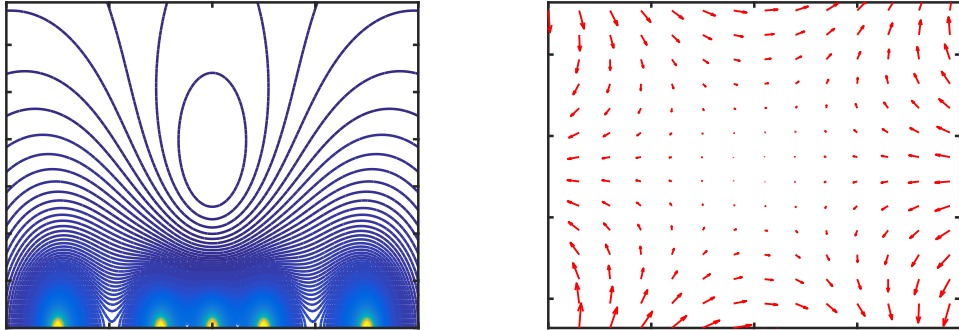


Figure 2.5 *Iso-B contours and magnetic field lines of a hexapole guide generated with five wires.*

By passing equal but opposite currents between any two adjacent wires a guide is formed at a distance $d = \sqrt{3}l$ above the central wire. Splitting is achieved by ramping up the current in the central wire while decreasing the current in the outer pair of wires. In general, with n parallel wires on a chip utmost n zeros exist [62].

2.1.4 Waveguides with curvature

A curved waveguide can be obtained by simply bending the wires on the chip. However, there are some difficulties: a) the bias field that is necessary to suppress Majorana losses can be challenging to apply along the guide, b) the terminals through which currents are supplied to the wires can perturb the symmetry of the potential. Sauer *et al.* [29] demonstrated guiding of atoms in a ring waveguide of diameter 2cm , generated from two wires with co-propagating currents. A guide is formed between the wires, atoms were shown to go around the ring guide upto seven times. Luo *et al.* [63] demonstrated an omnidirectional spiral guide with

two wires arranged in spiral geometry with counter propagating currents, and a bias field perpendicular to the chip surface resulting in a quadrupole guide. Using this configuration, thermal atoms were guided for more than two turns in the spiral guide with a radius of curvature as short as $200 \mu m$. Atoms spiralled inwards and outwards after hitting the barrier at the centre of the spiral. The problem of Majorana losses is not addressed in both these guides and hence are not suitable to guide ultra cold atoms or a BEC. To overcome the perturbing effects of the terminals some elegant solutions were already proposed [64, 30, 65]. It is worth mentioning that in the proposal of Baker *et al.* [30] the ring waveguide is based on a multilayered chip with seven concentric wires, such that the terminals of a set of three wires lie on one end of the guide and the terminals of the remaining four wires lie on the diametrically opposite end of the guide. As the atoms approach a set of terminals, the atoms are adiabatically loaded to a ring guide created by the wires from the farthest terminals, minimizing the perturbation. Jiang *et al.* [65] proposed a ring guide using an Archimedean spiral. Another promising approach to reduce the terminal effect is to generate currents in a perfect loop through magnetic induction [66]. This configuration will be discussed in another section. In the following section, a strategy to generate the rotating field in an integrated way using the three wire configuration (Fig.2.3) on an atom chip is discussed in detail.

2.2 Waveguides with time dependent magnetic fields

By employing time dependent magnetic fields, traps can be realized both for high field and low field seekers [67, 68, 69, 70]. Trapping or guiding potentials created with time dependent fields can be divided into two categories depending on the frequency at which the fields oscillate: i) if the oscillation frequencies are well below the Larmor frequency, atoms experience a potential which is the time-average of the instantaneous potential; ii) if the oscillation frequencies approach the Larmor frequency, atoms experience a 'dressed potential'. In the subsequent sections, both kinds of these potentials are discussed at length. Time orbiting potentials (TOP) fall in the former category, whereas radio frequency (rf) guides belong to the latter. We end the section describing time averaged adiabatic potentials (TAAPs) which combine both these regimes.

2.2.1 TOP guides

The problem of Majorana losses associated with linear quadrupole traps can be circumvented by introducing a rotating magnetic field which moves the zero of the magnetic field in a circle of radius $r = B_0/b$, where B_0 is the strength of the rotating magnetic field. If the magnetic field is rotated fast enough compared to the time scale of the motion, atoms do not have the time to respond to the

instantaneous potential and experience a time averaged potential. This configuration often called as a TOP trap allowed for the creation of the first BEC by increasing the lifetime of a quadrupole trap [71, 72]. Similarly, waveguides with-

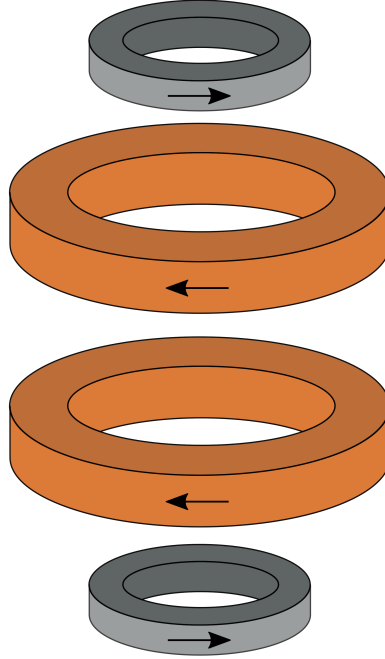


Figure 2.6 A configuration of coils to generate a TORT guide [26].

out Majorana losses can be created by adding a rotating bias field in a direction transverse to the guide. An idea to create a circular waveguide with this strategy was proposed by Arnold [73] using coplanar or coaxial loops and is referred as a time orbiting ring trap (TORT). For instance a ring guide can be produced by two pairs of coaxial coils in Helmholtz configuration such that the field due to one pair opposes the field due to the other pair to create a ring of zeros. The mechanism to rotate the zeros can be understood by considering the general form of a cylindrically symmetric magnetic field Taylor expanded about a point which can be taken as origin [74]

$$\mathbf{B}(\mathbf{r}, \mathbf{z}) = \left[-\frac{B_1 r}{2} - \frac{B_2 r z}{2} \right] \mathbf{r} + \left[B_3 + B_1 z + \frac{B_2}{2} \left(z^2 - \frac{r^2}{2} \right) \right] \mathbf{k}. \quad (2.2.1)$$

If $B_3 B_2 > 0$, the position of the ring of field zeros is given by the coordinates

$$r_0 = \sqrt{\frac{4B_3}{B_2} - \frac{2B_1^2}{B_2^2}}, \quad z_0 = -\frac{B_1}{B_2}. \quad (2.2.2)$$

The above expressions suggest that the field zeros can be moved axially by a homogeneous field (B_3) and radially by a quadrupole field (B_1). Hence the field

zeros can be rapidly moved in a closed trajectory by oscillating the homogeneous field and the quadrupole field with a properly chosen phase relationship between them. Both these fields can be produced by adding ac currents to the two pairs of coils (see Fig.2.6). A thermal cloud of about 2×10^7 atoms was successfully loaded in a few millimeter sized TORT and were evaporatively cooled to produce a BEC of 6×10^5 atoms [26]. A TOP waveguide with microstructured wires was first suggested in Luo *et al.* [63], but has not been experimentally demonstrated until now. Another way to create a linear quadrupole guide is using two wires

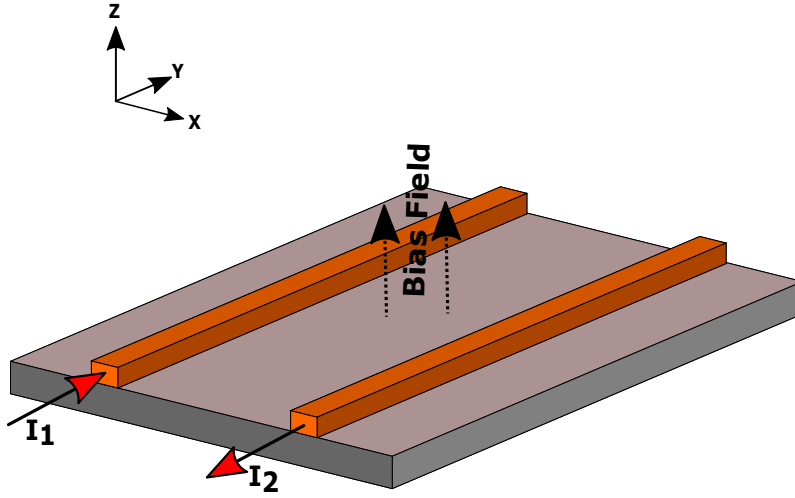


Figure 2.7 Configuration of currents and bias field to generate a quadrupole guide with two wires.

carrying counter propagating currents and an additional bias field perpendicular to the surface of the chip. Let the wires be at $x = -l$ and $x = l$, with constant currents I_1, I_2 respectively and a bias field B_0 along z-axis as shown in Fig.2.7. For this geometry, a guide is formed at

$$x = \frac{\mu_0}{4\pi B_0}(I_1 - I_2) , \quad (2.2.3)$$

$$z = \sqrt{\frac{\mu_0}{2\pi B_0}(I_1 + I_2)l - \frac{\mu_0^2}{16\pi^2 B_0^2}(I_1 - I_2)^2 - l^2} , \quad (2.2.4)$$

if and only if $8\pi B_0 \mu_0 (I_1 + I_2)l - 16\pi^2 B_0^2 l^2 - \mu_0^2 (I_1 - I_2)^2 > 0$. If the currents in both wires are equal, the guide is formed exactly halfway between the wires at a distance $d = l\sqrt{\mu_0 I / \pi B_0 l - 1}$ above the chip surface and the bias field must be less than a critical value given by $B_c = \mu_0 I / \pi l$. The magnitude of the field gradient at the guide centre is $b = (2\pi B_0^2 / \mu_0 I)\sqrt{I/I_0 - 1}$, with $I_0 = \pi B_0 l / \mu_0$. The position of the guide centre can be moved by adding an alternating current in each wire of frequency ω with an amplitude I_m and a phase difference of $\pi/2$ between them, i.e. by choosing $I_1 = I + I_m \sin \omega t$ and $I_2 = I - I_m \cos \omega t$. The

position of the field zero as a function of time is given by

$$x = \frac{\mu_0 I_m}{2\sqrt{2}\pi B_0} \sin\left(\omega t + \frac{\pi}{4}\right), \quad (2.2.5)$$

$$z = d \sqrt{1 + \frac{\mu_0 I_m l}{\sqrt{2}\pi B_0 d^2} \sin\left(\omega t - \frac{\pi}{4}\right) + \frac{\mu_0^2 I_m^2}{8\pi^2 B_0^2 d^2} \sin^2\left(\omega t + \frac{\pi}{4}\right)}. \quad (2.2.6)$$

From the above equations it is evident that the x coordinate varies about the centre of the guide with an amplitude proportional to the amplitude of the oscillating current and the z coordinate varies periodically about d . Therefore, the guide moves typically in a region of size $r_0 \approx \mu_0 I_m / \sqrt{2} B_0$. If the amplitude of the modulation is small, i.e. $I_m \ll I$, Taylor expansion of z upto first order in I_m gives

$$x = \frac{\mu_0 I_m}{2\sqrt{2}\pi B_0} \sin\left(\omega t + \frac{\pi}{4}\right), \quad z = d + \frac{\mu_0 I_m}{2\sqrt{2}\pi B_0} \sin\left(\omega t - \frac{\pi}{4}\right). \quad (2.2.7)$$

Therefore, the position of the zero moves approximately in a circle of radius $r_0 = \mu_0 I_m / 2\sqrt{2}\pi B_0$. If the distance between the guide and the chip surface is half the separation between the wires, i.e. $d = l$, the trap frequency is given by,

$$\omega_{trap} = \frac{2\pi}{\mu_0} \sqrt{\frac{g_F m_F \mu_B B_0^3}{\sqrt{2} m I I_m}}, \quad (2.2.8)$$

and the Larmor frequency at the centre of the guide is,

$$\omega_L = \frac{g_F m_F \mu_B}{\sqrt{2} \hbar} \frac{I_m}{I}. \quad (2.2.9)$$

In this situation, the radius of the circle simplifies to $r_0 = (\sqrt{2} I_m / I) l$. The trap depth, which is defined as the difference between the time-averaged potentials at a distance r_0 and the guide centre

$$V_{depth} = \left(\frac{4}{\pi} - 1\right) \frac{I_m}{\sqrt{2} I} g_F m_F \mu_B B_0. \quad (2.2.10)$$

For the adiabaticity condition to be fulfilled the guide parameters have to be chosen such that $\omega_{trap} \ll \omega \ll \omega_L$, the first inequality ensures that the modulation does not lead to transverse mode excitations, whereas the second inequality concerns the adiabatic following of the spin.

Waveguides based on two wires with counter propagating currents need an external bias field perpendicular to the chip surface. The external bias field can be avoided altogether and a TOP guide can be generated using the three wire configuration. Consider the linear waveguide with currents I_1 and $I_2 = I_3 = I$. A quadrupole guide is formed at a distance $d = l \sqrt{I_1 / (2I - I_1)}$ from the chip

surface. The zero can be moved around by a rotating field in the transverse direction, which can be generated by adding oscillating currents to the external wires with a phase difference of $\pi/2$ i.e. by choosing $I_2 = I + I_m \sin(\omega t)$ and $I_3 = I - I_m \cos(\omega t)$. If the amplitude of the oscillating current is small i.e. if $I_m \ll 2I - I_1$. The position of the field zero can be obtained by a Taylor expansion of the exact expression, and upto first order in I_m , it gives

$$x \approx \frac{l}{\sqrt{2}} \frac{I_m}{2I - I_1} \sin(\omega t + \pi/4), \quad z \approx d + \frac{d}{\sqrt{2}} \frac{I_m}{2I - I_1} \sin(\omega t - \pi/4). \quad (2.2.11)$$

As the fields generated by the two external wires near the guide centre are not orthogonal, the rotating field's magnitude changes with time. Therefore, the zero of the field moves nearly in an ellipse around the guide centre. However, if the dc currents in all the three wires are chosen to be equal i.e. $I_1 = I$. The guide is formed at a distance l above the chip surface, which is equal to the separation between the wires. And the fields due to the external wires are orthogonal with equal magnitude, in which case the field zero moves in a nearly circular trajectory of radius $r_0 = (I_m/\sqrt{2}I)l$. If we consider, for example, three straight wires separated by $15 \mu\text{m}$, the central wire carrying a current of $I = 30 \text{ mA}$, and the external ones carrying an ac current of amplitude 2 mA , the field zero rotates in a circle of radius $2 \mu\text{m}$ (see Fig.2.8). Magnetic field lines around the

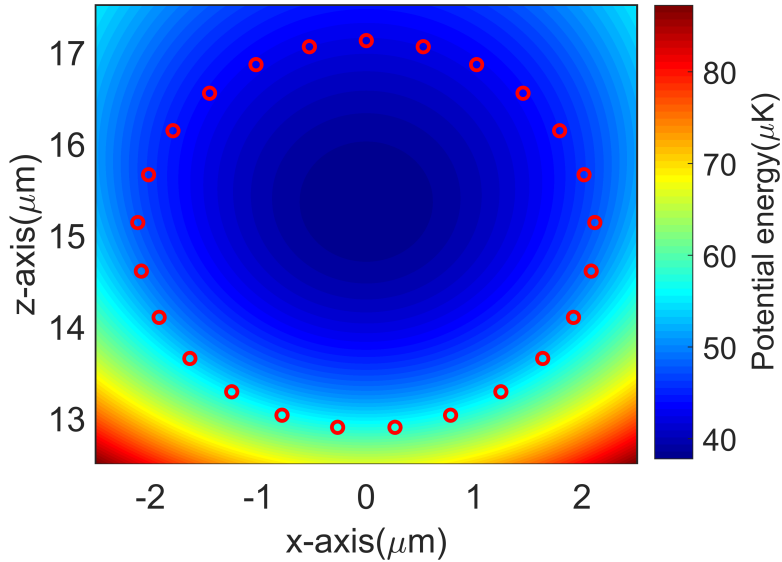


Figure 2.8 *Time-averaged potential of a TOP guide generated from three straight wires with $I = 30 \text{ mA}$, $I_m = 6 \text{ mA}$ and $l = 15 \mu\text{m}$. The red \circ 's show the trajectory of the instantaneous field zeros, trap depth is approximately $20 \mu\text{K}$.*

TOP guide centre for the above mentioned parameters can be seen in Fig.2.9.

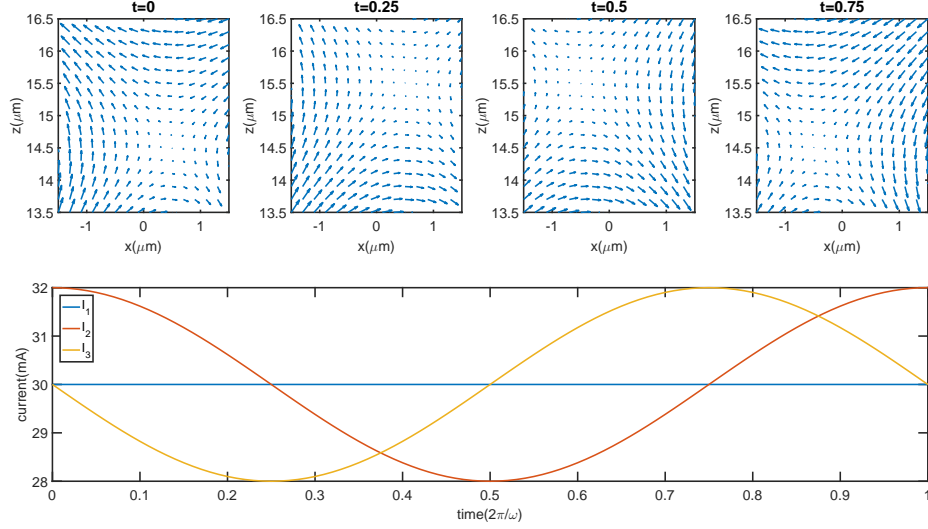


Figure 2.9 *Field lines due to TOP guide created by three wires, at times $t = \pi/2\omega$, π/ω , $3\pi/2\omega$, $2\pi/\omega$. We consider the parameters: $I = 30$ mA, $I_m = 2$ mA and $l = 15$ μm . The variation of currents in the central and external wires over one modulation period can be seen in the bottom figure.*

The magnitude of the rotating bias field is given by $B_0 = \mu_0 I_m / 2\sqrt{2}\pi l$. The field close to the guide can be expressed as

$$\mathbf{B}(x, z, t) = (bz + B_0 \sin(\omega t - \pi/4)) \mathbf{i} + (bx + B_0 \sin(\omega t + \pi/4)) \mathbf{k}, \quad (2.2.12)$$

where the field gradient is $b = \mu_0 I / 2\pi l^2$. The Larmor frequency at the trap centre is

$$\omega_L = \frac{\mu_B g_F m_F}{\hbar} \frac{\mu_0 I_m}{2\sqrt{2}\pi l}. \quad (2.2.13)$$

If the oscillating currents are modulated fast enough (i.e. $\omega_{trap} \ll \omega \ll \omega_L$), atoms experience a time-averaged potential which is approximately harmonic with a trap frequency given by

$$\omega_{trap} = \frac{I}{l^{3/2}} \sqrt{\frac{\mu_0 \mu_B g_F m_F}{2\sqrt{2}\pi m I_m}}, \quad (2.2.14)$$

and the depth of the trap which is the difference between the potential energy at the guide centre and the potential energy over the circle of death, depends solely on the amplitude of the oscillating currents in the external wires. This energy is given by

$$V_{depth} = \left(\frac{4}{\pi} - 1\right) \frac{\mu_B g_F m_F}{2\sqrt{2}\pi} \frac{\mu_0 I_m}{l}. \quad (2.2.15)$$

$l(\mu m)$	$I(mA)$	$I_m(mA)$	$\omega_L/2\pi(MHz)$	$\omega_{trap}/2\pi(kHz)$	$r_0(\mu m)$	$V_{depth}(\mu K)$
15	250	100	13.19	6.52	4.24	158.32
15	200	100	13.19	5.22	5.33	158.32
30	300	120	7.91	2.52	8.48	94.99
30	300	150	9.89	2.26	10.60	118.74
50	200	100	3.95	0.85	17.67	47.49
50	300	120	4.75	1.17	14.14	56.99
50	300	150	5.93	1.05	17.67	71.24

Table 2.1 *Characteristics of a TOP guide generated using three wires for a set of experimentally realisable parameters using atom chip for a ^{87}Rb atom in $|F = 2, m_F = 2\rangle$ state.*

The guide parameters can be varied over a considerable range by adjusting the separation between the wires and the currents in the wires (see Table 2.1). For instance, if we take a wire separation of $15 \mu m$ by passing $200 mA$ of dc currents in the three wires and with a modulating current of $100 mA$ in the external wires, we can obtain a very tight ($\omega_{trap}/2\pi = 5.2 kHz$) and deep guide ($V_{depth} = 158.32 \mu K$). The main interest in TOP guide stems from the fact that using atom chips almost arbitrarily curved waveguides can be produced without spin flip losses as this does not require a bias field. On the other hand, dc currents in the wires can create a rough potential (a detailed description of the roughness problem is presented in another section) and fragment the cloud. Nevertheless, fragmentation can be minimized by increasing the distance between the atoms and the chip.

2.2.2 Rf dressed waveguides

Rf dressing proposed by Zabay and Garraway [75, 76], allow for the creation of versatile potentials by coupling different Zeeman sublevels of a given hyperfine level. Atoms move in a adiabatic potential resulting from the dressing of a static field. If the static potential is an Ioffe-Pritchard trap the iso-B surface resulting from dressing with a linearly polarized rf field is an ellipsoid. The first experimental demonstration of atoms trapped in a rf dressed potential is done by Colombe *et al.* [77]. The observation of the shell structure is difficult in the presence of gravity, due to which the atoms were collected at the bottom of the egg-shell potential. Only a brief introduction to the subject of rf dressed potentials is given here, a thorough discussion of rf dressed potentials can be found in the recent review article by B. Garraway and H. Perrin [78].

The Hamiltonian of an atom in a weak magnetic field $\mathbf{B}(\mathbf{r}, t)$ is governed by

the equation

$$\mathcal{H} = \frac{\mathbf{p}^2}{2m} + g_F \mu_B \mathbf{F} \cdot \mathbf{B}(\mathbf{r}, t) , \quad (2.2.16)$$

where the spin operators F_x , F_y and F_z are of dimension $2F + 1$, for an atom in an hyperfine level F . Let us suppose that the magnetic field $\mathbf{B}(\mathbf{r}, t)$ is composed of a static field $\mathbf{B}_s(\mathbf{r})$ and an oscillating field $\mathbf{B}_{\mathbf{RF}} \cos(\omega t)$. Static field gives a well defined local quantization axis and also provides a trapping potential in the absence of rf field. Let us first consider the case when the static part is homogeneous and the rf field linearly polarized. Without loss of generality, the coordinate system can be chosen such that the static field is aligned with the z-axis and the component of rf field perpendicular to the static field is along x-axis i.e. $\mathbf{B}_s(\mathbf{r}) = B_0 \mathbf{k}$ and the rf field can be expressed as $[B_{RF\perp} \mathbf{i} + B_{RF\parallel} \mathbf{k}] \cos(\omega t)$ and the Hamiltonian is³

$$\mathcal{H} = g_F \mu_B [B_0 + B_{RF\parallel} \cos(\omega t)] F_z + g_F \mu_B B_{RF\perp} \cos(\omega t) F_x , \quad (2.2.17)$$

which can be written as

$$\mathcal{H} = \hbar[\epsilon\omega_L + \frac{g_F \mu_B B_{RF\parallel}}{\hbar} \cos(\omega t)] F_z + \hbar\epsilon\Omega \cos(\omega t) F_x , \quad (2.2.18)$$

where $\omega_L = |g_F| \mu_B B_0 / \hbar$, the Rabi frequency $\Omega = |g_F| \mu_B B_{RF\perp} / \hbar$ and $\epsilon = g_F / |g_F|$ is the sign of the Landé factor. In the representation where F_z is a diagonal operator, F_z does not mix the Zeeman levels, whereas the operators F_x and F_y mix the Zeeman levels of the hyperfine state F . Therefore, the component of the rf field parallel to the static field can be ignored, giving

$$\mathcal{H} = \hbar\epsilon\omega_L F_z + \hbar\epsilon\Omega \cos(\omega t) F_x . \quad (2.2.19)$$

To diagonalize the above Hamiltonian, we first move to a coordinate system which rotates about z by an angle $\epsilon\omega t$. This can be done by applying the time dependent unitary transformation $U = \exp(-i\epsilon\omega t F_z)$. The effect of this unitary transformation U , is to replace \mathcal{H} by $U^\dagger \mathcal{H} U - i\hbar U^\dagger \frac{\partial U}{\partial t}$, which transforms the Hamiltonian as

$$\mathcal{H} = \hbar\epsilon(\omega_L - \omega) F_z + \hbar\epsilon\Omega [\cos^2(\omega t) F_x - \epsilon \sin(\omega t) \cos(\omega t) F_y] . \quad (2.2.20)$$

Using the rotating wave approximation⁴, which essentially means to replace the oscillating terms with their time averages, we obtain,

$$\mathcal{H} = \hbar\epsilon(\omega_L - \omega) F_z + \hbar\epsilon \frac{\Omega}{2} F_x . \quad (2.2.21)$$

³Here, we neglect the kinetic energy operator. Including the momentum operator leads to additional gauge potentials whose effect is normally negligible.

⁴RWA is valid if $\sqrt{(\omega_L - \omega)^2 + \Omega^2/4} \ll \omega$.

Hence, in the presence of a rf field, atoms experience an effective time independent magnetic field

$$\mathbf{B}_{\text{eff}}(\mathbf{r}) = \frac{\hbar}{g_F \mu_B} \sqrt{(\omega - \omega_L)^2 + \frac{\Omega^2}{4}} \mathbf{u}, \quad (2.2.22)$$

where the direction of the effective field is along \mathbf{u}

$$\mathbf{u} = \frac{\Omega/2}{\sqrt{(\omega - \omega_L)^2 + \Omega^2/4}} \mathbf{i} + \frac{\omega_L - \omega}{\sqrt{(\omega - \omega_L)^2 + \Omega^2/4}} \mathbf{k}. \quad (2.2.23)$$

Therefore, the effective potential depends only on the frequency of the rf field and the component of the rf field perpendicular to the static field ($B_{RF\perp}$). Interesting potentials can be generated by employing an inhomogeneous static field in a spatially varying and arbitrarily polarized rf field. For example, dressing a biased 2D quadrupole field $\mathbf{B}_s(\mathbf{r}) = bz\mathbf{i} + B_0\mathbf{j} + bx\mathbf{k}$, with a linearly polarized rf field $\mathbf{B}_{RF} = B_{RF}\mathbf{i}$ generates a double well [79]. The effective potential in this case can be evaluated from $B_{RF\perp}$, which is given by

$$B_{RF\perp}(\mathbf{r}) = \frac{|\mathbf{B}_s(\mathbf{r}) \times \mathbf{B}_{RF}|}{|\mathbf{B}_s(\mathbf{r})|} = \frac{B_{RF} \sqrt{b^2 x^2 + B_0^2}}{\sqrt{b^2(x^2 + z^2) + B_0^2}}, \quad (2.2.24)$$

and the potential is⁵,

$$V_{AP}(x, z) = m'_F g_F \mu_B \sqrt{\left[\frac{\hbar\omega}{|g_F| \mu_B} - \sqrt{b^2(x^2 + z^2) + B_0^2} \right]^2 + \frac{B_{RF}^2 (b^2 x^2 + B_0^2)}{4(b^2(x^2 + z^2) + B_0^2)}}. \quad (2.2.25)$$

Depending on the strength of the rf field the above potential has either one or two minima. For a sufficiently strong rf field, it can be shown that the above adiabatic potential has two minima located above and below x-axis at $z = \pm z_0$, where

$$z_0 = \frac{1}{\sqrt{2}b} \sqrt{B_{RF}^2 - 4 \frac{B_0 \hbar \Delta}{|\mu_B g_F|}}, \quad (2.2.26)$$

and $\Delta = |\mu_B g_F| B_0 / \hbar - \omega$. The two wells are formed at the points where the rf field and the quadrupole field are parallel [79], as the rf coupling is minimum at these points. The double well can be rotated dynamically about y- axis by adiabatically changing the polarization of the rf field. The necessary fields can be simply generated with a three wire configuration on an atom chip. A quadrupole field can be obtained by passing dc currents in the three wires, whereas the rf field polarized along x-axis can be obtained from the central wire. A double well potential obtained from rf dressing can be seen in Fig.2.10.

⁵ m'_F here corresponds to the Zeeman sublevels in the effective magnetic field.

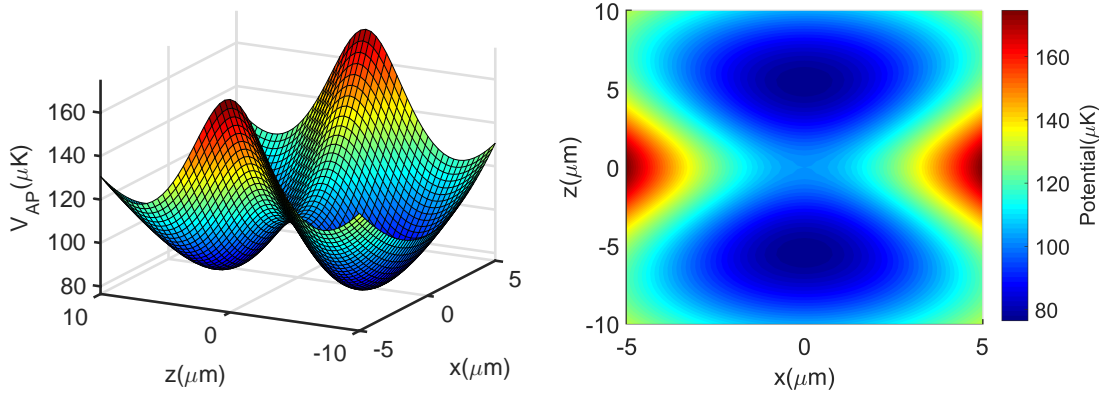


Figure 2.10 *Double well adiabatic potential of a ^{87}Rb atom in $|F = 2, m'_F = 2\rangle$ for a quadrupole gradient of $b = 2000 \text{ G/cm}$ with a bias field $B_0 = 0.75 \text{ G}$, dressed with a rf field of magnitude 0.51 G and frequency 500 kHz , the energy barrier between the wells is about $20 \mu\text{K}$.*

If a homogeneous static field $\mathbf{B} = B_0 \mathbf{k}$ is dressed by an elliptically polarized rf field $\mathbf{B}_{\text{RF}} = B_{\text{RF}x} \cos(\omega t) \mathbf{i} + B_{\text{RF}z} \sin(\omega t) \mathbf{k}$, the resultant adiabatic potential after rotating wave approximation is given by

$$V_{\text{AP}} = m'_F g_F \mu_B \sqrt{\left(\frac{\hbar\omega}{|g_F| \mu_B} - B_0\right)^2 + (B_{\text{RF}x} + B_{\text{RF}z})^2}. \quad (2.2.27)$$

If we now consider the adiabatic potential of a biased 2D quadrupole field $\mathbf{B}(\mathbf{r}) = b\rho \mathbf{r} + B_0 \mathbf{k}$ dressed with a circularly polarized rf field $\mathbf{B}_{\text{RF}} = B_{\text{RF}} \cos(\omega t) \mathbf{i} + B_{\text{RF}} \sin(\omega t) \mathbf{k}$, the resulting adiabatic potential can be obtained by finding the rf components perpendicular to the static field's direction and we obtain

$$V_{\text{AP}} = m'_F \mu_B g_F \sqrt{\left(\frac{\hbar\omega}{|g_F| \mu_B} - \sqrt{b^2 \rho^2 + B_0^2}\right)^2 + \frac{B_{\text{RF}}^2}{2} \left[1 + \frac{B_0}{\sqrt{b^2 \rho^2 + B_0^2}} - \frac{b^2 \rho^2}{2(b^2 \rho^2 + B_0^2)}\right]}, \quad (2.2.28)$$

which is radially symmetric. Under the approximation $b\rho \ll B_0$, the radial coordinate of the potential minima can be expressed as

$$\rho_0 = \frac{1}{\sqrt{2}b} \sqrt{2B_{\text{RF}}^2 - 4B_0 \frac{\hbar\Delta}{|\mu_B g_F|}}. \quad (2.2.29)$$

If $B_{\text{RF}} > \sqrt{2\hbar\Delta/|\mu_B g_F|}$, we get a ring potential (see Fig.2.11), whereas if $B_{\text{RF}} < \sqrt{2\hbar\Delta/|\mu_B g_F|}$ we obtain a single well. A longitudinal confinement can be achieved by using a rf field whose magnitude varies along y-axis, resulting in a circular waveguide. For example, a spatial dependence of the form,

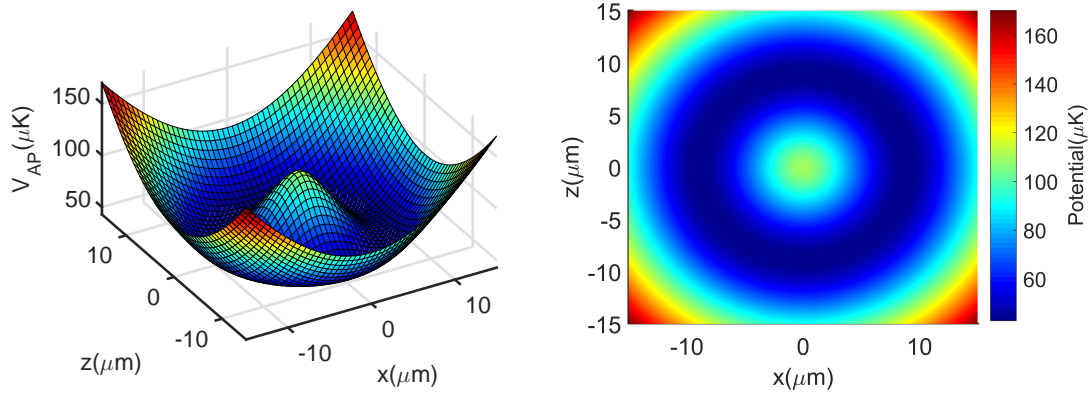


Figure 2.11 *Ring adiabatic potential of a ^{87}Rb atom in $|F=2, m'_F=2\rangle$ for a quadrupole gradient of $b = 2000 \text{ G/cm}$ and bias field $B_0 = 0.5 \text{ G}$, dressed with a circularly polarized rf field of magnitude 2 G and frequency 1.26 MHz . The radius of the ring is approximately $9 \mu\text{m}$. Note that the confinement along y -axis is absent here.*

$B_{RF}(y) = B_{RF} + b_{RF}y^2$ creates a nearly harmonic longitudinal confinement. The radius of circular guide can be tuned in several ways, by varying the parameters of rf field (amplitude and frequency) or by changing static fields (b and B_0). The ring potential can also be generated with a three wire configuration on an atom chip, the rf field with circular polarization can be generated by the two external wires. The spatial dependence in the rf field along the y direction can be introduced by varying the separation between the wires.

The adiabatic potentials discussed here are obtained after a RWA, however experimentally one can be in a situation where the rf frequency is far from resonance and the Rabi coupling can be comparable to the rf frequency. In both these cases, the RWA breaks down and one must resort to a full calculation. The effects on the potential beyond the RWA can be computed using the dressed state formalism by quantizing the rf field [80].

2.2.3 Waveguide based on TAAPs

We can notice in the above section that the adiabatic potential of a static field dressed with a linear rf field depends on the rf coupling, strength of the static field and the frequency of the rf field. If one of these parameters are modulated at a frequency smaller than the Larmor frequency, but faster than the trap frequency of the adiabatic potential ($\omega_{trap} \ll \omega_m \ll \omega_L$), atoms experience a TAAP [81].

The TAAP can be expressed as

$$V_{TAAP}(\mathbf{r}) = \frac{\omega_m}{2\pi} \int_0^{2\pi/\omega_m} V_{AP}(\mathbf{r}, t) dt . \quad (2.2.30)$$

Time averaging extends further the realm of adiabatic potentials, and a complex set of tunable potentials can be generated. A three dimensional quadrupole field $\mathbf{B}_Q(\mathbf{r}) = b\rho \cos \phi \mathbf{i} + b\rho \sin \phi \mathbf{j} - 2bz \mathbf{k}$ dressed with linear rf field aligned with the axis of the quadrupole field creates a shell shaped trap. The adiabatic potential is given by

$$V_{AP}(\mathbf{r}) = m'_F \hbar \sqrt{(\omega_L - \omega)^2 + \frac{\Omega_{RF}^2}{4}} , \quad (2.2.31)$$

where the Larmor frequency $\omega_L = |g_F| \mu_B |\mathbf{B}_Q(\mathbf{r})| / \hbar$ and the Rabi frequency $\Omega_{RF} = |g_F| \mu_B |\mathbf{B}_Q(\mathbf{r})| / |\mathbf{B}_Q(\mathbf{r})| \times |\mathbf{B}_{RF}| / \hbar$. The iso-potential surface is defined by surface over which $|\mathbf{B}_Q(\mathbf{r})|$ is a constant and is an ellipsoidal shell. If an additional field $\mathbf{B}_0(t) = B_0 \cos(\omega_m t) \mathbf{k}$ is added to $\mathbf{B}_Q(\mathbf{r})$, the equipotential shell oscillates along z -axis with an amplitude $B_0/2b$. The introduction of the new field modifies the position at which the rf field is at resonance and makes the Rabi coupling term time dependent, these effects can be avoided by using a rf field with appropriate frequency and amplitude modulation [81]. The integral to compute the time average needs to be done numerically and the resultant TAAP gives a circular waveguide as is evident from the axial symmetry of the adiabatic potential. The radius of the circular waveguide is the position where the rf field is at resonance, which is given by

$$\rho_0 = \frac{\hbar \omega}{|g_F| \mu_B b} , \quad (2.2.32)$$

and depends on the rf frequency and the quadrupole gradient. For a given rf frequency, the radius of the guide can be increased by decreasing the quadrupole gradient. However, the radius can not be increased indefinitely as a minimum gradient is necessary to hold the atoms against gravity. An experimental demonstration of a circular guide using TAAP was first done by C. Foot's research group in Oxford [82] where a circularly polarized rf field was used for dressing a three dimensional quadrupole trap with the modulating field along the axis of the quadrupole. A BEC of 4×10^5 atoms with a small fraction of thermal atoms was loaded in circular guides of various sizes. Lifetimes of more than 11 seconds were observed for guide radii greater than $200 \mu m$, and guides of shorter radii suffered spin flip losses which limited the lifetime. A more recent demonstration of a TAAP circular guides of diameter in the range $400 \mu m - 2.6 mm$ were reported in Crete [27]. There are at least two research groups (in Crete and Nottingham) in the pursuit of a guided Sagnac interferometer using a TAAP. Apart from the usual guided Sagnac interferometer, these research groups also envisage a fully trapped Sagnac interferometer, where atoms are completely trapped in

all directions in a state dependent trap (atoms in different hyperfine levels see a different potential) and moved around in a circular trajectory [45]. Although the waveguide and moving traps necessary for the interferometer were successfully demonstrated, interference fringes are yet to be seen.

2.3 Modulated waveguides

The effects of fabrication defects in the wires pose a serious threat to the atom chip based waveguides. Modulating the currents was shown to be quite effective in combating the roughness in the potential. In this section, a description of the roughness problem is given followed by a discussion on waveguides produced by alternating currents.

2.3.1 Roughness due to wire corrugation and the concept of current modulation

The magnetic field due to a conductor, carrying a current I , at a distance l typically scales as $\sim I/l$, its gradient scales as $\sim I/l^2$ and the field curvature scales as $\sim I/l^3$. The above scaling laws indicate that strong fields can be applied on atoms by passing relatively low currents if the atoms are brought close to the conductors producing them. Microfabricated wires on atom chips allow to trap atoms close to the wires. For example, a wire with 100 mA current produces a field of about 200 G and a gradient of $\sim 2 \times 10^4$ G/cm at a distance of 100 μm from the wire. The availability of strong gradients allows the creation of waveguides with very tight transverse confinement ($\omega_{\text{trap}}/2\pi \sim \text{kHz}$) as is required in the studies of 1D physics. This tight confinement might be also necessary for a guided Sagnac interferometer.

Most atom chip experiments in 2000's reported (see Fig.2.13 for a comparison) the presence of an anomalous field along the waveguide which led to cloud fragmentation, especially when the atoms are brought closer to the chip surface [83]. However, cloud fragmentation was not observed when atoms are far ($> 200 \mu\text{m}$) from the chip surface. Fragmentation was observed to be proportional to the currents in the wire indicating that it is magnetic in origin. It was later found that this undesired magnetic field is produced by the deformation of the current flow in the wires caused by fabrication defects [85]. Wang *et al.* addressed the microscopic nature of the problem by assuming a deformed surface. The authors estimated the strength of the anomalous field and showed that the rough potential ΔV scales with the atom to wire separation as $d^{-5/2}$ which is close to the experimentally observed law $d^{-2.2}$. A detailed calculation of the mean squared fluctuations of the longitudinal field due to lateral edge and top

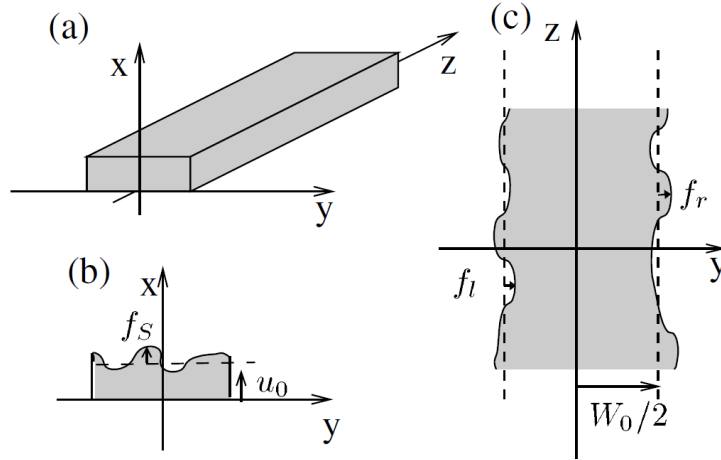


Figure 2.12 a) An ideal rectangular wire on an atom chip, b) top surface meandering and c) edge surface meandering change the direction of the flow of current and lead to an unwanted rough potential (image taken from [84]).

surface corrugations of a rectangular wire gives the following scaling laws [84]

$$\langle B_z^2 \rangle_{edge} = 0.044 J_e \frac{(\mu_0 I)^2}{2d^5}, \quad \langle B_z^2 \rangle_{surface} = 0.044 J_s \frac{\pi W}{6H^2} \frac{(\mu_0 I)^2}{d^5}, \quad (2.3.1)$$

where J_e and J_s are the power spectral densities of the edge and surface roughness (assuming white noise power spectrum) and W and H are the mean width and height of the wires respectively. These scaling results were also experimentally tested by measuring the cold atom density distributions. The field due to the edge roughness is independent of the dimensions of the wire. It was also found that the root mean squared roughness to a large extent depends on the fabrication process. In general, wires grown by evaporation technique are better in terms of surface quality compared to the wires grown by the electroplating technique, as the grain size of evaporated gold is generally lower than the one obtained in electrodeposited gold [84].

Let us consider the side wire guide with a bias field along the wire (to avoid Majorana spin flips). If the bias field is strong enough, the transverse and longitudinal potentials are uncoupled. Kraft *et al.* [83] measured the potential due to wire corrugation and showed that the role of maxima and minima of the rough potential (along the wire) were exchanged when the currents in the wire are reversed. This observation suggests that the rough potential can be averaged if the currents in the wires are modulated. Therefore, if the atoms are sufficiently close to the wires generating the field, the use of alternating currents is almost inevitable to avoid fragmentation. In the following sections, some configurations to generate guides using modulated currents are discussed.

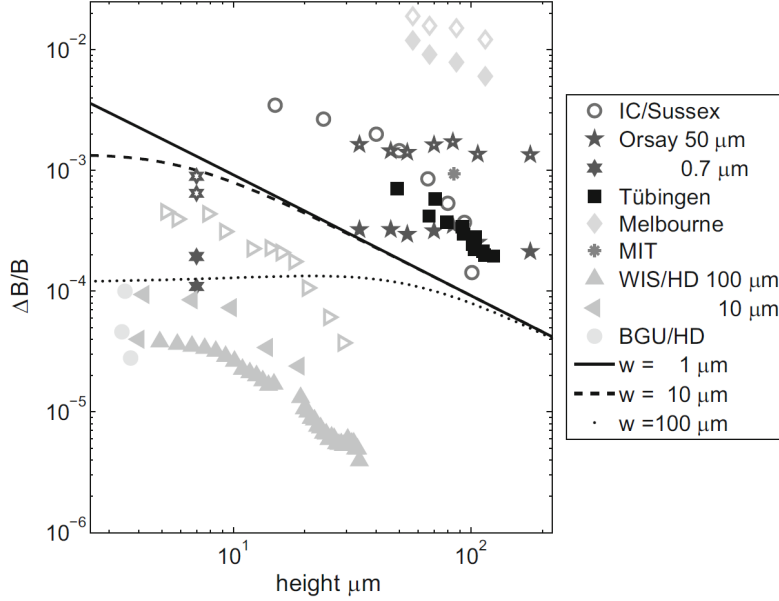


Figure 2.13 Comparison of the magnitude of the roughness measured in various atom chip experiments (image taken from [40]).

2.3.2 Waveguide based on induction

A ring waveguide based on inductively coupled coils is a good candidate to remove the effects of the terminals, feeding the current in the loop wires. In this kind of waveguides, the coil producing them is current supplied through induction and does not require external wires. In addition, since the induced currents are by default alternating, the resulting potential is automatically free from roughness due to wire corrugations [44]. A ring guide based on induction was proposed by Griffin *et al.* [66]. To understand the working principle, let us consider a small wire loop of radius r placed in a homogeneous field \mathbf{B}_0 perpendicular to the plane of the loop (the homogeneous field can be created by a Helmholtz pair). If the field oscillates in time $\mathbf{B}(\mathbf{t}) = \mathbf{B}_0 \cos(\omega t)$, the magnetic flux $\phi = \pi r^2 B_0 \cos(\omega t)$ through the loop changes, inducing an ac current $I_{ind}(t)$ in the loop with a phase lag δ

$$I_{ind}(t) = -\frac{\pi r^2 B_0 \omega}{\sqrt{R^2 + L^2 \omega^2}} \cos(\omega t + \delta), \quad (2.3.2)$$

where R and L are the resistance and the inductance of the loop, respectively⁶. The phase lag depends on the modulation frequency of the field, resistance and the inductance of the loop and is given by $\delta = \tan^{-1}(R/\omega L)$. The induced current in the loop generates a field which cancels the external field producing a

⁶Assuming that the loop has a circular cross-section of radius r_0 and is made up of material of resistivity ρ , $R = 2\rho r/r_0^2$ and $L \approx \mu_0 r [\ln(8r/r_0) - 1.75]$.

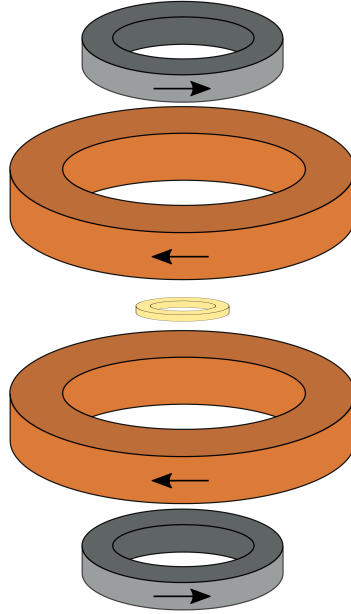


Figure 2.14 A configuration of coils to generate a ring guide using induction [66]. Currents in a pair of coils are oscillated inducing a current in the wire loop placed at the centre. The other pair of coils generate a quadrupole field to push the field zeros.

ring of zeros in the plane of the loop. The total field is then given by

$$\mathbf{B}_{\text{tot}}(\mathbf{r}, t) = B_0 \cos(\omega t) \mathbf{k} + \mathbf{B}_{\text{ind}}(I_{\text{ind}}, r, z) . \quad (2.3.3)$$

The field due to the loop can be expressed in terms of the elliptic integrals and can be evaluated numerically [74]. If the field is modulated relatively fast, the atoms experience a potential averaged over one period which is a ring potential, because of the axial symmetry. As the fields are time dependent, the instantaneous position of the field zero changes with time. Since, the zeros are always formed in the plane of the loop, the zero goes through the time averaged minimum of the potential once per modulation period. This effect is therefore a loss channel. However, it can be mended by superposing a quadrupole field, which displaces the zero from the trapping region. All the necessary fields can be generated by two pairs of coils as in TORTs with a small additional loop placed between the coils, as shown in Fig.2.14. One pair can be used to generate the oscillating field and the other pair can be used to produce the quadrupole field. An experimental demonstration of the inductively coupled ring trap was reported by Pritchard *et al.* [38]. A small copper loop of inner diameter 7 mm and outer diameter 12 mm was placed in a homogeneous field of 110 G, which was modulated at 30 kHz, inducing a current of 140 A in the copper loop. The resulting circular guide has a radius of 5 mm. Instead of a quadrupole field, a constant bias field of 5 G was

employed to push the field zeros from the location of the time averaged potential minima.

A systematic study of the lifetime of the trapped atoms as a function of the strength of the bias field was done and the lifetime was observed to increase with the bias field reaching a maximum of 220 *ms* as the guide becomes more adiabatic. This approach to create a ring guide has its own drawbacks, as remarked in [38]. Indeed, the heat dissipation in the copper loop (about 4 *W*) led to an increase in the background pressure reducing the lifetime of the trapped atoms. Secondly, considering the macroscopic coils and power requirements, it may not be a viable approach to develop a compact and low power consuming device, for terrain and mobile applications like inertial navigation.

Another approach to produce ring potential is based on the use of rf fields with oscillation frequencies in the *MHz* regime. In this regime static magnetic fields are dressed by rf radiation. Radio frequency dressed ring guides using induction were recently proposed using macroscopic coils [86]. The homogeneous oscillating field, combined with the induced field, dress a static field to create a ring guide. Another version of rf dressed potentials using induction was proposed in [87] and might be possible to realise it using an atom chip. Though this approach looks promising, an experimental demonstration of rf dressed guides based on induction is still lacking.

2.3.3 Modulated TOP: New guide concept for an atom chip

In the usual TOP guide configuration, a rotating field is added to a static quadrupole field. Modulating the quadrupole field along with the rotating bias field with a properly chosen phase difference moves the field zero back and forth above the cloud of atoms. Reeves *et al.* [88] demonstrated such a linear guide to create a weak transverse confinement while supporting the atoms against gravity by modulating the quadrupole field. Linear guide with transverse trapping frequencies as low as few tens of *Hz* were loaded with condensate of about 10^4 atoms. The underlying mechanism can be understood by considering the magnetic fields close to the guide centre. Let the modulated quadrupole field be $\mathbf{B}_Q(\mathbf{r}, t) = bz \cos(\omega t) \mathbf{i} + bx \cos(\omega t) \mathbf{k}$, and the rotating field be $\mathbf{B}_T(t) = B_0 \cos(\omega t) \mathbf{i} + B_0 \sin(\omega t) \mathbf{k}$. The position of the magnetic field zero is given by the coordinates

$$x = -\frac{B_0}{b} \tan(\omega t) , \quad z = -\frac{B_0}{b} , \quad (2.3.4)$$

and the field zero moves along a line parallel to x-axis. The instantaneous potential under adiabatic approximation is

$$V_{inst}(x, z, t) = \mu_B g_F m_F \sqrt{(B_0 + bz)^2 \cos^2(\omega t) + [bx \cos(\omega t) + B_0 \sin(\omega t)]^2} . \quad (2.3.5)$$

The time-averaged potential experienced by the atoms upon Taylor expansion upto second order in x and z is⁷

$$V_{avg}(x, z) = \langle V_{inst} \rangle = \mu_B g_F m_F \left[B_0 + \frac{b}{2}z + \frac{b^2}{16B_0}(3x^2 + z^2) \right]. \quad (2.3.6)$$

The transverse potential is asymmetric and the trapping frequency along the

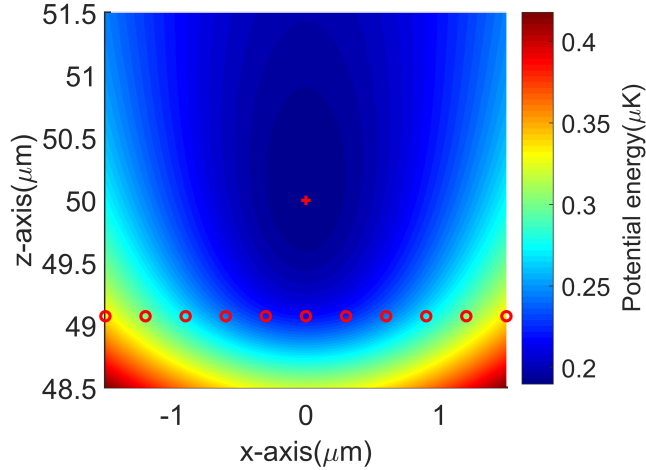


Figure 2.15 *Time-averaged potential of a modulated TOP guide (including gravitational energy) generated by three straight wires with a separation of 50 μm . The red \circ 's define the line along which the instantaneous field zero moves and the position of the guide centre is denoted by +. Gravity is along positive z -axis, and pulls atoms away from the field zeros.*

direction of the gravity is weaker than the frequency along x direction, the trap frequencies are given by

$$\omega_x = b \sqrt{\frac{3\mu_B g_F m_F}{8mB_0}}, \quad \omega_z = b \sqrt{\frac{\mu_B g_F m_F}{8mB_0}}. \quad (2.3.7)$$

If the gravity is along positive z direction, the total potential energy including the gravitational potential is

$$V_{total}(x, z) = \mu_B g_F m_F \left[B_0 + \frac{b^2}{16B_0}(3x^2 + z^2) \right] + \mu_B g_F m_F \frac{b}{2}z - mgz. \quad (2.3.8)$$

By choosing an appropriate quadrupole gradient ($b = 2mg/\mu_B g_F m_F$), the effect of the gravity can be cancelled and the field zero moves above the atomic cloud

⁷This is only valid in the region where $b\sqrt{x^2 + z^2} \ll B_0$ and can be ensured by applying a sufficiently strong rotating field.

along a line parallel to the x-axis, as can be seen in Fig.2.15. The distance between atoms and the "line of death" is given by $z_0 = -\mu_B g_F m_F B_0 / 2mg$. The resulting trap frequencies are

$$\omega_x = \sqrt{\frac{3mg^2}{2\mu_B g_F m_F B_0}}, \quad \omega_z = \sqrt{\frac{mg^2}{2\mu_B g_F m_F B_0}}. \quad (2.3.9)$$

The trap depth of this modulated TOP guide can be defined as

$$V_{depth} = V_{total}(0, z_0) - V_{total}(0, 0) = \frac{\mu_B g_F m_F B_0}{16}, \quad (2.3.10)$$

where the modulation frequencies of the field need to satisfy the following stable trapping conditions

$$\omega_x, \omega_z \ll \omega \ll \omega_L = \frac{\mu_B g_F m_F B_0}{\hbar}. \quad (2.3.11)$$

The first inequality is required for the adiabaticity of the motional degree of the freedom, whereas the second inequality guarantees that the atomic spin follows the changing direction of the magnetic field. Increasing the bias field B_0 keeps the field zero far from the trapping region and makes the guide more adiabatic, on the other hand, this increase in B_0 reduces the trapping frequencies. Reeves

$l(\mu m)$	$I(mA)$	$I_m(mA)$	$\omega_x/2\pi(Hz)$	$\omega_z/2\pi(Hz)$	$z_0(\mu m)$
15	0.34	1	77.60	44.80	30.91
15	0.34	0.5	109.75	63.36	15.45
30	1.4	0.5	155.2	89.61	7.72
30	1.4	1	109.75	63.36	15.45
60	5.5	2	109.75	63.36	15.45
60	5.5	3	89.613	51.73	23.18

Table 2.2 *Transverse trapping frequencies of a modulated TOP guide generated using three straight wires for a set of experimentally realisable parameters on an atom chip. These values are obtained for a ^{87}Rb atom in $|F = 2, m_F = 2\rangle$ state.*

et al. [88] used four macroscopic rods (each of them is a coaxial pair) of outer diameter 5 mm and length 5 cm, located at the four corners of a square of size 15 mm to generate the quadrupole field as in an Ioffe type trap.

Let us now address the realisation of a modulated TOP guide on an atom chip. This study will be done using straight wires, a configuration that allows to obtain analytical results valid for a ring trap geometries with relatively large radii as required for large sensitivity Sagnac atom interferometer. We have verified the validity of the analytical results using numerical simulations for a ring trap of 500 μm , corresponding to the atom chip we are developing.

In this novel configuration, the modulated quadrupole field can be created by passing a current $I \cos(\omega t)$ in the central wire and a current $I \cos(\omega t + \pi)$ in the external wires. The rotating field can be generated by passing additional ac currents in the external wires as in the TOP guide. In order to create a rotating field that compensates gravity, the phases of the additional oscillating currents have to be chosen with a very well defined values. For example, the following choice of currents in the wires generates a modulated TOP guide

$$\begin{aligned} I_1 &= I \cos(\omega t) , \\ I_2 &= I \cos(\omega t + \pi) + I_m \sin(\omega t - \pi/4) , \\ I_3 &= I \cos(\omega t + \pi) - I_m \cos(\omega t - \pi/4) . \end{aligned} \quad (2.3.12)$$

The magnitude of the rotating bias field is $B_0 = \mu_0 I_m / 2\sqrt{2}\pi l$ and the current I , needed to compensate gravity is only defined by the distance between the wires $I = 4\pi m g l^2 / \mu_0 \mu_B g_F m_F$. Although this current need to be held fixed at this value, the trap frequencies can be tuned by varying the amplitude of the additional modulating currents in the external wires. They can be expressed as

$$\omega_x = \sqrt{\frac{3\sqrt{2}\pi m g^2 l}{\mu_B g_F m_F \mu_0 I_m}} \quad \omega_z = \sqrt{\frac{\sqrt{2}\pi m g^2 l}{\mu_B g_F m_F \mu_0 I_m}} . \quad (2.3.13)$$

Here, the line of death is at a distance $z_0 = \mu_B g_F m_F \mu_0 I_m / 4\sqrt{2}\pi m g l$ from the minimum of the total potential, we can also define a trap depth that can be expressed in terms of I_m as

$$V_{depth} = \frac{\mu_0 \mu_B g_F m_F I_m}{32\sqrt{2}\pi l} . \quad (2.3.14)$$

The oscillating current I_m responsible for the rotating bias field has to be chosen so as to keep the line of death as far as possible from the atoms. On the other hand increasing I_m reduces the trap frequencies. From an implementation point of view, the currents in the wires can be rewritten as

$$\begin{aligned} I_1 &= I \cos(\omega t) , \\ I_2 &= I_0 \cos(\omega t + \phi + \pi) , \\ I_3 &= I_0 \cos(\omega t - \phi + \pi) , \end{aligned} \quad (2.3.15)$$

where $I_0 = \sqrt{I^2 + I_m^2 + \sqrt{2}II_m}$ and the phase shift is $\phi = \sin^{-1}(I_m/\sqrt{2}I_0)$. Realistic parameters for a modulated TOP guide using atom chip can be seen in Table 2.2.

We can notice that, the currents required to generate the modulated TOP guide can be of the order of a few milliamperes, when the wire separation is less than $20 \mu m$. This result is important when considering compact and embedded applications of atom interferometers. However, given the current levels involved,

we need very low noise and stable current sources to generate the guide, as the noise in the current source translates into a noise in the trapping frequencies. Low noise current sources with a relative stability of 10^{-5} are readily available in SYRTE. It was shown by Barnowski *et al.* [89] that such a stability is required in order to achieve a coherence time of one second for interferometric purposes. Since the modulated TOP guide does not require a bias field a circular guide can also be produced by bending the wires.

2.3.4 Palaiseau solution to remove the waveguide roughness

As remarked earlier, overcoming the problem of roughness is very crucial for guided atom interferometry. A method to reduce the longitudinal roughness was first demonstrated by Trebbia *et al.* [44] at Institut d'Optique in Palaiseau. Following the suggestion of [83], all the currents that are responsible for the hexapole guide created by five wires were modulated at few tens of kHz and the effect of roughness was shown to be reduced by at least a factor of ten. In particular, the cloud fragmentation was not observed when a BEC was brought as close as $5 \mu m$ to the chip surface.

This modulation technique can be understood by analysing a simple linear guide generated by three wires. Let us consider the quadrupole field generated by the three wires, biased with a strong field $B_0 \mathbf{k}$ along the longitudinal direction. The total field near the guide centre is given by

$$\mathbf{B}(\mathbf{r}) = bz \mathbf{i} + (B_0 + u(y)) \mathbf{j} + bx \mathbf{k} , \quad (2.3.16)$$

where b is the quadrupole gradient and $u(y)$ is a spatially varying longitudinal component of the unwanted fields due to wire imperfections. Both these terms are proportional to the currents in the wires, and the potential seen by the atoms is

$$V(x, y, z) = \mu_B g_F m_F \{b^2(x^2 + z^2) + [B_0 + u(y)]^2\}^{1/2} . \quad (2.3.17)$$

If the currents are modulated keeping the bias field B_0 constant, the instantaneous potential experienced by the atoms is

$$V_{inst}(x, y, z) = \mu_B g_F m_F \{b^2(x^2 + z^2) \cos^2(\omega t) + [B_0 + u(y) \cos(\omega t)]^2\}^{1/2} , \quad (2.3.18)$$

which in the case of a strong bias field, i.e. $b\sqrt{x^2 + z^2} \ll B_0$,⁸ allows a Taylor expansion of the instantaneous potential. Up to second order in x and z , we obtain⁹

$$V_{inst}(x, y, z) = \mu_B g_F m_F B_0 \left[1 + \frac{b^2}{2B_0^2} (x^2 + z^2) \cos^2(\omega t) + \frac{u(y) \cos(\omega t)}{B_0} \right] . \quad (2.3.19)$$

⁸Usually $u(y) \ll B_0$.

⁹The contribution due to the second order terms in $u(y)$ is negligible.

Therefore, in the presence of a strong bias field the transverse and longitudinal potentials are uncoupled. If the currents are modulated at sufficiently high frequencies, atoms see the time-averaged potential

$$V_{avg}(x, z) = \mu_B g_F m_F B_0 \left[1 + \frac{b^2}{4B_0^2} (x^2 + z^2) + \left\langle \frac{u(y) \cos(\omega t)}{B_0} \right\rangle \right]. \quad (2.3.20)$$

Since the longitudinal potential is proportional to the currents, it averages to zero ($\langle u(y) \cos(\omega t) \rangle = 0$) over one modulation period. Hence, modulation of currents produces a trapping potential free from roughness. A word of caution is necessary here, the modulation technique does not suppress the roughness entirely. A longitudinal potential scaling as¹⁰ $(\partial u / \omega \partial y)^2$ still remains [90, 91]. However, the residual roughness can be made as low as possible by increasing the modulation frequency. For example, in the Palaiseau experiment the residual roughness was estimated to be eight orders of magnitude less than the transverse potential. Bounds to the modulation frequency can be obtained from the adiabaticity criteria

$$\sqrt{\frac{\mu_B g_F m_F}{m B_0}} b \ll \omega \ll \frac{\mu_B g_F m_F B_0}{\hbar}. \quad (2.3.21)$$

A detailed analysis of the limitation of the modulation technique can be found in Bouchoule *et al.* [92], where the modulation of currents was found to heat the atomic cloud. A quantum mechanical calculation using Floquet's theory shows that the heating rate can be as high as $3 \mu K/s$ for a cloud at a temperature of $0.7 \mu K$, when the modulation frequency is $1 kHz$. On the other hand, the heating rate drops significantly with the modulation frequency, for example heating rate can be as low as $64 nK/s$ for a cloud temperature of $1.8 mK$ when the modulation frequency is $50 kHz$.

The modulation also increases the Majorana transitions as one approaches the Larmor frequency. The approximate expression for the Majorana loss rate in the modulated guide is [92]

$$\gamma = \frac{\pi^3 \hbar \omega_{trap}^3 \omega^2}{2 (k_B T)^3} e^{-\hbar \Delta / k_B T}, \quad (2.3.22)$$

where the detuning Δ is the difference between the modulation frequency and the Larmor frequency at the guide centre, $\Delta = \mu_B B_0 / \hbar - \omega$. Therefore, for a given modulation frequency, loss rate can be kept low by applying a large enough bias field along the guide. Experimentally, a Larmor frequency of few MHz can be achieved with a bias field of few Gauss and modulation frequencies of few tens of kHz . Such a choice guarantees the adiabaticity of the atomic spin.

Modulation frequencies in the above guide are deliberately kept well below the Larmor frequency so that atoms adiabatically follow the instantaneous field

¹⁰This requires an analysis beyond a simple time-averaged description.

preserving their Zeeman state. If the modulation frequencies approach Larmor frequency, the linear quadrupole field can be seen as a rf field coupling the Zeeman levels (associated to the bias field B_0 which provides the quantization axis) and atoms experience an adiabatic potential. The double well and the circular potentials discussed earlier result from dressing an inhomogeneous field with a homogeneous rf field, in contrast to the present case where a homogeneous field is dressed with an inhomogeneous rf field to produce the adiabatic trapping potential.

2.4 Conclusion

In this chapter, we reviewed the proposed and realized magnetic waveguides. In particular when considering the realization of a circular waveguide on an atom chip, the TOP configuration is the straight forward one to implement as it does not require any external bias field. However, the TOP guide is prone to cloud fragmentation due to the use of dc currents. Nevertheless it is still possible to avoid this problem by positioning the guide sufficiently far ($> 100 \mu m$) from the chip surface. The minimal distance depends on the root mean squared roughness of the wires, which depends on the fabrication technique.

Here we also discussed a novel solution to generate a circular waveguide on an atom chip, the modulated TOP guide. Although the presented results are obtained for a linear waveguide, they remain valid for a large radius ring trapping potentials as confirmed from our numerical simulations. The modulated TOP guide is naturally free from roughness due to the use of alternating currents, but the requirement of gravity compensation by a field gradient results in a reduction of the transverse trapping frequencies. They are on the order of few hundred Hz, relatively large compared to the typical frequencies of cold atom experiments but one order of magnitude smaller than the typical atom chip trapping frequencies. The depth of the modulated TOP guide is of the order of $1 \mu K$, which still allows the confinement of Bose-Einstein condensed atoms. In Chapter 4, we will discuss the effect of this relatively low trapping frequencies on the monomode propagation of cold atoms in the ring waveguide.

We can also generate a toroidal guide with trapping frequencies on the order of kHz for the guided Sagnac interferometry on an atom chip. This requirement is important to reduce possible biases when using the interferometer for inertial sensing. The next chapter will be devoted to this investigation and we will discuss a new configuration to generate a smooth toroidal tight guide using three wires.

Chapter 3

Modulated waveguides and simulation of the atom dynamics

In this chapter, we present a novel magnetic waveguide using three wires on an atom chip. This guide is based on the current modulation technique [44] which allows to address simultaneously the problem of Majorana losses and cloud fragmentation due to the proximity of the waveguide to the chip surface. The new solution that we found to tackle simultaneously both problems is to add a small phase shift to the phase difference between the central and the external microwire currents. This idea allows the realisation of an intermediate regime where the roughness is still suppressed to a level compatible with matterwave propagation, generating at the same time a non zero bias field. This chapter also includes a study of the adiabaticity of atomic spin, in the time dependent magnetic field of our proposed modulated guide.

3.1 Generation of bias field through modulation

We will start by considering the configuration of three wires to generate the linear guide discussed in the previous chapter. Let the currents in the wires be modulated at a frequency ω so as to overcome the roughness problem. In order to create a bias field that is needed for the guide, the currents in the external wires need to be modulated with a phase difference of π with respect to the current in the central wire. Suppose that the currents in the central and external wires have the form $I_1 = A_1 \cos(\omega t)$ and $I_2 = A_2 \cos(\omega t + \pi + \phi)$ respectively, where ϕ is an additional phase shift. Then, the field due to the external wires cancels that of the central wire at a distance d from the chip surface, which is given by

$$d(t) = l \sqrt{\frac{A_1 \cos(\omega t)}{2A_2 \cos(\omega t + \phi) - A_1 \cos(\omega t)}}. \quad (3.1.1)$$

If the phase shift is exactly equal to zero ($\phi = 0$) the time dependence in the position of the guide vanishes. And the guide is formed at the same distance

as in the unmodulated case. On the other hand, if a small phase shift $\phi \ll \pi$ is introduced, the position of the guide becomes time dependent. Therefore, modulating the currents with a phase shift slightly different from zero moves the position of the guide centre. The time dependence in the position of field zero can be seen as arising from an additional field generated at the guide centre. To see this, let us write the total magnetic field in terms of the field generated by each wire

$$\mathbf{B}(\mathbf{r}, t) = \mathbf{B}_1(\mathbf{r}) \cos(\omega t) + \mathbf{B}_2(\mathbf{r}) \cos(\omega t + \phi) + \mathbf{B}_3(\mathbf{r}) \cos(\omega t + \phi) , \quad (3.1.2)$$

where $\mathbf{r} = x \mathbf{i} + z \mathbf{k}$ and $\mathbf{B}_1(\mathbf{r})$ is the field due to the central wire with an amplitude A_1 and $\mathbf{B}_2(\mathbf{r}), \mathbf{B}_3(\mathbf{r})$ are the fields due to the external wires with an amplitude A_2 . If the phase difference ϕ is small, we can approximate the total field as

$$\mathbf{B}(\mathbf{r}, t) \approx \mathbf{B}_Q(\mathbf{r}) \cos(\omega t) + \phi \mathbf{B}_b(\mathbf{r}) \sin(\omega t) , \quad (3.1.3)$$

where $\mathbf{B}_Q(\mathbf{r}) = \mathbf{B}_1(\mathbf{r}) + \mathbf{B}_2(\mathbf{r}) + \mathbf{B}_3(\mathbf{r})$ is the quadrupole guide field and $\mathbf{B}_b(\mathbf{r}) = -\mathbf{B}_2(\mathbf{r}) - \mathbf{B}_3(\mathbf{r})$ is the field generated by the two external wires. Therefore, we find that current modulation with a phase shift generates an extra field at the trap centre, with an amplitude scaling linearly with the additional phase shift ϕ . Close to the trap center $\mathbf{B}_b(\mathbf{r})$ can be taken as a constant and is equal to the field due to the central wire

$$\mathbf{B}_b(\mathbf{r}) = \mathbf{B}_b = -\frac{\mu_0 A_1}{2\pi d} \mathbf{i} . \quad (3.1.4)$$

Although this approximation is not valid if the phase shift ϕ between the currents is relatively large or if we consider a region far from the guide centre it allows to gain some physical intuition on the guide seen by the atoms during their motion. When the above approximation is not valid, a full calculation of the magnetic fields is necessary. Therefore, to obtain completely reliable results we use the exact expressions of the fields in all the results and plots in the subsequent sections.

3.2 Adiabatic guide with tunable radius

If we modulate the currents with a non zero phase difference ϕ , the instantaneous field zero goes through the trapping region twice (line of red crosses) in every modulation period as we can see in Fig.3.1(a). This can reduce the lifetime of the guided atoms due to Majorana losses. However, the problem can be circumvented simply by applying an additional bias field B_0 perpendicular to the chip, which can be produced by a pair of Helmholtz coils. The effect of this additional bias field can be understood, by considering the total magnetic field around the guide centre

$$\mathbf{B}(\mathbf{r}, t) = \mathbf{B}_Q(\mathbf{r}) \cos(\omega t) + \phi \mathbf{B}_b \sin(\omega t) + B_0 \mathbf{k} , \quad (3.2.1)$$

using $\mathbf{B}_Q(\mathbf{r}) \approx bz \mathbf{i} + bx \mathbf{k}$ we can approximate the total field as

$$\mathbf{B}(\mathbf{r}, t) = [bz \cos(\omega t) + \phi B_b \sin(\omega t)] \mathbf{i} + [bx \cos(\omega t) + B_0] \mathbf{k} . \quad (3.2.2)$$

The position of the field zeros as a function of time is given by

$$x = -\frac{B_0}{b \cos(\omega t)} , \quad z = -\frac{\phi B_b}{b} \cot(\omega t) . \quad (3.2.3)$$

We can see the trajectory followed by the field zero in Fig.3.1, and in particular we can see how the additional bias field pushes the field zeroes from the trapping region, improving the guide stability against spin losses. If the fields are modulated faster than the typical transverse oscillation frequencies, the atoms experience a time-averaged potential. Under this adiabatic approximation, the potential experienced by the atoms is

$$V_{avg}(\mathbf{r}, \phi, B_0) = \frac{2\pi}{\omega} \mu_B g_F m_F \int_0^{2\pi/\omega} |\mathbf{B}(\mathbf{r}, t)| dt . \quad (3.2.4)$$

From the equations 3.2.3 and the numerical results obtained using Eq.3.2.4, we

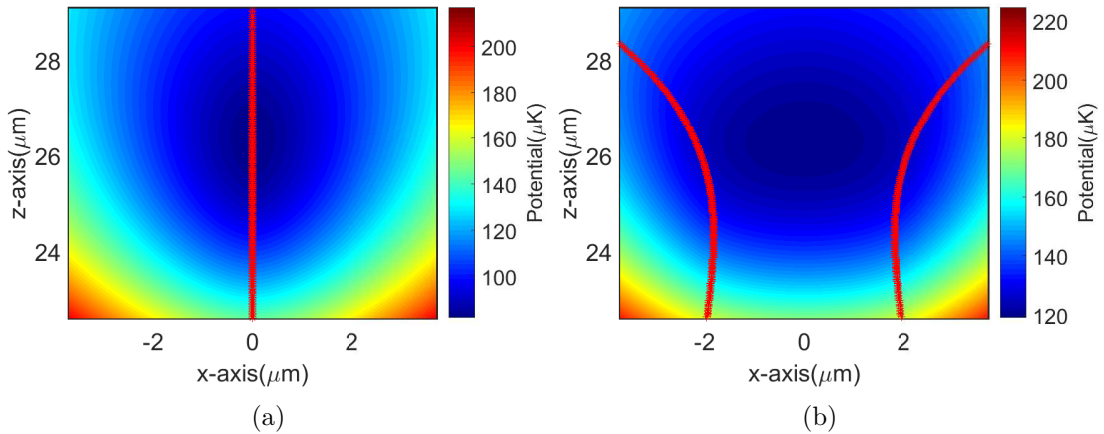


Figure 3.1 *Time-averaged potential in the absence of the bias field (a) and in the presence of a 1.2 G bias field (b). In both cases currents are modulated with amplitudes $A_1 = 400$ mA and $A_2 = 267$ mA with a phase difference of $\phi = \pi/50$. The path followed by the field zeros is shown in red, and the exclusion of the field zeros from the trapping region can also be seen in Fig.3.1(b).*

observed as expected that the waveguide becomes more adiabatic as the strength of the bias field B_0 and the phase shift ϕ are increased.

So far we have considered fixed radius toroidal guide configurations. The guide radius is mostly determined by the radius of the central wire and the separation between the wires, which are fixed once the chip is fabricated. However,

having a guide with adjustable radius can be advantageous, as we will see in the next chapter. In fact, the tunability of the guide radius can be achieved simply by adding an additional oscillating field $B_1 \cos(\omega t)$ perpendicular to the chip. To understand how this tunability works, let us consider the field close to the guide centre

$$\mathbf{B}(\mathbf{r}, t) = [\phi B_b \sin(\omega t) + bz \cos(\omega t)] \mathbf{i} + [bx \cos(\omega t) + B_0 + B_1 \cos(\omega t)] \mathbf{k} . \quad (3.2.5)$$

Notice that the additional field can be simply produced by adding an ac current to the Helmholtz coils. However, this oscillating current must be phase locked to the current in the central wire. The time dependent coordinates of the field zero is now given by

$$x = -\frac{B_1}{b} - \frac{B_0}{b \cos(\omega t)} , \quad z = -\frac{\phi B_b}{b} \cot(\omega t) . \quad (3.2.6)$$

Due to the additional oscillating field, the field zero oscillates about a point $x = -B_1/b$ excluding a region of size B_0/b on either side of it, i.e. the position of the guide gets displaced by an amount proportional to the strength of the oscillating field. The effect of this oscillating field can be verified by comparing Fig.3.2 with Fig.3.1(b).

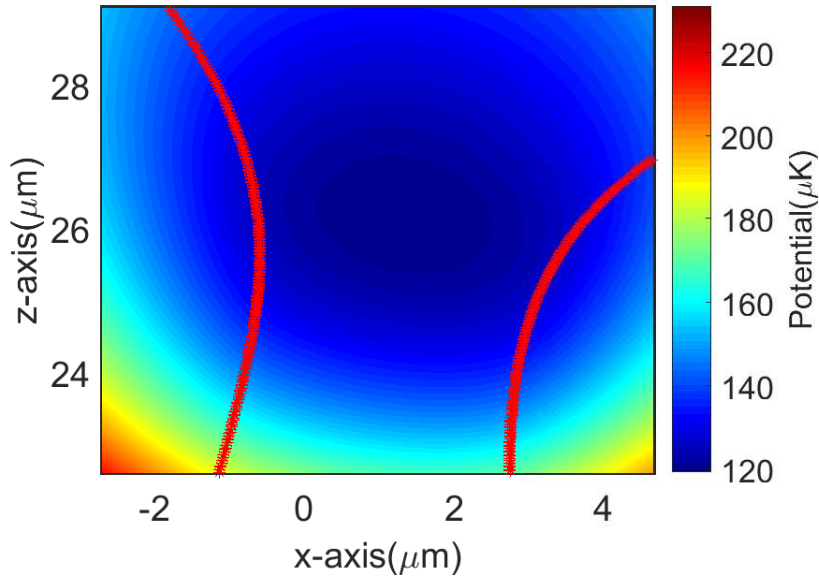


Figure 3.2 *Time-averaged potential of a guide after the addition of a 0.7 G oscillating magnetic field perpendicular to the chip. The guide is shifted by approximately 1.5 μm .*

An important feature of this configuration is that the additional oscillating field merely shifts the position of the guide while the gradient at the trap centre is still the same.

3.3 Semiclassical simulations of the atom dynamics

Time dependent potentials are usually described by considering a time average of the magnetic field, which is only valid in the adiabatic limit. To understand the adiabaticity of the atomic spin in the modulated waveguide proposed here, we numerically integrate the classical equations of motion taking into account the spin dynamics. The equations of motion of an atom in the direction transverse to the guide are given in our case by [93, 94, 95, 96]

$$m \frac{d^2 x}{dt^2} = \mu \partial_x (\mathbf{n} \cdot \mathbf{B}(\mathbf{r}, t)) , \quad (3.3.1)$$

$$m \frac{d^2 z}{dt^2} = \mu \partial_z (\mathbf{n} \cdot \mathbf{B}(\mathbf{r}, t)) , \quad (3.3.2)$$

$$\frac{d\mathbf{n}}{dt} = \gamma \mu \mathbf{n} \times \mathbf{B}(\mathbf{r}, t) , \quad (3.3.3)$$

where $\gamma = 1/\hbar$ and \mathbf{n} is a unit vector in the direction of the magnetic moment. As we saw previously, the time dependent magnetic field generated by three straight wires with modulated currents is

$$\mathbf{B}(\mathbf{r}, t) = [bz \cos(\omega t) + \phi B_b \sin(\omega t)] \mathbf{i} + [bx \cos(\omega t) + B_0] \mathbf{k} . \quad (3.3.4)$$

Substituting this field in the equations of motion, we get the following expressions

$$m \frac{d^2 x}{dt^2} = -\mu_B g_F n_z b \cos(\omega t) , \quad (3.3.5)$$

$$m \frac{d^2 z}{dt^2} = -\mu_B g_F n_x b \cos(\omega t) , \quad (3.3.6)$$

$$\frac{dn_x}{dt} = -\gamma \mu_B g_F n_y [bx \cos(\omega t) + B_0] , \quad (3.3.7)$$

$$\frac{dn_y}{dt} = -\gamma \mu_B g_F \{n_z [bz \cos(\omega t) + \phi B_b \sin(\omega t)] - n_x [bx \cos(\omega t) + B_0]\} , \quad (3.3.8)$$

$$\frac{dn_z}{dt} = \gamma \mu_B g_F n_y [bz \cos(\omega t) + \phi B_b \sin(\omega t)] . \quad (3.3.9)$$

To integrate the equations numerically, we first rewrite the above equations in dimensionless form. The spacing between the wires l , gives a length scale and the inverse of modulation frequency gives a time scale. Therefore, we introduce the dimensionless variables $X = x/l$ and $T = \omega t$ which automatically define a scale for velocity $V_x = v_x/l\omega$, $V_z = v_z/l\omega$. With this definitions, we end up with

the following set of dimensionless coupled equations

$$\frac{dX}{dT} = V_x , \quad (3.3.10)$$

$$\frac{dV_x}{dT} = -\alpha_1 n_z \cos(T) , \quad (3.3.11)$$

$$\frac{dZ}{dT} = V_z , \quad (3.3.12)$$

$$\frac{dV_z}{dT} = -\alpha_1 n_x \cos(T) , \quad (3.3.13)$$

$$\frac{dn_x}{dT} = -\alpha_2 n_y (X \cos(T) + \alpha_4) , \quad (3.3.14)$$

$$\frac{dn_y}{dT} = -\alpha_2 [n_z (Z \cos(T) + \alpha_3 \sin(T)) - n_x (X \cos(T) + \alpha_4)] , \quad (3.3.15)$$

$$\frac{dn_z}{dT} = \alpha_2 n_y [Z \cos(T) + \alpha_3 \sin(T)] , \quad (3.3.16)$$

with the dimensionless constants given by

$$\alpha_1 = \frac{\mu_B g_F b}{m l \omega^2} , \quad (3.3.17)$$

$$\alpha_2 = \frac{\gamma \mu_B g_F b l}{\omega} , \quad (3.3.18)$$

$$\alpha_3 = \frac{\phi B_b}{b l} , \quad (3.3.19)$$

$$\alpha_4 = \frac{B_0}{b l} . \quad (3.3.20)$$

We numerically solve the above coupled equations for a given set of initial conditions. To check the stability of the guiding, we placed the atom at different locations and align initially the atomic spin along the local direction of the instantaneous field. Notice that the magnitude of unit vector \mathbf{n} is a conserved quantity and can be used to test the numerical accuracy of the simulation.

3.3.1 Determination of a set of guide parameters for stable dynamics

Currents in the wires, phase shift between the currents, the strength of the bias field perpendicular to the chip and the modulation frequency of the currents

must be chosen so that the guide is stable for the atom internal and external degrees of freedom dynamics with tight and deep transverse confinement. Using numerical simulations of the time-averaged potential and the atom dynamics, we identify the parameter range, for which a stable guide is possible.

Choice of currents

The presence of the bias field and the phase shift significantly reduce the trapping frequencies. In order to achieve trapping frequencies of the order of few kHz , our numerical simulations suggest that it is necessary to use currents in the order of few hundreds of milliamperes. For instance, we take the amplitudes of the oscillating currents to be 400 mA and 267 mA in the central and external wires, respectively. For these parameters the guide is formed approximately at a distance $26\text{ }\mu\text{m}$ from the chip surface and the quadrupole field gradient close to the guide centre is $b = 3\text{ kG/cm}$.

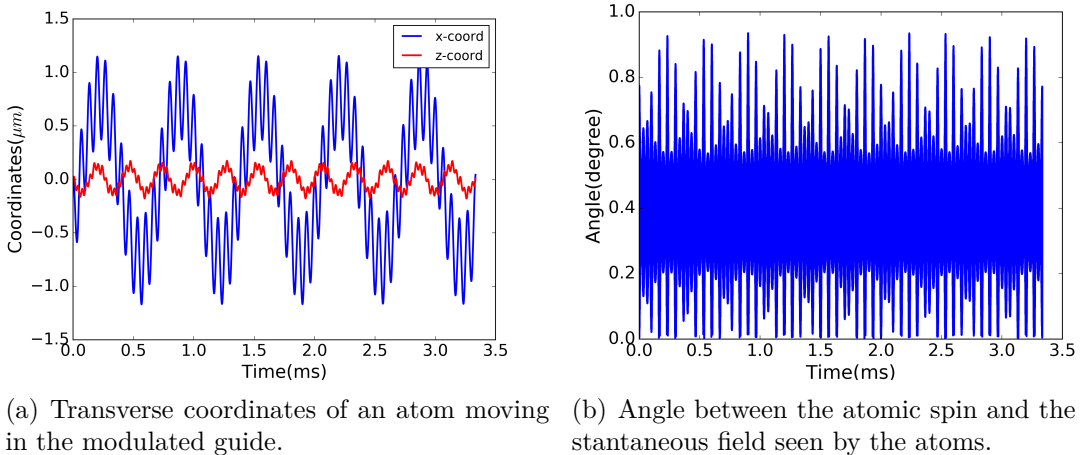


Figure 3.3 *Results obtained from a numerical simulation of atom dynamics in a guide with currents modulated at $\omega = 2\pi \times 15\text{ kHz}$.*

In the figure 3.3, we show the external and internal degree of freedom dynamics. In this simulation, the temperature of the atom cloud is taken to be 500 nK and the observed, from these trajectories (see Fig.3.3(a)), transverse trapping frequencies are $\omega_x = 2\pi \times 1.4\text{ kHz}$ and $\omega_z = 2\pi \times 3.5\text{ kHz}$. Micro motion about the mean trajectory, are visible in Fig.3.3(a) are due to non-adiabatic effects. They are due to imperfect adiabatic following of the magnetic field by the spin. For the parameters considered in the simulation, we observe that the angle between the atomic spin and the local magnetic field is always less than 1° (see Fig.3.3(b)).

Phase ϕ and bias field B_0

The adiabaticity of the atom spin depends on ϕ and B_0 as demonstrated in Fig.3.4(a).

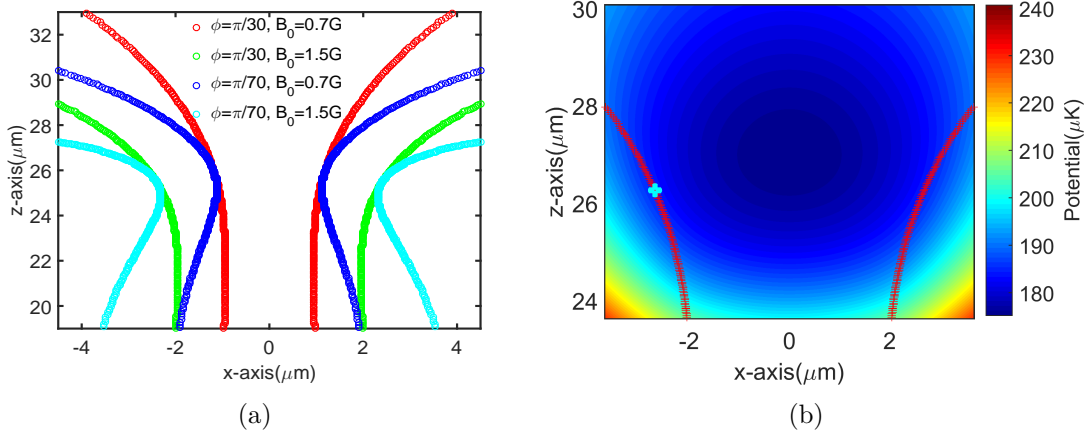


Figure 3.4 Numerical computation of the fields due to the three straight wires separated by $15\ \mu\text{m}$. a) Trajectory of the field zero over one modulation period for different ϕ and B_0 . Both these parameters have to be chosen to keep the field zero as far as possible from the trapping region. b) Time-averaged potential for $\phi = \pi/30$ and $B_0 = 1.5\text{ G}$, the field zero's trajectory is shown in red color. The point marked in cyan has the lowest potential in the path traversed by the field zero and it is used to compute the trap depth.

The choice of the guide parameters determines how far the instantaneous field zeros are located with respect to the trap centre. The phase difference between the currents in the central and external wires has to be chosen carefully, and as mentioned earlier, the perpendicular bias field helps to push the magnetic field zeros away from the trapping region. Increasing B_0 moves the field zero trajectory farther from the trapping region, consequently the guide becomes more elongated along the x-axis as we can see in Fig.3.4(a). On the other hand, increasing the phase difference ϕ also makes the guide more adiabatic while weakening the confinement along the vertical axis. If we increase ϕ and B_0 indefinitely, the time-averaged potential opens up and the guide breaks down. Moreover, the approximation of small phase difference (Eq.3.1.3) is not valid for large phase shifts.

To investigate the effect of the ϕ and B_0 on trap depth we numerically evaluated the time-averaged potential. A point on the field zero trajectory that has the lowest time-averaged potential is used to compute the trap depth (see Fig3.4(b)).

From these results we can see that the trap depth usually increases with ϕ and B_0 up to about $8 \mu K$ (for the chosen guide parameters) before the guide fails. We observe stable motion, when $\phi \in (\pi/150, \pi/30)$ and $B_0 \in (0.7 G, 2 G)$.

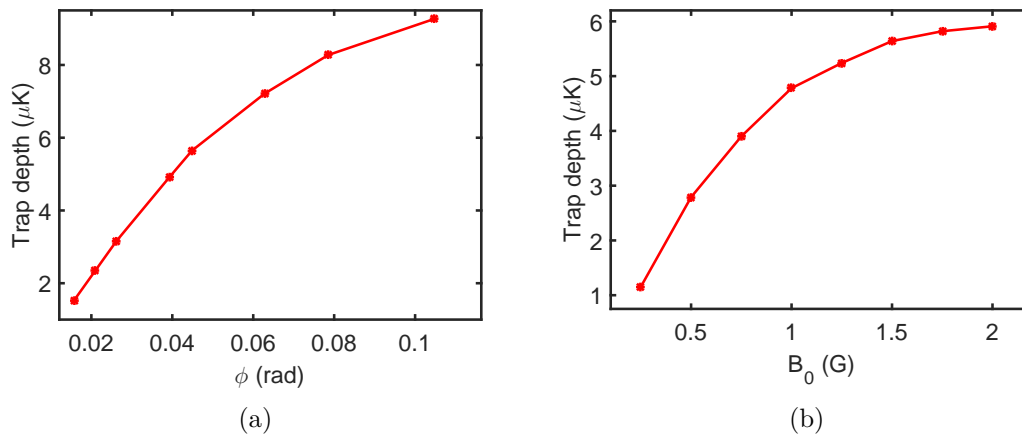


Figure 3.5 *Trap depth of the time-averaged potential measured from a numerical computation of the fields due to three straight wires separated by $15 \mu m$. a) Trap depth vs. phase difference between the currents with a bias field of $1.5 G$. b) Trap depth vs. bias field perpendicular to the chip with a phase difference of $\frac{\pi}{70}$ rad.*

Modulation frequency ω

The trap frequencies in the transverse direction are estimated from the atom trajectories computed for $\phi = \pi/70$ rad and $B_0 = 1.5 G$. The obtained values are $\omega_x = 2\pi \times 1.4 kHz$ and $\omega_z = 2\pi \times 3.5 kHz$. The magnetic field at the guide centre is always greater than B_0 , therefore close to the guide centre at any given time the instantaneous Larmor frequency is at least $\omega_L = \frac{\mu_B g_F m_F B_0}{\hbar}$. Choosing the modulation frequency such that $\omega_x, \omega_z \ll \omega \ll \omega_L$ automatically guarantees the adiabaticity of the atomic spin and the external degree of freedom. We found stable atom motion for frequencies above $10 kHz$. However, increasing modulation frequencies beyond $30 kHz$ was found to increase both, the amplitude of oscillations, and the angle between the spin and the magnetic field. In fact stable trapping was observed upto frequencies as high as few hundred kHz , but the angle between the instantaneous field and the spin was found to oscillate with an amplitude as high as 40° , indicating a mixing of Zeeman levels. The usual time-averaged description of the potential is not valid in this regime. Though the modulation frequency is much less than the Larmor frequency $\omega_L/2\pi = 2 MHz$ for a bias field B_0 as the one considered here, equal to $1.5 G$.

The angle between the instantaneous field and atomic spin was used to check

Guide parameter	value
Current in the central wire (A_1)	400 mA
Current in the external wires (A_2)	267 mA
Quadrupole gradient (b)	3 kG/cm
distance between guide and chip (d)	26 μm
Bias field (B_0)	1.5 G - 2 G
Phase difference (ϕ)	$\pi/30$ - $\pi/150$
Modulation frequency (ω)	10 kHz - 30 kHz

Table 3.1 *A set of parameters for which modulated guide is adiabatic for a ^{87}Rb atom in $|F = 2, m_F = 2\rangle$ state.*

the adiabaticity of the atomic spin. For the guide parameters we used here, the angle is found to be less than one degree which indicates that the guide is adiabatic and shows the validity of the time-averaged potential description (see Fig.3.3(b)). Theoretical studies of the motion of atoms in a TOP trap predicted small oscillations about the mean trajectory due to the non-adiabatic spin dynamics in the time-dependent magnetic field [95]. Numerical simulations of the atom trajectory show similar effects in our guide as we can see in Fig.3.3(a).

Toroidal waveguide

Because of the important computational costs associated to the elliptic integrals determining the magnetic field of a ring waveguide, we focussed here on the simulations of the atom dynamics in linear modulated guides. To estimate the accuracy of the quantitative results we obtained, we compute the guide characteristics that change when going from a linear geometry to a toroidal one. This characteristics are the guide height and position, and the magnetic field gradients. Indeed, the waveguide gets displaced slightly towards the centre and this descends towards the chip surface due to the ring curvature.

A toroidal waveguide can be created with three concentric wires with radii r_1 , $r_2 = r_1 + l$ and $r_3 = r_1 - l$, by choosing the direction of the currents in the wires as shown in Fig.3.6. In Fig.3.7 we plot the guide position and height as a function of the central microwire radius r_1 . As we can see in this figure, when we increase r_1 (approaching the linear waveguide limit), the trap height tends towards a constant value which coincides with the one obtained for a linear waveguide. On the other hand, the form of the potential close to the trap centre is found to be independent of the radius of the central loop for $r_1/l \gg 1$. Therefore, if the guide radius satisfies $r_1/l \gg 1$, the formula for the guide height and the field gradient close to the trap centre in the linear guide are still applicable to the toroidal guide. As long as the radius of the central loop is much larger than the separation between the wires, the effect of the curvature of the loops will

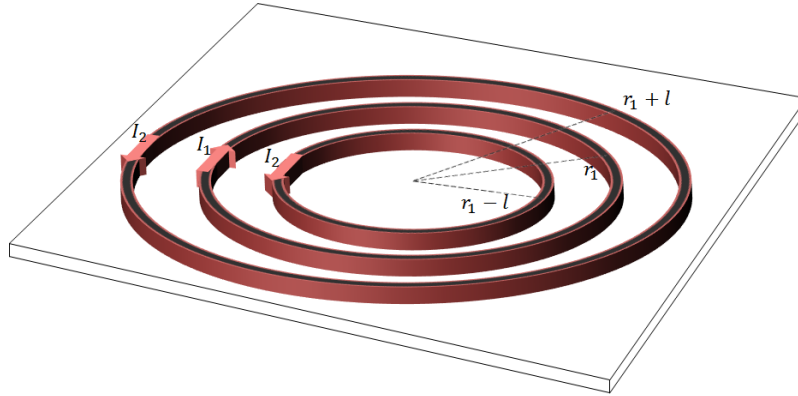


Figure 3.6 Configuration of the wires showing the toroidal guide.

be limited to produce a deflection, bending of the trajectories of the atoms such that they remain guided in the torus. As we will see in the next chapter, the guide curvature will be responsible for a transverse heating experienced by the atoms during their propagation in the guide. This effect and its consequences for atom interferometry are investigated classically and quantum mechanically.

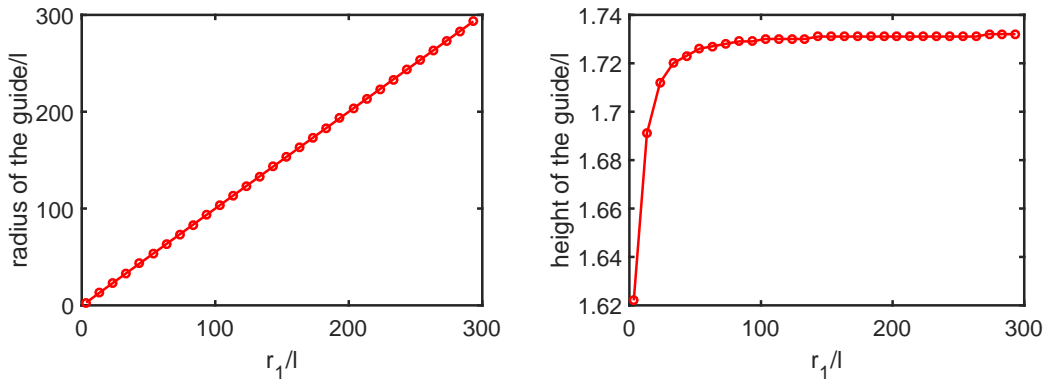


Figure 3.7 Toroidal guide position in units of the separation between the wires for $\frac{l_1}{l_2} = 1.5$ at constant separation between the wires.

Practical considerations

From the implementation point of view, we plan to fabricate a chip with a central wire radius of $500 \mu\text{m}$ and the separation between the wires of $15 \mu\text{m}$. Each wire has a square cross-section of size $3 \mu\text{m} \times 3 \mu\text{m}$. By neglecting the resistance due to the terminals (assuming perfectly closed loops), the resistance¹ of the inner

¹We compute the resistance with the equation $R = \frac{2\pi\rho r_0}{A}$ and the resistivity of gold at

wire is 7.4Ω , central wire is 7.6Ω and the outer most wire has a resistance of 7.9Ω . The self inductance of the wires are $3.3 nH$, $3.42 nH$ and $3.54 nH$ for the inner, central and outer wires, respectively. With the above values, the cut-off frequency R/L is on the order of $1 GHz$, which is well above the modulation frequencies ($\sim kHz$) that are necessary for the modulated guide.

3.4 Conclusion

A magnetic waveguide using the current modulation technique is presented. The use of alternating currents to generate the waveguide helps to overcome the roughness problem, which is a critical technical limitation in the realisation of circular waveguides for wavepacket propagation on an atom chip. A novel solution is introduced here based on the modulation to generate a bias field with a same micro wires used to produce the guide. With an additional bias field perpendicular to the chip surface we improve the guide stability against Majorana losses.

We have also discussed in this chapter a scheme to tune the position of the guide by the addition of an oscillating field perpendicular to the chip. Using numerical simulations of the atoms dynamics, we identified the range of parameters for which the guide is tight and the atomic motion is stable and adiabatic. The numerical tools discussed in this chapter are essential as they can serve as a roadmap to the optimal design and realization of a circular waveguide.

300 K is 2.2×10^{-8} .

Chapter 4

Matterwave interferometry with propagating atoms

Guided Sagnac interferometry is a promising solution for inertial sensing applications owing to the allowed long interrogation times. However, the coherent guiding of the matterwaves requires a careful study of the guiding potential. The guiding potential should not induce any systematic phase shifts or any such effects must be well quantified and removed in order to extract the interferometric signal. In section 4.1, we discuss the motion of an atom in a toroidal guide from the classical and quantum mechanical points of view. In section 4.2, using a 2D model we investigate the heating of the atoms in the guide and the conditions for the transverse monomode matterwave propagation. This study allows to obtain corrections to the Sagnac phase and the scale factor of the interferometer. We consider the two situations when the interferometer is operated with an ultra cold gas and with a cloud of thermal atoms. In both cases the effect of the atom temperature on the interference signal contrast is analysed.

4.1 Atom propagation in a toroidal guide

In a toroidal waveguide, the transverse and longitudinal motion of the atoms are coupled due to the centrifugal force. If an atom is launched tangentially along the guide, for an azimuthal free propagation, due to the interplay between the radial and longitudinal degrees of freedom, the transverse energy of the atom increases. Therefore, a study of the consequences of this "transverse heating" is necessary in the design of a circular waveguide for Sagnac interferometry [97, 98]. This heating can excite the transverse modes of the waveguide. In order to achieve a good fringe contrast, atom propagation in the guide has to be monomode. Motivated by a need to identify the guide parameters and the launching conditions for which atom propagation is monomode, we analyse the motion of atoms in a toroidal guide, classically and quantum mechanically .

4.1.1 Excitation of transverse modes: Classical analysis

Let us consider a waveguide of radius r_0 , and let us suppose that the transverse potential of the guide is harmonic with trapping frequencies ω_r and ω_z in the radial and vertical directions, respectively. The magnetic potential of an atom in the toroidal guide can be taken as [99]

$$V(r, z) = \frac{1}{2}m\omega_r^2(r - r_0)^2 + \frac{1}{2}m\omega_z^2z^2 . \quad (4.1.1)$$

We will assume that the atoms are initially held at a given location on the guide at $r = r_0$ and $z = 0$. We assume that the atoms are launched in the guide with an exact speed v_0 tangential to the guide, without any radial component i.e. $\dot{r}(0) = 0$. As there are no forces in the azimuthal direction, the angular momentum ($l = mv_0r_0$) of the atom is an integral of motion. In fact since l is an integral of motion, the atoms launched in a plane XY, located at a given coordinate Z, will remain on this plane. The motion of the atom in the vertical z direction is trivial and therefore, it will not be considered hereafter. The equations governing the radial motion of the atom are therefore

$$m\ddot{r} = -m\omega_r^2(r - r_0) + \frac{mv_t^2}{r} , \quad (4.1.2)$$

$$mv_t r = l , \quad (4.1.3)$$

where v_t is the velocity of the atom along the guide, such that $v_t r = \text{const}$ and $v_t = v_0$ when $r = r_0$. Notice that v_t changes as the atom moves radially and this leads to an exchange of energy between the transverse and the longitudinal motion. After eliminating v_t in the above equations we obtain

$$m\ddot{r} = -m\omega_r^2(r - r_0) + \frac{l^2}{mr^3} . \quad (4.1.4)$$

To compute the amount of energy that is transferred to the transverse direction, we first Taylor expand $1/r^3$ about r_0 up to first order in $r - r_0$, which is valid if the displacement from the centre of the guide is smaller than the guide radius i.e., if $|r - r_0| < r_0$

$$m\ddot{r} = -m\omega_r^2(r - r_0) + \frac{l^2}{mr_0^3} - \frac{3l^2}{mr_0^4}(r - r_0) . \quad (4.1.5)$$

By introducing the effective radial trapping frequency $\omega_{eff} \equiv \omega_r \sqrt{1 + \frac{3l^2}{m^2 r_0^4 \omega_r^2}}$, the above equation can be written as

$$m\ddot{r} = -m\omega_{eff}^2(r - r_0 - \epsilon) , \quad (4.1.6)$$

where the guide centre displacement ϵ is defined by the equation

$$\epsilon \equiv l^2 / \omega_{eff}^2 m^2 r_0^3 . \quad (4.1.7)$$

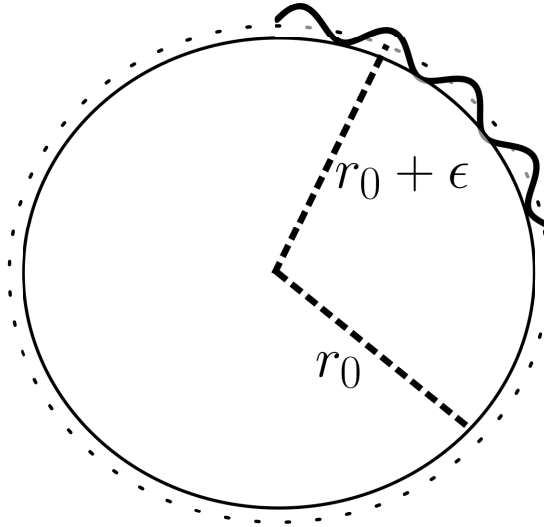


Figure 4.1 *Classical trajectory of an atom launched in a guide of radius r_0 . The atom position oscillates radially about $r_0 + \epsilon$, where the amplitude of the motion ϵ depends on the launch velocity and the radial trap frequency. Note that the radial coordinate of the atom is always greater than r_0 .*

Therefore, the motion of the atom is approximately harmonic with an effective radial trapping frequency ω_{eff} about a point at a distance $r_0 + \epsilon$. Solving Eq. 4.1.6, using the initial conditions $r(0) = r_0$ and $\dot{r}(0) = 0$, we obtain the radial coordinate of the atom as a function of time

$$r(t) = r_0 + 2\epsilon \sin^2\left(\frac{1}{2}\omega_{eff}t\right). \quad (4.1.8)$$

Therefore, after a tangential velocity kick atoms oscillate radially such that $r(t) \geq r_0$ as depicted in Fig.4.1.

The deflection of the atom trajectories induced by the guide curvature translates into a transverse heating of the cloud. Indeed, let us consider that the atoms are initially located at $r = 0$. Since $\dot{r}(0) = 0$, the initial transverse energy is $E(0) = 0$. After a time t , the increase in the transverse energy is given by

$$\Delta E = E(t) - E(0) = \frac{1}{2}m\dot{r}^2 + \frac{1}{2}m\omega_r^2(r - r_0)^2, \quad (4.1.9)$$

which can be approximated as

$$\Delta E \approx 2m\epsilon^2\omega_r^2 \sin^2\left(\frac{1}{2}\omega_r t\right). \quad (4.1.10)$$

Therefore, from the Eq.4.1.10 we can see that the transverse energy oscillates periodically, due to the exchange of energy between the transverse and longitudinal motional degrees of freedom. The time-averaged transverse energy over

one oscillation period evaluates to

$$\langle \Delta E \rangle = \frac{mv_0^4}{\omega_r^2 r_0^2}. \quad (4.1.11)$$

We can notice from the above expression that the transverse heating $\langle \Delta E \rangle$ increases rapidly with the launch velocity ($\propto v_0^4$), while heating decreases with the guide radius and radial trapping frequency, as expected. As an example, for a guide of $500 \mu\text{m}$ radius, the transverse heating as a function of the launch velocity and trapping frequency is shown in Fig.4.2. Thus, for a given waveguide, the launch velocity must be chosen so as to keep the heating as low as possible. The effect of the heating can be estimated by comparing the transverse energy to the energy separation $E_{n+1} - E_n = \hbar\omega_r$ between the radial modes, if the problem would have been treated quantum mechanically. For single mode propagation, we expect the transverse heating to be lower than the energy separation, i.e.

$$\frac{mv_0^4}{\omega_r^2 r_0^2} \leq \hbar\omega_r. \quad (4.1.12)$$

For a given launch velocity and guide radius, the above inequality defines a

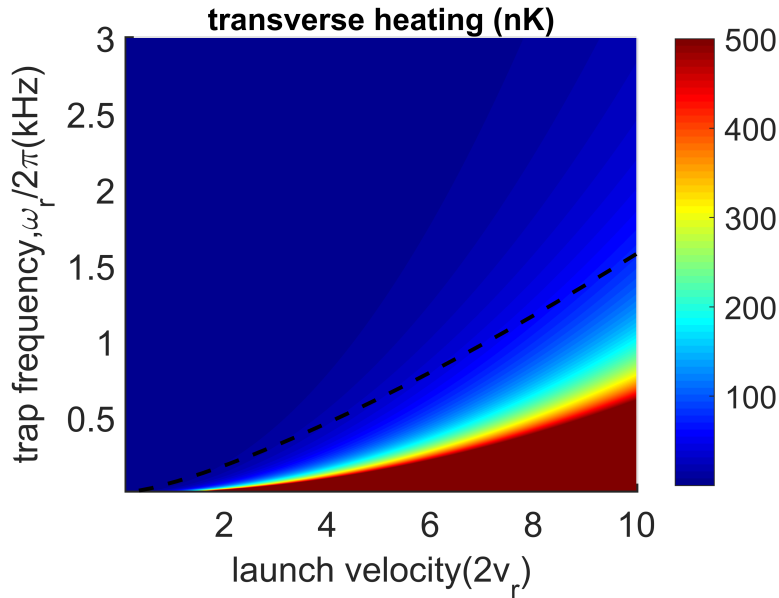


Figure 4.2 *Time-averaged transverse heating $\langle \Delta E \rangle$ of the atom in a guide of radius $500 \mu\text{m}$. The dashed line shows the critical trap frequency ω_c for a given launch velocity. Transverse energy increases rapidly with the launch velocity.*

critical radial trapping frequency, at which the transverse heating is enough to

excite a transverse mode

$$\omega_c = \sqrt[3]{\frac{mv_0^4}{\hbar r_0^2}}. \quad (4.1.13)$$

Alternatively, the critical trap frequency can be obtained from a simple scaling argument. The extent of the wavefunction in a harmonic oscillator of frequency ω_r is $\sqrt{\hbar/m\omega_r}$. We expect that the transverse excitations are negligible if the displacement in the equilibrium position ϵ due to the velocity kick is smaller than $\sqrt{\hbar/m\omega_r}$, i.e.

$$\epsilon = \frac{l^2}{\omega_{eff}^2 m^2 r_0^3} \approx \frac{v_0^2}{\omega_r^2 r_0} < \sqrt{\frac{\hbar}{m\omega_r}} \quad (4.1.14)$$

$$\implies \omega_r \geq \omega_c = \sqrt[3]{\frac{mv_0^4}{\hbar r_0^2}}. \quad (4.1.15)$$

Therefore, the radial trapping frequency ω_r must be greater than the critical trap frequency ω_c for monomode transverse propagation. For instance, if we consider a ^{87}Rb atom launched in a guide of $500 \mu\text{m}$ radius with twice the recoil velocity $v_0 = 11 \text{ mm/s}$, then the critical radial trapping frequency $\omega_c/2\pi$ comes out to be 92 Hz . The above semi-classical results give an indication as to when the transverse heating is significant. In the next section, we present a quantum mechanical calculation of the excitation probability after a sudden tangential velocity kick along the azimuthal direction.

4.1.2 Excitation of transverse modes: Quantum mechanical analysis

The time independent Schrodinger equation of an atom in a toroidal guide can be expressed in cylindrical coordinates as

$$\left[-\frac{\hbar^2}{2m}(\partial_r^2 + \frac{1}{r}\partial_r + \frac{1}{r^2}\partial_\theta^2 + \partial_z^2) + \frac{1}{2}m\omega_r^2(r-r_0)^2 + \frac{1}{2}m\omega_z^2 z^2\right]\Psi(r, \theta, z) = E\Psi(r, \theta, z). \quad (4.1.16)$$

Using the ansatz, $\Psi(r, \theta, z) = R(r)\Theta(\theta)Z(z)$, justified by the decoupling of the dynamics of the different degrees of freedom, the eigenvalue problem can be expressed as

$$\left[-\frac{\hbar^2}{2m}(\ddot{R} + \frac{1}{r}\dot{R} - \frac{l_\theta^2}{r^2}) + \frac{1}{2}m\omega_r^2(r-r_0)^2\right]R(r) = E_r R(r), \quad (4.1.17)$$

$$\ddot{\Theta}(\theta) = -l_\theta^2 \Theta(\theta), \quad (4.1.18)$$

$$-\frac{\hbar^2}{2m}\ddot{Z}(z) + \frac{1}{2}m\omega_z^2 z^2 Z = E_z Z(z), \quad (4.1.19)$$

$$E_r = E - E_z. \quad (4.1.20)$$

In the azimuthal direction, periodic boundary conditions constrain the quantum number l_θ to be an integer and the corresponding eigenfunctions are the plane waves $\exp(\pm il_\theta\theta)$. Along the vertical axis, the equation is an harmonic oscillator with energy levels $E_z = (n_z + \frac{1}{2})\hbar\omega_z$, where n_z is a non negative integer. The non trivial equation for the radial wavefunction can be recast as a harmonic oscillator equation by using the transformation $\tilde{R} = \sqrt{r}R$, which results in

$$-\frac{\hbar^2}{2m}\ddot{\tilde{R}} + \left[\frac{1}{2}m\omega_r^2(r-r_0)^2 + \frac{\hbar^2(4l_\theta^2-1)}{8mr^2}\right]\tilde{R} = E_r\tilde{R}. \quad (4.1.21)$$

Further analysis can be simplified, if we treat the motion along the guide classically considering a large orbital angular momentum quantum number l_θ . Indeed, in a guide of radius $500 \mu m$, $l_\theta = mv_0r_0/\hbar \gg 1$ if the launch velocity is $11 mm/s$. We can therefore replace $\hbar l_\theta$ with the classical parameter value l . Initially the atoms are localized at a given position in the guide and therefore $l = 0$

$$-\frac{\hbar^2}{2m}\ddot{\tilde{R}} + \left[\frac{1}{2}m\omega_r^2(r-r_0)^2 - \frac{\hbar^2}{8mr^2}\right]\tilde{R} = E_r\tilde{R}. \quad (4.1.22)$$

The effect of the term $\hbar^2/8mr^2$ in the above equation can be neglected if the radius of the guide is much larger than the typical size of the wavefunction, i.e., if $r_0 \gg \sqrt{\hbar/m\omega_r}$. In fact this term merely shifts all the energy levels by $\hbar^2/8mr_0^2$ and under this approximation the lowest energy state is a Gaussian

$$\tilde{R} \propto e^{-\frac{m\omega_r}{2\hbar}(r-r_0)^2}, \quad (4.1.23)$$

$$R \propto \frac{1}{\sqrt{r}}e^{-\frac{m\omega_r}{2\hbar}(r-r_0)^2}. \quad (4.1.24)$$

The wavefunction is usually localized around r_0 for a sufficiently tight guide, and the integral to normalize the radial wavefunction R can be approximated as

$$N^{-2} = \int_0^\infty r|R|^2 dr \approx \int_{-\infty}^\infty r|R|^2 dr = \sqrt{\frac{\pi\hbar}{m\omega_r}}. \quad (4.1.25)$$

Finally, the radial ground state wavefunction can be approximated as

$$R_0 = \left(\frac{m\omega_r}{\pi\hbar r^2}\right)^{1/4} \exp\left(-\frac{m\omega_r}{2\hbar}(r-r_0)^2\right). \quad (4.1.26)$$

Notice that the radial wavefunction differs from the harmonic oscillator wavefunction only in the normalization constant. After the tangential velocity kick, the equation for the radial wavefunction can be approximated as

$$-\frac{\hbar^2}{2m}\ddot{\tilde{R}} + \left[\frac{1}{2}m\omega_r^2(r-r_0)^2 + \frac{l^2}{2mr^2}\right]\tilde{R} = E_r\tilde{R}, \quad (4.1.27)$$

which is valid, since $l = mv_0 r_0 \gg \hbar$ for launching velocities of few millimetres per second in a $500 \mu\text{m}$ guide. The term $l^2/2mr^2$ can be Taylor expanded about r_0 up to second order

$$-\frac{\hbar^2}{2m}\ddot{R} + \left\{ \frac{1}{2}m\omega_r^2(r-r_0)^2 + \frac{l^2}{2mr_0^2} \left[1 - 2\frac{r-r_0}{r_0} + 3\frac{(r-r_0)^2}{r_0^2} \right] \right\} \tilde{R} = E_r \tilde{R}, \quad (4.1.28)$$

which can be rewritten as

$$-\frac{\hbar^2}{2m}\ddot{R} + \left[\frac{1}{2}m\omega_{eff}^2(r-r_0-\epsilon)^2 \right] \tilde{R} = E'_r \tilde{R}, \quad (4.1.29)$$

$$E'_r = E_r - \frac{l^2}{2mr_0^2} + \frac{1}{2}m\omega_{eff}^2\epsilon^2. \quad (4.1.30)$$

The effect of the velocity kick can be seen as a change in the radial trapping frequency with a slight displacement in the equilibrium position, which we have already noticed in the classical treatment.

In summary, the effective radial Hamiltonian experienced by the atom is given by (a similar treatment can be found in Dutta *et al.* [100] except that the authors consider terms up to first order in the Taylor expansion of the centrifugal term)

$$\mathcal{H}_r = \begin{cases} -\frac{\hbar^2}{2m}\ddot{R} + \frac{1}{2}m\omega_r^2(r-r_0)^2\tilde{R} & t \leq 0 \\ -\frac{\hbar^2}{2m}\ddot{R} + \frac{1}{2}m\omega_{eff}^2(r-r_0-\epsilon)^2\tilde{R} & t > 0 \end{cases}, \quad (4.1.31)$$

the above assumption is valid if we assume that the tangential velocity change happens at a time scale much shorter than the time scale of the radial oscillations.

Having derived the Hamiltonian governing the wavefunction dynamics, we are now in the position to obtain the quantum mechanical behaviour of the atoms in the toroidal guide. Suppose that the atoms are initially cold enough to occupy the ground state of the Hamiltonian at $t = 0$, i.e.

$$\Psi_0(r) = R_0 = \left(\frac{m\omega_r}{\pi\hbar r^2} \right)^{1/4} \exp\left[-\frac{m\omega_r}{2\hbar}(r-r_0)^2 \right]. \quad (4.1.32)$$

Then, after the velocity kick, the atoms evolve under a new harmonic potential, and the state $|\Psi_0\rangle$ can be expressed as a linear combination of the new eigenstates of the Hamiltonian, $\mathcal{H}_r(t > 0)$.

$$|\Psi_0\rangle = \sum_{n=0}^{\infty} a_n |\Psi'_n\rangle, \quad (4.1.33)$$

where a_n is the probability amplitude for the atom to be in the n^{th} state after the velocity kick. The probability amplitudes can be straightforwardly evaluated, in

particular for the ground and three first excited states we obtain¹

$$a_0 = \langle \Psi'_0 | \Psi_0 \rangle = \sqrt{2} \frac{(\omega_r \omega_{eff})^{\frac{1}{4}}}{(\omega_r + \omega_{eff})^{\frac{1}{2}}} e^{-\frac{m}{2\hbar} \frac{\omega_r \omega_{eff}}{\omega_r + \omega_{eff}} \epsilon^2}, \quad (4.1.34)$$

$$a_1 = \langle \Psi'_1 | \Psi_0 \rangle = -2\epsilon \sqrt{\frac{m}{\hbar}} \frac{\omega_r^{\frac{5}{4}} \omega_{eff}^{\frac{3}{4}}}{(\omega_r + \omega_{eff})^{\frac{3}{2}}} e^{-\frac{m}{2\hbar} \frac{\omega_r \omega_{eff}}{\omega_r + \omega_{eff}} \epsilon^2}, \quad (4.1.35)$$

$$a_2 = \langle \Psi'_2 | \Psi_0 \rangle = -\frac{(\omega_r \omega_{eff})^{\frac{1}{4}}}{(\omega_r + \omega_{eff})^{\frac{5}{2}}} [\omega_r^2 (1 - 2 \frac{m \omega_{eff}}{\hbar} \epsilon^2) - \omega_{eff}^2] e^{-\frac{m}{2\hbar} \frac{\omega_r \omega_{eff}}{\omega_r + \omega_{eff}} \epsilon^2}, \quad (4.1.36)$$

$$a_3 = \langle \Psi'_3 | \Psi_0 \rangle = \epsilon \sqrt{\frac{2m}{3\hbar}} \frac{\omega_r^{\frac{5}{4}} \omega_{eff}^{\frac{3}{4}}}{(\omega_r + \omega_{eff})^{\frac{7}{2}}} [3(\omega_r^2 - \omega_{eff}^2) - \frac{2m \omega_{eff}}{\hbar} \omega_r^2 \epsilon^2] e^{-\frac{m}{2\hbar} \frac{\omega_r \omega_{eff}}{\omega_r + \omega_{eff}} \epsilon^2}. \quad (4.1.37)$$

For a guide radius of 500 μm , and for velocities in the range of $[1 v_r; 20 v_r]$, the effective radial trapping frequency can be approximated as ω_r and the probability amplitudes can be simplified as,

$$a_0 = e^{-\frac{m \omega_r}{4\hbar} \epsilon^2}, \quad (4.1.38)$$

$$a_1 = -\epsilon \sqrt{\frac{m \omega_r}{2\hbar}} e^{-\frac{m \omega_r}{2\hbar} \epsilon^2}, \quad (4.1.39)$$

$$a_2 = \frac{1}{\sqrt{8}} \frac{m \omega_r}{\hbar} \epsilon^2 e^{-\frac{m \omega_r}{4\hbar} \epsilon^2}, \quad (4.1.40)$$

$$a_3 = -\epsilon^3 \sqrt{\frac{(m \omega_r)^3}{48 \hbar^3}} e^{-\frac{m \omega_r}{4\hbar} \epsilon^2}. \quad (4.1.41)$$

In general, the amplitude probability to be in the n^{th} state is [101],

$$a_n = (-1)^n \epsilon^n \sqrt{\frac{(m \omega_r)^n}{2^n n! \hbar^n}} e^{-\frac{m \omega_r}{4\hbar} \epsilon^2}. \quad (4.1.42)$$

The occupational probabilities of the first four transverse states after a velocity kick are plotted in Fig.4.3. The probability to be in the excited states increases with the launching velocity and decreases with the radial trapping frequency. For instance, the probability to be in the ground state is given by

$$|a_0|^2 = e^{-\frac{m v_0^4}{2 \hbar r^2 \omega_r^3}} = e^{-\frac{\omega_c^3}{2 \omega_r^3}}. \quad (4.1.43)$$

The Eq.4.1.43 implies that the critical trap frequency obtained from the semi-classical arguments corresponds to a ground state occupation probability of $1/\sqrt{e} \approx 0.6065$. Iso-probability contours to be in the transverse ground state

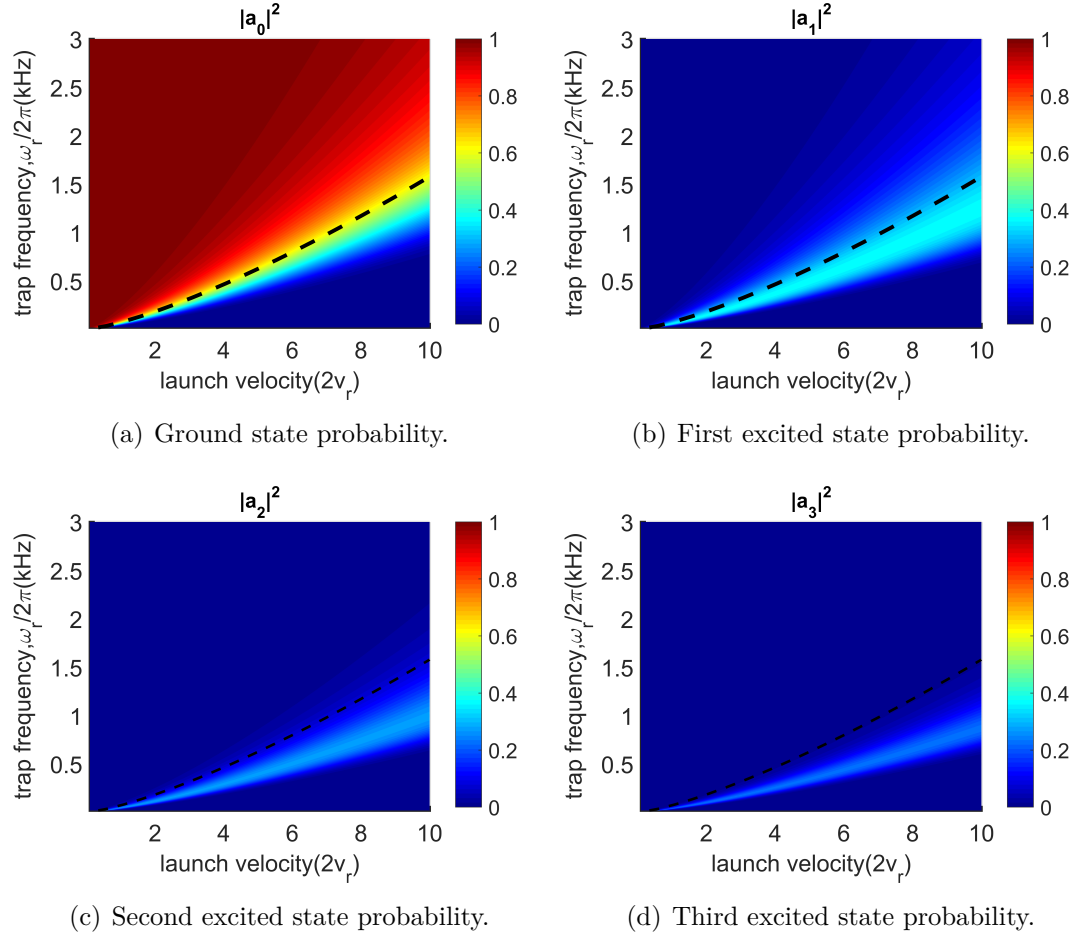


Figure 4.3 *Density plots of the atomic occupation probability in the $v_0 - \omega_r$ plane. The ground and the first three excited states are plotted for a guide of radius $500 \mu\text{m}$. The dashed line in each plot indicates the critical trap frequency given by the equation Eq.4.1.13.*

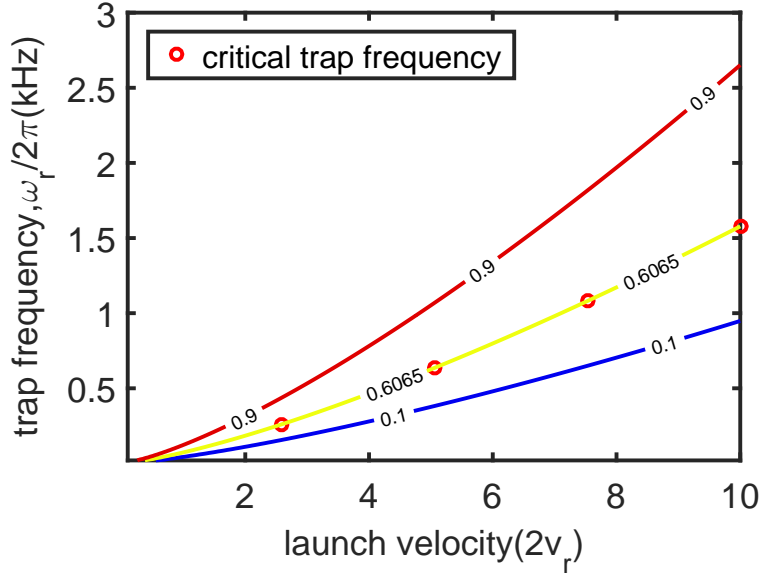


Figure 4.4 Iso-probability lines to be in the ground state for a guide of radius $500 \mu\text{m}$. The iso-probability line $1/\sqrt{e} \approx 0.6065$ coincides with the critical trap frequency (Eq.4.1.13) obtained by semi-classical arguments.

after the velocity kick are shown in Fig.4.4. Expressing the probabilities to be in the excited states, in terms of the critical trap frequency we get

$$|a_1|^2 = \frac{\omega_c^3}{2\omega_r^3} e^{-\frac{\omega_c^3}{2\omega_r^3}}, \quad (4.1.44)$$

$$|a_2|^2 = \frac{1}{8} \frac{\omega_c^6}{\omega_r^6} e^{-\frac{\omega_c^3}{2\omega_r^3}}, \quad (4.1.45)$$

$$|a_3|^2 = \frac{1}{48} \frac{\omega_c^9}{\omega_r^9} e^{-\frac{\omega_c^3}{2\omega_r^3}}. \quad (4.1.46)$$

Following Eq.4.1.42, the probabilities to be in the n^{th} excited state can be expressed as

$$|a_n|^2 = \frac{1}{n!} \left[\frac{\omega_c}{2\omega_r} \right]^{3n} e^{-\frac{\omega_c^3}{2\omega_r^3}}, \quad (4.1.47)$$

which is nothing but a Poissonian distribution if we set $\alpha = \sqrt{\frac{\omega_c^3}{2\omega_r^3}}$

$$|a_n|^2 = \frac{\alpha^{2n}}{n!} e^{-\alpha^2}. \quad (4.1.48)$$

¹Probability amplitudes are computed by extending the integration limits from $-\infty$ to ∞ assuming that the wavefunctions are sufficiently localized around $r = r_0$.

The appearance of the Poissonian distribution suggests that the radial state can be expressed as a coherent state. Indeed using Eq.4.1.42 the radial wavefunction after the velocity kick can be written as a coherent state

$$|\Psi_0\rangle = \sum_{n=0}^{\infty} a_n |\Psi'_n\rangle = e^{-\frac{\alpha^2}{2}} \sum_{n=0}^{\infty} \frac{(-\alpha)^n}{\sqrt{n!}} |n\rangle = |-\alpha\rangle , \quad (4.1.49)$$

where $\{|n\rangle\}$ denote the usual number states of a harmonic oscillator. As long as the trap frequency is well above the critical trap frequency, the excitation probability can be kept relatively low, which preserves the monomode character of the matterwave propagation in the guide.

4.2 Matterwave interferometry

In this section, we discuss the Sagnac effect in a guided atom interferometer considering the effect of the guiding potential. We study the relevance of the multimode propagation to the Sagnac phase shift and the contrast of the interferometer. We focus here on a specific implementation, using double Bragg diffraction where the internal states of the atoms are unchanged during the interferometer sequence [102, 103]. In particular, the different stages of a guided interferometer using Bragg pulses are shown in Fig.4.5. A $\pi/2$ Bragg pulse splits an atom cloud into two, which is initially at rest in the lab frame. This pulse launches the atoms along the guide with equal and opposite velocities in the lab frame. The two counter propagating clouds come back to the launch point after some time, where a second $\pi/2$ pulse is applied to interfere the clouds.

The rotation rate of the lab can then be obtained by measuring the population of atoms in the different output momentum states of the interferometer. In fact, the different momentum modes of the interferometer, after the application of a $\pi/2$ pulse transform according to the equations

$$\begin{aligned} |0\rangle &\xrightarrow{\pi/2} \frac{i}{\sqrt{2}} (|-2\hbar k\rangle + |2\hbar k\rangle) , \\ |-2\hbar k\rangle &\xrightarrow{\pi/2} \frac{1}{2} (-|2\hbar k\rangle + |-2\hbar k\rangle) + \frac{i}{\sqrt{2}} |0\rangle , \\ |2\hbar k\rangle &\xrightarrow{\pi/2} \frac{1}{2} (|2\hbar k\rangle - |-2\hbar k\rangle) + \frac{i}{\sqrt{2}} |0\rangle , \end{aligned} \quad (4.2.1)$$

that allows to read the phase information imprinted by the light pulses. We are interested in this signal which carries the inertial effects acting on the interferometer. In section 4.2.1, we introduce the mathematical framework required to analyse the operation of this guided atom interferometer, by assuming that the guide is infinitely tight. In section 4.2.2, we present a more realistic model that takes into account the radial potential of the guide. Finally, the effect of the finite temperature of the atoms on the interferometer contrast is discussed in section 4.2.3.

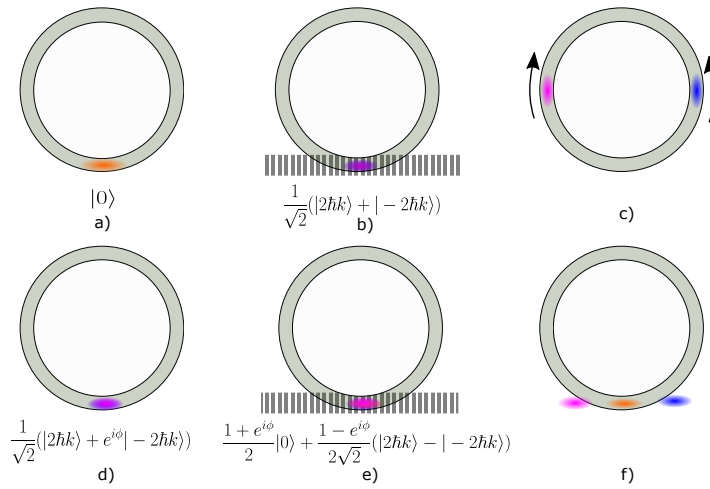


Figure 4.5 *Illustration of the interferometry sequence as seen from the lab frame. Images are to be read from left to right and from top to bottom: a) input state of the interferometer; b) after the first $\pi/2$ pulse the cloud is split into two with momentum $\pm 2\hbar k$; c) the position of the two wavepackets after a time $t = T/2$; d) after completing one rotation around the waveguide ($t = 2T$), the wavepackets $|2\hbar k\rangle$ and $|-2\hbar k\rangle$ acquire a relative phase Φ proportional to the lab's angular velocity; e) output state of the interferometer after the second $\pi/2$ pulse, where the phase information is imprinted on the population of atoms in different states; f) the population in each state can be extracted by imaging the clouds after a given separation time.*

4.2.1 1D interferometer model

We first consider a simple model, where the atoms are assumed to be confined to a ring of radius r_0 , while the azimuthal direction is free. The Hamiltonian describing the atom dynamics in the inertial reference frame is therefore

$$\mathcal{H} = -\frac{\hbar^2}{2mr_0^2}\partial_\theta^2, \quad (4.2.2)$$

whose eigenfunctions are plane waves characterized by an integer l_θ and energy E_{l_θ}

$$\psi_{l_\theta} = \frac{1}{\sqrt{2\pi}}e^{il_\theta\theta}, \quad (4.2.3)$$

$$E_{l_\theta} = \frac{\hbar^2 l_\theta^2}{2mr_0^2}. \quad (4.2.4)$$

Let us assume that the lab frame is rotating about z axis with an angular velocity Ω with respect to the inertial frame. If the atoms are launched in the guide with a Bragg pulse, the three states involved in the interferometer are

$$\psi_{l_0} = \frac{1}{\sqrt{2\pi}}e^{il_0\theta}; \quad l_0 = \frac{m\Omega r_0^2}{\hbar}, \quad (4.2.5)$$

$$\psi_{l_+} = \frac{1}{\sqrt{2\pi}}e^{il_+\theta}; \quad l_+ = \frac{2\hbar k r_0 + m\Omega r_0^2}{\hbar}, \quad (4.2.6)$$

$$\psi_{l_-} = \frac{1}{\sqrt{2\pi}}e^{il_-\theta}; \quad l_- = \frac{-2\hbar k r_0 + m\Omega r_0^2}{\hbar}. \quad (4.2.7)$$

Initially, we assume that the atoms are at rest in the lab frame, i.e. $\psi(t=0) = \psi_{l_0}$. The wavefunction of the atoms after the first $\pi/2$ pulse is

$$\psi(t=0^+) = \frac{i}{\sqrt{2}}(\psi_{l_+} + \psi_{l_-}). \quad (4.2.8)$$

which after a free evolution of duration $2T = \pi m r_0 / \hbar k$ seconds transforms into

$$\psi(t=2T) = e^{-i\frac{\mathcal{H}2T}{\hbar}}\psi(t=0^+). \quad (4.2.9)$$

The wavefunction can be written as

$$\psi(t=2T) = \frac{i}{\sqrt{2}}e^{-iE_{l_+}\frac{2T}{\hbar}}(\psi_{l_+} + e^{i\Phi}\psi_{l_-}), \quad (4.2.10)$$

where the Sagnac phase Φ acquired due to the rotation of the lab frame (the device) is given by

$$\Phi = \frac{8\pi m A \Omega}{h}, \quad (4.2.11)$$

and $A = \pi r_0^2$ is the area enclosed by the interferometer. When the atoms return to the launch point, another $\pi/2$ Bragg pulse is applied to recombine the two counter propagating clouds. The wavefunction at the end of the interferometer sequence up to an arbitrary global phase factor is

$$\psi(t = 2T^+) = \frac{i(1 + e^{i\Phi})}{2} \psi_{l_0} + \frac{1 - e^{i\Phi}}{2\sqrt{2}} (\psi_{l_+} - \psi_{l_-}), \quad (4.2.12)$$

and the Sagnac phase Φ , is imprinted on the population of atoms in different output momentum states with probabilities

$$P_{l_0} = \frac{N_{l_0}}{N_{l_+} + N_{l_0} + N_{l_-}} = \frac{1 + \cos \Phi}{2}, \quad (4.2.13)$$

$$P_{l_{\pm}} = \frac{N_{l_{\pm}}}{N_{l_+} + N_{l_0} + N_{l_-}} = \frac{1 - \cos \Phi}{2}. \quad (4.2.14)$$

After the interferometric sequence, the population of atoms in different output momentum states can be determined by imaging the clouds after a free evolution, sufficient enough to spatially discriminate atoms in the different angular momentum states.

Matrix formalism

Alternatively, we can model the interferometer using matrices. This formalism allows to easily explore from the theoretical point of view different ways to operate the interferometer. Let us consider the interferometer sequence previously discussed. The effect of a $\pi/2$ pulse on the different angular momentum states involved in the interferometer can be taken into account with the matrix

$$S_{\frac{\pi}{2}} = \begin{bmatrix} \frac{1}{2} & \frac{i}{\sqrt{2}} & -\frac{1}{2} \\ \frac{i}{\sqrt{2}} & 0 & \frac{i}{\sqrt{2}} \\ -\frac{1}{2} & \frac{i}{\sqrt{2}} & \frac{1}{2} \end{bmatrix}, \quad (4.2.15)$$

where the 1st row corresponds to the state $|\psi_{l_+}\rangle$, the 2nd row to the state $|\psi_{l_0}\rangle$ and the 3rd row to the state $|\psi_{l_-}\rangle$. With this convention, the initial state of the interferometer is

$$|\Psi_{in}\rangle = \begin{bmatrix} 0 \\ 1 \\ 0 \end{bmatrix}. \quad (4.2.16)$$

The time evolution of the states during the free propagation, for a duration of $2T = \pi m r_0 / \hbar k$ seconds is then given by the diagonal matrix

$$S_{2T} = \begin{bmatrix} e^{-i \frac{(2\hbar k + m\Omega r_0)^2}{2m} \frac{2T}{\hbar}} & 0 & 0 \\ 0 & e^{-i \frac{(m\Omega r_0)^2}{2m} \frac{2T}{\hbar}} & 0 \\ 0 & 0 & e^{-i \frac{(-2\hbar k + m\Omega r_0)^2}{2m} \frac{2T}{\hbar}} \end{bmatrix}, \quad (4.2.17)$$

by factoring out the term $e^{-i[\frac{(2hk+m\Omega r_0)^2}{2m} + \frac{(-2hk+m\Omega r_0)^2}{2m}] \frac{T}{\hbar}}$, we can write S_{2T} in terms of the Sagnac phase Φ as

$$S_{2T} = e^{-i\frac{(m\Omega r_0)^2 + (2hk)^2}{2m} \frac{2T}{\hbar}} \begin{bmatrix} e^{i\frac{\Phi}{2}} & 0 & 0 \\ 0 & e^{-i2\pi k r_0} & 0 \\ 0 & 0 & e^{-i\frac{\Phi}{2}} \end{bmatrix}. \quad (4.2.18)$$

A second $\pi/2$ pulse is applied to recombine the counter propagating clouds. The final state $|\Psi_{out}\rangle$ at the output of the interferometer can be computed by multiplying the matrix $S_{\pi/2} S_{2T} S_{\pi/2}$ with the initial state $|\Psi_{in}\rangle$, which up to an arbitrary global phase factor is given by,

$$|\Psi_{out}\rangle = S_{\pi/2} S_{2T} S_{\pi/2} |\Psi_{in}\rangle = \begin{bmatrix} \frac{1-e^{i\Phi}}{2\sqrt{2}} \\ \frac{i(1+e^{i\Phi})}{2} \\ -\frac{1-e^{i\Phi}}{2\sqrt{2}} \end{bmatrix}. \quad (4.2.19)$$

Now, let us suppose that, instead of shining the second $\pi/2$ pulse we let the clouds to freely propagate in the guide. Both the clouds meet again at the launching point after another $2T$ seconds, if a $\pi/2$ pulse is now applied the output state is given by

$$|\Psi_{out}\rangle = S_{\pi/2} S_{2T} S_{2T} S_{\pi/2} |\Psi_{in}\rangle = \begin{bmatrix} \frac{1-e^{2i\Phi}}{2\sqrt{2}} \\ \frac{i(1+e^{2i\Phi})}{2} \\ -\frac{1-e^{2i\Phi}}{2\sqrt{2}} \end{bmatrix}, \quad (4.2.20)$$

which is expected as the enclosed area of the interferometer is twice enlarged. In general, if the clouds are recombined after $2nT$ seconds (or after n round trips) the accumulated phase shift is simply $n\Phi$ i.e.

$$|\Psi_{out}\rangle = S_{\pi/2} (S_{2T})^n S_{\pi/2} |\Psi_{in}\rangle = \begin{bmatrix} \frac{1-e^{ni\Phi}}{2\sqrt{2}} \\ \frac{i(1+e^{ni\Phi})}{2} \\ -\frac{1-e^{ni\Phi}}{2\sqrt{2}} \end{bmatrix}. \quad (4.2.21)$$

This formalism is relevant for the study of quantum metrology protocols using $O(3)$ matrices to describe the engineering of atomic quantum states like, for instance a spin squeezing.

4.2.2 2D interferometer model

The model discussed in the previous section neglects the motion in the radial direction. Atom clouds propagating in a curved guide wiggle radially due to non negligible centrifugal forces and has been observed experimentally in a curved optical potential [104]. If we analyse the problem from an inertial frame, it is clear that the centrifugal forces are different for the clockwise and the counter

clockwise moving clouds, as they propagate with different angular momentum. Therefore, the radial motion is different for both the clouds. As we will see, this asymmetry in the radial motion leads to additional phase shifts and a loss in the contrast of the interferometer if the counter propagating clouds do not overlap at the end of the interferometer, especially when the radial trapping frequencies are relatively low. To quantify such phenomena, we consider a realistic situation, where the transverse potential of the waveguide is taken to be harmonic²

$$V(r) = \frac{1}{2}m\omega_r(r - r_0)^2 . \quad (4.2.22)$$

If we neglect the interatomic interactions, the Hamiltonian governing the dynamics of the atom in an inertial frame is

$$\mathcal{H} = -\frac{\hbar^2}{2m}(\partial_r^2 + \frac{1}{r}\partial_r + \frac{1}{r^2}\partial_\theta^2) + V(r) . \quad (4.2.23)$$

The eigenvalue problem can be simplified by using the ansatz $\psi(r, \theta) = \frac{1}{\sqrt{r}}R(r)\Theta(\theta)$, which gives

$$-\frac{\hbar^2}{2m}\frac{d^2R}{dr^2} + \frac{1}{2}m\omega_r^2(r - r_0)^2R + \frac{(4l^2 - 1)\hbar^2}{8mr^2}R = ER , \quad (4.2.24)$$

$$\frac{d^2\Theta}{d\theta^2} = -l^2\Theta . \quad (4.2.25)$$

The solution of the azimuthal wavefunction is a plane wave, where l takes integer values due to periodic boundary conditions. The equation for the radial wavefunction can be written as a harmonic oscillator equation by Taylor expanding the centrifugal term³ $l^2\hbar^2/2mr^2$ about r_0 up to second order, which results in

$$-\frac{\hbar^2}{2m}\frac{d^2R}{dr^2} + \frac{1}{2}m\omega_l^2(r - r_0 - \epsilon_l)^2R = E_lR , \quad (4.2.26)$$

where the effective trap frequency ω_l and the displacement in the equilibrium position ϵ_l are defined by the expressions (see section 4.1)

$$\omega_l \equiv \omega_r \sqrt{1 + \frac{3l^2\hbar^2}{m^2r_0^4\omega_r^2}} , \quad (4.2.27)$$

$$\epsilon_l \equiv \frac{l^2\hbar^2}{m^2r_0^3\omega_r^2} , \quad (4.2.28)$$

²We ignore the potential in the z direction, as the motion in this direction is not coupled to the azimuthal and radial motion and does not induce any excitations due to the propagation along the guide.

³The term $\frac{(4l^2-1)\hbar^2}{8mr^2}$ can be approximated as $\frac{l^2\hbar^2}{2mr^2}$ if the launch velocities are of the order of few millimeters per second for a guide of radius $\sim 500\mu\text{m}$.

and the eigenenergies are given by

$$E = E_l + \frac{l^2 \hbar^2}{2mr_0^2} - \frac{1}{2}m\omega_l^2 \epsilon_l^2 . \quad (4.2.29)$$

The solution of Eq.4.2.26 can be expressed in terms of the Hermite polynomials and $E_l = (n + \frac{1}{2})\hbar\omega_l$. Therefore, for a given angular momentum number l , the eigenfunctions of Eq.4.2.23 can be written as

$$\psi_{n,l}(r, \theta) = \frac{1}{\sqrt{2\pi r}} R_{n,l}(r) e^{il\theta} , \quad (4.2.30)$$

where $R_{n,l}(r)$ ⁴ denote the wavefunction of the n^{th} excited state of the harmonic potential $\frac{1}{2}m\omega_l^2(r - r_0 - \epsilon_l)^2$

$$R_{n,l} = \left(\frac{m\omega_l}{\pi\hbar}\right)^{1/4} \frac{1}{\sqrt{2^n n!}} e^{-\frac{m\omega_l}{2\hbar}(r-r_0-\epsilon_l)^2} H_n\left[\sqrt{\frac{m\omega_l}{\hbar}}(r - r_0 - \epsilon_l)\right] . \quad (4.2.31)$$

The eigenenergy of $\psi_{n,l}$ is

$$E_{n,l} = \left(n + \frac{1}{2}\right)\hbar\omega_l + \frac{l^2 \hbar^2}{2mr_0^2} - \frac{1}{2}m\omega_l^2 \epsilon_l^2 . \quad (4.2.32)$$

At the beginning of the interferometer sequence, the atoms are at rest in the lab frame. We assume that the atoms are cold enough to occupy only the ground state of the radial potential with angular momentum l_0 , i.e.⁵

$$\psi(t = 0) = \frac{1}{\sqrt{2\pi r}} R_{0,l_0} e^{il_0\theta} . \quad (4.2.33)$$

The wavefunction after the first $\pi/2$ pulse is

$$\psi(t = 0^+) = \frac{1}{2\sqrt{\pi r}} R_{0,l_0} (e^{il_0\theta} + e^{il_0\theta}) . \quad (4.2.34)$$

To compute the evolution of the wavefunction between the two $\pi/2$ pulses, we need to evaluate the action of the operator $e^{-2i\mathcal{H}T/\hbar}$ on each term in Eq.4.2.34, which can be done easily if we express the radial part R_{0,l_0} in the basis $\{R_{n,l_+}\}$ and $\{R_{n,l_-}\}$ as

$$\psi(t = 0^+) = \frac{1}{2\sqrt{\pi r}} \left[\sum_{n=0}^{\infty} a_{n0}^+ R_{n,l_+} e^{il_0\theta} + \sum_{n=0}^{\infty} a_{n0}^- R_{n,l_-} e^{il_0\theta} \right] , \quad (4.2.35)$$

⁴The normalization constant $(\frac{m\omega_l}{\pi\hbar})^{1/4}$ is obtained under the approximation, $\int_0^\infty R_{n,l}^2 dr \approx \int_{-\infty}^\infty R_{n,l}^2 dr = 1$ and is valid if the wavefunction is sufficiently localised around r_0 i.e., if $\sqrt{\frac{\hbar}{m\omega_l}} \ll r_0$.

⁵Here after, we do not indicate the explicit dependence of the radial wavefunction on r .

where a_{n0}^+ and a_{n0}^- are the overlap integrals given by

$$a_{n0}^+ = \int_0^\infty R_{n,l_+} R_{0,l_0} dr , \quad (4.2.36)$$

$$a_{n0}^- = \int_0^\infty R_{n,l_-} R_{0,l_0} dr . \quad (4.2.37)$$

The wavefunction at $t = 2T$ is then given by

$$\psi(t = 2T) = \frac{1}{2\sqrt{\pi r}} \left[\sum_{n=0}^\infty a_{n0}^+ e^{-iE_{n,l_+} \frac{2T}{\hbar}} R_{n,l_+} e^{il_+\theta} + \sum_{n=0}^\infty a_{n0}^- e^{-iE_{n,l_-} \frac{2T}{\hbar}} R_{n,l_-} e^{il_-\theta} \right] , \quad (4.2.38)$$

by noting that $E_{n,l_\pm} = (n + \frac{1}{2})\hbar\omega_{l_\pm} + \frac{\hbar^2 l_\pm^2}{2mr_0^2} - \frac{1}{2}m\omega_{l_\pm}^2 \epsilon_{l_\pm}^2$, we can express Eq.4.2.38 by factoring the term $\exp[-i(\frac{\hbar^2 l_\pm^2}{2mr_0^2} - \frac{1}{2}m\omega_{l_\pm}^2 \epsilon_{l_\pm}^2) \frac{2T}{\hbar}]$ as

$$\psi(t = 2T) = \frac{1}{2\sqrt{\pi r}} \left[\sum_{n=0}^\infty a_{n0}^+ e^{-i(2n+1)\omega_{l_+} T} R_{n,l_+} e^{il_+\theta} + e^{i\Phi_T} \sum_{n=0}^\infty a_{n0}^- e^{-i(2n+1)\omega_{l_-} T} R_{n,l_-} e^{il_-\theta} \right] , \quad (4.2.39)$$

where the phase Φ_T is

$$\Phi_T = \Phi + m(\omega_{l_+}^2 \epsilon_{l_+}^2 - \omega_{l_-}^2 \epsilon_{l_-}^2) \frac{T}{\hbar} . \quad (4.2.40)$$

Φ_T consists of the expected Sagnac phase Φ and a correction. The wavefunction after the second $\pi/2$ pulse can be written as

$$\begin{aligned} \psi(t = 2T^+) &= \frac{1}{2\sqrt{\pi r}} \left[\frac{i}{\sqrt{2}} \sum_{n=0}^\infty (a_{n0}^+ e^{-i(2n+1)\omega_{l_+} T} R_{n,l_+} + e^{i\Phi_T} a_{n0}^- e^{-i(2n+1)\omega_{l_-} T} R_{n,l_-}) e^{il_0\theta} \right. \\ &\quad \left. + \frac{1}{2} \sum_{n=0}^\infty (a_{n0}^+ e^{-i(2n+1)\omega_{l_+} T} R_{n,l_+} - e^{i\Phi_T} a_{n0}^- e^{-i(2n+1)\omega_{l_-} T} R_{n,l_-}) (e^{il_+\theta} - e^{il_-\theta}) \right] , \end{aligned} \quad (4.2.41)$$

and therefore, the probabilities to be in different output momentum states at the end of the interferometer sequence are⁶

$$P_{l_0} = \frac{1}{4} \sum_{m,n}^\infty [a_{m0}^+ a_{n0}^+ \delta_{mn} e^{i(m-n)2\omega_{l_+} T} + a_{m0}^- a_{n0}^- \delta_{mn} e^{i(m-n)2\omega_{l_-} T} + 2a_{m0}^+ a_{n0}^- b_{mn} \cos(\theta_{mn} + \Phi_T)] , \quad (4.2.42)$$

$$P_{l_\pm} = \frac{1}{4} \sum_{m,n}^\infty [a_{m0}^+ a_{n0}^+ \delta_{mn} e^{i(m-n)2\omega_{l_+} T} + a_{m0}^- a_{n0}^- \delta_{mn} e^{i(m-n)2\omega_{l_-} T} - 2a_{m0}^+ a_{n0}^- b_{mn} \cos(\theta_{mn} + \Phi_T)] , \quad (4.2.43)$$

⁶ δ_{mn} is the usual Kronecker delta.

where we introduce for the sake of compactness

$$\theta_{mn} = (m + \frac{1}{2})2\omega_{l_+}T - (n + \frac{1}{2})2\omega_{l_-}T , \quad (4.2.44)$$

$$b_{mn} = \int_0^\infty R_{m,l_+}R_{n,l_-} dr . \quad (4.2.45)$$

The summation on the first two terms in the probabilities can be done by noting that $\sum_n a_{n0}^{+2} = \sum_n a_{n0}^{-2} = 1$, and we get

$$P_{l_0} = \frac{1}{2} [1 + \sum_{m,n} a_{m0}^+ a_{n0}^- b_{mn} \cos(\theta_{mn} + \Phi_T)] , \quad (4.2.46)$$

$$P_{l_\pm} = \frac{1}{2} [1 - \sum_{m,n} a_{m0}^+ a_{n0}^- b_{mn} \cos(\theta_{mn} + \Phi_T)] . \quad (4.2.47)$$

To compute the contrast of the interferometer we rewrite the above probabilities as

$$P_{l_0} = \frac{1}{2} [1 + C \cos(\Phi_T + \Phi_0)] , \quad (4.2.48)$$

$$P_{l_\pm} = \frac{1}{2} [1 - C \cos(\Phi_T + \Phi_0)] , \quad (4.2.49)$$

where the contrast C and the phase shift Φ_0 can be expressed in terms of the overlap integrals between the eigenstates

$$C = [[\sum_{m,n} a_{m0}^+ a_{n0}^- b_{mn} \cos \theta_{mn}]^2 + [\sum_{m,n} a_{m0}^+ a_{n0}^- b_{mn} \sin \theta_{mn}]^2]^{1/2} , \quad (4.2.50a)$$

$$\Phi_0 = \cos^{-1} [\frac{1}{C} \sum_{m,n} a_{m0}^+ a_{n0}^- b_{mn} \cos \theta_{mn}] . \quad (4.2.50b)$$

Due to the multimode propagation of the wavepackets, the contrast of the interferometer depends on the angular velocity of the lab frame, the launching velocity and the guide parameters (i.e. guide radius and radial trap frequency) and gives rise to an additional phase Φ_0 . The additional phase Φ_0 , should either be much below the Sagnac phase or well characterized in order to extract the angular velocity of the lab frame. Despite the fact that the overlap integrals between arbitrary states can be computed exactly [105, 101], it is hard to obtain analytical expressions for the contrast. Nevertheless, numerical computations can be done using the following analytical expressions for the overlap integrals

$$a_{n0}^+ = \frac{1}{\sqrt{n!}} (-1)^n \Delta_+^n e^{-\frac{\Delta_+^2}{2}} , \quad (4.2.51)$$

$$a_{n0}^- = \frac{1}{\sqrt{n!}} (-1)^n \Delta_-^n e^{-\frac{\Delta_-^2}{2}} , \quad (4.2.52)$$

$$b_{mn} = \sqrt{\frac{2\gamma^{1/2}}{1+\gamma}} e^{[-\frac{\gamma}{1+\gamma}\Delta'^2]} \frac{m!n!}{2^{m+n}} \left(\frac{\gamma-1}{\gamma+1}\right)^{\frac{m+n}{2}} \sum_{k=0}^{[m,n]} \frac{1}{k!(n-k)!(m-k)!} \left(\frac{4\gamma^{1/2}}{\gamma-1}\right)^k \quad (4.2.53)$$

$$H_{m-k}(\Delta'(\frac{2\gamma^2}{\gamma^2-1})^{1/2}) F_{n-k}(\Delta'(\frac{2\gamma}{\gamma^2-1})^{1/2}),$$

where $F_n(x) = i^n H_n(ix)$ is a real polynomial, $\gamma = \omega_{l_+}/\omega_{l_-}$, $[m, n]$ denotes the minimum of the two integers (m, n) and

$$\Delta_+ = (\epsilon_{l_+} - \epsilon_{l_0}) \sqrt{\frac{m\omega_{l_0}}{2\hbar}}, \quad (4.2.54)$$

$$\Delta_- = (\epsilon_{l_-} - \epsilon_{l_0}) \sqrt{\frac{m\omega_{l_0}}{2\hbar}}, \quad (4.2.55)$$

$$\Delta' = \sqrt{\frac{m\omega_{l_-}}{2\hbar}} (\epsilon_{l_+} - \epsilon_{l_-}). \quad (4.2.56)$$

Despite the complexity of the above expressions, the expressions for contrast Eq.(4.2.50a) and the additional phase Eq.(4.2.50b) can be simplified if the trap frequencies are approximately equal (tight guide approximation), but with an appreciable difference in the displacements of the equilibrium position i.e., $\omega_r = \omega_{l_0} = \omega_{l_+} = \omega_{l_-}$ and $\epsilon_{l_+} \neq \epsilon_{l_-}$ ⁷. First of all, the term θ_{mn} can be approximated as $\theta_{mn} \approx 2(m-n)\omega_r T$. Secondly, the overlap integral b_{mn} can be expressed simply as [105, 101]⁸

$$b_{mn} = \begin{cases} \sqrt{\frac{n!}{m!}} \Delta^{m-n} L_n^{m-n}(\Delta^2) e^{-\frac{\Delta^2}{2}}, & m > n \\ (-1)^{n-m} \sqrt{\frac{m!}{n!}} \Delta^{n-m} L_m^{n-m}(\Delta^2) e^{-\frac{\Delta^2}{2}}, & n > m \end{cases} \quad (4.2.57)$$

where L_m^n denote the generalized Laguerre polynomials and $\Delta = \Delta_+ - \Delta_-$. Under these approximations and with the help of the exact formulae for overlap integrals, the contrast loss can be computed numerically by considering a sufficient number of radial modes.

To gain some insight, let us consider the problem within the above mentioned approximations. In fact, the contrast loss and additional phases can be analytically computed by rewriting the problem as a forced harmonic oscillator. In the tight guide approximation, the radial wavefunction R_{0,l_0} with an angular momentum $l_{\pm}\hbar$ evolves according to the Hamiltonian

$$\mathcal{H}_{\pm} = \frac{-\hbar^2}{2m} \frac{d^2}{dr^2} + \frac{1}{2} m \omega_r^2 (r - r_0 - \epsilon_{l_{\pm}})^2 + \frac{l_{\pm}^2 \hbar^2}{2mr_0^2} - \frac{1}{2} m \omega_r^2 \epsilon_{l_{\pm}}^2. \quad (4.2.58)$$

⁷This is a valid approximation if $\frac{l_{\pm}^2 \hbar^2}{m^2 r_0^2 \omega_r^2} \ll 1$ and if $\epsilon_{\pm} \sim \sqrt{\hbar/m\omega_r}$. This approximation amounts to considering only the first order Taylor expansion of the centrifugal term $l^2 \hbar^2 / 2mr^2$.

⁸We remark once again that these integrals are obtained by extending the limits of the integration from $-\infty$ to ∞ .

By introducing the ladder operators $a = \sqrt{\frac{m\omega_r}{2\hbar}}[(r - r_0 - \epsilon_{l_0}) + \frac{\hbar}{m\omega_r} \frac{d}{dr}]$ and $a^\dagger = \sqrt{\frac{m\omega_r}{2\hbar}}[(r - r_0 - \epsilon_{l_0}) - \frac{\hbar}{m\omega_r} \frac{d}{dr}]$, we can rewrite the above Hamiltonian as

$$\mathcal{H}_\pm = \hbar\omega_r[a^\dagger a + \frac{1}{2} - \Delta_\pm(a^\dagger + a)] + E_\pm, \quad (4.2.59)$$

where $E_\pm = \frac{l_\pm^2 \hbar^2}{2mr_0^2} + \hbar\omega_r \Delta_\pm^2 - \frac{1}{2}m\omega_r^2 \epsilon_{l_\pm}^2$. The time evolution of the radial wavefunction R_{0,l_0} (which we represent with $|0\rangle$ hereafter) is given by

$$|\Psi_\pm\rangle = e^{i\frac{2T\mathcal{H}_\pm}{\hbar}} |0\rangle = e^{2iE_\pm T/\hbar} e^{2i\omega_r T[a^\dagger a + \frac{1}{2} - \Delta_\pm(a^\dagger + a)]} |0\rangle. \quad (4.2.60)$$

In order to compute the time evolution we multiply both sides with the displacement operator $\mathcal{D}(-\Delta_\pm)$ (a short introduction to the displacement operator and some useful properties needed for this calculation are given in the Appendix)

$$\mathcal{D}(-\Delta_\pm) |\Psi_\pm\rangle = e^{2i(\frac{E_\pm}{\hbar} + \frac{1}{2}\omega_r)T} \mathcal{D}(-\Delta_\pm) e^{2i\omega_r T[a^\dagger a - \Delta_\pm(a^\dagger + a)]} \mathcal{D}(\Delta_\pm) \mathcal{D}(-\Delta_\pm) |0\rangle, \quad (4.2.61)$$

using the properties of the displacement operator⁹ we can simplify the above expression in terms of coherent state,

$$\mathcal{D}(-\Delta_\pm) |\Psi_\pm\rangle = e^{2i[\frac{E_\pm}{\hbar} + (\frac{1}{2} - \Delta_\pm^2)\omega_r]T} |-\Delta_\pm e^{2i\omega_r T}\rangle. \quad (4.2.62)$$

Finally, the radial state after a free evolution of $2T$ seconds is obtained by multiplying on both sides with $\mathcal{D}(\Delta_\pm)$ ¹⁰

$$|\Psi_\pm\rangle = e^{2i[\frac{E_\pm}{\hbar} + (\frac{1}{2} - \Delta_\pm^2)\omega_r]T} e^{i\Delta_\pm^2 \sin(2\omega_r T)} |\Delta_\pm(1 - e^{2i\omega_r T})\rangle. \quad (4.2.63)$$

The probability for the atoms to have an angular momentum $l_0\hbar$ after the last $\pi/2$ pulse can be written as

$$P_{l_0} = \frac{1}{4} ||\Psi_+\rangle + |\Psi_-\rangle|^2, \quad (4.2.64)$$

which upon simplification gives

$$P_{l_0} = \frac{1}{2} [1 + C \cos(\phi_T + \Phi_0)]. \quad (4.2.65)$$

⁹Here we make use of the following relations:

$$\begin{aligned} \mathcal{D}(-\Delta_\pm) |0\rangle &= |-\Delta_\pm\rangle, \\ e^{2i\omega_r T a^\dagger a} |-\Delta_\pm\rangle &= |-\Delta_\pm e^{2i\omega_r T}\rangle, \\ \mathcal{D}(-\Delta_\pm) a \mathcal{D}(\Delta_\pm) &= a + \Delta_\pm, \\ \mathcal{D}(-\Delta_\pm) a^\dagger \mathcal{D}(\Delta_\pm) &= a^\dagger + \Delta_\pm. \end{aligned}$$

¹⁰ $\mathcal{D}(\Delta_\pm) |-\Delta_\pm e^{2i\omega_r T}\rangle = e^{i\Delta_\pm^2 \sin(2\omega_r T)} |\Delta_\pm(1 - e^{2i\omega_r T})\rangle$

The contrast of the interferometer in the above equation is given by

$$C = |\langle \Psi_+ | \Psi_- \rangle| = \exp[-|(\Delta_+ - \Delta_-)(e^{2i\omega_r T} - 1)|^2/2] = e^{-2\Delta^2 \sin^2(\omega_r T)}. \quad (4.2.66)$$

Expressing Δ in terms of the launch velocity and rotation rate of the lab frame, the contrast can be finally written as

$$C = e^{-\frac{16m_0^2\Omega^2}{\hbar\omega_r^3} \sin^2(\omega_r T)}. \quad (4.2.67)$$

Here we define the phases Φ_T and Φ_0 as

$$\Phi_T = 2\left[\frac{E_- - E_+}{\hbar} + (\Delta_+^2 - \Delta_-^2)\omega_r\right]T = \Phi + m\omega_r^2(\epsilon_{l_+}^2 - \epsilon_{l_-}^2)T/\hbar, \quad (4.2.68)$$

$$\Phi_0 = (\Delta_-^2 - \Delta_+^2) \sin(2\omega_r T). \quad (4.2.69)$$

and these definitions of Φ_0 and Φ_T allow a clear physical interpretation of Φ_T . Particularly striking in Eq.4.2.67 is the periodic variation in the contrast with respect to the trap frequency and launch velocity. We can understand the variations in the contrast and the additional phase shift Φ_0 by considering the expectation value of the radial coordinate of both the clouds. The time dependent mean position of the wavepacket going in the anti-clockwise direction is

$$\langle r \rangle_{l_+} = \sum_{m,n} a_{m0}^+ a_{n0}^+ \int_{-\infty}^{\infty} r R_{m,l_+} R_{n,l_+} e^{i(m-n)2\omega_r T} dr. \quad (4.2.70)$$

To compute this integral, note that the wavefunctions $\{R_{n,l_+}\}$ are centred around $r_0 + \epsilon_{l_+}$. Therefore, we first do a change of variable $r' = r - r_0 - \epsilon_{l_+}$

$$\langle r \rangle_{l_+} = \sum_{m,n} a_{m0}^+ a_{n0}^+ \int_{-\infty}^{\infty} (r' + r_0 + \epsilon_{l_+}) R_{m,0} R_{n,0} e^{i(m-n)2\omega_r T} dr', \quad (4.2.71)$$

where $\{R_{n,0}\}$ are the eigenfunctions of the harmonic oscillator centered around the origin. Since $\sum_n a_{n0}^{+2} = 1$, integrating the constant terms we obtain

$$\langle r \rangle_{l_+} = r_0 + \epsilon_{l_+} + \sum_{m,n} a_{m0}^+ a_{n0}^+ e^{i(m-n)2\omega_r T} \int_{-\infty}^{\infty} r' R_{m,0} R_{n,0} dr', \quad (4.2.72)$$

and the remaining integral can be computed by expressing r' in terms of the ladder operators¹¹ as

$$\langle r \rangle_{l_+} = r_0 + \epsilon_{l_+} + \sqrt{\frac{\hbar}{2m\omega_r}} \sum_{m,n} a_{m0}^+ a_{n0}^+ e^{i(m-n)2\omega_r T} (\sqrt{n+1}\delta_{m,n+1} + \sqrt{n}\delta_{m,n-1}), \quad (4.2.73)$$

¹¹ $\int_{-\infty}^{\infty} r' R_{m,0} R_{n,0} dr' = \sqrt{\frac{\hbar}{2m\omega_r}} \langle m | (a^\dagger + a) | n \rangle = \sqrt{\frac{\hbar}{2m\omega_r}} (\sqrt{n+1}\delta_{m,n+1} + \sqrt{n}\delta_{m,n-1}).$

which can be simplified as

$$\langle r \rangle_{l_+} = r_0 + \epsilon_{l_+} + \sqrt{\frac{2\hbar}{m\omega_r}} \sum_n \sqrt{n+1} a_{n0}^+ a_{n+10}^+ \cos(\omega_r t) . \quad (4.2.74)$$

Using the expressions in Eq.4.2.52 we get

$$\langle r \rangle_{l_+} = r_0 + \epsilon_{l_+} + \sqrt{\frac{2\hbar}{m\omega_r}} \cos(\omega_r t) \sum_n (-\Delta_+)^{2n+1} e^{-\Delta_+^2} , \quad (4.2.75)$$

which can be simplified using $\Delta_+ = (\epsilon_{l_+} - \epsilon_{l_0}) \sqrt{\frac{m\omega_r}{2\hbar}}$ as¹²

$$\langle r \rangle_{l_+} = r_0 + \epsilon_{l_+} + (\epsilon_{l_0} - \epsilon_{l_+}) \cos(\omega_r t) . \quad (4.2.76)$$

Similarly, the mean position of the cloud moving in the clockwise direction is

$$\langle r \rangle_{l_-} = r_0 + \epsilon_{l_-} + (\epsilon_{l_0} - \epsilon_{l_-}) \cos(\omega_r t) . \quad (4.2.77)$$

The mean separation between the packets is therefore

$$\langle \delta r \rangle = \langle r \rangle_{l_+} - \langle r \rangle_{l_-} = 2(\epsilon_{l_+} - \epsilon_{l_-}) \sin^2\left(\frac{\omega_r t}{2}\right) . \quad (4.2.78)$$

If we consider the mean separation of the wavepackets at the end of the interferometer, i.e. when the last $\pi/2$ pulse is applied, we obtain

$$\langle \delta r \rangle_{t=2T} = 2(\epsilon_{l_+} - \epsilon_{l_-}) \sin^2(\omega_r T) . \quad (4.2.79)$$

It is evident that whenever $\omega_r T = n\pi$, the wavepackets overlap perfectly and if $\omega_r T = (2n+1)\pi/2$ the mismatch is maximum (see Fig.4.6). An imperfect overlap of the wavepackets results in the loss of contrast.

Lastly, let us examine the phase Φ_T

$$\Phi_T = \Phi + m\omega_r^2(\epsilon_{l_+}^2 - \epsilon_{l_-}^2)T/\hbar , \quad (4.2.80)$$

assuming a launch velocity v_0 , the phase Φ_T can be written as

$$\Phi_T = \frac{8\pi m\Omega A}{h} \left[1 + 2\left(\frac{v_0^2}{\omega_r^2 r_0^2} + \frac{\Omega^2}{\omega_r^2}\right) \right] . \quad (4.2.81)$$

The above expression can be seen as the usual Sagnac phase shift but with an effective area A_{eff} given by

$$A_{eff} = A \left[1 + 2\left(\frac{v_0^2}{\omega_r^2 r_0^2} + \frac{\Omega^2}{\omega_r^2}\right) \right] . \quad (4.2.82)$$

Note that A_{eff} is nothing but the average of the areas enclosed by the clockwise moving and the anti-clockwise moving clouds¹³. In principle, large launch and

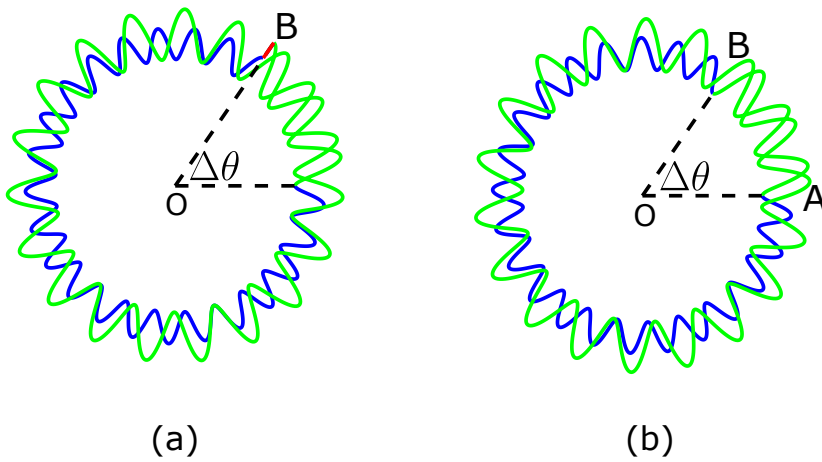


Figure 4.6 An illustration of the paths followed by the clockwise (blue) and the counter clockwise (green) moving wavepackets in a circular waveguide. Two cases are shown, where there is: a) a maximum overlap ($\omega_r T = n\pi$) and b) a minimum overlap ($\omega_r T = (2n+1)\pi/2$), between the wavepackets, when the last $\pi/2$ pulse is applied. In case b), the mismatch in the radial direction is highlighted in red. The two plots (not to scale) are obtained for a fixed interrogation time $2T$ and they only differ in the radial trap frequency. $\angle BOA = \Delta\theta = 2\Omega T$ is the angle rotated by the lab frame during the interferometer sequence.

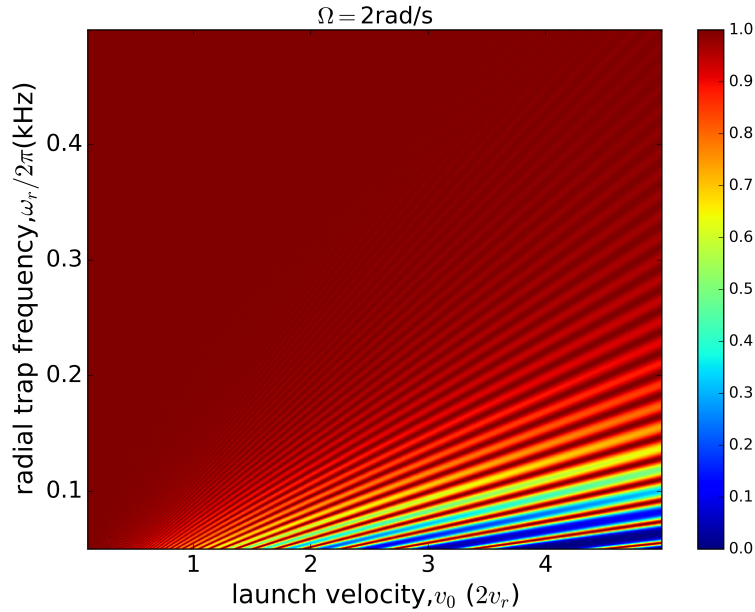


Figure 4.7 Contrast of the interferometer computed for different launching conditions by assuming a lab rotation of 2 rad/s for a waveguide radius of 500 μm .

angular velocities increase the sensitivity of the interferometer as long as the radial trapping forces are stronger than the centrifugal forces (this condition is essential for guiding).

We turn our attention towards the implications of the obtained results. We consider radial trap frequencies in the range of 50 – 500 Hz (we point out that the radial trap frequencies of the modulated TOP guide are about 100 Hz) and launch velocities¹⁴ between 0.1 and 10 recoil velocities. Theoretically speaking, contrast loss and additional phase shifts arise due to the asymmetric radial motion caused by the rotation of the lab frame and is noticeable when the angular velocity is sufficiently high. Considering the potential applications of a guided Sagnac interferometer in inertial navigation and geophysical studies, we take two cases where the lab frame angular velocity is $\Omega = 2 \text{ rad/s}$ (commercially available tactical grade gyroscopes typically have a dynamic range of few radians per second) and $\Omega = \Omega_{\text{Earth}}$. The contrast loss of the interferometer for a rotation rate $\Omega = 2 \text{ rad/s}$ is shown in Fig.4.7. We can notice that the contrast of the interferometer attains the maximum possible value when the trap frequency is

¹²It is worth noting that, $\langle r \rangle_{l_{\pm}}$ is the classical trajectory of an atom launched tangentially into the guide.

¹³ $A_{\text{eff}} = (A_+ + A_-)/2$ where $A_{\pm} \approx A(1 + \frac{2\epsilon_{l_{\pm}}}{r_0})$.

¹⁴In the derivation l_{\pm} are defined assuming a momentum kick of $2 \hbar k$, the formulae are valid for any other launch velocity v_0 by redefining l_{\pm} as $\pm m v_0 r_0 + m \Omega r_0^2$.

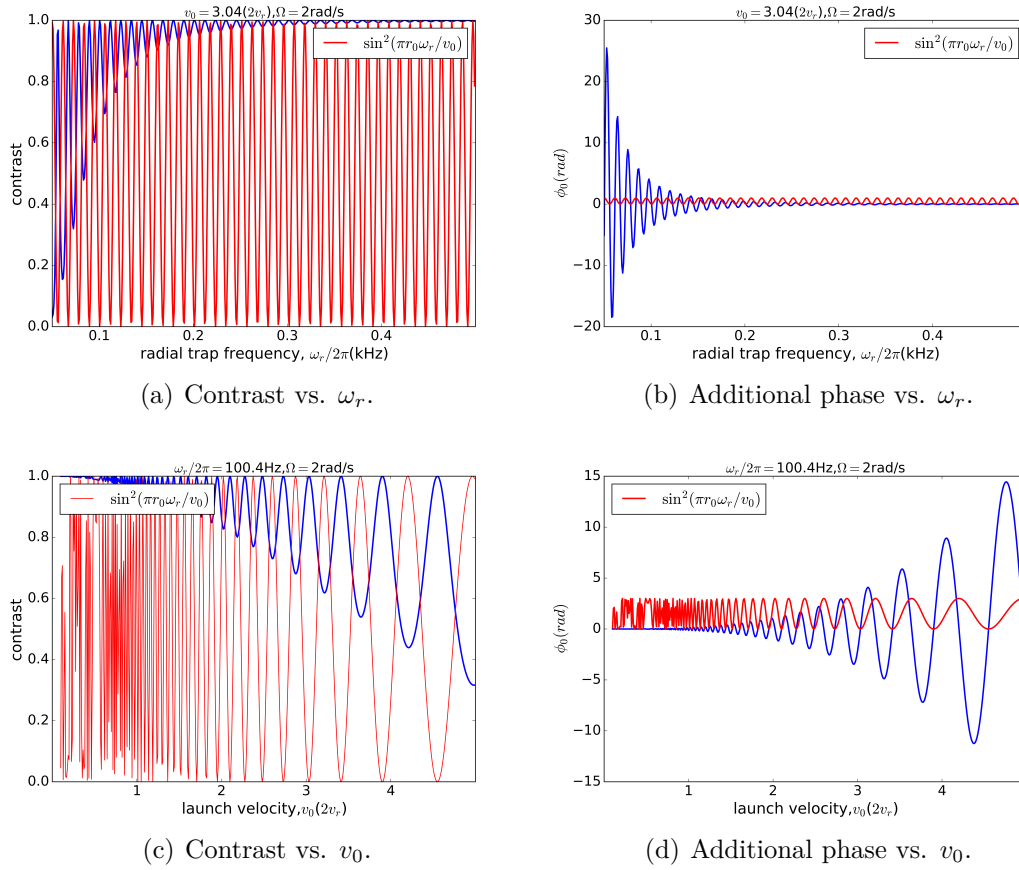


Figure 4.8 Dependence of the additional phase Φ_0 and contrast due to multimode propagation, considering a lab frame angular velocity $\Omega = 2 \text{ rad/s}$. The red curve in each plot is a quantity proportional to the separation between the wavepackets at the end of the interferometer.

high and the launch velocity is low, whereas the contrast decays with a decrease in the trap frequency and an increase in the launch velocity with some peaks in the contrast. The maxima in the contrast of Fig.4.7 correspond to the situation when $\omega_r T$ is an integer multiple of π or when $r_0 \omega_r / v_0$ is an integer (see Fig.4.8(a) and Fig.4.8(c)).

The additional phase Φ_0 can be seen to approach zero when $\omega_r T$ is an integer multiple of $\pi/2$ (see Fig.4.8(b) and Fig.4.8(d)), which essentially means that the phase difference accumulated due to multimode propagation of the wavepackets exactly gets compensated at these specific points when $r_0 \omega_r / v_0$ is a half integer, i.e. when the wavepackets overlap perfectly or when the relative velocity of the atomic wavepackets is zero. In other words, this additional phase is due to a separation in the phase space, since it is proportional to both the wavepacket radial separation and the relative radial velocity when the last pulse is applied. In the figure 4.8, we can notice that the contrast can be as low as 50% and can impact the dynamic range of the interferometer if the launching conditions are not properly chosen. Similarly, the additional phase can be significant (~ 10 rad). This result stresses the importance of operating the interferometer such that $r_0 \omega_r / v_0$ is an integer. By doing so, we can suppress the additional phase and contrast loss, which can help to achieve a good dynamical range for the interferometer. If the angular velocity of the lab frame is as low as earth's

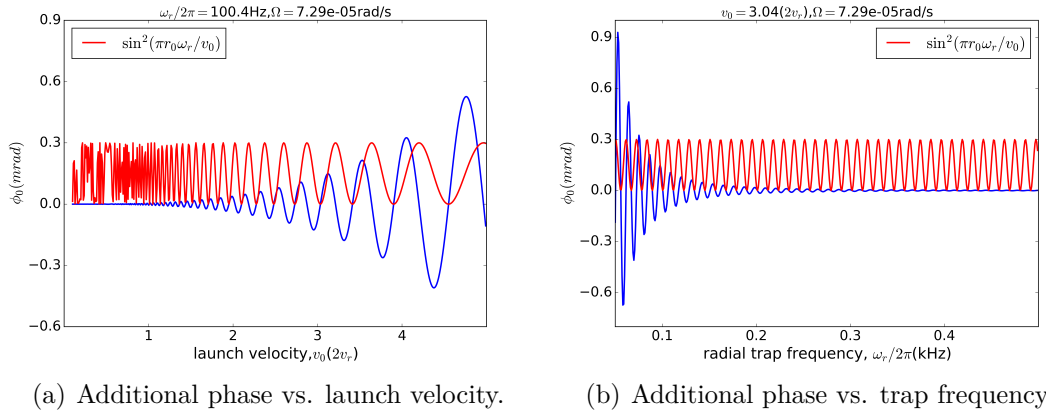


Figure 4.9 *Dependence of the additional phase Φ_0 caused by the multi modal propagation, on the radial trap frequency and the launch velocity, for a lab frame angular velocity equal to the earth's rotation rate.*

rotation rate, which is the case for geophysical applications. The contrast loss due to multimode propagation is negligible, though the additional phase Φ_0 maybe detectable depending on the sensitivity of the interferometer. As can be seen in Fig.4.9, the additional phase can be of the order of 0.5 mrad. For comparison, the Sagnac phase for a lab frame rotation rate $\Omega = \Omega_{Earth} = 7.29 \times 10^{-5}$ rad/s

is about 300 *mrad* with an enclosed area of 0.78 mm^2 (for a guide radius of 500 μm).

4.2.3 Interferometer with thermal atoms

We now consider the effects of multimode propagation with thermal atoms under the tight guide approximation. We assume that the initial state of the atoms before the first $\pi/2$ pulse to be a mixed state at temperature θ , where the probability to be in the n^{th} radial state is given by the Boltzmann distribution

$$P_n = (1 - e^{-\hbar\omega_r/k_B\theta})e^{-n\hbar\omega_r/k_B\theta} . \quad (4.2.83)$$

To evaluate the contrast, it is convenient to use the basis of coherent states $\{|\alpha\rangle\}$ and the corresponding occupation probability given by the Glauber-Sudarshan distribution (more details are provided in the Appendix)

$$P(\alpha) = \frac{1}{\pi}(e^{\hbar\omega_r/k_B\theta} - 1)\exp[-|\alpha|^2(e^{\hbar\omega_r/k_B\theta} - 1)] . \quad (4.2.84)$$

If the temperature is sufficiently high, i.e. $k_B\theta \gg \hbar\omega_r$, we can approximate the distribution as

$$P(\alpha) = \frac{1}{\pi} \frac{\hbar\omega_r}{k_B\theta} e^{-|\alpha|^2 \frac{\hbar\omega_r}{k_B\theta}} . \quad (4.2.85)$$

Using the density matrix $\rho = \int P(\alpha) |\alpha\rangle \langle \alpha| d^2\alpha$, the interferometer signal¹⁵ can be written as

$$\begin{aligned} C_\theta \cos(\Phi') &= Tr\{\rho e^{2i\mathcal{H}_+ \frac{T}{\hbar}} e^{-2i\mathcal{H}_- \frac{T}{\hbar}}\} \\ &= \int P(\alpha) \langle \alpha | e^{2i\mathcal{H}_+ \frac{T}{\hbar}} e^{-2i\mathcal{H}_- \frac{T}{\hbar}} | \alpha \rangle d^2\alpha , \end{aligned} \quad (4.2.86)$$

where C_θ is the thermal contrast of the interferometer and Φ' is the accumulated phase. To evaluate the above expression, let us first compute the term $e^{-2i\mathcal{H}_\pm \frac{T}{\hbar}} |\alpha\rangle$, which is

$$|\Psi_{\pm\alpha}\rangle = e^{2iE_\pm T/\hbar} e^{2i\omega_r T[a^\dagger a + \frac{1}{2} - \Delta_\pm(a^\dagger + a)]} \mathcal{D}(\alpha) |0\rangle . \quad (4.2.87)$$

This can be simplified using the same method as before, i.e., by exploiting the properties of displacement operator and we get

$$|\Psi_{\pm\alpha}\rangle = e^{2i[\frac{E_\pm}{\hbar} + (\frac{1}{2} - \Delta_\pm^2)\omega_r]T} e^{i\Delta_\pm \mathcal{I}m(\alpha)} e^{-i\Delta_\pm \mathcal{I}m[(\alpha - \Delta_\pm)e^{2i\omega_r T}]} \left| \Delta_\pm + (\alpha - \Delta_\pm)e^{2i\omega_r T} \right\rangle . \quad (4.2.88)$$

Let us define a constant C_α , which is the overlap between $|\Psi_{+\alpha}\rangle$ and $|\Psi_{-\alpha}\rangle$

$$C_\alpha = \langle \Psi_{+\alpha} | \Psi_{-\alpha} \rangle = \langle \alpha | e^{2i\mathcal{H}_+ \frac{T}{\hbar}} e^{-2i\mathcal{H}_- \frac{T}{\hbar}} | \alpha \rangle , \quad (4.2.89)$$

¹⁵Which is the probability difference to be in different output states of the interferometer i.e. $P_{l_0} - P_{l_\pm} = C_\theta \cos(\Phi')$.

which can be written as

$$C_\alpha = e^{i(\Phi_0 + \Phi_T)} e^{-i\Delta[-\mathcal{R}e(\alpha) \sin(2\omega_r T) + 2\mathcal{I}m(\alpha) \sin^2(\omega_r T)]} \langle \Delta_+ + (\alpha - \Delta_+) e^{2i\omega_r T} \mid \Delta_- + (\alpha - \Delta_-) e^{2i\omega_r T} \rangle . \quad (4.2.90)$$

The overlap between the coherent states in the above expression evaluates to

$$\langle \Delta_+ + (\alpha - \Delta_+) e^{2i\omega_r T} \mid \Delta_- + (\alpha - \Delta_-) e^{2i\omega_r T} \rangle = C e^{-i\Delta[-\mathcal{R}e(\alpha) \sin(2\omega_r T) + 2\mathcal{I}m(\alpha) \sin^2(\omega_r T)]} , \quad (4.2.91)$$

where C is the zero temperature contrast of the interferometer that we obtained in the previous section. Finally, C_α can be expressed as

$$C_\alpha = C e^{i(\Phi_0 + \Phi_T)} e^{-2i\Delta[-\mathcal{R}e(\alpha) \sin(2\omega_r T) + 2\mathcal{I}m(\alpha) \sin^2(\omega_r T)]} . \quad (4.2.92)$$

The interferometer signal can be obtained by averaging C_α over all coherent states with a weight given by the Glauber-Sudarshan distribution

$$C_\theta \cos(\Phi') = \int_{-\infty}^{\infty} \int_{-\infty}^{\infty} P(\alpha) C_\alpha d\mathcal{R}e(\alpha) d\mathcal{I}m(\alpha) , \quad (4.2.93)$$

after evaluating the Gaussian integrals we obtain

$$\begin{aligned} C_\theta \cos(\Phi') &= C e^{-\frac{4k_B\theta}{\hbar\omega_r} \Delta^2 \sin^2(\omega_r T)} \cos(\Phi_T + \Phi_0) , \\ &= e^{-\frac{16m v_0^2 \Omega^2}{\hbar\omega_r^3} \sin^2(\omega_r T) [1 + \frac{2k_B\theta}{\hbar\omega_r}]} \cos(\Phi_T + \Phi_0) . \end{aligned} \quad (4.2.94)$$

Therefore, the thermal contrast of the interferometer is

$$C_\theta = e^{-\frac{16m v_0^2 \Omega^2}{\hbar\omega_r^3} \sin^2(\omega_r T) [1 + \frac{2k_B\theta}{\hbar\omega_r}]} , \quad (4.2.95)$$

and $\Phi' = \Phi_T + \Phi_0$. This result also shows that, apart from the phase Φ_0 that we already noticed in the ultra cold gas case, operating the interferometer with thermal atoms does not introduce any additional phase shifts. However, it is clear from the above expression that the contrast decay is amplified when the temperature increases. Nevertheless, there is a striking feature contained in the Eq.4.2.95. Indeed, we can still have a maximum contrast in the worst case scenario corresponding to the use of a thermal gas in a guide with a radial guiding frequency way below the critical frequency.

For example, let us consider an important number of populated excited transverse states associated to a thermal gas of temperature $1 \mu K$, launched with a velocity of $10 v_r$ in a guide of $500 \mu m$ radius. With these conditions, if we choose the radial guide frequency such that $\omega_r T = (2n + 1)\pi/2$, for instance $\omega_r \approx 2\pi \times 50 Hz$, way below the critical trap frequency $\omega_c = 2\pi \times 92 Hz$ then we realize the worst case scenario shown in Fig.4.10. We observe in this figure that the interferometer contrast decays quite rapidly with the rotation rate Ω , in particular it approaches zero at angular velocities $\Omega \sim 30 mrad/s$. However, if we choose ω_r such that $\omega_r T$ is an integer multiple of π , then we recover the maximum interferometer contrast.

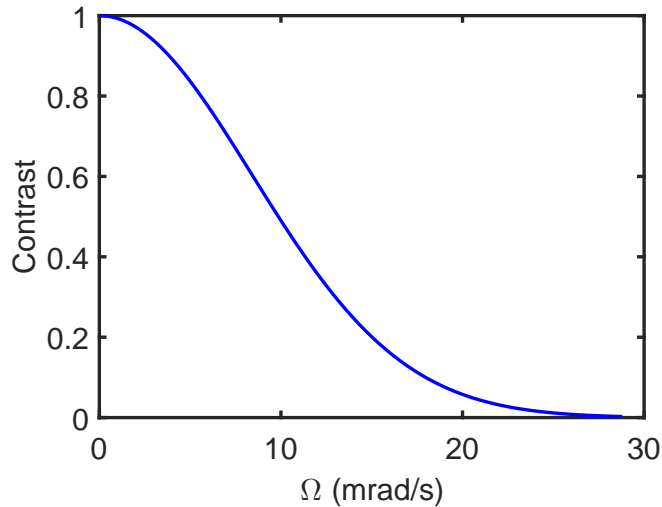


Figure 4.10 Contrast as function of the rotation rate in an interferometer using a thermal gas at $1 \mu\text{K}$ temperature, assuming a maximum mismatch between the interfering clouds. We consider here a radial trap frequency of 50 Hz .

4.3 Conclusion

We studied in this chapter the propagation of atoms in a circular guide. We derived the conditions under which we have monomode propagation of matterwaves in the guide. In particular, a critical radial trap frequency is found, above which the deflection of the atom trajectories imposed by the guide curvature does not introduce heating of the cloud. On the other hand, a model for guided Sagnac interferometer is discussed. The effect of the finite radial potential and the non negligible centrifugal forces and their impact on the guided Sagnac interferometer are also quantified. In summary, the effective area of the interferometer is shown to be slightly more than the area of the toroidal guide, thereby marginally increasing the sensitivity of the interferometer. On the other hand, multimode propagation along the guide affects the fringe contrast and induces additional phases apart from the Sagnac phase. This result was found using a 2D model for the transverse dynamics of the atoms in the guide, from a quantum mechanical point of view.

An important result is the demonstration of the existence of an additional phase caused by the difference in the angular momenta of the counter propagating clouds. The obtained analytical expressions demonstrate that not only we can make this additional phase zero by choosing the launch velocity and trapping frequency satisfying the condition $r_0\omega_r/v_0 = n$, where n is a positive integer, but also we can make the interferometer immune to systematics associated to the use of thermal cloud. These effects, like for instance the Coriolis effect and the finite

momentum width of the atom source, are completely suppressed restoring the value of the interference contrast to its nominal value when a zero T source is used. The key consequence of this being the possibility to realise a large dynamic range cold atom gyroscope for inertial applications.

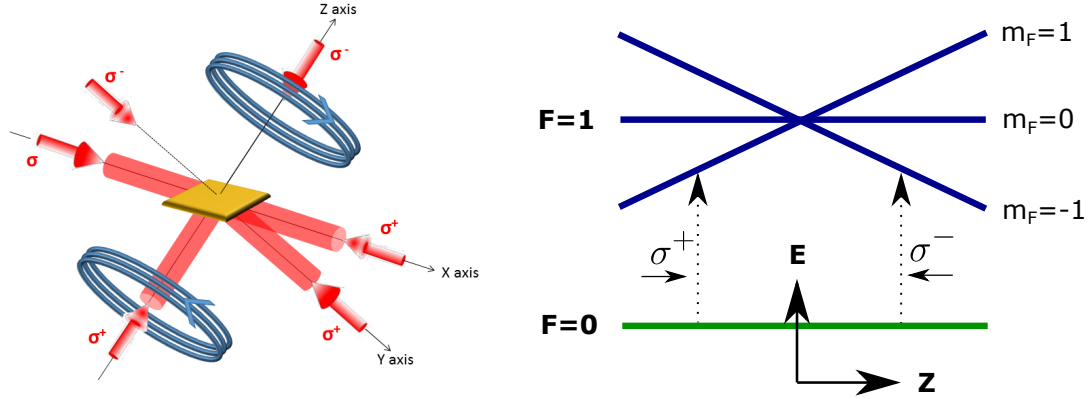
Chapter 5

Description of the experiment and characterisation of cold atom source

This chapter describes the current status of the GyrAChip experiment. Apart from the optical bench, all the optics for the realization of the mirror-MOT [106], the fluorescence and absorption imaging systems were designed and built during this thesis. The first mirror-MOT of the GyrAChip project was realised towards the end of January, 2015. In the following sections, after briefly discussing the basic principle of the MOT, we present the optics needed in the realisation of a mirror MOT and the atom detection systems. We optimized and performed a detailed preliminary characterisation of the mirror-MOT using absorption and fluorescence imaging systems. The results are discussed in Section 5.3. Finally, we present a study of the pressure dynamics in the vacuum chamber during the MOT phase of the experiment.

5.1 Mirror MOT

The first stage of any cold atom experiment is the realisation of a MOT [107], where atoms moving at few hundred Kelvin are trapped and cooled down to few hundred micro Kelvin using a combination of magnetic and optical fields. Conventional MOTs use six laser beams combined with a linear quadrupole field, which give cooling and trapping forces along the three orthogonal directions. In a typical experiment involving atom chips, in order to transfer the atoms efficiently to micro magnetic traps produced by the wires on the chip, it is necessary to trap the atoms close to the chip surface. If these wires carry currents in the order of few amperes, then we typically use four beams such that, two beams are shone at an angle of 45° with respect to the chip surface and the two other beams parallel to the chip and orthogonal to the former beams [106]. If we consider a region close to the chip surface, due to the beams reflection from the chip, atoms experience forces in all six directions. If a quadrupole field is added such that the axis of the quadrupole is along one of the 45° beams, atoms can be trapped in a



(a) Configuration of beams along with their polarisations necessary for mirror-MOT. Note that the two beams at 45° degree have the same polarization, due to the presence of the reflecting mirror, also shown are the MOT coils in anti-Helmholtz configuration.

(b) Energy levels of an atom with a $F = 0$ to $F = 1$ transition in a quadrupole field. An atom moving along negative z -direction is resonant with the beam propagating along positive z -direction and vice-versa, hence the confinement.

Figure 5.1 Working principle of MOT.

region near the chip surface common to the four beams. The trapping mechanism can be understood by considering a simple case of the force, due to two counter propagating beams along the z direction (see Fig.5.1(a)), acting on an atom with a $F = 0$ to $F = 1$ transition. The average cooling force experienced by an atom due to a laser of wave vector k_z (propagating in the positive z direction) is given by [108]

$$\langle F \rangle = \hbar k_z \frac{\Gamma}{2} \frac{s}{1 + s + 4 \frac{\delta^2}{\Gamma^2}}, \quad (5.1.1)$$

where δ is the detuning of the laser seen by the atom and $s = I/I_{sat}$ is the saturation parameter of the transition. If we consider an atom moving at a velocity v , the detuning seen by the atom due to Doppler effect is $\delta_D = \mp k_z v$. In the presence of a linear quadrupole field the atomic levels are also Zeeman shifted by $\pm \mu_B g_F m_F \frac{bz}{\hbar}$. The sign depends on the position of the atom in the quadrupole field and b is the quadrupole field gradient. In addition, if we also consider the detuning of the laser δ_L from the cooling transition, which is an experimentally controllable parameter, then the total detuning seen by the atom is given by

$$\delta_{\pm} = \mp k_z v \pm \mu_B g_F m_F \frac{bz}{\hbar} + \delta_L. \quad (5.1.2)$$

The combined force acting on the atom from two counter propagating beams is

$$F_{total} = \langle F_+ \rangle + \langle F_- \rangle = \hbar k_z \frac{\Gamma}{2} s \left[\frac{1}{1 + s + 4 \frac{\delta_+^2}{\Gamma^2}} - \frac{1}{1 + s + 4 \frac{\delta_-^2}{\Gamma^2}} \right]. \quad (5.1.3)$$

Substituting the value of δ_+ and δ_- in the above equation and assuming that the Doppler shift and the Zeeman shift are small compared to Γ , the total force can be written under the form [109]

$$F_{total} = -\alpha v - \kappa z, \quad (5.1.4)$$

where the friction coefficient α and the spring constant κ are given by

$$\alpha = -4\hbar k^2 \frac{I}{I_{sat}} \frac{2\delta_L/\Gamma}{[4\delta_L^2/\Gamma^2 + (1 + 2I/I_{sat})]^2}, \quad (5.1.5)$$

$$\kappa = \frac{\alpha g_F \mu_B b}{\hbar k}.$$

It is clear that, for red detuning ($\delta_L = \omega_L - \omega < 0$) the frictional force cools the atom, whereas a blue detuning ($\delta_L > 0$) heats the atom. Therefore, for a red detuned cooling beam, velocity dependant term dissipates the energy of a fast moving atom, whereas the position dependent restoring force confines atoms around the quadrupole field zero. The reasoning can be extended to other directions, and trapping is possible in all three directions. For a ^{87}Rb atom (the energy levels of ^{87}Rb can be found in the Appendix), the cooling transition is $F = 2 \rightarrow F' = 3$. After absorbing a photon, the spontaneous emissions bring back these atoms to either $F = 1$ or $F = 2$ hyperfine states. If an atom reaches the $F = 1$ state, the cooling beam becomes 'invisible' to the atom due to the 6.8 GHz of frequency difference between the hyperfine levels and the trap no longer works. In order to pump back the atoms to the $F = 2$ state, a repumper beam ($< 1 \text{ mW}$) is added by superposing it on the four beams shown in Fig.5.1(a)¹. Although it is still possible to cool the atoms in the absence of the magnetic field, atoms may diffuse out slowly due to the stochastic nature of the light atom interaction. Such a configuration is called optical molasses and it is used to cool the atoms in the MOT to lower temperatures. In the case of ^{87}Rb , the typical cooling temperatures are the Doppler limit in a MOT equal to 150 μK , and the molasses temperature is 350 nK set by the photon recoil energy.

5.2 Experimental setup

5.2.1 Optical bench

Laser system

All the optical frequencies required for the experiment are generated from two

¹It is strictly not necessary to have the repumper in all directions. However, by doing so, we can optimize the cooling forces.

home built Extended Cavity Diode Lasers (ECDL). The reference laser (ECDL1) is frequency stabilized to the transition $F = 1 \rightarrow F' = 1 \times 2$ of the $D2$ line ($5^2S_{1/2} \rightarrow 5^2P_{3/2}$) using Saturated Absorption Spectroscopy (SAS). The SAS helps to overcome the Doppler broadening of the atomic transition which is typically few MHz at room temperature. A schematic of the SAS system can be seen in Fig.5.2. A linearly polarized beam from ECDL1, which acts as a pump beam is sent through a Rb vapour cell², which is then reflected by a mirror. This beam is made to double pass through a quarter waveplate, therefore the reflected beam is orthogonally polarized with respect to the incident beam. The Doppler shift ($\delta_D = \mathbf{k} \cdot \mathbf{v}$) is different for the two beams, as they propagate in opposite directions. Hence, only the atoms which are at rest are resonant with the probe and pump beam. If we take into account other atomic transitions, we can observe other resonances at crossover frequencies due to two photon transitions for a given velocity class. For instance, let us consider a given velocity class v of the atoms. If the atoms are resonant with the probe beam at frequency ω in a transition $F = 1 \rightarrow F' = 1$ i.e.

$$kv = \omega - \omega_{F=1 \rightarrow F'=1} , \quad (5.2.1)$$

and, if the reflected beam is resonant with the transition $F = 1 \rightarrow F' = 2$

$$-kv = \omega - \omega_{F=1 \rightarrow F'=2} . \quad (5.2.2)$$

Solving for ω we obtain

$$\omega = \frac{1}{2}(\omega_{F=1 \rightarrow F'=1} + \omega_{F=1 \rightarrow F'=2}) = \omega_{F=1 \rightarrow F'=1 \times 2} . \quad (5.2.3)$$

Therefore, in addition to the usual resonances at the existing atomic transitions, we can observe additional peaks at the crossover of two transitions. ECDL1 is precisely locked to the crossover transition $F = 1 \rightarrow F' = 1 \times 2$. The intensity of the incident beam is usually well above the saturated intensity I_s . Therefore, the probe beam is nearly transparent, as the atom medium is saturated by the pump beam. This results in a peak in the saturated absorption signal at the crossover frequency. An error signal is generated by phase modulating the output of ECDL1 with an Electro Optic Modulator (EOM) and a feedback correction signal is fed to the diode laser [110].

In order to generate beams required for atom trapping and imaging, the slave laser (ECDL2) is frequency locked to the $F = 2 \rightarrow F' = 3$ transition with a controllable detuning. The frequency difference between hyperfine levels of the ground state is about $6.8 GHz$. Therefore, ECDL2 can be frequency locked to ECDL1 using a microwave frequency reference. The beat note between the two lasers is acquired on a fast photo diode and another beat note is generated with

²The Rb cell is heated to increase the partial pressure in the cell, which allows to achieve a strong absorption signal.

Fiber	Power
MOT (cooling+repumper)	60 mW
Imaging	200 μ W
Optical pumping	200 μ W
Raman beams	95 mW
Repumper (optical pumping)	150 μ W

Table 5.1 *Measured optical power at the output of the different fiber collimators shown in Fig.5.2.*

a 7 GHz microwave frequency which is generated via a frequency chain starting from a 10 MHz input [110]. The resulting beat note at a frequency of 400 MHz, is then divided by 4 and another beat note is generated around 100 MHz by a Direct Digital Synthesizer (DDS). The detuning of the ECDL2 from the cooling transition can be controlled with the frequency generated by the DDS. The frequency of the ECDL1 is 78.48 MHz detuned from $F = 1 \rightarrow F' = 2$ transition and the frequency of ECDL2 is also 78.48 MHz detuned from $F = 2 \rightarrow F' = 3$ transition and both these frequencies need to be compensated in order to use them. A more detailed description of the lasers can be found in the thesis of W. Yan [110].

Generation of optical frequencies

A schematic of the optical bench is shown in Fig.5.2. The optical frequencies needed for atom trapping and manipulation are obtained by frequency shifting appropriately the outputs of the two ECDLs with Acousto Optical Modulators (AOM), and by changing the frequency of the ECDL2 with the DDS. The outputs of the ECDLs are superposed and simultaneously frequency up shifted by 78.48 MHz with an AOM (MT80-B30A1-IR), to generate the cooling ($F = 2 \rightarrow F' = 3$) and repumper ($F = 1 \rightarrow F' = 2$) beams required for the MOT. The imaging beam is obtained from ECDL2 which is also frequency shifted by 78.48 MHz using another AOM. The detuning from the cooling transition is set to zero during the imaging phase with the help of the DDS. The MOT beam (cooling and repumper) can also be used to address Raman transitions between the hyperfine levels $F = 1$ and $F = 2$ by frequency down shifting them about 750 MHz. This is achieved by double passing the beams through an AOM (MT-350-A0.2-800). To optically pump the atoms into the $F = 2, m_F = 2$ state (magnetically most sensitive state of the $F = 2$ manifold), we use the transition $F = 2 \rightarrow F' = 3$. The optical power out of the ECDLs is about few tens of mW and it is not sufficient for MOT and Raman beams. Therefore, we amplify the power with a home made Master Oscillator Power Amplifier (MOPA). The output power of MOPA can be controlled by changing the current that drives

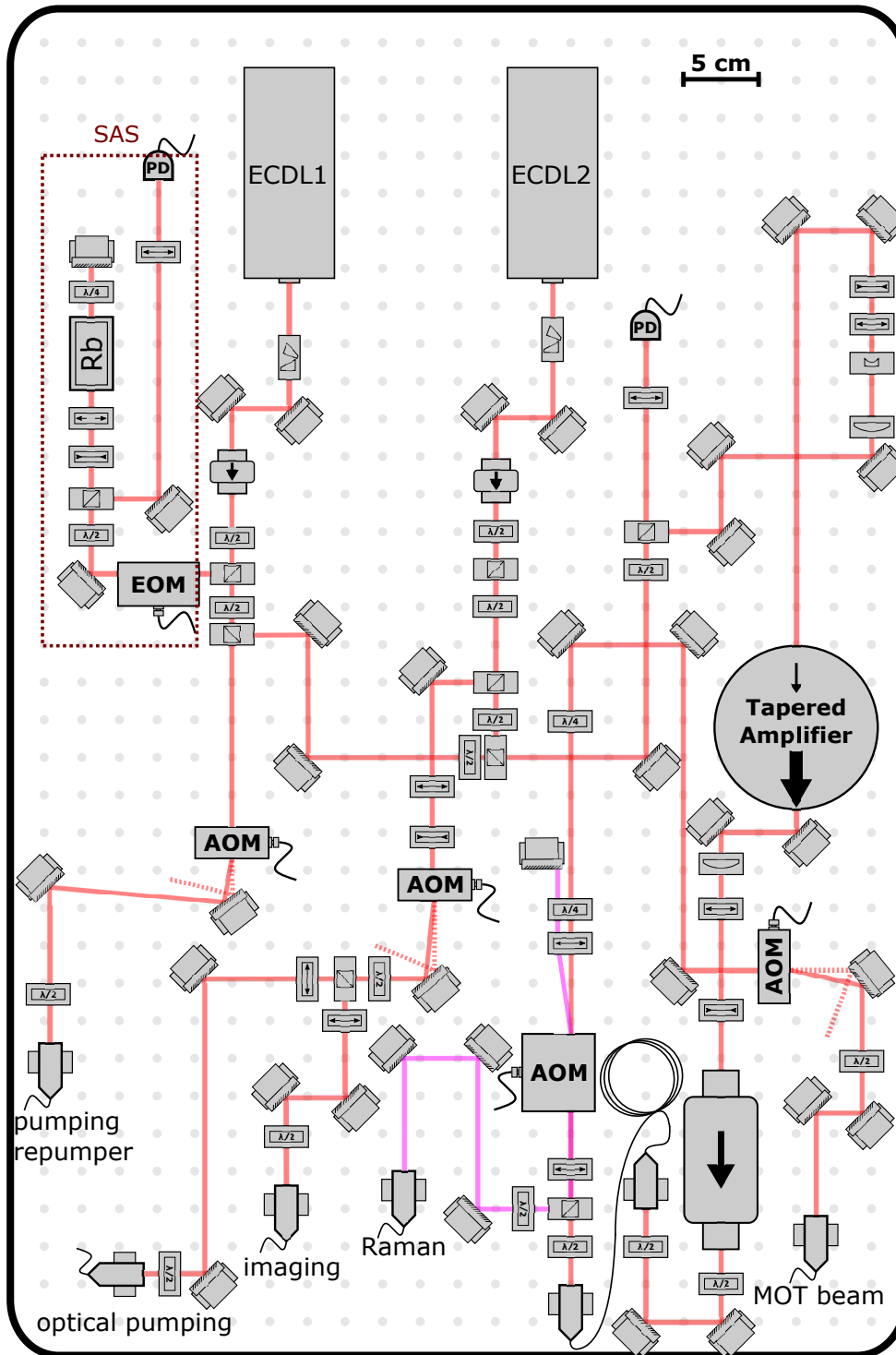


Figure 5.2 Schematics of the optical bench, ECDL1 is locked to the $F = 1 \rightarrow F' = 1 \times 2$ transition using SAS (highlighted with a red box.), ECDL2 is locked to ECDL1 by beat note to a 7 GHz reference. The output of the lasers are amplified with a TA and frequency shifted with AOMs before them coupling into single mode TM fibres that transport the beams to the science chamber.

the Tapered Amplifier (TA) in the MOPA. We typically operate the TA (m2k-TA-0780-1000) with 1.6 A, higher currents may affect the longevity of the TA.

5.2.2 Vacuum chamber

The stainless steel vacuum chamber of your experiment (see Fig.5.4) is approximately 7 litres in volume and it is connected to an ion pump (a sputter ion pump 45S Gamma Vacuum) through a 40 cm long CS63 tube. The pumping speed of the ion pump is 45 litres per second, and to determine the pressure P inside the vacuum chamber (in units of millibar) we use the ionization current I and the expression

$$P = \frac{0.066 \times 5600 \times 1.33}{7000 \times 40} \times I \quad (5.2.4)$$

$$= 0.0017556 \times I . \quad (5.2.5)$$

For example, in Fig.5.3, the vacuum pressure can be seen to vary between 4.8×10^{-10} mbar and 5×10^{-10} mbar over few typical MOT loading cycles.

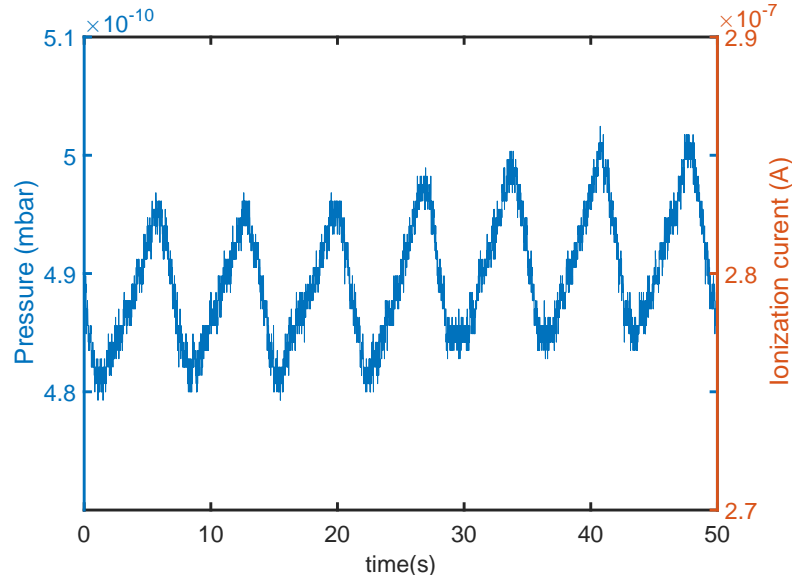


Figure 5.3 Variation of pressure (ionization current) during MOT loading cycles. The pressure is computed from the ionization current acquired from the ion pump controller.

The vacuum chamber is also equipped with two getters for backup. They can be triggered in case of any increase in the pressure or to further lower the pressure in the vacuum chamber, if needed.

The atom chip will be held³ at the centre of the vacuum chamber with the

³For the time being we have a gold coated substrate as a mirror, which will be replaced by an atom chip.

help of a chip holder. This chip holder is a copper block which acts as a heat sink to dissipate the ohmic heat generated on the atom chip. The quadrupole

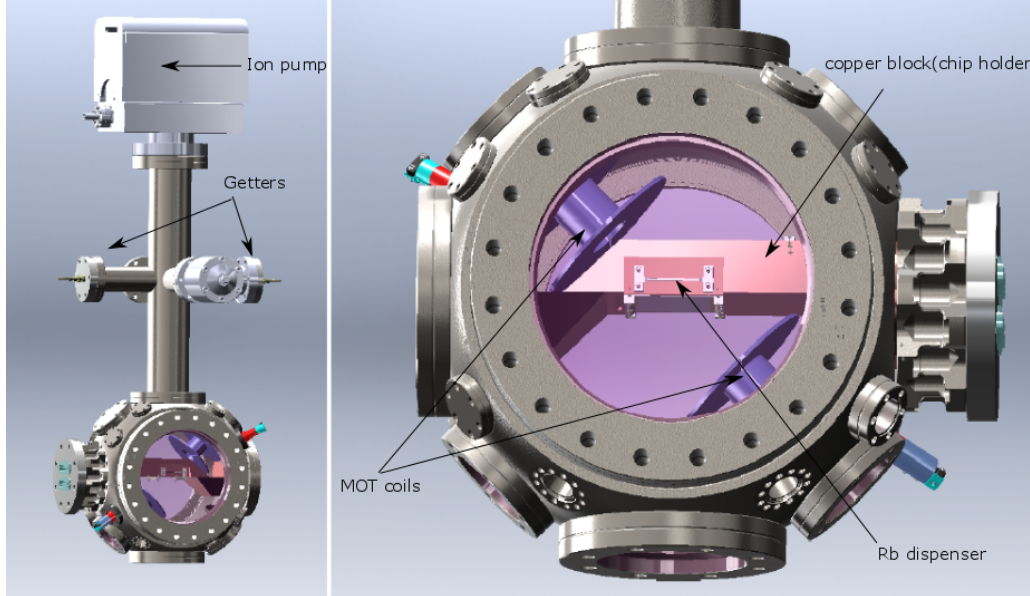


Figure 5.4 An image of the vacuum system together with the ion and getter pumps. The copper block which holds the chip, the MOT coils that generate quadrupole field and the Rb metal dispenser can be seen inside the vacuum chamber.

coils are fixed inside the vacuum chamber, so that the quadrupole axis is at 45° with respect to the copper block as we can see in Fig.5.4. Each of these coils are made by winding copper wires (of cross sectional radius 0.5 mm) covered with a vacuum compatible Kapton insulation. Both coils are approximately at a distance of 5 cm from the chip centre. This close proximity allows to the generate necessary quadrupole gradients for the MOT by passing relatively low currents. For example, by running 1.3 A in the coils, they generate an axial gradient of $|dB_z/dz| = 10.4\text{ G/cm}$ and radial gradient of $|dB_r/dr| = 5.2\text{ G/cm}$. These values are computed numerically by considering few millimeters around the quadrupole centre, and the computed fields are shown in Fig.5.5. The in-vacuum coils act as an atom source when they are switched on continuously for few hours. They liberate the absorbed Rb. Running a constant current of 1.3 A for two days (unintentionally) led to an increase in the pressure from $9 \times 10^{-10}\text{ mbar}$ to $1.9 \times 10^{-8}\text{ mbar}$. Therefore, we normally ensure that the quadrupole coils are turned off between two experimental cycles, leaving enough time for the coils to cool down.

Two Rb dispensers (from *SAES*) attached to the copper block on either side supply Rb atoms. The dispensers liberate Rb atoms from a reduction reaction which is triggered after reaching a certain critical temperature. We typically

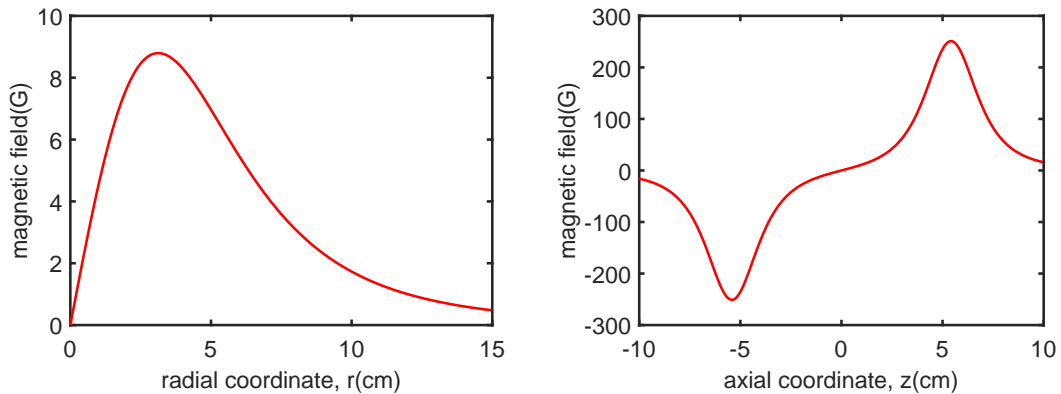


Figure 5.5 Variation of the total field of the quadrupole coils along the axial and radial directions. A current of 1.3 A is run through the coils in anti-Helmholtz configuration.

observe the MOT when the current in the dispenser is over 3 A.

5.2.3 Optics for the MOT

Cooling and repumper beams are superposed on the optical bench (see Fig.5.2). They are brought to the science chamber, which is located on another optical table, with a single mode TM fibre. We use a Schafer Kirchhoff's *fibre port cluster* 1 to 4 to split this beam into four beams needed for the mirror MOT. This fibre port cluster is equipped with a photodiode and about one percent of the input power is used for monitoring purposes. The powers of the four output beams can be equilibrated by rotating the half waveplates present before each PBS (see Fig.5.6). The input fibre of the fibre port cluster was replaced with a 2 m long fibre, as it was rather short to connect the optical bench with the science chamber. The maximum achievable coupling efficiency after realigning the new fibre is about 50% (increasing the coupling efficiency up to 80% may require a re-alignment of the four output fibres). According to the manufacturer's specification, the beam diameter after the collimator (60FC-4-A7.5-02) of the optical fibre is about 1.35 mm. The experimentally measured beam diameter is about 1.4 mm. In order to increase the capture volume of the MOT, we expand the MOT beams by a factor of 12 using a telescope with two lenses of focal lengths $f = -15$ mm and $f = 175$ mm separated by 150 mm. The final beam diameter of the MOT beam after the telescope is about 16 mm. For a larger capture volume it is favourable to increase the beam diameter, however the maximum possible beam diameter for our setup is about 19 mm. This beam size is limited by the inner diameter of the quadrupole coils, as one of the beams need to go through the quadrupole coil in the vacuum chamber. Finally, the polarization of

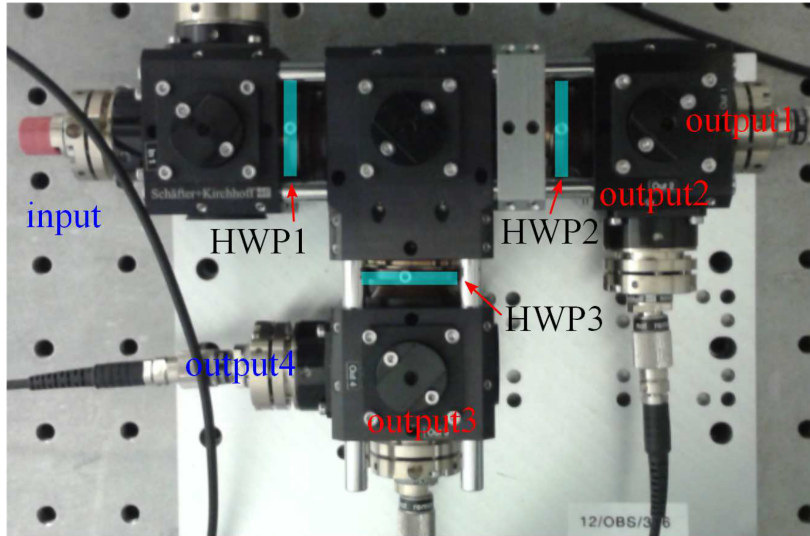


Figure 5.6 *Schafner Kirchoff's fibre port cluster 1 to 4 takes an input fibre and divides the optical power among four output fibres. The four half wave plates (HWP) can be used to distribute the power among the output beams.*

the cooling beam is set by a quarter wave plate. The two lenses of the telescope along with other optical components (half waveplate, quarter waveplate and a polarising beam splitter) are integrated in a 30 mm cage system using Thorlabs' components (see Fig.5.7). The cage system is then housed on an optical bread board which is fixed to the ELCOM posts holding the vacuum chamber. These cage systems with pre-aligned optics allow an easy (un)installation of optical elements around the vacuum chamber. Each cage system is designed to send an additional beam (for instance, imaging beam or optical pumping beam/repumper for optical pumping) with an orthogonal polarization, which is combined with the MOT beam using a polarising beam splitter.

Out of the four MOT beams, three are sent into the vacuum chamber using the cage system shown in Fig.5.7. Whereas, we use a different scheme to send the fourth MOT beam due to the presence of the absorption imaging system (part of the optical path is common to both MOT and imaging beams Fig.5.8). The beam is expanded using a combination of two telescopes made of lenses of focal lengths $f = -20 \text{ mm}$, $f = 60 \text{ mm}$ and $f = 75 \text{ mm}$, $f = 300 \text{ mm}$, which gives a combined magnification of 12 as shown in Fig.5.8. The two telescope systems give a beam diameter of 16.2 mm (though this is not exactly the same diameter as for the other three beams, the difference in the diameter is only 0.5 mm and it is negligible). The two beams which are at 45° with respect to the chip surface are deflected from the two horizontal beams using mirrors of 50 mm diameter. They are glued to an aluminium block at an angle of 22.5° with respect to the optical bench (see Fig.5.9). Finally, the quarter waveplate

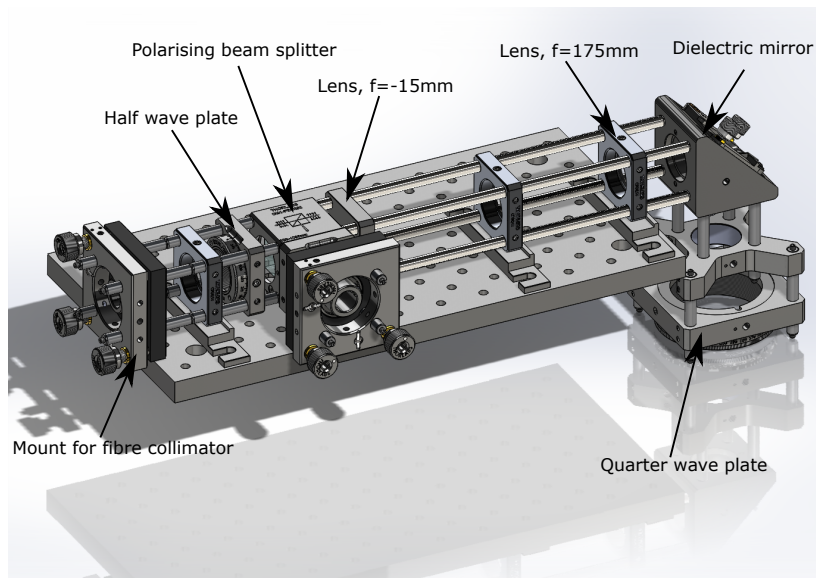


Figure 5.7 Collimator in a 30 mm cage system to expand the MOT beam, two beams can be simultaneously sent into the vacuum chamber using the cage system.

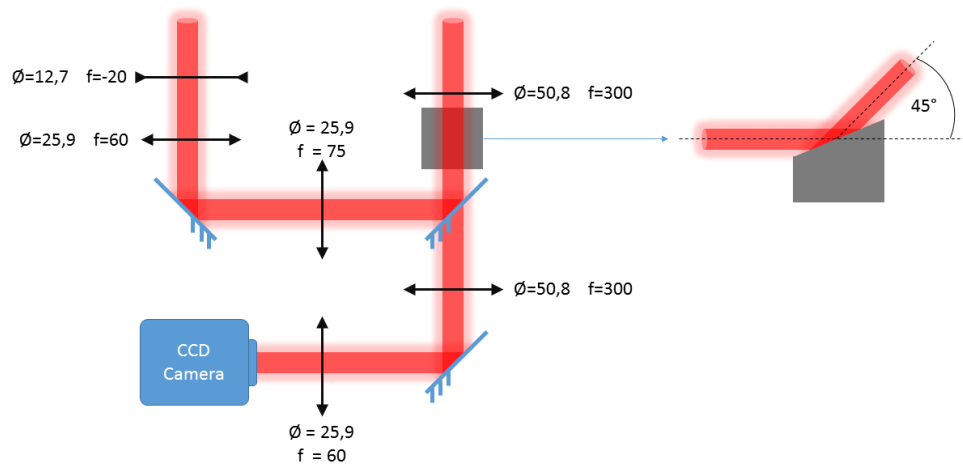


Figure 5.8 A schematic showing the path common to MOT beams and the absorption imaging system. The two telescopes expand the MOT beam by a factor 12 and the mirror steers the beam at an angle of 45° towards the vacuum chamber.

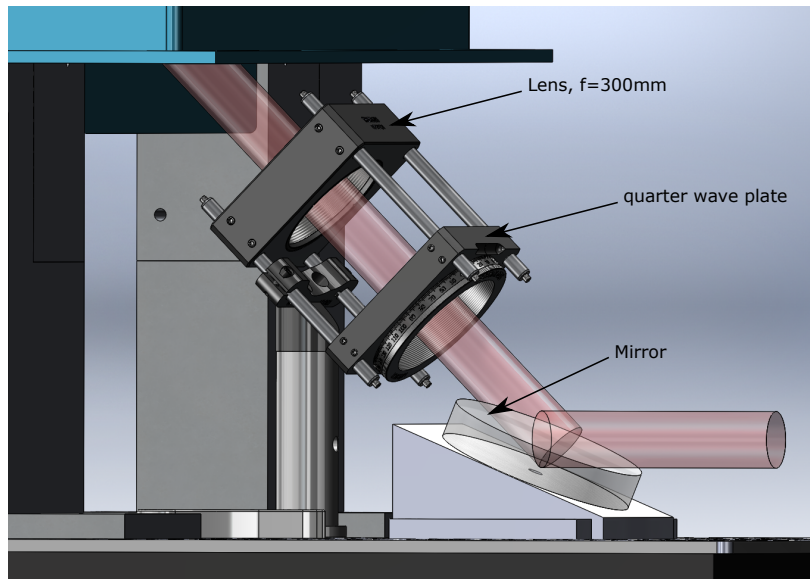


Figure 5.9 A 60 mm cage system, holding a quarter waveplate and a 300 mm focal length lens. The mirror glued to an aluminium block, to launch the beam at a 45° angle into the vacuum chamber can also be seen.

along with the $f = 300 \text{ mm}$ lens is mounted on a 60 mm cage system (as shown in Fig.5.9), which is fixed to a post at an angle of 45° with respect to the optical bench. The maximum power available in each MOT beam is about 8 mW, and it can be controlled with the TA current.

5.2.4 Bias coils

The vacuum chamber is surrounded by three pairs of square shaped coils in Helmholtz configuration, each pair produces approximately a homogeneous field at the centre of the vacuum chamber (see Fig.5.10). These three mutually orthogonal pairs of coils give a full control of the magnetic field near the chip surface and are useful at different stages of the experiment. For instance, the zero of the quadrupole coils coincides with the centre of the chip (by construction). If the four MOT beams are aligned to intersect at the centre of the chip, then with these coils the position of the field zero needs to be well centred with respect to the volume common to the MOT beams. Half of the horizontal MOT beams get reflected by the copper block that holds the chip (or gold mirror). This reduces the capture volume which in turn decreases the number of trapped atoms in the MOT. Therefore, we lower the horizontal MOT beams and the bias coils help to move downwards the zero of the quadrupole field by half a centimetre. Despite this functionality, these coils are in fact meant to produce the bias field during the U MOT and Z-trap stages of the experiment.

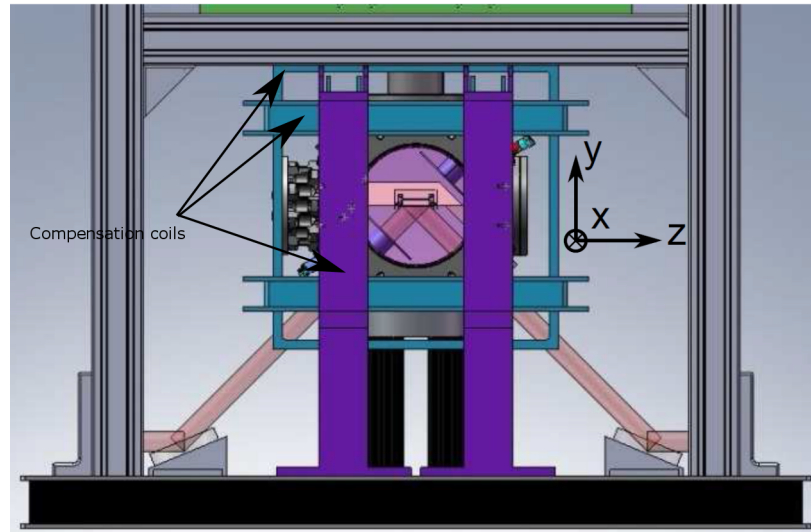


Figure 5.10 *Three orthogonal pairs of square shaped coils in Helmholtz configuration, surrounding the vacuum chamber help to control the field near the trapping region. The coils along Y-axis and Z-axis help to lower the quadrupole field zero by few millimetres during the MOT phase of the experiment.*

5.2.5 Low noise power supplies

Low noise current sources are indispensable for the experiment, as the noise in the current sources can alter the trapping parameters, especially, during the magnetic guiding stage of the experiment. The quadrupole coils, dispenser and the compensation coils are supplied with home built ultra low noise current sources. The power supplies can be controlled manually or with an analogue signal. These current sources can give up to 3 A (with minor changes this can be increased up to 5 A), with a relative noise of 10^{-5} and can deliver up to 20 W. The internal circuit of the current source can be altered, so that the power supply can be operated in two configurations: grounded and floating. The measured noise in the current source in these two configurations is shown in Fig.5.11. We typically run at least 4 A in the dispenser, so we power the dispensers by combining a commercial current source with the low noise power supply as shown Fig.5.12. In order to increase the dynamic range of the dispenser, a constant current of 2 A is run continuously through the dispenser using the commercial power supply. During the MOT stage of the experiment another 2 A are added through the home built power supply.

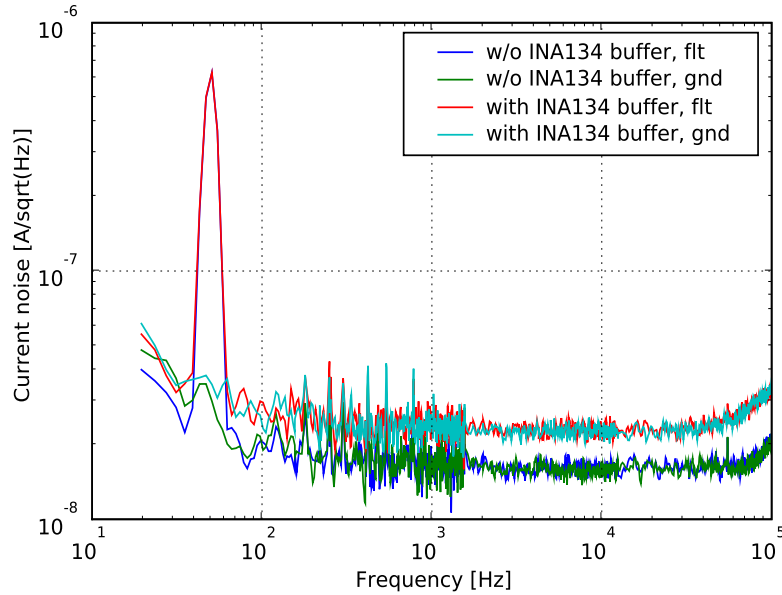


Figure 5.11 *Power spectral density of the current source noise at $I_{out} = 2.2$ A in the grounded (gnd) and floating (flt) configurations. The spike corresponds to the usual 50 Hz of the power line (taken from [111]).*

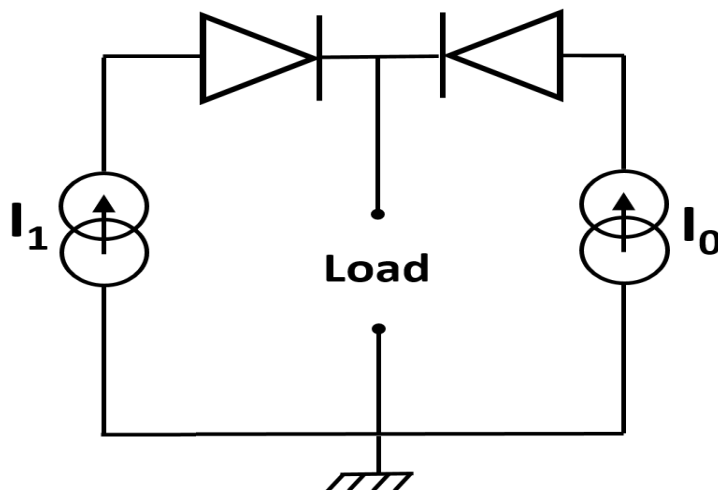


Figure 5.12 *A simple circuit to add current sources for the dispenser.*

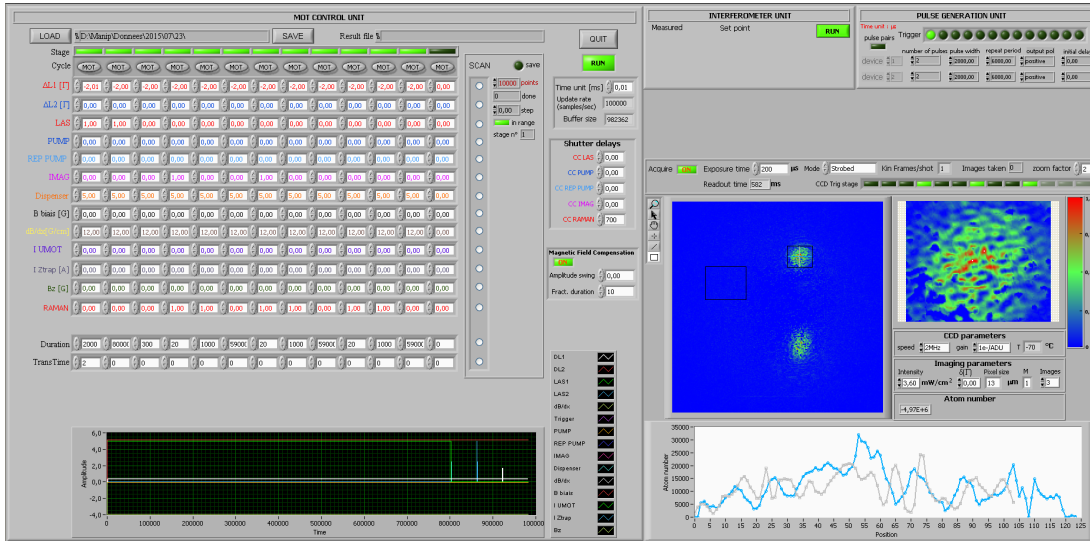


Figure 5.13 A snapshot of the LabView interface during a MOT loading sequence. A treated image of the MOT from the absorption imaging system can also be seen.

5.2.6 Computer control

The experiment is fully controlled with the LabView program. Different stages of the experiment are synchronized up to $1 \mu\text{s}$ through two National Instruments cards (NI-PCI-6733). Each card contains 8 channels, which generate the different analogue and digital signals needed for the synchronization. A sample picture of the interface can be seen in Fig.5.13. The LabView program was designed to control the DDS (this sets the detuning of the cooling beam), RF drivers of the AOMs (to turn on and off various beams), shutters (taking into account the delay of $3 - 4 \text{ ms}$ due to the slow response), current supplies of MOT coils and dispenser. The program automatically treats the images taken by the CCD during the absorption imaging sequence and it displays the treated image on the screen.

5.2.7 Fluorescence imaging system

For the purpose of characterising the MOT, a fluorescence imaging system was installed using the bottom window (facing the chip) of the vacuum chamber. The schematic of the fluorescence system can be seen in Fig.5.14. A 75 mm focal length lens of diameter 50.8 mm , was placed just below the window of the vacuum chamber at a distance of approximately 150 mm from the chip surface. This lens collects the fluorescence light from the atoms in the MOT with an efficiency η (the fraction of the total photons falling on the photo diode). The captured fluorescence light is then reflected by a mirror onto a fast photo diode

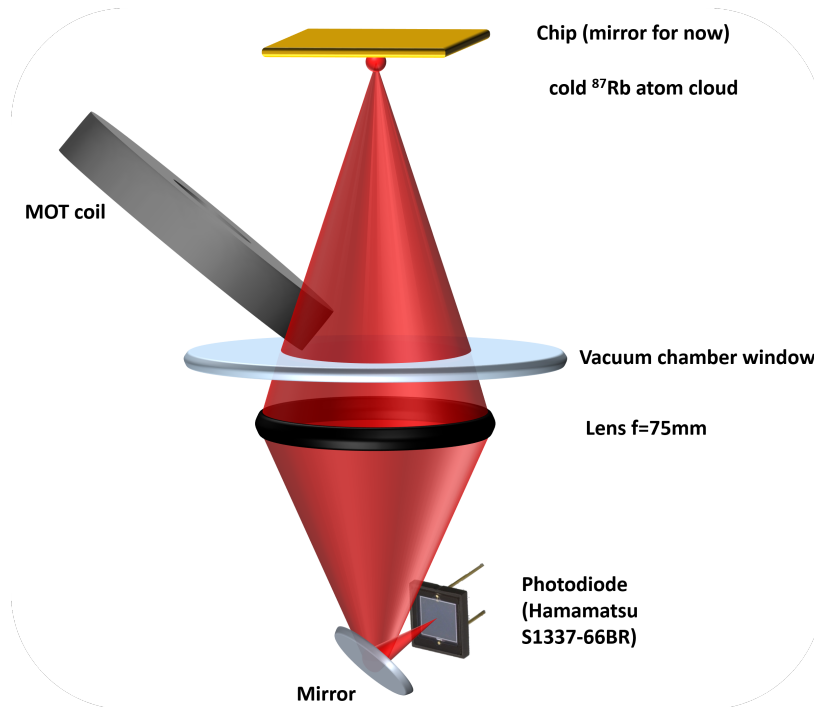


Figure 5.14 *Schematic diagram of the fluorescence imaging system.*

(Hamamatsu S1337-66BR). The rise time of the photo diode is about $1 \mu\text{s}$ and its photosensitive area has a cross-section $5.8 \text{ mm} \times 5.8 \text{ mm}$. This photo diode is mounted on a translational platform to precisely image the MOT. The $2f - 2f$ imaging system replicates the image of the MOT on the photo diode without any magnification.

The entire fluorescence system is covered to isolate the photo diode from external light. A photo current proportional to the number of fluoresced photons is generated from the diode, and its usually of the order of few micro amperes (the power due to fluoresced light from the MOT was found to be few tens of nano watts). Therefore, we amplify the signal with a circuit shown in the Fig. 5.15. The gain factor of the signal is given by the value of the resistance $R = 1.2 \text{ M}\Omega$. The capacitance was chosen in order to keep the time constant of the RC circuit $\tau = RC$ in the microsecond range, which is much smaller than the time scale at which MOT dynamics occur.

Collection efficiency

In order to obtain the atom number from the fluorescence signal, it is necessary to know what fraction of the photons emitted by the atoms reach the photo diode. Atoms usually fluoresce in all directions i.e. over a solid angle 4π . But, experimentally it is only possible to capture a fraction of the photons due to various optical losses and finite Numerical Aperture (NA) of the imaging system.

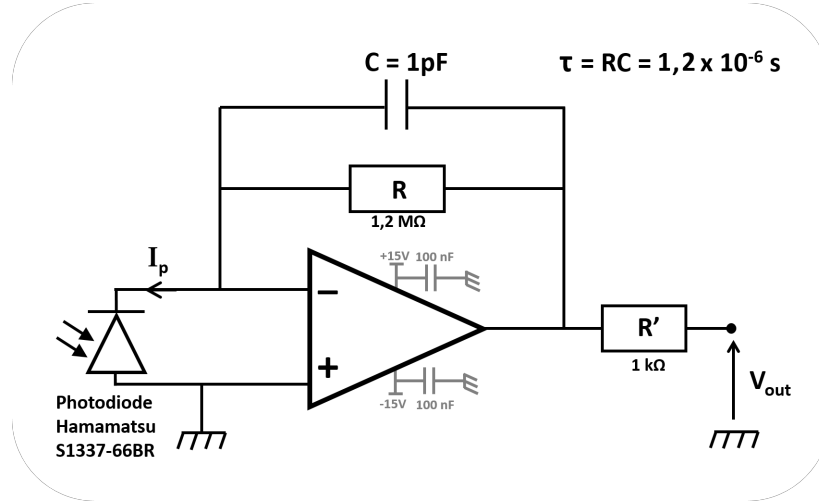


Figure 5.15 Schematics of the trans-impedance electronic circuit. The resistance $R = 1.2 \text{ M}\Omega$ was chosen to amplify the response of the photo diode. The response time of the circuit is $\tau = 1.2 \mu\text{s}$.

The collection efficiency of the imaging system takes into account these photon losses. A technical detail in the calculation of collection efficiency in our setup is the presence of the MOT coil (as shown in Fig.5.14) inside the vacuum chamber, which obstructs the fluorescence light falling on the photo diode. In addition, the usual solid angle has to be doubled as the photo diode captures light coming from the MOT and its reflection in the chip surface (see Fig.5.16). In order to compute the solid angle we measured the distance between the chip surface, the MOT coil and the window of the vacuum chamber from the solid works file of the setup. The solid angle is then numerically evaluated with a ray tracing simulation (details of the calculation are given in Appendix).

In the figure 5.17, we show the part of the lens which accepts the light from the MOT, only the solid angle subtended by the area of the part shown in red has to be included (the blue part is the shadow of the MOT coil). The collection efficiency computed from the simulation is $\eta = 2 \times 0.0061$, the factor 2 accounts for the reflection of MOT in the mirror. We use this value to estimate the atom number from the fluorescence signal.

Estimation of the atom number

The photo diode converts the photon counts (proportional to the atom number N_{at}) to a current, which is acquired as a voltage signal on an oscilloscope. Atoms in the MOT scatter photons at a rate given by

$$R_{sc} = \frac{1}{2} \frac{\Gamma s}{1 + s + 4 \frac{\delta^2}{\Gamma}}, \quad (5.2.6)$$

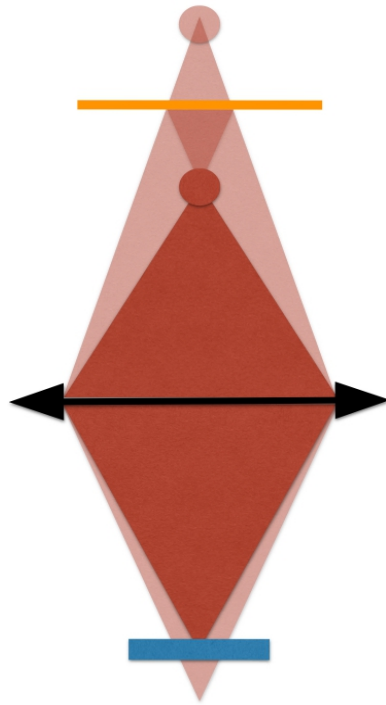


Figure 5.16 *Light from the MOT and its reflection are captured by photo diode.*

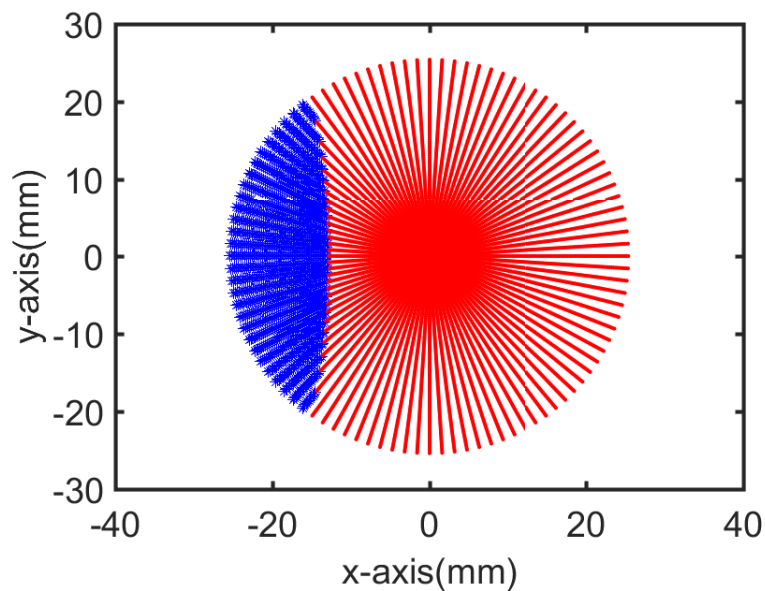


Figure 5.17 *Result of a ray tracing simulation, of the light from the MOT on the 2 inch lens. The shadow of the quadrupole coil is shown in blue and the solid angle subtended by the region in red gives the collection efficiency.*

where $s = I/I_{sat}$ is the saturation parameter proportional to the intensity of the MOT beams seen by the atoms, δ is the detuning of the MOT beam from resonance and Γ is the natural linewidth. The relation between voltage and the atom number is given by,

$$N_{at} = \frac{(V - V_0)\lambda}{hc\rho R\eta R_{sc}}, \quad (5.2.7)$$

where ρ is the responsivity of the photo diode and we remove the contribution V_0 due to stray light, i.e. $V - V_0$ is the voltage due to fluoresced light from the atoms in the MOT. The responsivity of the photo diode according to the manufacturer

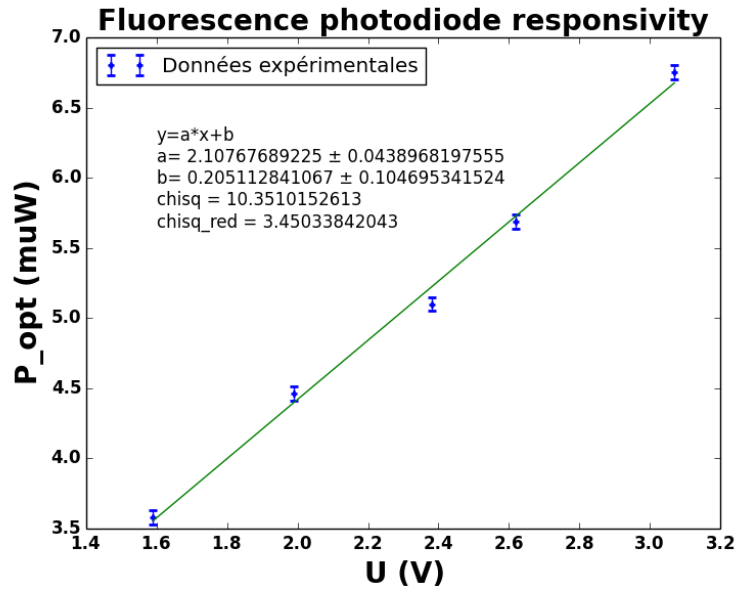


Figure 5.18 *Characterisation of the responsivity of the photo diode.*

is 0.51. We experimentally characterized the responsivity of the photo diode by shining a known power⁴ P on the photo diode. By measuring the voltage, we can obtain responsivity through the relation

$$V = \rho P R. \quad (5.2.8)$$

The experimentally measured responsivity is about 0.47 A/W (the linear fit is shown in Fig.5.18). Even after a perfect isolation, the voltage V obtained from the photo diode includes photon counts from back ground light due to the reflections of MOT beams inside the vacuum chamber (which we measure by turning of the quadrupole coils) and it needs to be subtracted to extract the atom number. A sample fluorescence signal measured during the MOT stage of the experiment can be seen in Fig.5.19, about 2.2×10^7 atoms are loaded in the MOT in 8 seconds. The atom number is computed using a detuning of -2Γ and by neglecting the presence of the quadrupole field.

⁴Measured with OPHIR Nova II power meter.

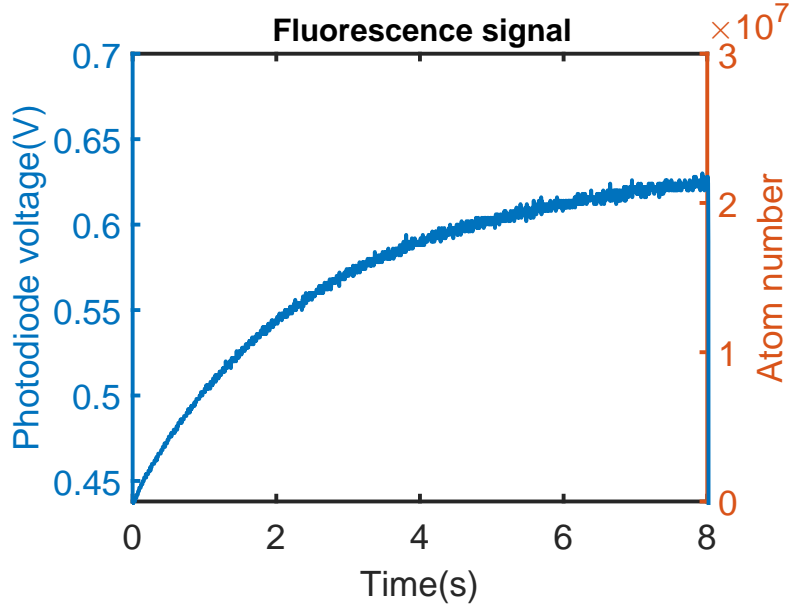


Figure 5.19 Fluorescence signal obtained from atoms in MOT, atom number after removing the contribution from background light is also shown.

5.2.8 Absorption imaging system

The fluorescence system described before uses a diode which integrates all the photons falling on it. Therefore, the information of the spatial density of atoms is lost. The spatial density of atoms can be useful, for instance, to estimate the velocity distribution of atoms. We built an absorption imaging system using a CCD camera (PIXIS 1024BR, Princeton Instruments), which gives the spatial information of the cloud by integrating the density along one direction (imaging axis). Thanks to the presence of the reflecting surface (or chip), if the imaging axis is at an angle with respect to the chip, we simultaneously obtain the atom density along the two orthogonal directions (see Fig.5.20). The basic principle of absorption imaging is to shine the cloud of atoms with a beam and image the shadow on a CCD. By measuring the amount of light absorbed, atom number can be deduced. If we consider an imaging beam of intensity I , propagating along z -axis and passing through an atomic medium of density $n(x, y, z)$. The variation of the intensity of the beam with the z coordinate is given by

$$\frac{dI}{dz} = -\frac{n\sigma_0}{1 + \frac{\delta^2}{\Gamma^2} + \frac{I}{I_{sat}}} I, \quad (5.2.9)$$

where δ is the detuning of the imaging beam expressed in half linewidth units and $\sigma_0 = \frac{\hbar\omega\Gamma}{2I_{sat}}$ is the resonance cross-section of the transition. Integrating the

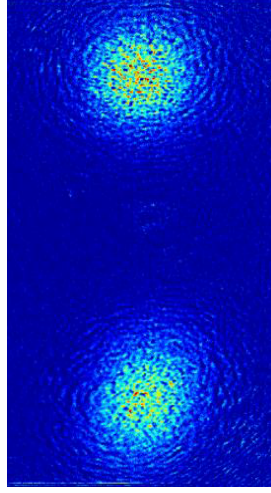


Figure 5.20 *An image of the MOT obtained from the absorption imaging system. The upper image is the real image and the lower image is due to the reflection of the MOT in the chip surface.*

above equation we obtain the column density of the atom cloud

$$N(x, y) = \int_{z_0}^{z_1} n(x, y, z) dz = \frac{1}{\sigma_0} [(1 + \delta^2) OD + \frac{I_{in}}{I_{sat}} (1 - e^{-OD})], \quad (5.2.10)$$

where the optical density $OD = -\ln(\frac{I(z_1)}{I(z_0)})$. Therefore, by measuring the intensity of the beam before $I(z_0)$ and after $I(z_1)$ passing through the atom cloud we can estimate the atomic column density along the imaging axis.

Choice of the parameters

The power of the imaging beam and the duration of the imaging pulse has to be chosen properly. During the imaging sequence, the atoms are pushed away due to the transfer of momentum from the imaging beam. Secondly, each pixel of the CCD has a finite well depth, which sets the maximal intensity that can be imaged. Imaging with intense beams washes the image due to spilling of electrons. Considering the above effects, we typically use beam powers of about $100 \mu W$ and a duration of $20 \mu s$.

Optical system

The imaging beam is shone at an angle of 45° degree with respect to the chip surface. The shadow of the atom cloud is then imaged onto the CCD with a $f - 2f - f$ optical system. The main advantage of this system is that it creates an exact copy of the atom cloud outside the vacuum chamber without any magnification. If the position of the atom cloud moves by a small distance,

the position of the image also moves by the same amount while keeping the magnification one. The focal length of the first lens is $f = 300 \text{ mm}$ and the diameter of the lens is $D = 50.8 \text{ mm}$, therefore the diffraction limited resolution Δr_{diff} of the optical system given by the Rayleigh criterion is

$$\Delta r_{diff} = 1.22 \frac{\lambda f}{D} = 5.7 \text{ } \mu\text{m} , \quad (5.2.11)$$

where f is the distance between the object and the first lens and D is the diameter of the lens. Considering that the closest window of the vacuum chamber is

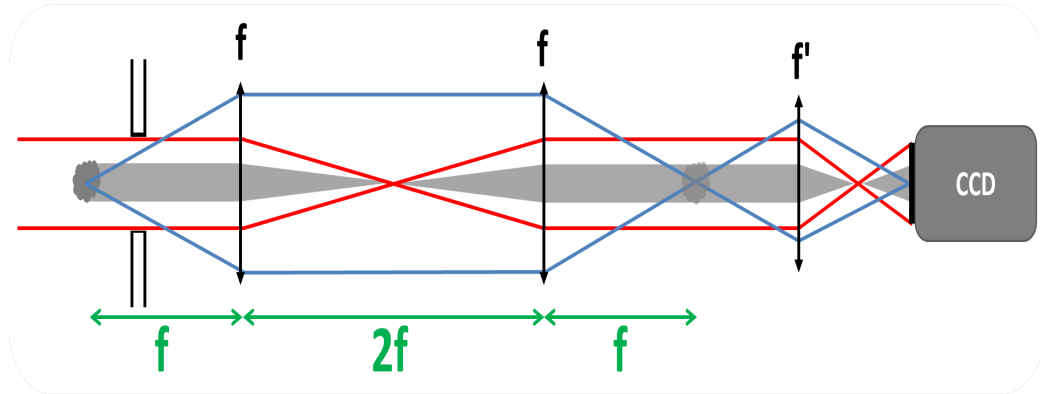


Figure 5.21 Schematics of the absorption imaging system, the focal length is $f = 300 \text{ mm}$.

$f \sim 300 \text{ mm}$ from the chip surface. The first lens of the optical system can not be closer than this distance. The diameter of the first lens is $D \sim 50.8 \text{ mm}$, therefore, a resolution of $\sim 5.7 \text{ } \mu\text{m}$ is the best we can achieve. The pixel size of the CCD is $13 \text{ } \mu\text{m}$ and is larger than the theoretical limit of the optical system. Therefore, the resolution is limited by the pixel size of CCD and not by the diffraction limit. To overcome this limitation, we magnify the image of atom cloud with another lens of focal length $f' = 60 \text{ mm}$ such that the image of two points separated by a distance Δr_{diff} falls on several pixels of the CCD. The necessary magnification M is given by the condition

$$M \gg \frac{\Delta r_{pixel}}{\Delta r_{diff}} = 2.33 . \quad (5.2.12)$$

We chose a magnification of $M = 5$ and place a lens of diameter $D' = 25.4 \text{ mm}$ at a distance of $6f'/5 = 72 \text{ mm}$ from the image of the MOT. The CCD is placed at a distance of $6f'$ from the lens. All the lenses used in the imaging system are cemented achromatic doublets (from Thorlabs) free from chromatic and spherical aberrations. They are also coated with an anti reflection coating for infra red light. The spherical aberrations of the lenses are usually corrected for infinite

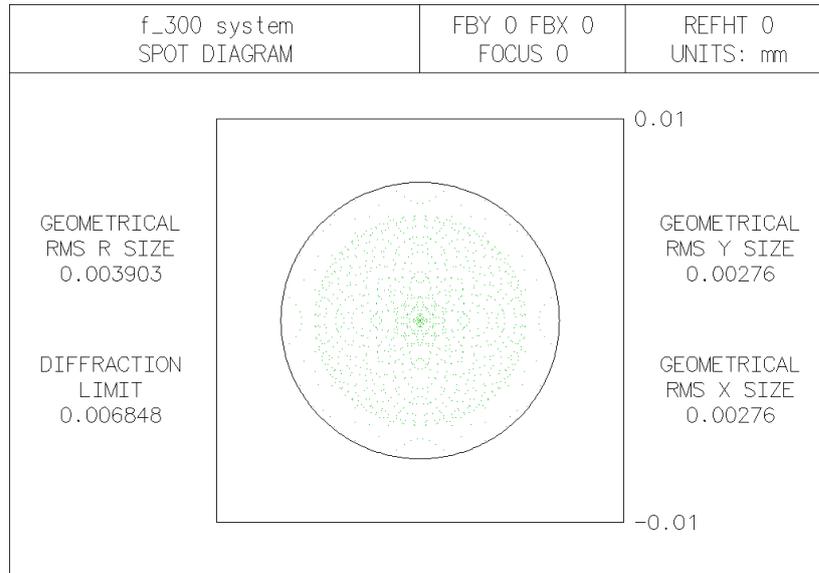


Figure 5.22 *Spot diagram obtained from a simulation of the optical system in OSLO Edu, the green dots show the intersection of the rays (emitted from the object) with the image plane and the black circle defines the diffraction limit of the optical system.*

conjugate ratios, whereas the lens with $f' = 60 \text{ mm}$ images the atom cloud at a finite distance onto the CCD (hence the conjugated ratio is finite).

To understand the limitations due to the spherical aberrations of this lens, we simulated the optical system in *OSLO Edu* taking into account the different surfaces and the refractive indices of the doublets. The diffraction limit obtained from the simulation is $6.84 \mu\text{m}$. The simulation also shows that the imaging system is mainly limited by the diffraction and not by spherical aberrations. All the rays emitted from the object can be seen to intersect the image plane within a circle of radius $6.84 \mu\text{m}$, which is the diffraction limit (see Fig.5.22).

The camera has an internal shutter of about 25 mm in diameter. According to the manufacturer's specifications, internal shutter has a finite lifetime (typically a million cycles) and it does not respond fast enough. Therefore, we designed a box which covers part of the optical system (including the camera) and placed a small mechanical shutter (typical response time of the shutter measured with the help of the CCD is $3 - 4 \text{ ms}$) at the entrance of the box. This allows us to leave the internal shutter of the CCD always open, when the experiment is running and only the external shutter is triggered while taking the images.

Characterization of the imaging resolution

A replica of the imaging system has been mounted to characterize the resolution of the imaging system. A one inch positive 1951 USAF target from Thorlabs

(R1DS1P) was illuminated with a beam of diameter 7 mm and power $51\ \mu\text{W}$. By placing the target at the object plane of optical system, image was recorded on the CCD. The exposure time was chosen to be 100 ms and an optical density (NE04A) with an attenuation factor of 10^{-4} was placed on the CCD in order not to saturate the pixels of the CCD. USAF target has different sets of horizontal and vertical lines, a set of 6 lines form an element and each group has 6 elements with varying line spacings. The resolution of the imaging system is given by the least resolvable set of lines in the image of the USAF target. Once the group and element number is identified, the separation between the lines (in mm) is given by the formula

$$\Delta r = 2^{\text{group} + \frac{\text{element} - 1}{6}}. \quad (5.2.13)$$

In the Fig.5.23 obtained on the CCD, we can clearly see the separation between

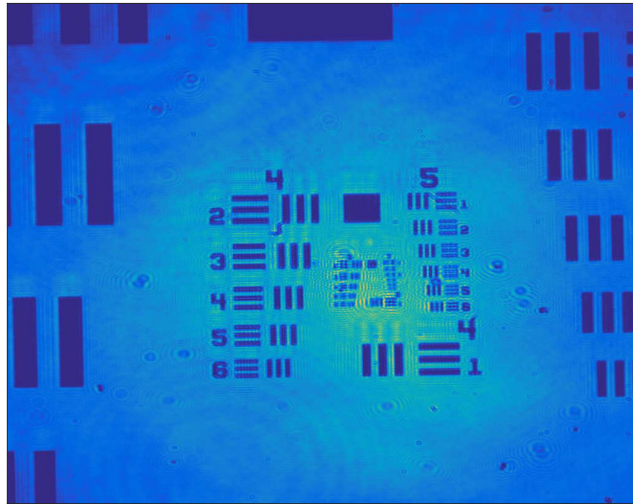


Figure 5.23 *Image of the USAF target obtained on the CCD using the optical system identical to the absorption imaging system. The separation between the lines in the group 5 and element 6 gives the resolution of the imaging system, which is $8.76\ \mu\text{m}$.*

the lines in the group number 5 and element 6. Therefore, the resolution of the imaging system using Eq.5.2.13 is at least half the separation between the lines i.e. $2^{-41/6}\text{ mm} = 8.76\ \mu\text{m}$, which is close to the diffraction limited resolution given by *OSLO Edu*.

Estimation of the atom number

In a typical absorption imaging sequence, we take three images. The first image I_{atoms} is taken with the imaging beam in the presence of atoms, the second

image I_{light} is taken only with the imaging beam and the final image I_{dark} is taken without atoms and imaging beam to remove the contribution of photons due to all other sources. The images obtained from the CCD are discrete with 1024×1024 pixels. From the three images, $I_{z_1} = I_{atoms} - I_{dark}$ and $I_{z_0} = I_{light} - I_{dark}$ can be computed and the atom number in a pixel (i, j) , can be written by multiplying the atom density in each pixel with the area of the pixel,

$$N(i, j) = \frac{\Delta r_{pixel}^2}{\sigma_0} [(1 + \delta^2) OD(i, j) + \frac{I_{z_0}(i, j)}{I_{sat'}} (1 - e^{-OD(i, j)})], \quad (5.2.14)$$

where $\Delta r_{pixel}^2 = 169 \mu m^2$ is the area of each pixel on the CCD and $OD(i, j) = -\ln[\frac{I_{z_1}(i, j)}{I_{z_0}(i, j)}]$. The constant $I_{sat'}$ is the saturated intensity expressed in ADU counts of the CCD, which is given by

$$I_{sat'} = \frac{\eta \tau \Delta r_{pixel}^2 \lambda I_{sat}}{G h c}, \quad (5.2.15)$$

where η is the quantum efficiency of the CCD (which is 0.98 at 780 nm according to the specifications provided by *Princeton Instruments*), τ is the exposure time of the image and G is the number of the electrons generated in each pixel per photon⁵. The total number can then be computed by summing over all the pixels

$$N_{atom} = \sum_{i, j=1}^N N_{i, j}. \quad (5.2.16)$$

A sample image of the MOT can be seen in Fig.5.20, the real image of the MOT and it's reflection in the chip surface can be seen. The distance between the atom cloud and the chip surface d can be deduced from the distance between the two images Δr_{images} using the relation, $d = \frac{\Delta r_{images}}{\sqrt{2M}}$, where M is the magnification due to the optical system. Since, the size of the MOT is several hundred microns, we directly image it on the CCD without magnifying the image with the 60 mm lens that is shown in Fig.5.21 (i.e. $M = 1$). The measured distance between the MOT and the mirror is about 5 mm.

5.3 Characterisation of the cold atom source

5.3.1 Phenomological models

The time evolution of the trapped atom number in the MOT can be understood with phenomenological models [112]. This model helps to obtain experimentally, the pressure in the vacuum chamber is normally measured with dedicated gauges

⁵We can select the value of G through the WinView program of the CCD, we normally operate the CCD with $G \approx 1$.

or through the ionization current of the ion pump. Often such measurements are not reliable when the pressure drops below 10^{-9} mbar and the MOT can be used to estimate the vacuum pressure [113, 114]. The rate of change of atom number in the MOT is described by the following equation

$$\frac{dN}{dt} = R - \gamma N - \frac{\beta}{V} N^2, \quad (5.3.1)$$

where N denotes the atom number in the MOT, R denotes the rate at which the atoms are trapped that depends on several experimental parameters. Here, γ denotes the loss rate due to the collisions between the trapped atoms and background atoms, summed over all the different gas species in the vacuum chamber (this also includes the un-trapped Rb atoms in the vacuum chamber)

$$\gamma = n_{Rb} \sigma_{Rb,Rb} v_{Rb} + \sum_i n_i \sigma_{Rb,i} v_i, \quad (5.3.2)$$

where n_i , v_i denote the atom density and average velocity respectively of a given atom species i and $\sigma_{Rb,i}$ denotes the collisional cross-section. The term βN^2 takes into account atom losses due to collisions among the trapped atoms, the corresponding loss rate is given by β and V is the volume of the MOT region. Solving Eq.5.3.1 with the initial condition $N(0) = 0$, we obtain

$$N(t) = N_s \frac{1 - e^{-\gamma' t}}{1 + \frac{N_s \beta}{V R} e^{-\gamma' t}}, \quad (5.3.3)$$

where $\gamma' = \gamma \sqrt{1 + \frac{4\beta R}{V \gamma^2}}$ gives the characteristic loading time of the MOT. The steady state atom number in the MOT, which arises from a balance ($dN/dt = 0$) between the loading and loss rates is given by

$$N_s = \frac{\sqrt{\gamma^2 + \frac{4\beta R}{V}} - \gamma}{2\beta/V}. \quad (5.3.4)$$

If the density of atoms in the MOT is relatively low, we can neglect the losses due to collisions between the trapped atoms and the atom number evolves according to

$$\frac{dN}{dt} = R - \gamma N. \quad (5.3.5)$$

Solving 5.3.5 we get

$$N(t) = N_s (1 - e^{-\gamma t}), \quad (5.3.6)$$

and the steady state atom number is simply the ratio between the loading rate and loss rate due to background atom collisions $N_s = R/\gamma$. Experimentally, we acquire (see Fig.5.24) the florescence signal emitted from the trapped atoms in the MOT. Therefore, we can compute the atom number in the MOT as a function of time. By fitting the above model, we can obtain the loading rate and the time constant.

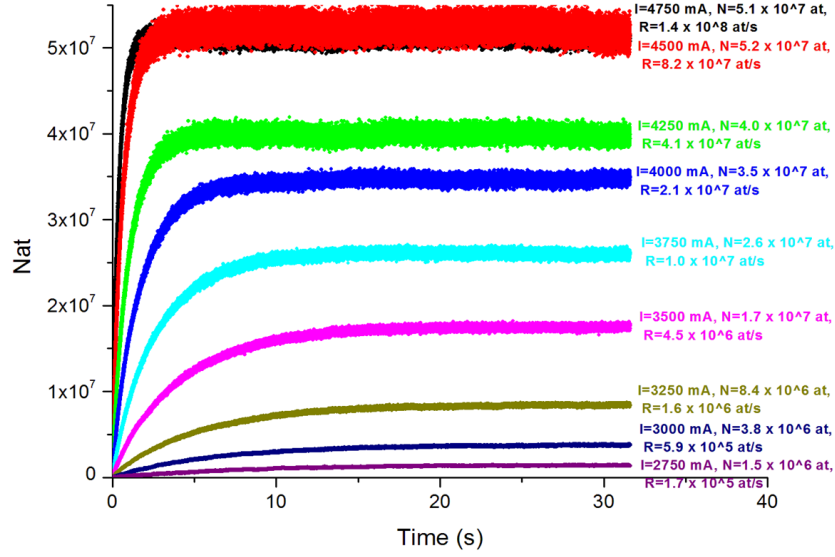


Figure 5.24 *MOT loading vs. time for different currents in the dispenser.*

5.3.2 Loading rate

As stated earlier, the loading rate in the MOT depends on several experimental parameters: background pressure of Rb, effective capture volume of the MOT beams, surface area of the trappable region, MOT beam power, its detuning from resonance etc. Knowledge of the loading rate R helps to deduce useful information of the above mentioned parameters. We can associate a capture velocity v_c to the MOT, which is the maximum trappable velocity of an atom that depends on the beam parameters. The loading rate is nothing but the flux of atoms with a velocity less than v_c , that enter the volume of the MOT common to all the beams. This quantity can be estimated as [115]

$$R = \int_0^{v_c} n_{Rb} A v f(v) dv , \quad (5.3.7)$$

where n_{Rb} is the density of background rubidium vapour in the vicinity of the MOT region, A is the surface area of the MOT. We can suppose that the velocity distribution of rubidium atoms in the vacuum chamber is given by the Maxwell-Boltzmann distribution

$$f(v) = \left(\frac{m}{2\pi k_B T}\right)^{3/2} 4\pi v^2 e^{-mv^2/2k_B T} . \quad (5.3.8)$$

Evaluating the integral under the approximation, where the capture velocity is much smaller than the thermal velocity at temperature T (i.e. $v_c \ll v_T =$

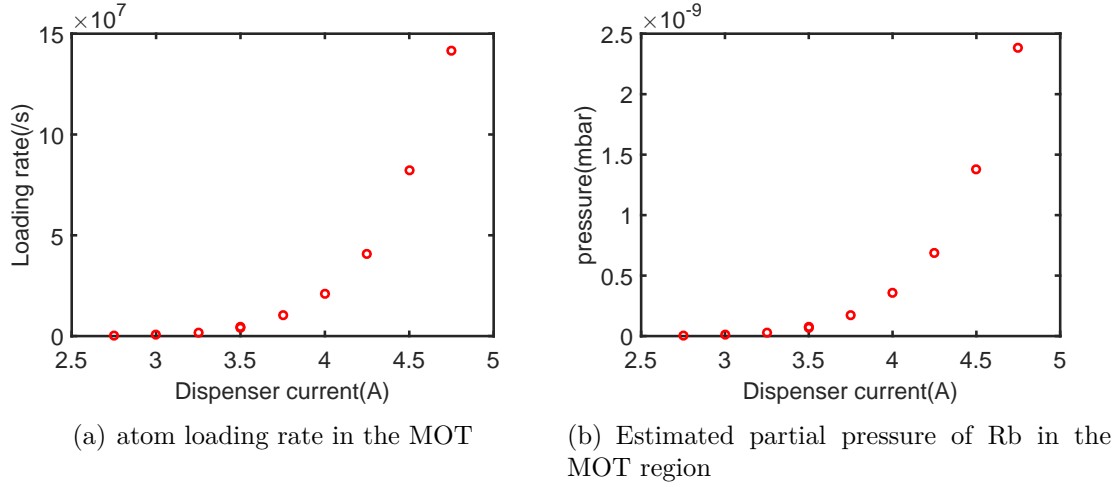


Figure 5.25 *Dependence of the loading rate and the partial pressure of Rb on the dispenser current.*

$(8k_B T / \pi m)^{1/2}$), we obtain

$$R = \frac{2}{\pi} n_{Rb} A \frac{v_c^4}{v_T^3} . \quad (5.3.9)$$

The loading rate R measured from the fit can be used to compute the density of the background Rb atoms in the vacuum chamber. Eventually, the partial pressure due to Rb in the MOT region can be estimated if all the other experimental parameters used in the model are well known

$$P_{Rb} = n_{Rb} k_B T . \quad (5.3.10)$$

To experimentally measure the loading rates, we operated the dispenser with a constant current in the range of 2.7 A – 5.2 A. The detuning of the MOT beams was set to -2Γ and a quadrupole gradient of 12 G/cm was used throughout the experiment. For each chosen current, we waited about 30 – 40 minutes for the pressure in the vacuum chamber to equilibrate before acquiring the data. Between successive measurements we allowed the pressure to reach the normal level ($\sim 1 \times 10^{-9}$ mbar), in order to minimize the pressure rise in the vacuum chamber due to the previous measurement. For a given current, once a steady state in the pressure is reached, we acquired the fluorescence signal from the MOT and averaged it over 16 MOT loadings. The resulting averaged data for each current is then fitted to the model in Eq. 5.3.6, to extract the loading rate, steady state atom number and characteristic loading time.

The steady state atom number and the loading time extracted from a data of two different days are shown in Fig. 5.26. The data shows that the steady atom number and the loading time vary slightly from day to day, due to the variation of the pressure in the vacuum chamber. Whereas, the MOT loading

rates were observed to be quite reproducible over those two days Fig.5.25(a). This suggests that the partial pressure in the vacuum chamber due to Rb is quite

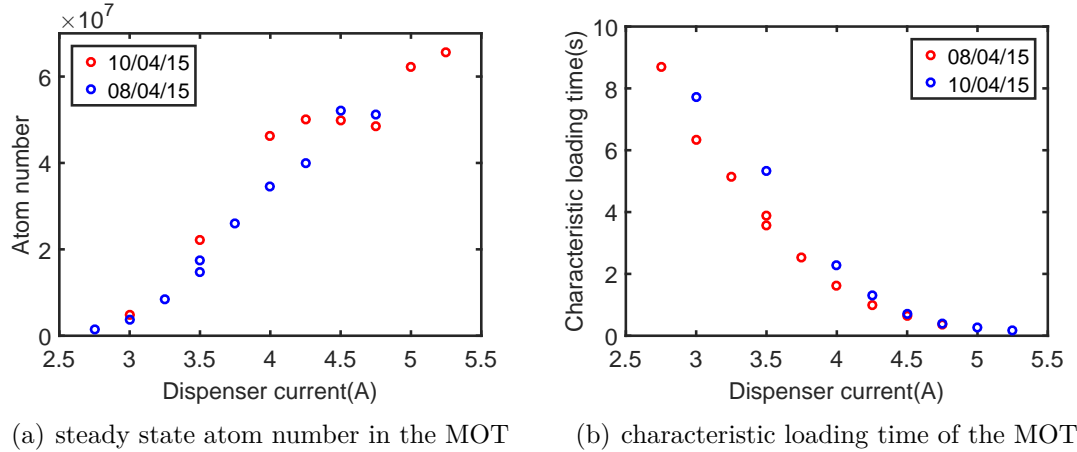


Figure 5.26 *Dependence of the steady state atom number and the characteristic loading on the dispenser current. The data acquired on two different days is shown in the figures.*

reproducible, whereas the pressure due to the remaining species may fluctuate from day to day⁶. Partial pressure due to Rb is estimated from the loading rate with the following parameters: the temperature of the Rb atoms liberated from the dispenser is around 500 K, but the temperature quickly drops to 300 K after few collisions with the walls of the vacuum chamber which are at room temperature, therefore $v_T = 270$ m/s. Assuming a trap region of size $l = 1.5$ mm, capture velocity can be expressed⁷ as $v_c = \sqrt{\hbar k \Gamma l / m} = 18.3$ m/s. The pressure of Rb gas computed with the above parameters can be seen in Fig.5.25(b). The characteristic loading time of the MOT decreases with an increase in the current in the dispenser Fig.5.25(b) as the partial pressure of the Rb increases rapidly. Loading time varies from 10 seconds at 2.7 A down to half a second for 5.2 A in the dispenser. Though faster loading can be achieved with higher currents, it may not be desirable owing to the increase in the pressure in the vacuum chamber, which can limit the lifetime of atoms in magnetic trap.

5.3.3 Lifetime of the MOT

After loading the MOT, if we assume that the supply of rubidium atoms in the MOT region is cut off (i.e. $R = 0$), the trapped atom number decays due to

⁶Adsorption and desorption gasses on the walls of the vacuum chamber can be reason.

⁷Considering the maximum possible laser force $F = \hbar k \Gamma / 2$, the velocity of the atom that can be brought to rest in a distance l .

collisions with the background atoms. The trapped atom number dynamics are then governed by

$$\frac{dN}{dt} = -\gamma N - \frac{\beta}{V} N^2 . \quad (5.3.11)$$

Solving the above equation with the initial condition $N(t) = N_s$ we obtain

$$N(t) = N_s \frac{e^{-\gamma t}}{1 + \frac{\beta N_s}{V} (1 - e^{-\gamma t})} . \quad (5.3.12)$$

If the density of the MOT is negligible, we can ignore the two body losses and we get $N(t) = N_s e^{-\gamma t}$. In our experiment, loading takes place due to background

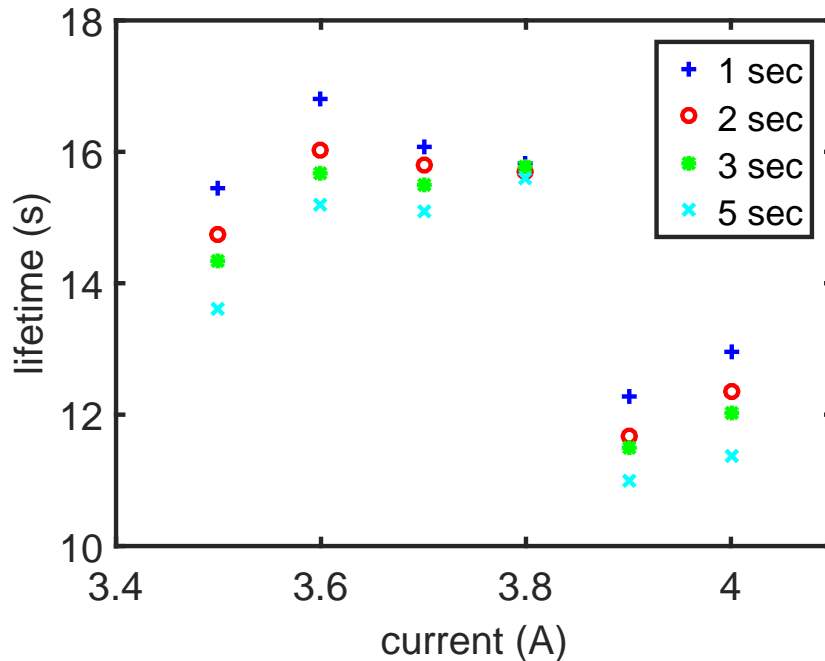


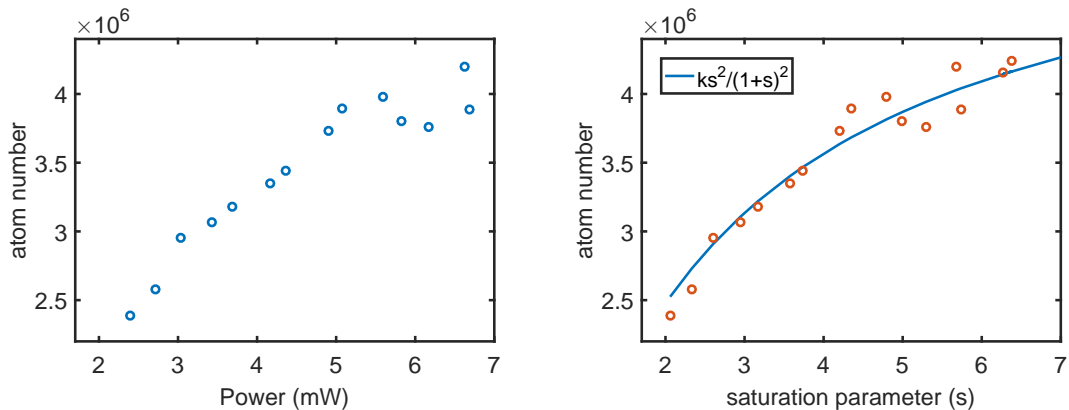
Figure 5.27 *Lifetime of the atoms in the MOT vs. current. Lifetime extracted by removing the first few seconds of the data, to remove the effect of loading due to the dispenser and the background Rb atoms in the vacuum chamber.*

vapour pressure of Rb and we do not have a means to switch off the loading of Rb atoms abruptly (which is possible in the experiments where the 3D MOT is loaded using a beam of atoms from 2D MOT). If the current in the dispenser is completely turned off, liberation of atoms does not stop until the temperature of the dispenser drops below the critical value. In addition, even if the dispenser stops emitting Rb atoms, loading takes place due to the presence of Rb atoms in the vacuum chamber. This makes it hard to precisely estimate the lifetime of the MOT in our setup. After a MOT loading sequence, the dispenser was switched

off and we acquired the fluorescence signal. By removing the first few seconds of the data⁸ we fit the atom number to the decay model. Results of the lifetime measurement as a function of dispenser current are shown in Fig.5.27. The data shows that the lifetime is at least 10 seconds for a constant dispenser current up to 5 A.

5.3.4 Steady state atom number in the MOT

The atom number in the MOT needs to be optimized considering several parameters. The MOT is usually robust to the fine alignment of the beams, power imbalance and imperfect polarizations of the MOT beams. We manually optimized the alignment and polarizations so that the fluorescence signal is maximum. The MOT beam power is balanced among the four beams up to few percent by rotating the half waveplates of the Schafter-Kirchoff fibre port cluster. The critical parameters that need to be studied are, the detuning of the MOT beam from the cooling transition and the quadrupole gradient. Additionally, characterization of the atom number with MOT beam power is also useful to redistribute the power of the ECDLs across different optical fibres.



(a) Steady state atom number vs. MOT beam power.

(b) Steady state atom number vs. $s = I/I_{sat}$, the value of k is 5.5×10^6 .

Figure 5.28 *Dependence of the steady state atom number on the MOT beam power.*

Atom number vs. laser power

Steady state trapped atom number in a MOT typically increases with the MOT beam power, as the cooling force increases. However, if the power is increased indefinitely beyond the saturation intensity, cooling forces also saturate, so does the number of trappable atoms. In a MOT loading sequence, the atom number

⁸To remove the effect of MOT loading due to the dispenser and the background.

reaches a steady state due to the balance between the loading and loss rates and is given by $N_s = R/\gamma$. If we substitute the expression for R we get

$$N_s = \frac{2}{\gamma\pi} n_{Rb} A \frac{v_c^4}{v_T^3}, \quad (5.3.13)$$

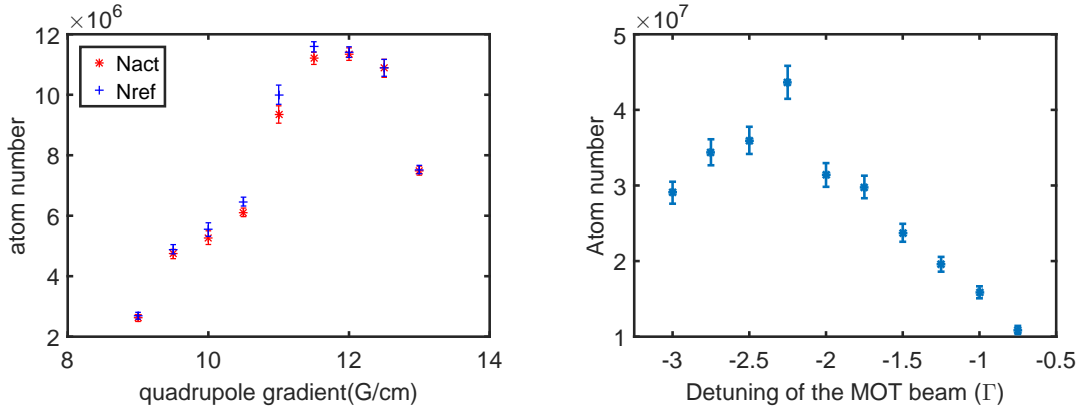
where the capture velocity of the MOT depends on the cooling force and it is easy to see that v_c scales as $\sqrt{\langle F \rangle}$. The cooling force depends on the velocity of the atom and its position in the MOT, if we assume a maximal cooling force, $\langle F \rangle$ scales as $\frac{s}{1+s}$. Therefore, the steady state atom number varies with the saturation parameter as

$$N_s \propto \frac{s^2}{(1+s)^2}. \quad (5.3.14)$$

A measurement of the atom number in the MOT with the beam power can be seen in Fig.5.28. We varied the MOT beam powers in the range of 2 – 8 mW keeping all other parameters fixed (a constant current of 3A was run through the dispensers), and acquired the fluorescence signal. The atom number grows with the saturation parameter as $s^2/(1+s)^2$ and can be seen to saturate with the MOT beam power. From the fit, we can deduce that the atom number in the MOT saturates at 5×10^6 .

Atom number vs. detuning and quadrupole field gradient

To find the optimum value of quadrupole field gradient, we set the MOT beam



(a) Atom number as a function of the quadrupole gradient at fixed detuning of -2Γ . Atom number attains a maximum value at a gradient of 12 G/cm. (b) Atom number vs. cooling beam detuning at a fixed quadrupole gradient of 12 G/cm. Atom number peaks at approximately -2.25Γ

Figure 5.29 *Dependence of the steady state atom number on the quadrupole gradient and the MOT beam detuning.*

detuning at -2Γ and varied the quadrupole gradient from 9 G/cm to 13 G/cm . For each value of field gradient, we obtained the images of 50 MOTs using absorption imaging system. Atom numbers extracted from these images⁹ can be seen in Fig.5.29(a). Atom number reaches a maximum value between 11.5 G/cm and 12 G/cm . To find the optimum value of MOT detuning, we set the quadrupole gradient at 12 G/cm and varied the detuning between -3Γ and -0.75Γ , fluorescence signal is used to extract the steady state number. Steady state atom number is peaked around -2.25Γ (see Fig.5.29(b)).

5.3.5 Estimation of the temperature

We estimated the temperature of the MOT using two independent techniques: a) Release recapture method and b) Time of flight (TOF) method. The temperature determination from release recapture method was done with the fluorescence imaging system whereas absorption imaging system was used in the TOF method.

Release recapture method

In the release recapture method [116], we begin by loading atoms in the MOT. After the atom number reaches a steady state, MOT beams are then switched off (release) and switched on (recapture) after few milliseconds by controlling the RF power of the AOM used to shift the frequency of the cooling beam. From the fluorescence acquired signal (see Fig.5.30) we can compute the fraction of atoms that remain in the trapping volume of the MOT. The fraction of atoms that remain in the MOT region depends on the temperature of atoms in the MOT and the release time. It is given by [117]

$$f_r(\Delta t) = \frac{N(\Delta t)}{N(0)} = \frac{4}{\sqrt{\pi}} \int_0^{v_c/v_T} u^2 e^{-\frac{v^2}{v_T^2}} du, \quad (5.3.15)$$

where $v_c = D/\Delta t$ is the maximum velocity of the atoms that starting at the centre of the MOT, to reach the edge of the trappable region defined by the beam diameter D in Δt seconds. Evaluating the integral yields

$$f_r(\Delta t) = \text{Erf}\left[\frac{D}{\Delta t v_T}\right] - \frac{2}{\sqrt{\pi}} \frac{D}{\Delta t v_T} e^{-\frac{D^2}{\Delta t^2 v_T^2}}. \quad (5.3.16)$$

Experimentally, we can measure the fraction of the recaptured atoms for different release times. By fitting the resulting curve to the Eq.5.3.16 we can compute v_T and the temperature of the MOT can be deduced. The uncertainty in the temperature depends on the accuracy of the estimation of the size of the MOT region. We considered release times between 10 ms and 150 ms . The fraction of the atoms recaptured was measured with the fluorescence imaging system. By

⁹Atom numbers are computed from the MOT and its reflection in the chip.

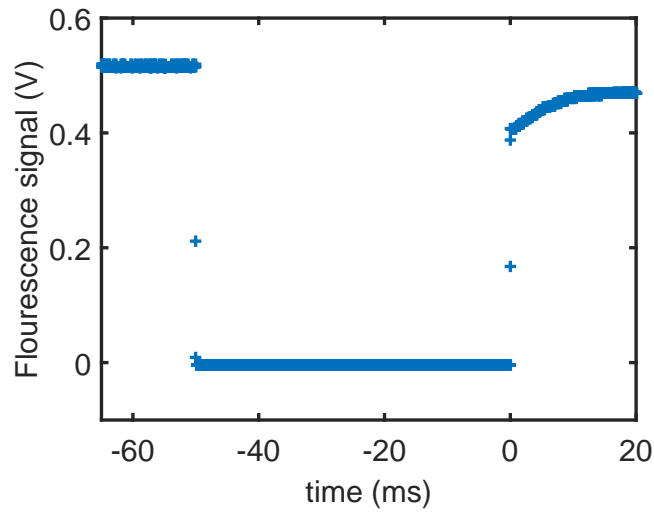


Figure 5.30 *Fluorescence signal of a typical release recapture sequence. MOT beams are switched off at $t_1 = -50$ ms and switched on at $t_2 = 0$ ms (i.e. a release time of $\delta t = 50$ ms). After the recapture atom number increases slightly until it saturates in few milliseconds. The saturated atom number is considered to compute the fraction of atoms recaptured.*

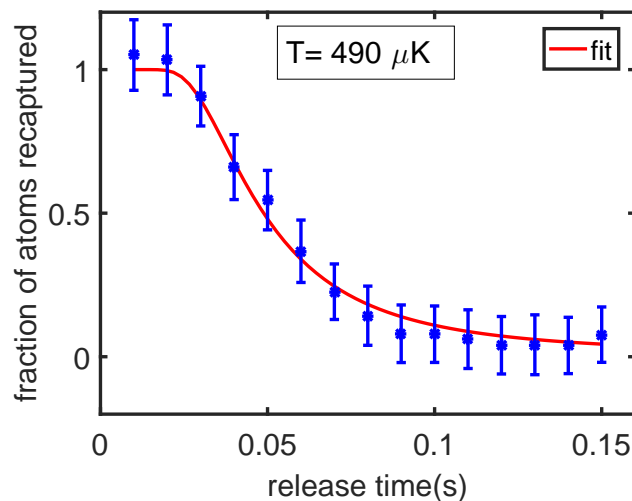


Figure 5.31 *The temperature of the MOT measured from the release recapture method. For a beam diameter of 16mm, the temperature computed from the fit is $490\mu K$.*

using a beam diameter of 16 mm, the temperature obtained from the fit is about 490 μK .

Time of flight method

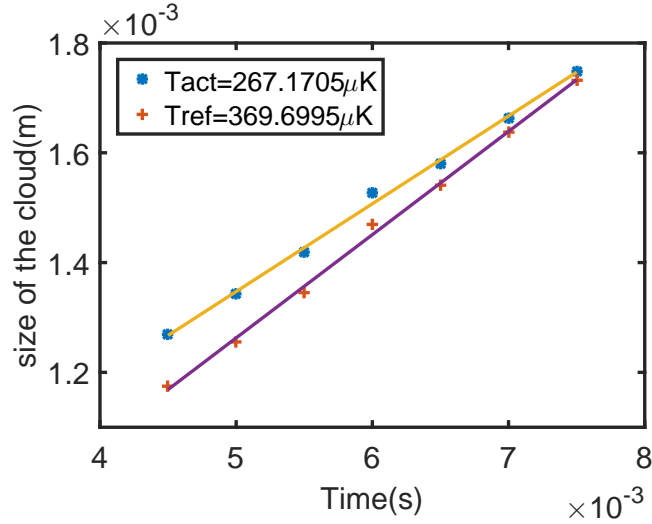


Figure 5.32 *Temperature of the MOT measured from a TOF measurement. The temperatures of the image of the MOT and the reflection in the mirror are shown. Temperatures are not the same as the quadrupole field gradients are different, along the two directions.*

The basic idea of the TOF method is to image the cloud of atoms at different time intervals after switching off the trapping fields. The information of the velocity distribution of the atom cloud can be linked to the size of the cloud. Knowing the size of the atom cloud at different instants, temperature of the cloud can be accurately measured. Let us assume that the atom density distribution is a Gaussian with a width σ_0 at a time $t = 0$,

$$n(\mathbf{r}, 0) = \frac{1}{(2\pi\sigma_0)^{3/2}} e^{-\frac{\mathbf{r}^2}{2\sigma_0^2}}. \quad (5.3.17)$$

If the MOT beams are turned off at time $t = 0$, the atom cloud expands. The atom density at a later time $t = t'$, can be computed from Eq.5.3.17 by knowing the transition probability $T(\mathbf{r}, t'; \mathbf{r}_0, 0)$ of an atom located at a position \mathbf{r}_0 at time $t = 0$ to be at a position \mathbf{r} at time $t = t'$. It is nothing but the probability for the atom to have a speed $|\mathbf{r} - \mathbf{r}_0|/t'$ and it is given by the Maxwell-Boltzmann distribution

$$T(\mathbf{r}, t'; \mathbf{r}_0, 0) = \left[\frac{m}{2\pi k_B T t'^2} \right]^{3/2} e^{-\frac{m|\mathbf{r} - \mathbf{r}_0|^2}{2k_B T t'^2}}. \quad (5.3.18)$$

Finally, the atom density at a position \mathbf{r} and a time t' can be obtained by integrating over the initial position \mathbf{r}_0

$$n(\mathbf{r}, t') = \int T(\mathbf{r}, t'; \mathbf{r}_0, 0) n(\mathbf{r}, 0) d^3 r_0 . \quad (5.3.19)$$

After the integration, atom density distribution at time $t = t'$ is,

$$n(\mathbf{r}, t') = \frac{1}{(2\pi\sigma(t'))^{3/2}} e^{-\frac{\mathbf{r}^2}{2\sigma(t')^2}} , \quad (5.3.20)$$

where $\sigma(t')^2 = \sigma_0^2 + \frac{k_B T t'^2}{m}$. If we consider the size of the atom cloud after a sufficiently long interval we get,

$$\sigma(t') \approx \sqrt{\frac{k_B T}{m}} t' . \quad (5.3.21)$$

By imaging the cloud at different time intervals, the information of the temperature can then be extracted from the rate at which the Gaussian width of the cloud increases. To characterize the temperature of the MOT, images were acquired after a time interval. The interval was varied between 4.5 *ms* and 7 *ms*. For each time interval we took a set of 50 images obtained from consecutive MOT loading. The size of the cloud was computed by fitting a 2D Gaussian to the atom density images. By fitting a linear curve to the average size of the cloud, computed from the 50 images, we evaluated the temperature of the atom cloud (see Fig.5.32 for the linear fit). Since, we image the cloud and its reflection in the mirror, we simultaneously get the information of the cloud temperature in two orthogonal directions. We can see in Fig.5.32 that the temperatures in the two directions are 267.17 μK and 369.69 μK . The difference in temperatures can be attributed to the different field gradients of the MOT coils in the two directions.

5.3.6 Pressure dynamics

In cold atom experiments that use single vacuum chamber, atoms are trapped from the background vapour pressure in the vacuum chamber. During the MOT loading stage of the experiment, it is necessary to raise the background pressure of Rb atoms (with the help of dispenser), in order to increase the atom loading rate. For an inertial sensor, a fast loading rate is desirable, as it reduces the dead time of the device. However, after the MOT stage, if the background atoms are not pumped out quickly, the increase in pressure can reduce the lifetime of the magnetically trapped atoms. This limits the interrogation time of the interferometer and it effects the sensitivity of the sensor. Therefore, an in-depth study of the pressure variation near the atom chip can be helpful in finding an optimal configuration to operate the dispenser.

With an aim to understand the pressure dynamics in our setup, we monitor the pressure using the ion pump. Once the pressure at the ion pump location

is determined from the ionization current. We can use pressure conductivity models or a simulation software (for e.g. Molflow +) to estimate the pressure at any point in the vacuum chamber. More specifically, the quantity of our interest is the pressure near the atom chip.

Relation between pressure and ionization current

The pressure displayed on the ion pump controller is usually proportional to the ionization current. When the pressure in the vacuum chamber drops below 10^{-9} mbar (i.e in the ultra high vacuum regime), the pressure given by the ion pump controller is not reliable. To estimate the vacuum pressure more accurately, we need to investigate closely the processes that take place inside the ion pump.

The basic principle of the ion pump operation is as follows, a set of permanent magnets inside the ion pump guide and sustain electrons in a circular trajectory. A high voltage (3000 – 7000 V) applied across the electrodes, accelerates these electrons inside the anodes. If an atom in the vacuum chamber collides with these fast moving electrons, they get ionized and generate a current proportional to the gas pressure in the anode region. The positive ion accelerates towards cathode and the collision sputters matter on the cathode and holds ions. This phenomena affects the linear relation between the ionization current and the pressure due to leakage current and field emissions. If the ion pump is operated long enough, a layer of alkali atoms gets deposited on the electrodes and it leads to a leakage current. This extra current adds to the usual current from ionization and causes a bias in the pressure measurement. When the free accelerated ions hit the electrodes holding ions, also leads to an increase in the ionization current. Field emissions arise due to the sputtered matter forming micro or nano antennas over the electrodes. These structures add a random current noise to the pump current, which depends on the high voltage applied across the electrodes. However, the field emission effect can be suppressed by applying a high voltage (~ 10000 V) across electrodes. In our case, we do this by using the Hi-potting option in the ion pump controller, which cleans the electrodes. The pressure dynamics at the ion pump location considering these phenomena are described by

$$\frac{dP}{dt} = -aP - aP \times bI + (c_1I - c_2I) + L, \quad (5.3.22)$$

where the first term take into account the pressure at the pump location, the second term takes into account the probability for an atom or a molecule in the gas to be trapped by the titanium being actually sputtered from the cathode, the third term considers the competition between the relaxation of previously trapped ions and the new ions being trapped in the cathode and finally the last term takes into account the leaks in the vacuum chamber. Since the pressure displayed on the pump controller is proportional to the ionization current, we take $P_{disp} = kI$ and we assume a non linear relation $P = hI^n$ between the real

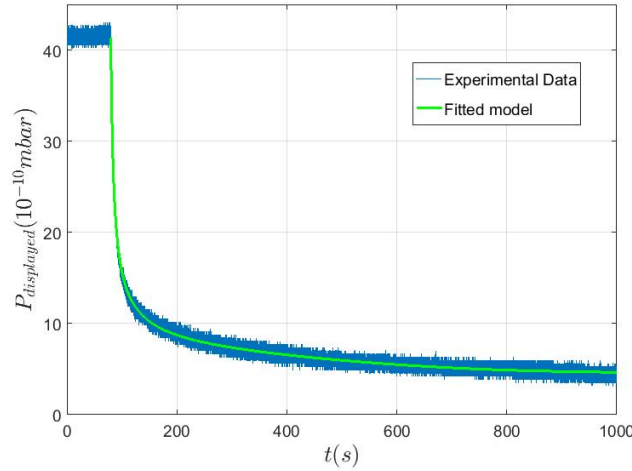


Figure 5.33 A fit of the displayed pressure (blue) with the model (green) in Eq.5.3.23, the dispenser is switched off at 79 seconds.

pressure and the ionization current. This leads to the following expression

$$\frac{dP_{disp}}{dt} = -a'P_{disp} - b'P_{disp}^2 + (c'P_{disp} + f') \times P^{1-\frac{1}{n}} . \quad (5.3.23)$$

To obtain the real pressure in the vacuum chamber, we run a constant current of 5 A in the dispenser until the pressure saturates. We turn off the current and let the vacuum pressure to decay, by fitting the displayed pressure to the above model we can obtain the value of n . The result of the fitting can be seen in Fig.5.33. The value of n given by the fit is 1.04 and it allows for an accurate estimation of the pressure. However, the value of n must be verified with an alternative measurement of pressure, for instance, using the MOT.

Pressure variation during the experiment

Here we study the pressure variation at the ion pump during a typical experimental cycle. We considered an experimental cycle of duration 8 seconds. We run a constant current of 2 A in the dispenser and we add an additional 2 A of current for a duration which is varied between 3 seconds and 8 seconds i.e. duty cycle is varied between 37.5% and 100%. For a duty cycle of 62.5%, variation of pressure at the ion pump location can be seen in Fig.5.34. After the addition of 2 A to the dispenser, pressure at the ion pump starts to increase after a time Δt_1 . Similarly, once the additional current is cut off, pressure starts to decrease with a delay Δt_2 . The delay Δt_1 (Δt_2) arises due to the time needed to increase (decrease) the temperature of the dispenser to a level, sufficient enough to liberate (stop the emission of) Rb atoms from the dispenser. Δt_1 and Δt_2 are experimentally measured for different duty cycles and are found to be independent of the

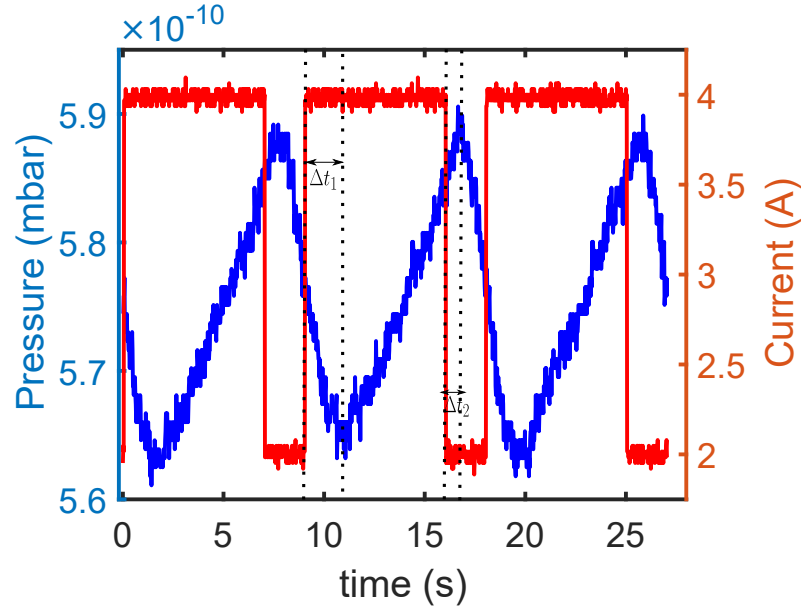
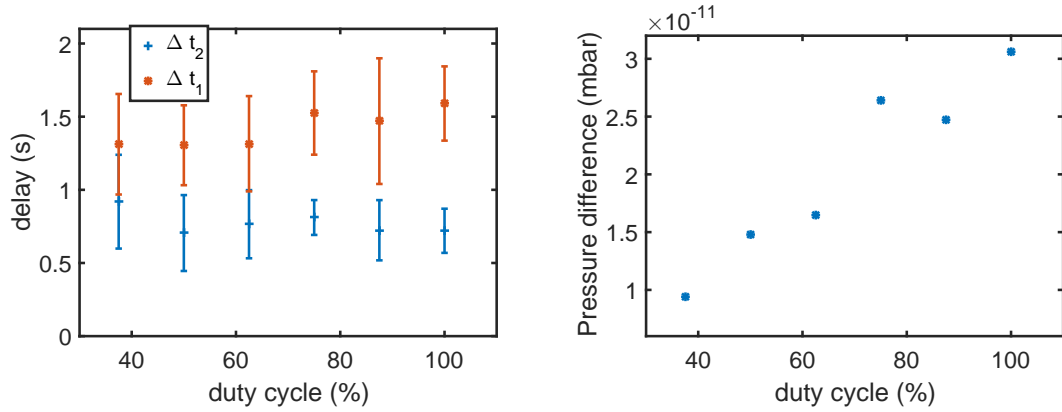


Figure 5.34 Variation of the pressure at the ion pump for a duty cycle of 62.5%, the current in the dispenser is also shown in the figure. The delay between the moments when the dispenser is turned on (off) and the instant when the pressure starts to rise (drop) can be seen.

duty cycle and their values are 0.76 and 1.5 respectively (see Fig.5.35(a)). The pressure difference between the minima and the maxima of the pressure cycle for different duty cycles can be seen in Fig.5.35(b), the difference is at a level of few 10^{-11} mbar.

5.4 Conclusion

The current state of the GyrAChip's experimental setup is described in this chapter. The optical systems assembled for the realization of mirror MOT are presented. The typical MOT loading rate in our experiment is about $2.1 \times 10^7/s$ (for a dispenser current of 4 A). The typical steady state atom number in the mirror MOT is about 3×10^7 atoms. The steady state atom number in the MOT is found to be optimum for a quadrupole gradient of ~ 11.5 G/cm and for a cooling beam detuning of -2.25 Γ . The temperature of the MOT is measured from the TOF method is about $267\mu K$ and $369\mu K$ along the axes of the quadrupole field, whereas the temperature measure from the release recapture method is about $490\mu K$. The measured lifetime of the atoms trapped in the MOT is at least 10 seconds. Two atom detection systems: a) florescence and b) absorption imaging systems have been added to the setup, to facilitate the characterisation of cold atom source. The resolution of the absorption imaging system is characterized



(a) Variation of delays (Δt_1 and Δt_2) with respect to duty cycle.

(b) Difference in the pressure between the maximum and minimum.

Figure 5.35 *Pressure variation in the vacuum chamber during a MOT cycle.*

with the USAF target. The measured resolution of the f-2f-f optical system is about $8.76 \mu m$, which is better than the resolution offered by the CCD. The first steps towards a model explaining the pressure dynamics in our setup have been discussed. The pressure dynamics study is still at a preliminary stage and a systematic investigation using the MOT is required to fully characterize these processes.

Chapter 6

Perspectives & Conclusion

We have presented in this thesis the theoretical elements required in the optimal design of a magnetic roughness free waveguide, for guided atom interferometry on an atom chip. The study of the dynamics of the atoms is also discussed in detail, as well as the main implications of the motion of the atoms on an interferometric signal meant for inertial sensing. The main result of this theoretical investigation is the generation of a stable guiding in a ring geometry, using wires fabricated directly on the chip. The experimental work focussed on the realisation of a source of cold atoms with a microfabricated mirror, and the next step is to replace it with the atom chip. The different wire structures on the chip will allow, on one hand the realisation of the standard cooling processes including the rf forced evaporation; on the other hand, the generation of the magnetic guiding potential. In the following sections, we present the first version of the atom chip that is currently under fabrication. We discuss the important elements incorporated on the chip and their functionality. A schematic of the Bragg system needed to launch atoms in the waveguide is also discussed. Finally, the planned experimental sequence, starting from the mirror MOT is shown.

6.1 Atom chip

A key component of the GyrAChip experiment is the atom chip. Using this atom chip, we envisage to generate a circular guide of $500 \mu m$ radius necessary for the guided Sagnac interferometer. As a first step, with the first atom chip (see Fig.6.1) that will be placed in the vacuum chamber, we plan to optimize the experimental sequence up to the forced evaporative cooling in the Z-trap. The three equally spaced linear wires (which go through the **U** and **Z** wires, shown in Fig.6.1(c)) can be used to demonstrate the three ideas presented in Chapter 2 and 3. This opens up the possibility to experimentally verify the adiabaticity of the guide within the parameter range identified numerically in Chapter 3. The effect of wire corrugation and the efficiency of the modulation technique can then be quantitatively measured. This preliminary detailed study can give

us a deeper insight into the experimental challenges in the demonstration of the circular waveguide. In the following, an overview of various wires present on the first atom chip is given.

The layout of the mask used for chip fabrication can be seen in Fig.6.1. The central part of the chip consists of **U** and **Z** wires and they will be used in the initial cooling stages of the experiment. The two long wires on either side of the legs of the **U** and **Z** wires will provide an additional longitudinal confinement to the **Z**-trap. The two smaller **U** wires in the upper half of the chip will be responsible for the precise control of the longitudinal position of the atom cloud in the **Z**-trap at the beginning of the atom interferometric sequence. As mentioned earlier, the three straight wires with a separation of $5 \mu m$, can be used to generate a linear guide. As proposed in [118, 119], a circular guide is not the only geometry that can be used for a guided Sagnac interferometer. An area enclosed interferometer may be realized with a linear waveguide by simultaneously exciting the transverse and longitudinal [120, 121] motions of the atoms. In the image of the mask, we can also see a small circular loop next to the three wires. It can be used to generate, for instance a magnetic field which can imprint a phase shift on the atom cloud.

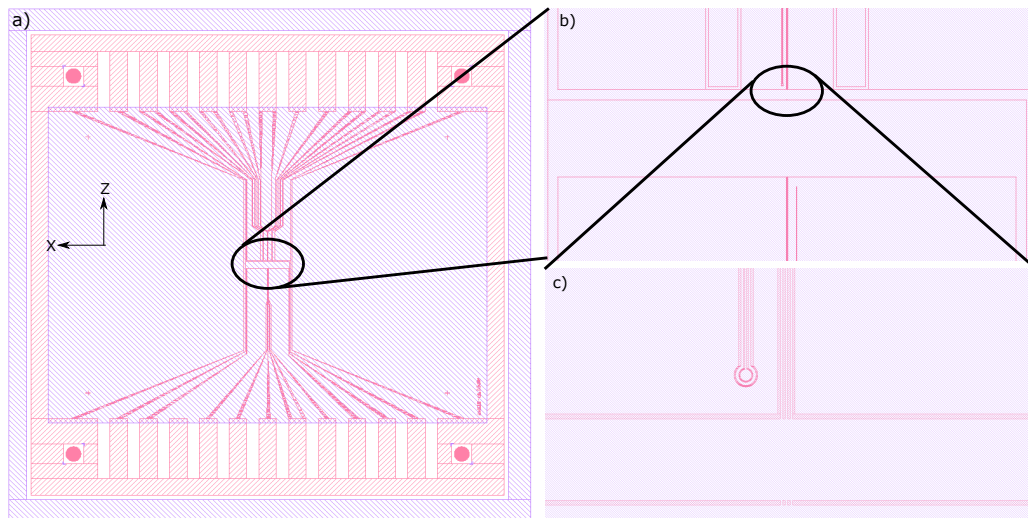


Figure 6.1 *Mask of the first atom chip used in the chip fabrication, relevant sections of the mask at the central part are zoomed to show the details.*

6.1.1 Fabrication of the atom chip

The atom chip fabrication is being carried out in the clean room facility of Observatoire de Paris and also at Thales Research and Technology (TRT) under

the OnACIS (On Atom-Chip Inertial Sensing) collaboration between SYRTE and TRT.

Choice of the substrate

One of the important design and the fabrication criterion of an atom chip is the microwire resistance. Indeed, depending on the resistance of the wires (which depends on the cross-sectional area), the ohmic heat generated can significantly increase the temperature of the chip and can even melt the wires if the excess heat is not drained properly. The copper block holding the chip acts as a heat sink and is the only way to dissipate the heat. The substrate plays therefore a key role in the heat conduction between the wires and the copper block. A good substrate would be electrically insulating in order not to short-circuit different wires on the chip and at the same time it would be a good thermal conductor. We chose Aluminium Nitride (AlN) substrates for the chip, in view of its relatively high thermal conductivity (170 – 280 W/m/K [40]). To minimize the wire roughness, we use polished AlN substrates of 600 μm thickness, with a surface roughness of few tens of nano meters. For the metallic wires on the substrate, we use gold for its chemical neutrality and high conductivity.

Process

Depending on the technique with which the microwires are realised on the substrate, there are two methods widely used in the fabrication of atom chips: a) evaporation and b) electroplating [122]. Electroplating is often used when the height of the wires is several microns, while evaporation is the preferred choice for excellent wire quality. Nevertheless, it was shown that the evaporation technique can be used to grow wires as tall as 5 μm [122]. In our atom chip, all wires were designed to be 3 μm high. Such a thickness allows us to run high enough currents (sufficient for our needs), without destroying the wires. In order to achieve better wire quality, which is very critical to avoid coherence loss or cloud fragmentation, we use the evaporation technique¹ [123]. The main steps in our atom chip fabrication using evaporation are shown in Fig.6.2.

The two different metallization processes have been tested for the fabrication of the trapping microwires. A comparison between the processes will allow us to identify the one that produces wires with the smallest wall roughness, a critical fabrication limitation for the coherent propagation of atomic wavepacket in magnetic guides. The results obtained so far for this test are presented in Fig.6.3 where we can see that both processes are equivalent and can be equally employed for the fabrication of our atom chips.

¹Nevertheless, steps have also been taken to produce atom chips with electroplating.

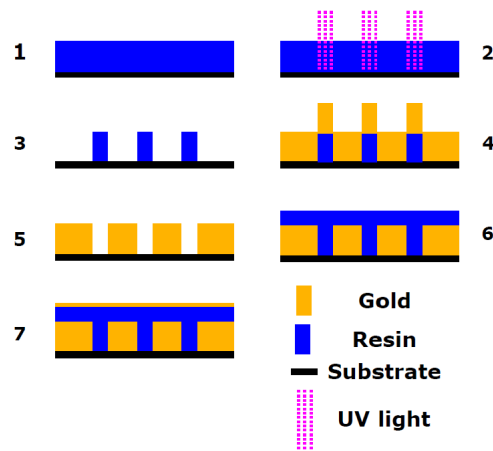


Figure 6.2 *Different stages in the development of our atom chip: 1) A resin is spin coated on AlN substrate. 2) The sample is then covered with a mask (glass piece with a chromium layer) and is exposed to UV light. Part of the resin exposed to UV light is hardened. 3) The soft part of the resin is then dissolved leaving a negative copy of the wires. 4) Substrate is then transferred to a vacuum chamber where gold is evaporated. 5) The resin is lifted off leaving the wires on the chip. 6) Few microns of resin is coated to insulate the wires. 7) Finally, a layer of gold is coated to create a reflecting surface.*

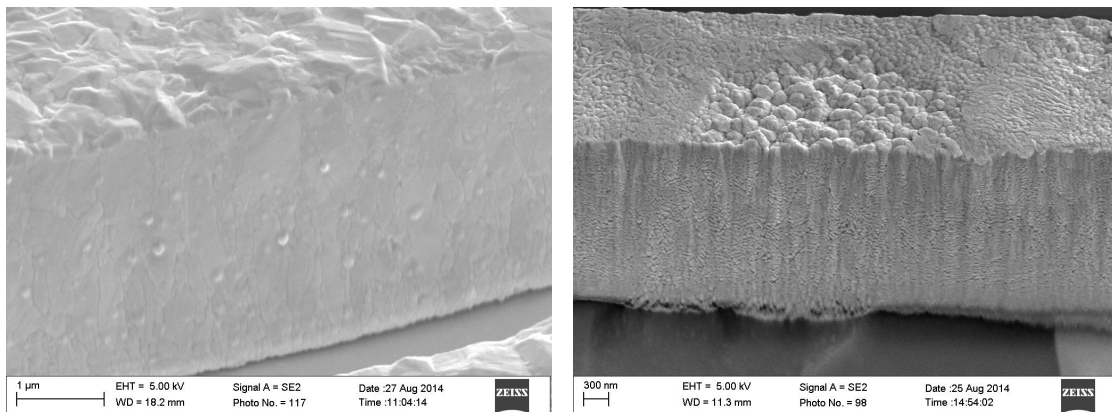


Figure 6.3 *Left, microwire fabricated by electroplating. Right, microwire fabricated by thermal evaporation. The observed wall roughness has a typical spatial correlation length on the order of tens of nm.*

6.2 Bragg system

For the realisation of atom interferometers, we need to implement matterwave coherent beam splitters and mirrors. The splitting can be achieved either magnetically [124, 125, 35] or by using two photon transitions [126, 103]. Atoms loaded into the guide from the Z-trap are in the state $|F = 2, m_F = 2\rangle$. Since the guiding potential depends on the internal state of the atom, any process used to manipulate the interferometer propagation modes should not alter the internal state of the atoms. The widely used two photon Raman transition [126] can be used for splitting the atom cloud. But this process is associated with a change in the internal state of the atoms, which is not desirable for magnetically guided atoms. Therefore, double Bragg diffraction [103] is a natural choice to split and launch the atoms along the guide. We have designed and built the Bragg system for our experiment, and its schematic is shown in Fig.6.4.

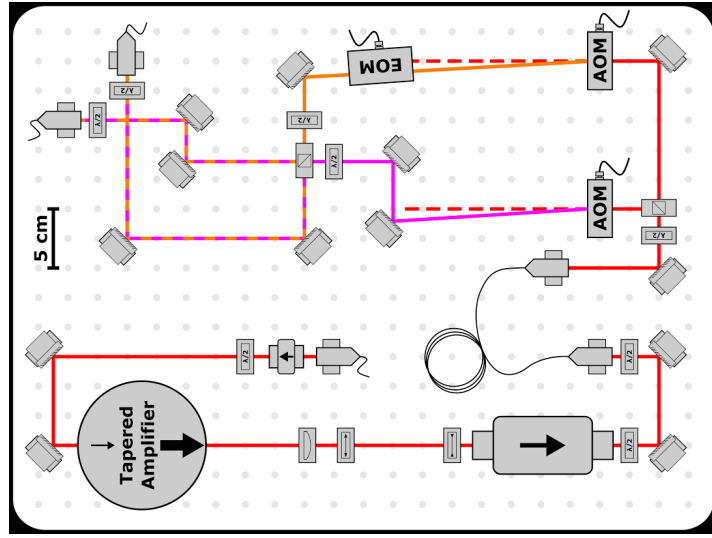


Figure 6.4 *Schematic of the Bragg bench. A beam which is approximately 7 GHz blue detuned to the cooling transition ($F = 2 \rightarrow F' = 3$) is amplified with a TA, which is then split into two with a PBS. The frequency difference between the beams is controlled with the AOMs and the EOM can be used to compensate phase fluctuations between the paths. The beams are then superposed and split again before coupling into the single mode fibres.*

To reduce the spontaneous emissions, the double Bragg diffraction uses beams which are highly detuned from atomic transitions. An atom in $F = 2$ hyperfine level, sees the repumper beam as a cooling beam blue detuned by about 7 GHz and hence it can be used to generate Bragg beams. Therefore, part of the beam from ECDL1 was chosen to generate the necessary beams. Since, the duration

of the Bragg pulses is inversely proportional to the beam intensity, to achieve short pulses the output of the ECDDL1 is amplified (up to 300 mW) with a TA. The amplified beam is then split into two with a PBS, each of the two beams is then frequency shifted with an AOM. To launch the atoms with twice the recoil velocity $2v_r = 11.77 \text{ mm/s}$, a frequency difference of about 15 kHz is necessary to satisfy the resonance condition of the Bragg process. The frequency difference between the two beams can be tuned by setting the frequency difference between the rf sources (generated from a DDS) driving the AOMs. The EOM present in one of the paths can be used to correct the phase fluctuations between the two Bragg beams. The two beams are then overlapped with a PBS and are finally coupled into single mode polarisation maintaining fibres to transport them to the science chamber.

6.3 Projected experimental sequence

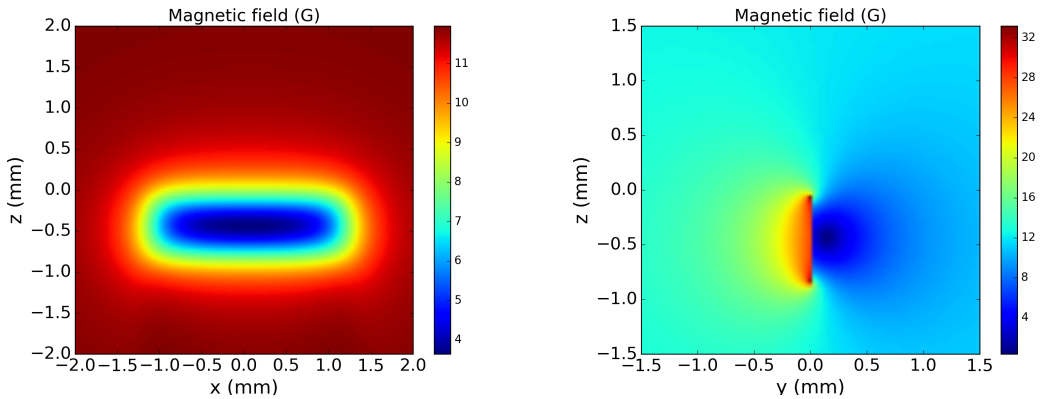
A typical experimental sequence leading to the production of an ultra cold gas or a BEC using an atom chip can be found in the literature (for instance, in the thesis of C. Aussibal [127]). A summary of the various stages of our experiment after the mirror MOT is briefly discussed here.

6.3.1 U-MOT

To manipulate the atoms with the microwires on the chip, they need to be brought closer to the chip surface. In our experiment, atoms are typically trapped at a distance of 5 mm from the chip surface during the mirror-MOT stage. By running a constant current I_U in a **U** shaped wire on the atom chip, and by applying a bias field \mathbf{B}_U parallel to the chip surface (which can be produced by the three pairs of Helmholtz coils surrounding the vacuum chamber) and perpendicular to the central part of the **U**-wire, we can generate a quadrupole field above the chip surface (note that the field due to the legs of the **U**-wire cancel at the point where the bias field balances the field due to the central part [128]). The transfer of atoms is achieved by adiabatically ramping up the currents in the **U**-wire and the bias coils while ramping down the current in the external quadrupole coils. In our case, the central part of the **U**-wire has dimensions 800 $\mu m \times 100 \mu m$, such an aspect ratio gives the required capture volume for an almost 100% efficient transfer of the atoms from the external MOT to U-MOT [127]. Considering the non-negligible width of the wire, by ignoring the height of the wire, the quadrupole gradient around the field zero is [129]

$$b = \frac{\mu_0}{2\pi} \frac{I_U}{r_0^2 + \frac{w^2}{4}}, \quad (6.3.1)$$

where w is the width of the wire and $r_0 = \frac{\mu_0}{2\pi} \frac{I_U}{B_U}$ is the distance between the



(a) Magnetic field in a plane parallel to the chip surface at a distance of $330 \mu\text{m}$. (b) Magnetic field in the vertical plane $x = 0$.

Figure 6.5 *Magnetic field due to the \mathbf{U} -wire and a parallel bias field \mathbf{B}_U considering the finite width and height of the wires. Fields are computed for $I_U = 2 \text{ A}$ and $B_U = 12 \text{ G}$.*

field zero and the chip surface. For instance, with a bias field of $B_U = 12 \text{ G}$ and a current $I_U = 2 \text{ A}$, we can obtain a spherical quadrupole field at a distance of $330 \mu\text{m}$ (see Fig.6.5). To transfer the atoms, the quadrupole field due to the external bias field can be turned off and I_U and B_U ramped from zero to the above values in few tens of milliseconds [127] while keeping the MOT beams on. After transferring the atoms to the U-MOT, the atoms can be brought further close to the chip surface by reducing the current I_U .

6.3.2 Optical molasses and optical pumping

To transfer the atoms efficiently from U-MOT to Z trap, the temperature of atoms needs to be reduced below the Doppler limit using molasses cooling. This step typically lasts few milliseconds: the current in the \mathbf{U} -wire and the bias field \mathbf{B}_U are ramped down to zero while increasing the detuning of the cooling beam to $\sim -15 \Gamma$. At this point the atoms are cooled only by optical forces. After molasses cooling, the atoms are optically pumped to the low field seeking state $|F = 2, m_F = 2\rangle$.

6.3.3 Z-trap

Following the optical pumping, the atoms need to be transferred to the Z-trap for forced evaporation. Contrary to the U-MOT, the atoms are trapped in the Z-trap due to the magnetic forces only. The Z-trap results from the cancellation of the field due to the central part of the \mathbf{Z} -wire with that of an external bias field as in the U-MOT case, but the fields due to the legs add up to produce an

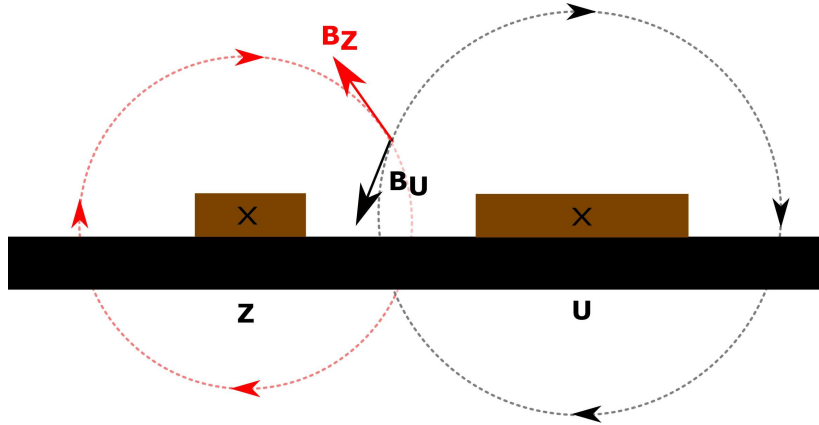
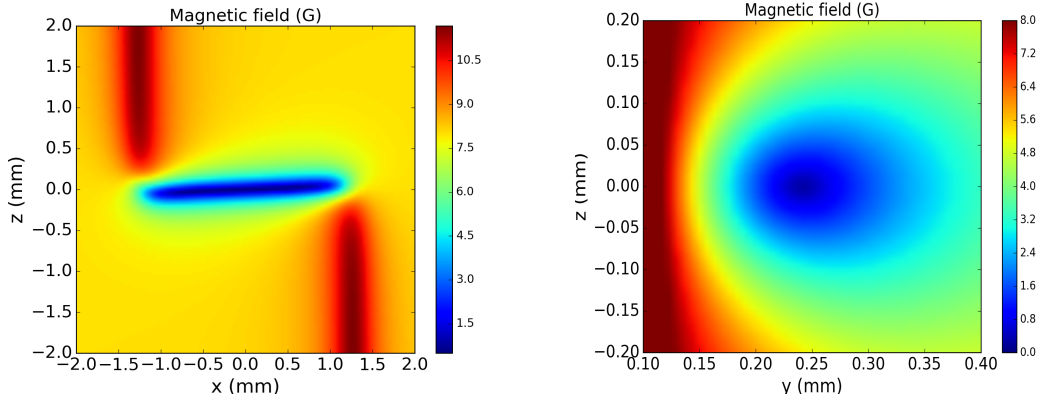


Figure 6.6 *Transfer of atoms between U-MOT and Z-trap requires bias fields at an angle with respect to the chip surface.*

additional bias field along the direction of the trap. This additional bias field helps to lift the degeneracy of the Zeeman levels and prevents Majorana losses. Thus, **Z**-wire in combination with a bias field generates a stable guide with the help of the integrated bias field. Atoms in the U-MOT are localised above the central part of the **U**-wire, in order to move the cloud towards the **Z**-wire requires a bias field at an angle with respect to the chip surface (as shown in Fig.6.6). The transfer can be achieved by simultaneously turning off I_U and B_U , and turning on I_Z and B_z . For instance, by taking $I_Z = 2$ A and applying a parallel bias field



(a) Magnetic field in a plane parallel to the chip surface at a distance of $230 \mu\text{m}$. (b) Magnetic field in the vertical plane $x = 0$.

Figure 6.7 *Magnetic field due to the **Z**-wire and a parallel bias field B_z considering the finite width and height of the wires. Fields are computed for $I_Z = 1$ A and $B_z = 8$ G.*

$B_z = 8$ G, a trap is formed approximately at $r = \mu_0 I_Z / 2\pi B_z = 230 \mu\text{m}$ from

the chip surface (see Fig.6.7).

6.3.4 Forced rf evaporation

After the atoms are transferred to the Z-trap, they need to be cooled to few hundred nano Kelvin in order to them efficiently into the magnetic waveguide. Taking advantage of the atom chip, a forced rf evaporation can be used to achieve few hundred nano Kelvin within few seconds. Since, the U-wire is unused when atoms are held in the Z-trap, it can therefore be used to generate the necessary rf field for the evaporation.

6.3.5 Guided Sagnac interferometer

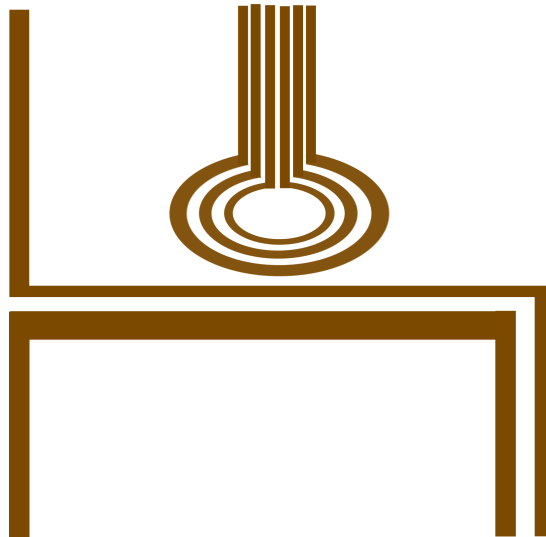


Figure 6.8 *A possible wire configuration to realize a circular waveguide using three concentric circular wires. Such a wire configuration allows to transfer atoms from U-MOT to Z-trap and eventually to the waveguide (note that the wires in the image are not shown to scale).*

Finally, the ultracold atom cloud (~ 300 nK) can be transferred to a circular guide created by three concentric wires located adjacent to the Z-wire as depicted in the Fig.6.8. These three concentric wires are not present in the first atom chip, but they will be incorporated in the second version. The transfer can be achieved by tilting the bias field of the Z-trap and by increasing the currents in the circular wires. As explained in Chapter 4, once the atoms are loaded into the circular guide, Bragg pulses can be used to split and recombine the atoms after one (or several) round trip(s) around the guide. The angular velocity of the lab frame can then be extracted by measuring atom population in different momentum output states of the interferometer.

This thesis discussed different strategies to generate a magnetic waveguide. The three considered configurations can be achieved by using the same wire configuration. Modulated waveguides use the current modulation technique, which simultaneously solves the problem of coherence and Majorana losses. Assuming that the transverse potential of the guide is harmonic, the propagation of the atoms in the circular guide was shown to be multimode. The effects of multimode propagation of the atoms and their finite temperature are quantified using a simple model to be verified experimentally. Our calculations show that for an ultra cold gas, launched at a velocity v_0 in a guide of radius r_0 and transverse guiding frequency ω_r , the multimode propagation leads to additional phase shifts apart from the usual Sagnac phase. An important result of our study is that this additional phase shift can be suppressed up to first order by operating the interferometer such that the quantity $r_0 v_0 / \omega_r$ is an integer. Operation of interferometer with thermal atoms was shown to amplify the contrast loss, without inducing any additional phase shifts. The contrast loss due to finite temperature can also be suppressed by choosing $r_0 v_0 / \omega_r$ as an integer. Consequently, we have found a necessary condition that allows the suppression of *an intrinsic to a circular waveguide phase shift*, that can produce a systematic effect deleterious for inertial sensing.

Appendices

A. Energy levels of ^{87}Rb

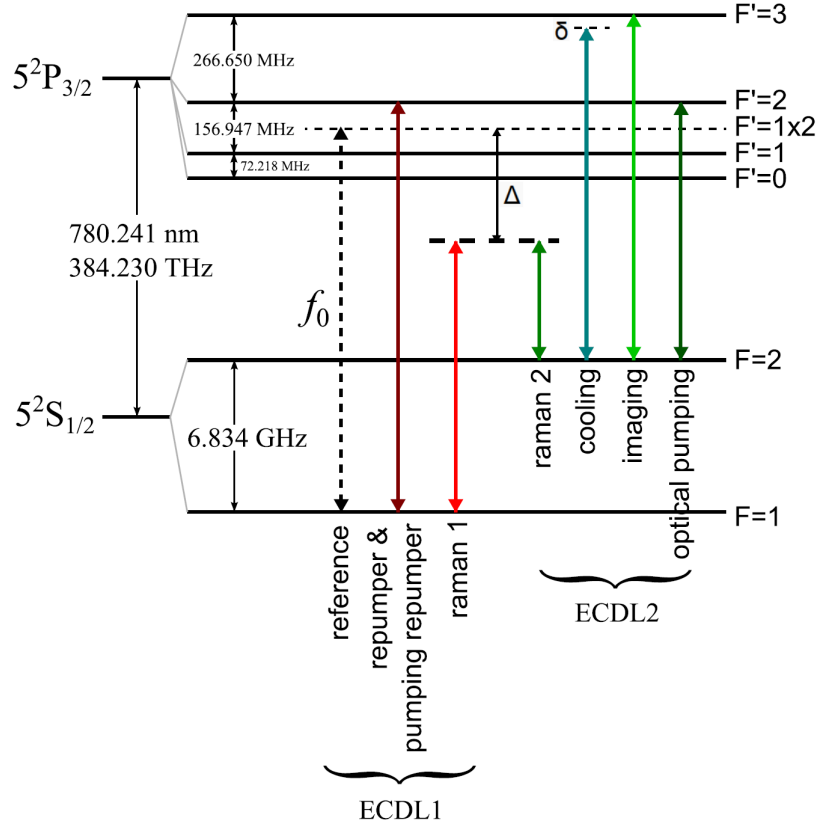


Figure .9 An overview of the optical frequencies needed for trapping, cooling, detection and interferometry. The frequency of ECDL1 is f_0 , δ is the detuning of the cooling transition and Δ denotes the detuning of the Raman transition (image taken from the thesis of W. Yan[110]).

Rubidium naturally exists in two isotopes ^{85}Rb and ^{87}Rb with an abundance of 72.2% and 27.8% respectively. Our experiment uses the isotope ^{87}Rb . Grossly, the energy levels of ^{87}Rb are characterised by the principal and orbital angular momentum quantum numbers n and L , of the outermost electron. The transitions between these gross energy levels possess a fine structure due to the coupling between orbital angular momentum \mathbf{L} and the spin angular momentum \mathbf{S} of the outer electron. The fine structure levels are characterised by the total angular momentum $\mathbf{J} = \mathbf{L} + \mathbf{S}$, which takes a value between $|L - S|$ and $|L + S|$. The ground state of ^{87}Rb has $L = 0$ (since the electronic configuration is $5s^1$), by taking the electron spin $S = 1/2$, the total electron angular momentum is $J = 1/2$. The ground state is succinctly written as $5^2S_{1/2}$, where 5 is the principal quantum number, superscript denotes $2S + 1$ and the subscript denotes J . Similarly, for

the first excited state $L = 1$, $J = 1/2$ or $J = 3/2$ and the corresponding states are $5^2P_{1/2}$ and $5^2P_{3/2}$. The transitions $5^2S_{1/2} \rightarrow 5^2P_{1/2}$ and $5^2S_{1/2} \rightarrow 5^2P_{3/2}$ are usually referred as D_1 and D_2 lines. Each of these lines has a hyperfine structure due to the coupling between the total electron angular momentum \mathbf{J} and the nuclear angular momentum \mathbf{I} . The total atomic angular momentum is $\mathbf{F} = \mathbf{J} + \mathbf{I}$. The hyperfine structure is characterised by F which takes values between $|J - I|$ and $|J + I|$. If we consider the D_2 transition (all the optical frequencies of our experiment are based on this transition), the ground state $5^2S_{1/2}$ has $J = 1/2$ and the nuclear angular momentum is $I = 3/2$, therefore $F = 1$ or 2 . The excited state $5^2P_{3/2}$ has $J = 3/2$ and the possible values of F are $0, 1, 2$ and 3 . The hyperfine transitions of the D_2 line are shown in Fig..9.

B. Calculation of collection efficiency

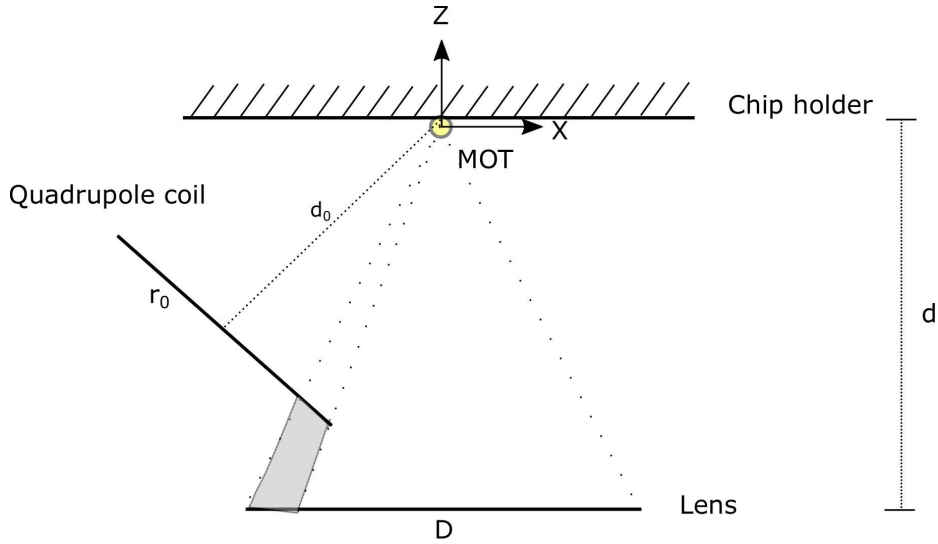


Figure .10 *Schematic of the solid angle enclosed by the fluoresced light from the MOT. Part of the solid angle blocked by the quadrupole coil is shaded in grey color.*

Numerical computation of the solid angle taking into account the obstruction of the quadrupole coil is discussed here. A projection of the schematic can be seen in Fig..10. The co-ordinate axis is chosen so that the MOT is at origin. Quadrupole coil is at an angle of 45° , with respect to the chip holder and the centre of the coil is at distance d_0 from MOT. The lens used to image fluoresced light on the photo diode has a diameter D and is at a distance d below the chip surface. To compute the solid angle we generate rays in all directions, if the ray reaches the lens we add the contribution to solid angle due to that direction. Let us consider a ray of light emitted from origin in the direction (θ, ϕ) where ϕ

is the polar angle and θ is the azimuthal angle. The equation of a straight line along (θ, ϕ) is

$$\frac{x}{\cos(\theta) \sin(\phi)} = \frac{y}{\sin(\theta) \sin(\phi)} = \frac{z}{\cos(\phi)} . \quad (.0.2)$$

It is clear that the domain of interest in the computation of the solid angle is $\theta \in [0, 2\pi)$ and $\phi \in [\pi - \tan^{-1}(\frac{D}{2d}), \pi]$. The equation of the plane defining the MOT coil is $x + z = -\sqrt{2}d_0$. The coordinates of the point of intersection between the straight line (Eq.0.2) and the plane ($x + z = -\sqrt{2}d_0$) are

$$x_1 = -\frac{\sqrt{2}d_0 \cos(\theta) \tan(\phi)}{1 + \cos(\theta) \tan(\phi)} , \quad (.0.3)$$

$$y_1 = -\frac{\sqrt{2}d_0 \sin(\theta) \tan(\phi)}{1 + \cos(\theta) \tan(\phi)} , \quad (.0.4)$$

$$z_1 = -\frac{\sqrt{2}d_0}{1 + \cos(\theta) \tan(\phi)} . \quad (.0.5)$$

Note that the coordinates of the centre of the quadrupole coil are $(x_0, y_0, z_0) = (-\frac{d_0}{\sqrt{2}}, 0, -\frac{d_0}{\sqrt{2}})$. A ray in a given direction intersects the quadrupole coil if and only if

$$(x_1 - x_0)^2 + (y_1 - y_0)^2 + (z_1 - z_0)^2 < r_0^2 . \quad (.0.6)$$

We discretize the domain of ϕ and θ , and for each direction we verify if the ray reaches the lens. If it does, the infinitesimal solid angle $dS = \sin(\phi)d\theta d\phi$ is added. For the parameters $d_0 = 49 \text{ mm}$, $r_0 = 40 \text{ mm}$, $d = 150 \text{ mm}$ and $D = 50.8 \text{ mm}$, the solid angle obtained from this algorithm is 0.0061. This value is used in the calculation of collection efficiency of the florescence imaging system.

C. Some properties of Displacement operator

Here we provide the derivation of some properties of the Displacement operator, that were used in the Section.4.2.2. Quantum mechanical harmonic oscillator can be described elegantly with the ladder operators, a and a^\dagger satisfying $[a, a^\dagger] = 1$. The Hamiltonian $\mathcal{H} = -\frac{\hbar^2}{2m} \frac{d^2}{dx^2} + \frac{1}{2}m\omega^2 x^2$ can be written as

$$\mathcal{H} = \hbar\omega[N + \frac{1}{2}] , \quad (.0.7)$$

where N is a number operator defined as $N = a^\dagger a$. Number operator and the Hamiltonian have common eigen vectors, which are denoted with $|n\rangle$, for $n \geq 0$ such that

$$N |n\rangle = n |n\rangle . \quad (.0.8)$$

The eigen energies of the Hamiltonian are given by $E_n = [n + \frac{1}{2}]\hbar\omega$. These number states are related to each other by the ladder operators as follows

$$a^\dagger |n\rangle = \sqrt{n+1} |n+1\rangle , \quad (.0.9)$$

$$a |n\rangle = \sqrt{n} |n-1\rangle . \quad (.0.10)$$

A coherent state $|\alpha\rangle$ is an eigen state of the operator a with the eigen value α

$$a |\alpha\rangle = \alpha |\alpha\rangle , \quad (.0.11)$$

where α is a complex number. Using Eq.0.11, expanding the coherent state in terms of number states we obtain

$$|\alpha\rangle = e^{-\frac{|\alpha|^2}{2}} \sum_{n=0}^{\infty} \frac{\alpha^n}{\sqrt{n!}} |n\rangle . \quad (.0.12)$$

The time evolution of the coherent state $|\alpha\rangle$ can be computed using the above relation

$$e^{i\mathcal{H}\frac{t}{\hbar}} |\alpha\rangle = e^{-\frac{|\alpha|^2}{2}} \sum_{n=0}^{\infty} \frac{\alpha^n}{\sqrt{n!}} e^{-i\omega t(a^\dagger a + \frac{1}{2})} |n\rangle , \quad (.0.13)$$

which can be simplified as

$$e^{i\mathcal{H}\frac{t}{\hbar}} |\alpha\rangle = |e^{-i\omega t}\alpha\rangle . \quad (.0.14)$$

Therefore a coherent state evolves into another coherent state or in other words a coherent state moves on a circle of radius $|\alpha|$ with an angular velocity ω in the complex plane. Let us define an operator called Displacement operator $\mathcal{D}(\alpha) = e^{\alpha a^\dagger - \alpha^* a}$. Using the Backer-Campbell-Hausdorff (BCH) identity, Displacement operator can be written as²

$$\mathcal{D}(\alpha) = e^{\alpha a^\dagger - \alpha^* a} = e^{-\frac{|\alpha|^2}{2}} e^{\alpha a^\dagger} e^{-\alpha^* a} = e^{\frac{|\alpha|^2}{2}} e^{-\alpha^* a} e^{\alpha a^\dagger} . \quad (.0.15)$$

With the above result, we can compute the action of the Displacement operator on the ground state

$$\begin{aligned} \mathcal{D}(\alpha) |0\rangle &= e^{-\frac{|\alpha|^2}{2}} e^{\alpha a^\dagger} e^{-\alpha^* a} |0\rangle \\ &= e^{-\frac{|\alpha|^2}{2}} e^{\alpha a^\dagger} |0\rangle \\ &= |\alpha\rangle . \end{aligned} \quad (.0.16)$$

Therefore, displacement operator can be used to generate a coherent state from the ground state.

²BCH identity is $e^{A+B} = e^{-[A,B]/2} e^A e^B$ if $[A, [A, B]] = [B, [A, B]] = 0$. By taking $A = \alpha a^\dagger$ and $B = -\alpha^* a$ we get $\mathcal{D}(\alpha) = e^{-\frac{|\alpha|^2}{2}} e^{\alpha a^\dagger} e^{-\alpha^* a}$. Exchanging the role of A and B , we can show that $\mathcal{D}(\alpha) = e^{\frac{|\alpha|^2}{2}} e^{-\alpha^* a} e^{\alpha a^\dagger}$.

Let us now consider the displacement operator $\mathcal{D}(\alpha + \beta)$ for some complex numbers α and β . Using the BCH identity we get³

$$\begin{aligned}\mathcal{D}(\alpha + \beta) &= e^{\alpha a^\dagger - \alpha^* a + \beta a^\dagger - \beta^* a} \\ &= e^{\alpha a^\dagger - \alpha^* a} e^{\beta a^\dagger - \beta^* a} e^{-\frac{1}{2}[\alpha a^\dagger - \alpha^* a, \beta a^\dagger - \beta^* a]} \\ &= \mathcal{D}(\alpha)\mathcal{D}(\beta)e^{-\mathcal{I}m(\alpha\beta^*)} .\end{aligned}\tag{.0.17}$$

The above identity helps to compute the overlap between two coherent states

$$\langle \alpha | \beta \rangle = \langle 0 | \mathcal{D}^\dagger(\alpha)\mathcal{D}(\beta) | 0 \rangle \tag{.0.18}$$

$$\begin{aligned}&= e^{\mathcal{I}m(\alpha\beta^*)} \langle 0 | \mathcal{D}(\beta - \alpha) | 0 \rangle \\ &= e^{\mathcal{I}m(\alpha\beta^*)} e^{-\frac{|\alpha - \beta|^2}{2}} .\end{aligned}\tag{.0.19}$$

Lastly, let us consider a similarity transformation of a using Displacement operator i.e. $\mathcal{D}^\dagger(\alpha)a\mathcal{D}(\alpha)$. To evaluate this, we can make use of the following identity

$$e^A B e^{-A} = B + [A, B] \quad \text{if } [A, [A, B]] = 0 . \tag{.0.20}$$

By taking $A = -\alpha a^\dagger + \alpha^* a$ and $B = a$ we obtain

$$\mathcal{D}^\dagger(\alpha)a\mathcal{D}(\alpha) = a + \alpha . \tag{.0.21}$$

Similarly, we have

$$\mathcal{D}^\dagger(\alpha)a^\dagger\mathcal{D}(\alpha) = a^\dagger + \alpha^* . \tag{.0.22}$$

D. Density matrix in coherent state basis

A thermal state of a harmonic oscillator at temperature θ can be described by the density matrix. Taking the occupation probability of a given number state as the Boltzmann distribution, the density matrix is given by

$$\rho = \sum_{n=0}^{\infty} P_n |n\rangle \langle n| . \tag{.0.23}$$

where $P_n = (1 - e^{-\hbar\omega_r/k_B\theta})e^{-n\hbar\omega_r/k_B\theta}$. Also, note that trace of the density operator is one i.e. $Tr(\rho) = 1$. The above density matrix can be expressed in the coherent state basis $\{|\alpha\rangle\}$. To do so, we first compute the matrix element $\langle \alpha | \rho | \alpha \rangle$, which can be expressed as

$$\langle \alpha | \rho | \alpha \rangle = \sum_{n=0}^{\infty} P_n |\langle \alpha | n \rangle|^2 . \tag{.0.24}$$

³Here we choose $A = \alpha a^\dagger - \alpha^* a$, $B = \beta a^\dagger - \beta^* a$.

Substituting $|\langle \alpha | n \rangle|^2 = e^{-|\alpha|^2} \frac{|\alpha|^{2n}}{n!}$ and summing over n we obtain

$$\langle \alpha | \rho | \alpha \rangle = (1 - e^{-\hbar\omega_r/k_B\theta}) e^{-|\alpha|^2(1-e^{-\hbar\omega_r/k_B\theta})} . \quad (.0.25)$$

Therefore, the density matrix in the basis of coherent states is

$$\rho = N \int (1 - e^{-\hbar\omega_r/k_B\theta}) e^{-|\alpha|^2(1-e^{-\hbar\omega_r/k_B\theta})} |\alpha\rangle \langle \alpha| d^2\alpha , \quad (.0.26)$$

where N is the normalisation constant. Since $\{|\alpha\rangle\}$ form an over complete basis, the normalization constant N needs to be chosen so that trace of the density matrix is equal to one. We can verify that it is achieved for $N = 1/\pi$. Finally, the density matrix in the coherent state basis is given by

$$\rho = \int P(\alpha) |\alpha\rangle \langle \alpha| d^2\alpha , \quad (.0.27)$$

where $P(\alpha) = \frac{1}{\pi} (1 - e^{-\hbar\omega_r/k_B\theta}) e^{-|\alpha|^2(1-e^{-\hbar\omega_r/k_B\theta})}$ is the Glauber-Sudarshan distribution.

Bibliography

- [1] J. W. David Titterton, *Strapdown Inertial Navigation Technology* (Institution of Engineering and Technology, 2004). URL : http://www.ebook.de/de/product/21923218/david_titterton_john_weston_strapdown_inertial_navigation_technology.html. 1
- [2] K. U. Schreiber, G. E. Stedman, H. Igel, et A. Flaws, “Ring laser gyroscopes as rotation sensors for seismic wave studies,” dans “Earthquake Source Asymmetry, Structural Media and Rotation Effects,” (Springer Science Business Media), p. 377–390. URL : http://dx.doi.org/10.1007/3-540-31337-0_29. 1
- [3] L. I. Schiff, “Possible new experimental test of general relativity theory,” *Phys. Rev. Lett.* **4**, 215–217 (1960). URL : <http://dx.doi.org/10.1103/PhysRevLett.4.215>. 1
- [4] C. W. F. Everitt, D. B. DeBra, B. W. Parkinson, J. P. Turneaure, J. W. Conklin, M. I. Heifetz, G. M. Keiser, A. S. Silbergleit, T. Holmes, J. Kolodziejczak, M. Al-Meshari, J. C. Mester, B. Muhlfelder, V. G. Solomonik, K. Stahl, P. W. Worden, W. Bencze, S. Buchman, B. Clarke, A. Al-Jadaan, H. Al-Jibreen, J. Li, J. A. Lipa, J. M. Lockhart, B. Al-Suwaidan, M. Taber, et S. Wang, “Gravity probe b: Final results of a space experiment to test general relativity,” *Phys. Rev. Lett.* **106** (2011). URL : <http://dx.doi.org/10.1103/PhysRevLett.106.221101>. 1, 1.2
- [5] M. Weinberg et A. Kourepenis, “Error sources in in-plane silicon tuning-fork MEMS gyroscopes,” *Journal of Microelectromechanical Systems* **15**, 479–491 (2006). URL : <http://dx.doi.org/10.1109/JMEMS.2006.876779>. 1
- [6] G. Sagnac, “Effet tourbillonnaire optique. la circulation de l’ether lumineux dans un interferographe tournant,” *J. Phys. Theor. Appl.* **4**, 177–195 (1914). URL : <http://dx.doi.org/10.1051/jphysap:019140040017700>. 1

- [7] H. J. Arditty et H. C. Lefèvre, “Sagnac effect in fiber gyroscopes,” *Optics Letters* **6**, 401 (1981). URL : <http://dx.doi.org/10.1364/OL.6.000401.1>
- [8] H. J. Arditty et H. C. Lefèvre, “Theoretical basis of sagnac effect in fiber gyroscopes,” dans “Springer Series in Optical Sciences,” (Springer Science Business Media, 1982), p. 44–51. URL : http://dx.doi.org/10.1007/978-3-540-39490-7_3.1
- [9] H. C. Lefèvre, “The fiber-optic gyroscope, a century after sagnac’s experiment: The ultimate rotation-sensing technology?” *Comptes Rendus Physique* **15**, 851–858 (2014). URL : <http://dx.doi.org/10.1016/j.crhy.2014.10.007.1>
- [10] G. B. Malykin, “Sagnac effect in ring lasers and ring resonators. how does the refractive index of the optical medium influence the sensitivity to rotation?” *Physics-Uspekhi* **57**, 714–720 (2014). URL : <http://dx.doi.org/10.3367/UFNe.0184.201407g.0775.1>
- [11] K. U. Schreiber, A. Gebauer, H. Igel, J. Wassermann, R. B. Hurst, et J.-P. R. Wells, “The centennial of the sagnac experiment in the optical regime: From a tabletop experiment to the variation of the earth’s rotation,” *Comptes Rendus Physique* **15**, 859–865 (2014). URL : <http://dx.doi.org/10.1016/j.crhy.2014.10.003.1>
- [12] P. Storey et C. Cohen-Tannoudji, “The feynman path integral approach to atomic interferometry. a tutorial,” *J. Phys. II France* **4**, 1999–2027 (1994). URL : <http://dx.doi.org/10.1051/jp2:1994103.1>
- [13] J. L. Staudenmann, S. A. Werner, R. Colella, et A. W. Overhauser, “Gravity and inertia in quantum mechanics,” *Phys. Rev. A* **21**, 1419–1438 (1980). URL : <http://dx.doi.org/10.1103/PhysRevA.21.1419.1>
- [14] F. Hasselbach et M. Nicklaus, “An electron optical sagnac experiment,” *Physica B C* **151**, 230–234 (1988). URL : [http://dx.doi.org/10.1016/0378-4363\(88\)90171-4.1](http://dx.doi.org/10.1016/0378-4363(88)90171-4.1)
- [15] F. Riehle, T. Kisters, A. Witte, J. Helmcke, et C. J. Bordé, “Optical ramsey spectroscopy in a rotating frame: Sagnac effect in a matter-wave interferometer,” *Phys. Rev. Lett.* **67**, 177–180 (1991). URL : <http://dx.doi.org/10.1103/PhysRevLett.67.177.1>
- [16] A. Lenef, T. D. Hammond, E. T. Smith, M. S. Chapman, R. A. Rubenstein, et D. E. Pritchard, “Rotation sensing with an atom interferometer,” *Phys. Rev. Lett.* **78**, 760–763 (1997). URL : <http://dx.doi.org/10.1103/PhysRevLett.78.760.1>

- [17] T. L. Gustavson, P. Bouyer, et M. A. Kasevich, “Precision rotation measurements with an atom interferometer gyroscope,” *Phys. Rev. Lett.* **78**, 2046–2049 (1997). URL : <http://dx.doi.org/10.1103/PhysRevLett.78.2046>. 1
- [18] T. L. Gustavson, A. Landragin, et M. A. Kasevich, “Rotation sensing with a dual atom-interferometer sagnac gyroscope,” *Class. Quantum Grav.* **17**, 2385–2398 (2000). URL : <http://dx.doi.org/10.1088/0264-9381/17/12/311>. 1
- [19] B. Canuel, F. Leduc, D. Holleville, A. Gauguier, J. Fils, A. Viridis, A. Clairon, N. Dimarcq, C. J. Bordé, A. Landragin, et P. Bouyer, “Six-axis inertial sensor using cold-atom interferometry,” *Phys. Rev. Lett.* **97** (2006). URL : <http://dx.doi.org/10.1103/PhysRevLett.97.010402>. 1, 1.4
- [20] S. M. Dickerson, J. M. Hogan, A. Sugarbaker, D. M. S. Johnson, et M. A. Kasevich, “Multiaxis inertial sensing with long-time point source atom interferometry,” *Phys. Rev. Lett.* **111** (2013). URL : <http://dx.doi.org/10.1103/PhysRevLett.111.083001>. 1
- [21] G. W. Hoth, B. Pelle, S. Riedl, J. Kitching, et E. A. Donley, “Point source atom interferometry with a cloud of finite size,” *Appl. Phys. Lett.* **109**, 071113 (2016). URL : <http://dx.doi.org/10.1063/1.4961527>. 1
- [22] I. Dutta, D. Savoie, B. Fang, B. Venon, C. G. Alzar, R. Geiger, et A. Landragin, “Continuous cold-atom inertial sensor with 1 nrad/sec Rotation stability,” *Phys. Rev. Lett.* **116** (2016). URL : <http://dx.doi.org/10.1103/PhysRevLett.116.183003>. 1, 1.5
- [23] M. Meunier, I. Dutta, R. Geiger, C. Guerlin, C. L. G. Alzar, et A. Landragin, “Stability enhancement by joint phase measurements in a single cold atomic fountain,” *Phys. Rev. A* **90** (2014). URL : <http://dx.doi.org/10.1103/PhysRevA.90.063633>. 1
- [24] J. Fils, F. Leduc, P. Bouyer, D. Holleville, N. Dimarcq, A. Clairon, et A. Landragin, “Influence of optical aberrations in an atomic gyroscope,” *The European Physical Journal D* **36**, 257–260 (2005). URL : <http://dx.doi.org/10.1140/epjd/e2005-00255-9>. 1
- [25] A. S. Arnold, C. S. Garvie, et E. Riis, “Large magnetic storage ring for Bose-Einstein condensates,” *Phys. Rev. A* **73** (2006). URL : <http://dx.doi.org/10.1103/PhysRevA.73.041606>. 1, ??
- [26] S. Gupta, K. W. Murch, K. L. Moore, T. P. Purdy, et D. M. Stamper-Kurn, “Bose-Einstein condensation in a circular waveguide,” *Phys. Rev. Lett.* **95** (2005). URL : <http://dx.doi.org/10.1103/PhysRevLett.95.143201>. 1, ??, 2.6, 2.2.1

- [27] P. Navez, S. Pandey, H. Mas, K. Poullos, T. Fernholz, et W. von Klitzing, “Matter-wave interferometers using TAAP rings,” *New Journal of Physics* **18**, 075014 (2016). URL : <http://dx.doi.org/10.1088/1367-2630/18/7/075014>. 1, ??, 2.2.3
- [28] W. H. Heathcote, E. Nugent, B. T. Sheard, et C. J. Foot, “A ring trap for ultracold atoms in an RF-dressed state,” *New Journal of Physics* **10**, 043012 (2008). URL : <http://dx.doi.org/10.1088/1367-2630/10/4/043012>. 1, ??
- [29] J. A. Sauer, M. D. Barrett, et M. S. Chapman, “Storage ring for neutral atoms,” *Phys. Rev. Lett.* **87** (2001). URL : <http://dx.doi.org/10.1103/PhysRevLett.87.270401>. 1, ??, 2.1.4
- [30] P. M. Baker, J. A. Stickney, M. B. Squires, J. A. Scoville, E. J. Carlson, W. R. Buchwald, et S. M. Miller, “Adjustable microchip ring trap for cold atoms and molecules,” *Phys. Rev. A* **80** (2009). URL : <http://dx.doi.org/10.1103/PhysRevA.80.063615>. 1, ??, 2.1.4
- [31] E. M. Wright, J. Arlt, et K. Dholakia, “Toroidal optical dipole traps for atomic Bose-Einstein condensates using laguerre-gaussian beams,” *Phys. Rev. A* **63** (2000). URL : <http://dx.doi.org/10.1103/PhysRevA.63.013608>. 1, ??
- [32] K. Henderson, C. Ryu, C. MacCormick, et M. G. Boshier, “Experimental demonstration of painting arbitrary and dynamic potentials for Bose-Einstein condensates,” *New Journal of Physics* **11**, 043030 (2009). URL : <http://dx.doi.org/10.1088/1367-2630/11/4/043030>. 1, ??
- [33] T. A. Bell, J. A. P. Glidden, L. Humbert, M. W. J. Bromley, S. A. Haine, M. J. Davis, T. W. Neely, M. A. Baker, et H. Rubinsztein-Dunlop, “Bose-Einstein condensation in large time-averaged optical ring potentials,” *New Journal of Physics* **18**, 035003 (2016). URL : <http://dx.doi.org/10.1088/1367-2630/18/3/035003>. 1, ??
- [34] S. Wu, E. Su, et M. Prentiss, “Demonstration of an area-enclosing guided-atom interferometer for rotation sensing,” *Phys. Rev. Lett.* **99** (2007). URL : <http://dx.doi.org/10.1103/PhysRevLett.99.173201>. 1
- [35] T. Schumm, S. Hofferberth, L. M. Andersson, S. Wildermuth, S. Groth, I. Bar-Joseph, J. Schmiedmayer, et P. Krüger, “Matter-wave interferometry in a double well on an atom chip,” *Nat Phys* **1**, 57–62 (2005). URL : <http://dx.doi.org/10.1038/nphys125>. 1, 6.2
- [36] Y. Shin, C. Sanner, G.-B. Jo, T. A. Pasquini, M. Saba, W. Ketterle, D. E. Pritchard, M. Vengalattore, et M. Prentiss, “Interference of Bose-Einstein

- condensates split with an atom chip,” *Phys. Rev. A* **72** (2005). URL : <http://dx.doi.org/10.1103/PhysRevA.72.021604>. 1
- [37] D. Cassettari, B. Hessmo, R. Folman, T. Maier, et J. Schmiedmayer, “Beam splitter for guided atoms,” *Phys. Rev. Lett.* **85**, 5483–5487 (2000). URL : <http://dx.doi.org/10.1103/PhysRevLett.85.5483>. 1
- [38] J. D. Pritchard, A. N. Dinkelaker, A. S. Arnold, P. F. Griffin, et E. Riis, “Demonstration of an inductively coupled ring trap for cold atoms,” *New Journal of Physics* **14**, 103047 (2012). URL : <http://dx.doi.org/10.1088/1367-2630/14/10/103047>. ??, 2.3.2
- [39] T. Müller, X. Wu, A. Mohan, A. Eyvazov, Y. Wu, et R. Dumke, “Towards a guided atom interferometer based on a superconducting atom chip,” *New Journal of Physics* **10**, 073006 (2008). URL : <http://dx.doi.org/10.1088/1367-2630/10/7/073006>. ??
- [40] J. Reichel et V. Vuletic, *Atom Chips* (Wiley VCH Verlag GmbH, 2011). URL : http://www.ebook.de/de/product/12974465/atom_chips.html. 1, 2.13, 6.1.1
- [41] M. Keil, O. Amit, S. Zhou, D. Groswasser, Y. Japha, et R. Folman, “Fifteen years of cold matter on the atom chip: promise, realizations, and prospects,” *Journal of Modern Optics* **63**, 1840–1885 (2016). URL : <http://dx.doi.org/10.1080/09500340.2016.1178820>. 1
- [42] C. Garrido Alzar, “Interférométrie optique et atomique dans l’ingénierie d’états quantiques et les mesures de précision,” (2016). 1
- [43] P. Cladé, S. Guellati-Khélifa, F. Nez, et F. Biraben, “Large momentum beam splitter using bloch oscillations,” *Phys. Rev. Lett.* **102** (2009). URL : <http://dx.doi.org/10.1103/PhysRevLett.102.240402>. 1
- [44] J.-B. Trebbia, C. L. G. Alzar, R. Cornelussen, C. I. Westbrook, et I. Bouchoule, “Roughness suppression via rapid current modulation on an atom chip,” *Phys. Rev. Lett.* **98** (2007). URL : <http://dx.doi.org/10.1103/PhysRevLett.98.263201>. 1, 2.3.2, 2.3.4, 3
- [45] R. Stevenson, M. R. Hush, T. Bishop, I. Lesanovsky, et T. Fernholz, “Sagnac interferometry with a single atomic clock,” *Phys. Rev. Lett.* **115** (2015). URL : <http://dx.doi.org/10.1103/PhysRevLett.115.163001>. 1, 2.2.3
- [46] W. Gerlach et O. Stern, “Der experimentelle nachweis der richtungsquantelung im magnetfeld,” *Zeitschrift fuer Anorganische und Allgemeine Chemier Physik* **9**, 349–352 (1922). URL : <http://dx.doi.org/10.1007/BF01326983>. 2

- [47] W. Ketterle et D. E. Pritchard, “Trapping and focusing ground state atoms with static fields,” *Applied Physics B Photophysics and Laser Chemistry* **54**, 403–406 (1992). URL : <http://dx.doi.org/10.1007/BF00325386>. 2.1
- [48] J. Schmiedmayer, “A wire trap for neutral atoms,” *Applied Physics B Laser and Optics* **60**, 169–179 (1995). URL : <http://dx.doi.org/10.1007/BF01135859>. 2.1
- [49] J. Schmiedmayer, “Guiding and trapping a neutral atom on a wire,” *Phys. Rev. A* **52**, R13–R16 (1995). URL : <http://dx.doi.org/10.1103/PhysRevA.52.R13>. 2.1
- [50] J. D. Weinstein et K. G. Libbrecht, “Microscopic magnetic traps for neutral atoms,” *Phys. Rev. A* **52**, 4004–4009 (1995). URL : <http://dx.doi.org/10.1103/PhysRevA.52.4004>. 2.1
- [51] J. Fortagh, A. Grossmann, C. Zimmermann, et T. W. Hänsch, “Miniaturized wire trap for neutral atoms,” *Phys. Rev. Lett.* **81**, 5310–5313 (1998). URL : <http://link.aps.org/doi/10.1103/PhysRevLett.81.5310>. 2.1.1
- [52] T. H. Bergeman, P. McNicholl, J. Kycia, H. Metcalf, et N. L. Balazs, “Quantized motion of atoms in a quadrupole magnetostatic trap,” *J. Opt. Soc. Am. B* **6**, 2249–2256 (1989). URL : <http://josab.osa.org/abstract.cfm?URI=josab-6-11-2249>. 2.1.1
- [53] I. Lesanovsky et P. Schmelcher, “Spectral properties and lifetimes of neutral fermions and bosons in a magnetic quadrupole trap,” *Phys. Rev. A* **71** (2005). URL : <http://dx.doi.org/10.1103/PhysRevA.71.032510>. 2.1.1
- [54] E. A. Hinds et C. Eberlein, “Quantum propagation of neutral atoms in a magnetic quadrupole guide,” *Phys. Rev. A* **61**, 033614 (2000). URL : <http://link.aps.org/doi/10.1103/PhysRevA.61.033614>. 2.1.1
- [55] E. A. Hinds et C. Eberlein, “Erratum: Quantum propagation of neutral atoms in a magnetic quadrupole guide [phys. rev. a **61** , 033614 (2000)],” *Phys. Rev. A* **64**, 039902 (2001). URL : <http://link.aps.org/doi/10.1103/PhysRevA.64.039902>. 2.1.1
- [56] R. M. Potvliege et V. Zehnlé, “Complex scaling calculation of the decaying quantum-propagation modes of neutral atoms in a magnetic guide,” *Phys. Rev. A* **63** (2001). URL : <http://dx.doi.org/10.1103/PhysRevA.63.025601>. 2.1.1
- [57] C. V. Sukumar et D. M. Brink, “Spin-flip transitions in a magnetic trap,” *Phys. Rev. A* **56**, 2451–2454 (1997). URL : <http://link.aps.org/doi/10.1103/PhysRevA.56.2451>. 2.1.1, 2.1.1

- [58] A. Günther, M. Kemmler, S. Kraft, C. J. Vale, C. Zimmermann, et J. Fortágh, “Combined chips for atom optics,” *Phys. Rev. A* **71**, 063619 (2005). URL : <http://link.aps.org/doi/10.1103/PhysRevA.71.063619>. 2.1.2
- [59] J. Thywissen, M. Olshanii, G. Zabow, M. Drndić, K. Johnson, R. Westervelt, et M. Prentiss, “Microfabricated magnetic waveguides for neutral atoms,” *The European Physical Journal D - Atomic, Molecular, Optical and Plasma Physics* **7**, 361–367 (1999). URL : <http://dx.doi.org/10.1007/s100530050579>. 2.1.3
- [60] N. H. Dekker, C. S. Lee, V. Lorent, J. H. Thywissen, S. P. Smith, M. Drndić, R. M. Westervelt, et M. Prentiss, “Guiding neutral atoms on a chip,” *Phys. Rev. Lett.* **84**, 1124–1127 (2000). URL : <http://link.aps.org/doi/10.1103/PhysRevLett.84.1124>. 2.1.3
- [61] J. Estève, T. Schumm, J.-B. Trebbia, I. Bouchoule, A. Aspect, et I. C. Westbrook, “Realizing a stable magnetic double-well potential on an atom chip,” *The European Physical Journal D - Atomic, Molecular, Optical and Plasma Physics* **35**, 141–146 (2005). URL : <http://dx.doi.org/10.1140/epjd/e2005-00190-9>. 2.1.3, 2.1.3
- [62] T. Davis, “2d magnetic traps for ultra-cold atoms: a simple theory using complex numbers,” *The European Physical Journal D - Atomic, Molecular, Optical and Plasma Physics* **18**, 27–36 (2001). URL : <http://dx.doi.org/10.1140/e10053-002-0003-x>. 2.1.3
- [63] X. Luo, P. Krüger, K. Brugger, S. Wildermuth, H. Gimpel, M. W. Klein, S. Groth, R. Folman, I. Bar-Joseph, et J. Schmiedmayer, “Atom fiber for omnidirectional guiding of cold neutral atoms,” *Optics Letters* **29**, 2145 (2004). URL : <http://dx.doi.org/10.1364/OL.29.002145>. 2.1.4, 2.2.1
- [64] M. B. Crookston, P. M. Baker, et M. P. Robinson, “A microchip ring trap for cold atoms,” *J. Phys. B: At. Mol. Opt. Phys.* **38**, 3289–3298 (2005). URL : <http://dx.doi.org/10.1088/0953-4075/38/18/001>. 2.1.4
- [65] X.-J. Jiang, X.-L. Li, X.-P. Xu, H.-C. Zhang, et Y.-Z. Wang, “Archimedean-spiral-based microchip ring waveguide for cold atoms,” *Chinese Physics Letters* **32**, 020301 (2015). URL : <http://dx.doi.org/10.1088/0256-307X/32/2/020301>. 2.1.4
- [66] P. F. Griffin, E. Riis, et A. S. Arnold, “Smooth inductively coupled ring trap for atoms,” *Phys. Rev. A* **77** (2008). URL : <http://dx.doi.org/10.1103/PhysRevA.77.051402>. 2.1.4, 2.3.2, 2.14

- [67] R. V. E. Lovelace, C. Mehanian, T. J. Tommila, et D. M. Lee, “Magnetic confinement of a neutral gas,” *Nature* **318**, 30–36 (1985). URL : <http://dx.doi.org/10.1038/318030a0>. 2.2
- [68] R. J. C. Spreeuw, C. Gerz, L. S. Goldner, W. D. Phillips, S. L. Rolston, C. I. Westbrook, M. W. Reynolds, et I. F. Silvera, “Demonstration of neutral atom trapping with microwaves,” *Phys. Rev. Lett.* **72**, 3162–3165 (1994). URL : <http://dx.doi.org/10.1103/PhysRevLett.72.3162>. 2.2
- [69] E. A. Cornell, C. Monroe, et C. E. Wieman, “Multiply loaded, ac magnetic trap for neutral atoms,” *Phys. Rev. Lett.* **67**, 2439–2442 (1991). URL : <http://dx.doi.org/10.1103/PhysRevLett.67.2439>. 2.2
- [70] L. Xu, J. Yin, et Y. Wang, “A proposal for guiding and trapping of cold atoms in the AC field of current-carrying wires,” *Jnl Chinese Chemical Soc* **48**, 549–553 (2001). URL : <http://dx.doi.org/10.1002/jccs.200100084>. 2.2
- [71] M. H. Anderson, J. R. Ensher, M. R. Matthews, C. E. Wieman, et E. A. Cornell, “Observation of Bose-Einstein condensation in a dilute atomic vapor,” *Science* **269**, 198–201 (1995). URL : <http://dx.doi.org/10.1126/science.269.5221.198>. 2.2.1
- [72] W. Petrich, M. H. Anderson, J. R. Ensher, et E. A. Cornell, “Stable, tightly confining magnetic trap for evaporative cooling of neutral atoms,” *Phys. Rev. Lett.* **74**, 3352–3355 (1995). URL : <http://dx.doi.org/10.1103/PhysRevLett.74.3352>. 2.2.1
- [73] A. S. Arnold, “Adaptable-radius, time-orbiting magnetic ring trap for Bose-Einstein condensates,” *J. Phys. B: At. Mol. Opt. Phys.* **37**, L29–L33 (2003). URL : <http://dx.doi.org/10.1088/0953-4075/37/2/L03>. 2.2.1
- [74] T. Bergeman, G. Erez, et H. J. Metcalf, “Magnetostatic trapping fields for neutral atoms,” *Phys. Rev. A* **35**, 1535–1546 (1987). URL : <http://dx.doi.org/10.1103/PhysRevA.35.1535>. 2.2.1, 2.3.2
- [75] O. Zobay et B. M. Garraway, “Two-dimensional atom trapping in field-induced adiabatic potentials,” *Phys. Rev. Lett.* **86**, 1195–1198 (2001). URL : <http://dx.doi.org/10.1103/PhysRevLett.86.1195>. 2.2.2
- [76] O. Zobay et B. M. Garraway, “Atom trapping and two-dimensional Bose-Einstein condensates in field-induced adiabatic potentials,” *Phys. Rev. A* **69** (2004). URL : <http://dx.doi.org/10.1103/PhysRevA.69.023605>. 2.2.2

- [77] Y. Colombe, E. Knyazchyan, O. Morizot, B. Mercier, V. Lorent, et H. Perrin, “Ultracold atoms confined in rf-induced two-dimensional trapping potentials,” *Europhysics Letters (EPL)* **67**, 593–599 (2004). URL : <http://dx.doi.org/10.1209/epl/i2004-10095-7>. 2.2.2
- [78] B. M. Garraway et H. Perrin, “Recent developments in trapping and manipulation of atoms with adiabatic potentials,” *J. Phys. B: At. Mol. Opt. Phys.* **49**, 172001 (2016). URL : <http://dx.doi.org/10.1088/0953-4075/49/17/172001>. 2.2.2
- [79] I. Lesanovsky, T. Schumm, S. Hofferberth, L. M. Andersson, P. Krüger, et J. Schmiedmayer, “Adiabatic radio-frequency potentials for the coherent manipulation of matter waves,” *Phys. Rev. A* **73** (2006). URL : <http://dx.doi.org/10.1103/PhysRevA.73.033619>. 2.2.2, 2.2.2
- [80] S. Hofferberth, B. Fischer, T. Schumm, J. Schmiedmayer, et I. Lesanovsky, “Ultracold atoms in radio-frequency dressed potentials beyond the rotating-wave approximation,” *Phys. Rev. A* **76** (2007). URL : <http://dx.doi.org/10.1103/PhysRevA.76.013401>. 2.2.2
- [81] I. Lesanovsky et W. von Klitzing, “Time-averaged adiabatic potentials: Versatile matter-wave guides and atom traps,” *Phys. Rev. Lett.* **99** (2007). URL : <http://dx.doi.org/10.1103/PhysRevLett.99.083001>. 2.2.3, 2.2.3
- [82] B. E. Sherlock, M. Gildemeister, E. Owen, E. Nugent, et C. J. Foot, “Time-averaged adiabatic ring potential for ultracold atoms,” *Phys. Rev. A* **83** (2011). URL : <http://dx.doi.org/10.1103/PhysRevA.83.043408>. 2.2.3
- [83] S. Kraft, A. G. nther, H. Ott, D. Wharam, C. Zimmermann, et J. F. gh, “Anomalous longitudinal magnetic field near the surface of copper conductors,” *J. Phys. B: At. Mol. Opt. Phys.* **35**, L469–L474 (2002). URL : <http://dx.doi.org/10.1088/0953-4075/35/21/102>. 2.3.1, 2.3.1, 2.3.4
- [84] T. Schumm, J. Estève, C. Figl, J.-B. Trebbia, C. Aussibal, H. Nguyen, D. Mailly, I. Bouchoule, C. I. Westbrook, et A. Aspect, “Atom chips in the real world: the effects of wire corrugation,” *The European Physical Journal D* **32**, 171–180 (2005). URL : <http://dx.doi.org/10.1140/epjd/e2005-00016-x>. 2.12, 2.3.1, 2.3.1
- [85] D.-W. Wang, M. D. Lukin, et E. Demler, “Disordered Bose-Einstein condensates in quasi-one-dimensional magnetic microtraps,” *Phys. Rev. Lett.* **92** (2004). URL : <http://dx.doi.org/10.1103/PhysRevLett.92.076802>. 2.3.1

- [86] M. Vangeleyn, B. M. Garraway, H. Perrin, et A. S. Arnold, “Inductive dressed ring traps for ultracold atoms,” *J. Phys. B: At. Mol. Opt. Phys.* **47**, 071001 (2014). URL : <http://dx.doi.org/10.1088/0953-4075/47/7/071001>. 2.3.2
- [87] G. A. Sinuco-León, K. A. Burrows, A. S. Arnold, et B. M. Garraway, “Inductively guided circuits for ultracold dressed atoms,” *Nature Communications* **5**, 5289 (2014). URL : <http://dx.doi.org/10.1038/ncomms6289>. 2.3.2
- [88] J. M. Reeves, O. Garcia, B. Deissler, K. L. Baranowski, K. J. Hughes, et C. A. Sackett, “Time-orbiting potential trap for Bose-Einstein condensate interferometry,” *Phys. Rev. A* **72** (2005). URL : <http://dx.doi.org/10.1103/PhysRevA.72.051605>. 2.3.3, 2.3.3
- [89] K. L. Baranowski et C. A. Sackett, “A stable ac current source for magnetic traps,” *J. Phys. B: At. Mol. Opt. Phys.* **39**, 2949–2957 (2006). URL : <http://dx.doi.org/10.1088/0953-4075/39/14/003>. 2.3.3
- [90] S. Rahav, I. Gilary, et S. Fishman, “Time independent description of rapidly oscillating potentials,” *Phys. Rev. Lett.* **91** (2003). URL : <http://dx.doi.org/10.1103/PhysRevLett.91.110404>. 2.3.4
- [91] R. J. Cook, D. G. Shankland, et A. L. Wells, “Quantum theory of particle motion in a rapidly oscillating field,” *Phys. Rev. A* **31**, 564–567 (1985). URL : <http://dx.doi.org/10.1103/PhysRevA.31.564>. 2.3.4
- [92] I. Bouchoule, J.-B. Trebbia, et C. L. G. Alzar, “Limitations of the modulation method to smooth wire-guide roughness,” *Phys. Rev. A* **77** (2008). URL : <http://dx.doi.org/10.1103/PhysRevA.77.023624>. 2.3.4
- [93] S. Gov et S. Shtrikman, “Dynamic stability of the time-averaged orbiting potential trap: Exact classical analysis,” *J. Appl. Phys.* **86**, 2250 (1999). URL : <http://dx.doi.org/10.1063/1.371038>. 3.3
- [94] S. Gov, S. Shtrikman, et H. Thomas, “1D toy model for magnetic trapping,” *American Journal of Physics* **68**, 334 (2000). URL : <http://dx.doi.org/10.1119/1.19436>. 3.3
- [95] R. Franzosi, B. Zambon, et E. Arimondo, “Nonadiabatic effects in the dynamics of atoms confined in a cylindric time-orbiting-potential magnetic trap,” *Phys. Rev. A* **70** (2004). URL : <http://dx.doi.org/10.1103/PhysRevA.70.053603>. 3.3, 3.3.1
- [96] B. Zambon et R. Franzosi, “Dynamics of atoms in a time-orbiting-potential trap: consequences of the classical description,” *Journal of Physics B:*

- Atomic, Molecular and Optical Physics **43**, 085302 (2010). URL : <http://dx.doi.org/10.1088/0953-4075/43/8/085302>. 3.3
- [97] N. Blanchard et A. Zozulya, “Transverse heating due to nonadiabatic propagation of cold atoms in an atomic guide,” *Optics Communications* **190**, 231–237 (2001). URL : [http://dx.doi.org/10.1016/S0030-4018\(01\)01065-3](http://dx.doi.org/10.1016/S0030-4018(01)01065-3). 4.1
- [98] M. W. J. Bromley et B. D. Esry, “Classical aspects of ultracold atom wave packet motion through microstructured waveguide bends,” *Phys. Rev. A* **69** (2004). URL : <http://dx.doi.org/10.1103/PhysRevA.69.053620>. 4.1
- [99] P. L. Halkyard, M. P. A. Jones, et S. A. Gardiner, “Rotational response of two-component Bose-Einstein condensates in ring traps,” *Phys. Rev. A* **81** (2010). URL : <http://dx.doi.org/10.1103/PhysRevA.81.061602>. 4.1.1
- [100] O. Dutta, M. Jääskeläinen, et P. Meystre, “Single-mode acceleration of matter waves in circular waveguides,” *Phys. Rev. A* **74** (2006). URL : <http://dx.doi.org/10.1103/PhysRevA.74.023609>. 4.1.2
- [101] S. Waldenstrøm et K. Naqvi, “The overlap integrals of two harmonic-oscillator wavefunctions: some remarks on originals and reproductions,” *Chemical Physics Letters* **85**, 581–584 (1982). URL : [http://dx.doi.org/10.1016/0009-2614\(82\)80362-X](http://dx.doi.org/10.1016/0009-2614(82)80362-X). 4.1.2, 4.2.2, 4.2.2
- [102] C. L. G. Alzar, W. Yan, et A. Landragin, “Towards high sensitivity rotation sensing using an atom chip,” dans “Research in Optical Sciences,” (The Optical Society, 2012). URL : <http://dx.doi.org/10.1364/HILAS.2012.JT2A.10>. 4.2
- [103] E. Giese, A. Roura, G. Tackmann, E. M. Rasel, et W. P. Schleich, “Double Bragg diffraction: A tool for atom optics,” *Phys. Rev. A* **88** (2013). URL : <http://dx.doi.org/10.1103/PhysRevA.88.053608>. 4.2, 6.2
- [104] C. Ryu et M. G. Boshier, “Integrated coherent matter wave circuits,” *New Journal of Physics* **17**, 092002 (2015). URL : <http://dx.doi.org/10.1088/1367-2630/17/9/092002>. 4.2.2
- [105] F. Ansbacher, “A note on the overlap integral of two harmonic oscillator wave functions,” *Zeitschrift für Naturforschung A* **14** (1959). URL : <http://dx.doi.org/10.1515/zna-1959-1006>. 4.2.2, 4.2.2
- [106] J. Reichel, W. Hänsel, et T. W. Hänsch, “Atomic micromanipulation with magnetic surface traps,” *Phys. Rev. Lett.* **83**, 3398–3401 (1999). URL : <http://dx.doi.org/10.1103/PhysRevLett.83.3398>. 5, 5.1

- [107] E. L. Raab, M. Prentiss, A. Cable, S. Chu, et D. E. Pritchard, “Trapping of neutral sodium atoms with radiation pressure,” *Phys. Rev. Lett.* **59**, 2631–2634 (1987). URL : <http://dx.doi.org/10.1103/PhysRevLett.59.2631>. 5.1
- [108] P. D. Lett, W. D. Phillips, S. L. Rolston, C. E. Tanner, R. N. Watts, et C. I. Westbrook, “Optical molasses,” *Journal of the Optical Society of America B* **6**, 2084 (1989). URL : <http://dx.doi.org/10.1364/JOSAB.6.002084>. 5.1
- [109] C. Adams et E. Riis, “Laser cooling and trapping of neutral atoms,” *Progress in Quantum Electronics* **21**, 1–79 (1997). URL : [http://dx.doi.org/10.1016/S0079-6727\(96\)00006-7](http://dx.doi.org/10.1016/S0079-6727(96)00006-7). 5.1
- [110] W. Yan, “Design of a magnetic guide for rotation sensing by on chip atom interferometry,” Theses, Université Pierre et Marie Curie (2014). 5.2.1, .9
- [111] F. Reinhard, “Design and construction of an atomic clock on a chip,” Theses, Université Pierre et Marie Curie - Paris VI (2009). 5.11
- [112] A. Browaeys, J. Poupard, A. Robert, S. Nowak, W. Rooijakkers, E. Arimondo, L. Marcassa, D. Boiron, C. Westbrook, et A. Aspect, “Two body loss rate in a magneto-optical trap of metastable he,” *The European Physical Journal D - Atomic, Molecular and Optical Physics* **8**, 199–203 (2000). URL : <http://dx.doi.org/10.1007/s100530050027>. 5.3.1
- [113] T. Arpornthip, C. A. Sackett, et K. J. Hughes, “Vacuum-pressure measurement using a magneto-optical trap,” *Phys. Rev. A* **85** (2012). URL : <http://dx.doi.org/10.1103/PhysRevA.85.033420>. 5.3.1
- [114] R. W. G. Moore, L. A. Lee, E. A. Findlay, L. Torralbo-Campo, G. D. Bruce, et D. Cassettari, “Measurement of vacuum pressure with a magneto-optical trap: A pressure-rise method,” *Rev. Sci. Instrum.* **86**, 093108 (2015). URL : <http://dx.doi.org/10.1063/1.4928154>. 5.3.1
- [115] C. Monroe, W. Swann, H. Robinson, et C. Wieman, “Very cold trapped atoms in a vapor cell,” *Phys. Rev. Lett.* **65**, 1571–1574 (1990). URL : <http://dx.doi.org/10.1103/PhysRevLett.65.1571>. 5.3.2
- [116] S. Chu, L. Hollberg, J. E. Bjorkholm, A. Cable, et A. Ashkin, “Three-dimensional viscous confinement and cooling of atoms by resonance radiation pressure,” *Phys. Rev. Lett.* **55**, 48–51 (1985). URL : <http://dx.doi.org/10.1103/PhysRevLett.55.48>. 5.3.5
- [117] L. Russell, R. Kumar, V. Tiwari, et S. N. Chormaic, “Measurements on release–recapture of cold ^{85}Rb atoms using an optical nanofibre in

- a magneto-optical trap,” *Optics Communications* **309**, 313–317 (2013).
URL : <http://dx.doi.org/10.1016/j.optcom.2013.07.080>. 5.3.5
- [118] J. H. T. Burke et C. A. Sackett, “Scalable Bose-Einstein-condensate sagnac interferometer in a linear trap,” *Phys. Rev. A* **80** (2009). URL : <http://dx.doi.org/10.1103/PhysRevA.80.061603>. 6.1
- [119] O. Garcia, B. Deissler, K. J. Hughes, J. M. Reeves, et C. A. Sackett, “Bose-Einstein-condensate interferometer with macroscopic arm separation,” *Phys. Rev. A* **74** (2006). URL : <http://dx.doi.org/10.1103/PhysRevA.74.031601>. 6.1
- [120] S. Wu, Y.-J. Wang, Q. Diot, et M. Prentiss, “Splitting matter waves using an optimized standing-wave light-pulse sequence,” *Phys. Rev. A* **71** (2005). URL : <http://dx.doi.org/10.1103/PhysRevA.71.043602>. 6.1
- [121] K. J. Hughes, B. Deissler, J. H. T. Burke, et C. A. Sackett, “High-fidelity manipulation of a Bose-Einstein condensate using an optical standing wave,” *Phys. Rev. A* **76** (2007). URL : <http://dx.doi.org/10.1103/PhysRevA.76.035601>. 6.1
- [122] S. Groth, P. Kruger, S. Wildermuth, R. Folman, T. Fernholz, J. Schmiedmayer, D. Mahalu, et I. Bar-Joseph, “Atom chips: Fabrication and thermal properties,” *Appl. Phys. Lett.* **85**, 2980 (2004). URL : <http://dx.doi.org/10.1063/1.1804601>. 6.1.1
- [123] S. Groth, “Development, fabrication, and characterisation of atom chips,” Theses, University of Heidelberg (2006). 6.1.1
- [124] W. Hänsel, J. Reichel, P. Hommelhoff, et T. W. Hänsch, “Trapped-atom interferometer in a magnetic microtrap,” *Phys. Rev. A* **64** (2001). URL : <http://dx.doi.org/10.1103/PhysRevA.64.063607>. 6.2
- [125] P. W. Courteille, B. Deh, J. Fortágh, A. Günther, S. Kraft, C. Marzok, S. Slama, et C. Zimmermann, “Highly versatile atomic micro traps generated by multifrequency magnetic field modulation,” *J. Phys. B: At. Mol. Opt. Phys.* **39**, 1055–1064 (2006). URL : <http://dx.doi.org/10.1088/0953-4075/39/5/005>. 6.2
- [126] K. Moler, D. S. Weiss, M. Kasevich, et S. Chu, “Theoretical analysis of velocity-selective raman transitions,” *Phys. Rev. A* **45**, 342–348 (1992). URL : <http://dx.doi.org/10.1103/PhysRevA.45.342>. 6.2
- [127] C. Aussibal, “Réalisation d’un condensat de Bose-Einstein sur une microstructure,” Theses, Université Paris Sud - Paris XI (2003). URL : <https://pastel.archives-ouvertes.fr/tel-00004429>. 6.3, 6.3.1, 6.3.1

- [128] S. Wildermuth, P. Krüger, C. Becker, M. Brajdic, S. Haupt, A. Kasper, R. Folman, et J. Schmiedmayer, “Optimized magneto-optical trap for experiments with ultracold atoms near surfaces,” *Phys. Rev. A* **69** (2004). URL : <http://dx.doi.org/10.1103/PhysRevA.69.030901>. 6.3.1
- [129] J. Reichel, “Microchip traps and bose einstein condensation,” *Applied Physics B: Lasers and Optics* **74**, 469–487 (2002). URL : <http://dx.doi.org/10.1007/s003400200861>. 6.3.1

Sujet : Propagation of atoms in a magnetic waveguide on a chip

Résumé : In this thesis we study the propagation of atoms in a magnetic toroidal waveguide, with the aim of developing an inertial sensor. Here, we present different strategies to create the waveguide on an atom chip for a guided Sagnac atom interferometer. We devised three solutions which can be achieved using the same wire configuration. They use the current modulation technique, from a new point of view, which simultaneously tackles the problem of wire corrugation and spin dependent Majorana atom losses. The effect of the multimode propagation of the atoms in the guide is also quantified in this thesis. Using a simple model, we covered the propagation of noninteracting ultracold and thermal gases. We identified the operating conditions to realize a cold atom interferometer with a large dynamic range essential for applications in inertial navigation. Experimentally, the thesis describes the realisation and characterisation of the cold atom source close to a gold coated substrate, as well as the implementation and the characterisation of the atom detection systems.

Mots clés : cold atoms, atom chip, guided atom interferometry, inertial sensors, magnetic waveguide, wavepacket propagation

Subject : Propagation d'atomes dans un guide magnétique sur puce

Résumé : Dans cette thèse, nous étudions la propagation d'atomes dans un guide magnétique toroïdal, dans le but de développer un capteur inertiel. Ici, nous présentons différentes stratégies pour créer un guide sur une puce atomique pour un interféromètre Sagnac atomique guidé. Nous avons mis au point trois solutions qui peuvent être réalisées avec la même configuration des fils. Elles utilisent la technique de modulation de courant avec un nouveau point de vue qui traite simultanément la problème de rugosité des fils et les pertes de Majorana dépendantes du spin. L'effet de la propagation multimode des atomes dans le guide est aussi quantifié dans cette thèse. En utilisant un modèle simple, nous avons couvert les cas de la propagation de gaz non interactif ultra froids et thermiques. Nous avons identifié les

conditions opérationnelles pour réaliser un interféromètre à atomes froids avec une grande gamme dynamique, essentielle pour les applications en navigation inertielle. Expérimentalement, cette thèse décrit la réalisation et la caractérisation de la source d'atomes froids proche d'un substrat avec un dépôt d'or, ainsi que l'implémentation et la caractérisation des systèmes de détection.

Keywords : atomes froids, puce atomique, interférométrie atomique guidé, capteurs inertiels , guide magnétique, propagation des paquets d'ondes